

# STELLINGEN

behorende bij het proefschrift

## Plutonium Burning in a Pebble-Bed Type High Temperature Nuclear Reactor

1. Voor een eerlijke vergelijking van de plutoniumconsumptie in verschillende reactoren, dient deze uitgedrukt te worden per eenheid thermische energie in plaats van per eenheid elektrische energie.  
*Dit proefschrift, hoofdstuk 2.*
2. Voor het verkrijgen van een negatieve splijfstoftemperatuurscoëfficiënt met 'reactor-grade' plutonium zijn geen additionele resonantie-absorbers vereist.  
*Dit proefschrift, hoofdstuk 3 en 4.*
3. Het maximum van de fractionele verandering van de resonantie-integraal per graad Kelvin is voor de 1-eV resonantie van Pu-240 kleiner dan voor de 6.7-eV resonantie van U-238, omdat de verhouding van de totale natuurlijke lijnbreedte tot de Doppler-breedte groter is bij de eerstgenoemde.  
*Dit proefschrift, appendix C.*
4. Voor een gegeven oneindige multiplicatiefactor heeft het Doppler-effect een maximum als functie van de effectieve koordlengte van de splijstofzone.  
*Dit proefschrift, appendix C.*
5. De exacte definitie van de factor  $p$  uit de 4-factoren formule is de oneindige multiplicatiefactor gedeeld door het product van de resterende factoren; de betiteling van resonantieontsnappingskans voor deze factor is derhalve onjuist.
6. Het gebruik van de eenheid Sievert per GWa voor de radiotoxiciteit van bestraalde óf van onbestraalde splijstof is onjuist; genoemde eenheid kan alleen betrekking hebben op het *verschil* in radiotoxiciteit tussen de bestraalde en onbestraalde splijstof nadat hiermee een bepaalde hoeveelheid energie is opgewekt.
7. Het concept van de gesmolten-zout reactor als transuranen-verbrander zoals voorgesteld door J. Bultman krijgt niet de aandacht die het verdient.  
*"Actinide Transmutation in Nuclear Reactors", J.H. Bultman, Ph.D. thesis (1995), NRG-Petten.*
8. Voor de optimale benutting van 'reactor-grade' plutonium als brandstof dient het niet te worden opgeslagen maar zo spoedig mogelijk te worden ingezet in reactoren.
9. Louter duurzame energiebronnen kunnen niet voorzien in de huidige energiebehoefte.

10. De beschrijving van een Sweet-Parker stroomlaag met behulp van een tweevloeistof-fenmodel, waarbij de resistiviteit van het plasma is verwaarloosd maar de traagheid van de elektronen niet, voorkomt - anders dan bij een beschrijving daarvan met behulp van Magneto-Hydro-Dynamica - dat een singulariteit van het magneetveld optreedt.  
*"Current-sheet dynamics with inertia and resistivity effects in a two-fluid plasma", Master's thesis E.E. Bende, Physics faculty of the University of Utrecht.*
11. Een koud biertje geeft minder schuim dan een lauw, maar de kraag van een koud biertje blijft wel langer intact.  
*Vertolking van enkele resultaten uit "Beer Foam Physics", L. Ronteltap, Proefschrift Landbouw Universiteit Wageningen (1989).*
12. Vanuit modern taxonomisch oogpunt heeft een koe meer gemeen met een walvis dan met een varken.  
*M. Shimamura et al., Nature, vol. 338 (1997), p. 667-670.*
13. Het vangen van witvis in eutrofe zoetwatermeren is een methode om het aantal visetende vogels dat ter plaatse overwintert te laten toenemen.
14. De door menigeen geconstateerde overeenkomst tussen de cultuur op het eigen werk en die op "het Bureau" zou het Meertens Instituut aanleiding moeten geven tot het verrichten van een gedegen studie naar de cultuur op Nederlandse werkplekken.  
*"Het Bureau", J.J. Voskuil.*

E.E. Bende, 20 december 1999

3468

732703

31362

TR3467

**Plutonium Burning  
in a Pebble-Bed Type  
High Temperature Nuclear Reactor**

Plutonium Burning in a Pebble-Bed Type High Temperature Nuclear Reactor  
Bende, Evert Eugène - Petten: Nuclear Research and Consultancy Group (NRG)  
Ph.D. Thesis, Delft University of Technology.  
ISBN 90-9013168  
NUGI: 837

Copyright ©1999 by E.E. Bende, NRG

All rights reserved. No part of this publication may be reproduced, stored in a retrieval system, or transmitted in any form or by any means without the prior written permission of the copyright owner.

# **Plutonium Burning in a Pebble-Bed Type High Temperature Nuclear Reactor**

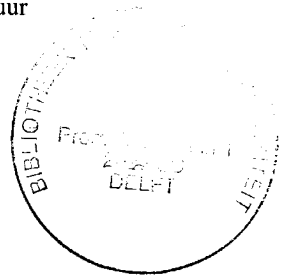
PROEFSCHRIFT

ter verkrijging van de graad van doctor  
aan de Technische Universiteit Delft,  
op gezag van de Rector Magnificus prof. ir K.F. Wakker,  
in het openbaar te verdedigen ten overstaan van een commissie,  
door het College voor Promoties aangewezen,  
op maandag 24 januari 2000 te 16.00 uur

door

**Evert Eugène BENDE**

doctorandus in de natuurkunde  
geboren te Zuidelijke IJsselmeerpolders



Dit proefschrift is goedgekeurd door de promotor:

♣  
Prof. dr ir H. van Dam

Samenstelling promotiecommissie:

Rector Magnificus, voorzitter

Prof. dr ir H. van Dam, Technische Universiteit Delft, promotor

Prof. dr ir A.H.M. Verkooijen, Technische Universiteit Delft

Prof. dr ir T.H.J.J. van der Hagen, Technische Universiteit Delft

Prof. dr ir C.W.E. van Eijk, Technische Universiteit Delft

Prof. dr ir C.D. Andriessse, Universiteit Utrecht

Prof. Dr-Ing. K. Kugeler, Technische Hochschule Aachen

Dr H. Gruppelaar †, NRG Petten

The work described in this thesis was performed at the Nuclear Research and Consultancy Group (NRG), Petten. This research was supported by the Ministry of Economic Affairs in the framework of PINK (Programme to maintain nuclear competence).

# Contents

<b>1</b>	<b>Introduction</b>	<b>1</b>
1.1	Problem description	1
1.2	Radiotoxicity	4
1.3	Pu-burning in different reactors	8
1.4	Objectives of this thesis	11
1.5	Potential of the pebble-bed HTR as a Pu-burner	12
1.6	Outline of this thesis	13
<b>2</b>	<b>The Pebble Bed High Temperature Reactor</b>	<b>17</b>
2.1	Passive Safety	17
2.2	Fuel scenarios	20
2.3	Pebbles	20
2.3.1	Pebble integrity	21
2.4	Coated particles	21
2.4.1	Coated Particle Performance	23
2.4.2	Experiences with irradiations experiments	27
2.5	Constraints assumed in this study	30
<b>3</b>	<b>Unit-cell calculations</b>	<b>31</b>
3.1	Specifications of pebbles and coated particles	31
3.2	Code descriptions	32
3.2.1	WIMS	32
3.2.2	The Dancoff factor	34
3.2.3	SCALE	34
3.2.4	MCNP4B	37
3.3	Results of calculations	38
3.3.1	Variation of pebble parameters	38
3.3.2	Variation of temperature	40

3.3.3	Burnup calculation . . . . .	42
<b>4</b>	<b>Reactor physics of plutonium fuelled pebbles</b>	<b>47</b>
4.1	Parameter study . . . . .	47
4.2	Reactor Physics Parameters of Fresh Fuel . . . . .	50
4.2.1	Infinite multiplication factor, spectral parameters, 4 factor formula	50
4.2.2	Temperature coefficients of reactivity . . . . .	54
4.2.3	Kinetic parameters . . . . .	59
4.3	Reactor Physics Parameters during Burnup . . . . .	60
4.3.1	Nuclide Composition during Burnup . . . . .	60
4.3.2	The Infinite Multiplication Factor during Burnup . . . . .	63
4.3.3	Kinetic Parameters during Burnup . . . . .	65
4.3.4	Influence of the historical temperature . . . . .	66
4.3.5	Fast fluence . . . . .	67
4.4	Temperature reactivity effects . . . . .	68
4.4.1	Abstract . . . . .	68
4.4.2	Historical back-ground . . . . .	68
4.4.3	Temperature reactivity effects during burnup . . . . .	70
4.4.4	Analysis of the moderator temperature coefficients . . . . .	75
4.4.5	The fuel temperature coefficient of reactivity . . . . .	80
4.4.6	Considerations with regard to reactor operation . . . . .	81
4.4.7	Autonomous reactor shutdown from an instable equilibrium after complete loss of cooling . . . . .	82
4.4.8	Conclusions as concerns temperature reactivity effects . . . . .	84
4.5	Conclusions . . . . .	85
<b>5</b>	<b>Core Calculations</b>	<b>87</b>
5.1	Reactor characteristics . . . . .	88
5.2	Nuclear data generation . . . . .	90
5.2.1	Pseudo reactor calculations with WIMS . . . . .	90
5.2.2	Providing data for PANTHER . . . . .	93
5.2.3	Data generation for the purpose of time-dependent solutions in PANTHER . . . . .	93
5.3	Neutronic and thermal-hydraulic core calculations with PANTHERMIX . .	94
5.3.1	PANTHER . . . . .	95
5.3.2	THERMIX/DIREKT . . . . .	99



5.4	Calculational results regarding normal reactor operation. . . . .	101
5.4.1	Burnup . . . . .	103
5.4.2	Delayed neutrons . . . . .	104
5.4.3	Power density . . . . .	107
5.4.4	Thermal-hydraulic properties . . . . .	107
5.4.5	Temperature and power coefficients of reactivity . . . . .	111
5.4.6	Flux . . . . .	115
5.4.7	Xenon . . . . .	118
5.5	Start-up and shut-down of the HTR-Pu . . . . .	121
5.6	The HTR-Pu under loss-of-cooling conditions . . . . .	126
5.6.1	Definition of loss-of-cooling scenarios . . . . .	126
5.6.2	Reactor-physics description of the transients . . . . .	127
5.6.3	Calculational results of loss-of-cooling incidents . . . . .	130
5.6.4	Comparison with point-reactor model . . . . .	136
5.7	Conclusions . . . . .	139
5.8	Recommendations for follow-up research . . . . .	140
5.8.1	Recommendations with regard to the calculations . . . . .	140
5.8.2	Recommendations with regard to the design . . . . .	141
<b>6</b>	<b>Conclusions &amp; Discussion</b>	<b>143</b>
6.1	Conclusions . . . . .	143
6.2	Discussion . . . . .	146
	<b>References</b>	<b>147</b>
<b>A</b>	<b>Analytical Derivation of the Average Dancoff-factor for a Fuel Kernel</b>	<b>159</b>
A.1	Introduction . . . . .	159
A.2	Calculation of Dancoff-factors . . . . .	161
A.3	Translation from pebble geometry to equivalent unit cells . . . . .	161
A.4	Transmission probabilities in a two-region white boundary unit cell . . . . .	162
A.5	Dancoff-factor for a random distribution of fuel kernels in an infinite medium	164
A.6	Transmission probabilities in a double heterogeneous system . . . . .	165
A.7	Calculation of the Dancoff factor . . . . .	168
A.7.1	The intra-pebble Dancoff factor . . . . .	168
A.7.2	The inter-pebble Dancoff factor . . . . .	170
A.7.3	Final expression for the Dancoff factor . . . . .	170

A.8	Comparison with Monte Carlo Results . . . . .	171
A.8.1	The infinite-medium Dancoff factor for the fuel zone . . . . .	172
A.8.2	Homogenisation of coatings and graphite matrix . . . . .	172
A.8.3	The infinite-medium Dancoff factor for a fuel kernel . . . . .	172
A.8.4	The intra-pebble Dancoff factor as a function of the fuel zone radius . . . . .	174
A.8.5	The Dancoff factor as a function of the pebble shell thickness . . . . .	174
A.8.6	The fuel kernel Dancoff factor for a standard pebble . . . . .	175
A.9	Dancoff-factor sensitivity of resonance integrals and other parameters . . . . .	177
A.9.1	Analytical approach . . . . .	178
A.9.2	Dancoff-factor sensitivity of several parameters obtained from calculations . . . . .	181
A.10	Conclusion . . . . .	182
<b>B</b>	<b>Average and effective temperatures in a power generating pebble.</b>	<b>183</b>
B.1	Average temperatures . . . . .	184
B.2	Effective temperatures . . . . .	185
B.2.1	Effective fuel temperature . . . . .	186
B.2.2	Effective graphite temperature in fuel zone . . . . .	186
B.2.3	Effective graphite temperature in pebble shell . . . . .	187
B.2.4	Effective graphite temperature for the entire pebble . . . . .	187
B.3	Average temperature of the fuel kernel . . . . .	188
B.4	Comparison of Average and Effective Temperatures . . . . .	188
<b>C</b>	<b>Maximisation of the Doppler effect</b>	<b>191</b>
C.1	Definition of the Doppler coefficient of reactivity . . . . .	192
C.2	Geometry and fuel properties . . . . .	193
C.3	Theory . . . . .	194
C.3.1	Introduction . . . . .	194
C.3.2	The slowing down equation for the fuel zone . . . . .	196
C.3.3	The NR(IM) approximation method . . . . .	197
C.3.4	The Nordheim Integral Method . . . . .	203
C.3.5	Method based on the four factor formula . . . . .	203
C.4	Calculation of the Doppler efficiency . . . . .	204
C.4.1	The NR(IM) approximation method and the Nordheim Integral Method . . . . .	204
C.4.2	Estimation of the optimal Dancoff-corrected mean chord length . . . . .	205

C.4.3	Comparison of the Nordheim Integral Method and the NR(IM) approximation . . . . .	206
C.5	Maximisation of the Doppler coefficient of reactivity with a constant $k_{\infty}$ as constraint . . . . .	210
C.5.1	Introduction . . . . .	210
C.5.2	Calculational Method . . . . .	213
C.5.3	Artificial fuels: The Doppler efficiency $\frac{1}{I_p} \frac{dI_p}{dT}$ . . . . .	215
C.5.4	Artificial fuels: The Doppler coefficient $\frac{1}{k_{\infty}} \frac{dk_{\infty}}{dT}$ . . . . .	218
C.5.5	Realistic Fuels . . . . .	221
C.6	Conclusions . . . . .	225
<b>D</b>	<b>First-Flight Escape Probability for a Sphere</b>	<b>229</b>
<b>E</b>	<b>Narrow Resonance Approximations</b>	<b>231</b>
E.1	The Doppler broadened resonance. . . . .	231
E.2	The energy-dependent flux . . . . .	232
E.3	The effective resonance integral . . . . .	232
E.4	Application of Wigner's rational approximation . . . . .	233
E.5	Resonance Parameters and Derived Parameters . . . . .	234
	<b>Nomenclature</b>	<b>237</b>
	<b>Summary</b>	<b>239</b>
	<b>Samenvatting</b>	<b>241</b>
	<b>Acknowledgement</b>	<b>243</b>
	<b>Curriculum Vitae</b>	<b>245</b>



# Chapter 1

---

## Introduction

---

### 1.1 Problem description

At present, the world-wide nuclear energy production is dominated by light water reactors (LWRs). These reactors are fuelled with uranium that is slightly enriched in the fissile isotope  $^{235}\text{U}$  (3-5 %). An important parameter that quantifies the fuel utilisation of an arbitrary nuclear reactor is the so-called burnup. It is defined as the amount of thermal energy that is extracted per unit mass heavy metal (HM) loaded into the reactor. The exit burnup depends on the enrichment; in the case of an LWR, it lies typically in the range from 30 to 50 MWd/kgHM. As an example we consider an LWR with a burnup of 47.5 MWd/kgHM. This number obviously means that 1/47.5 kg HM is required for the production of one MWd of thermal energy. This implies that the mass loaded into an LWR with an electric output of 1 GW and an efficiency of 33% amounts to about 23 tons of heavy metal per full-power year (FPY). The loading rate of 23 tons/FPY of fresh fuel is of course accompanied by the same discharge rate of spent fuel.

Table 1.1 shows the composition of the spent fuel per discharged ton HM<sup>1</sup>. The numbers refer to the mentioned 1 GW<sub>e</sub> LWR with an exit burnup of 47.5 MWd/kgHM. Recalling that the annual discharge of this reactor amounts to 23 tons, the numbers of table 1.1 need to be multiplied by 23 to get the absolute masses of the waste stream. The spent fuel contains about 94% unused uranium. The remaining 6% consists primarily of fission products (FPs) and to a lesser extent of so-called transuranium nuclides (TRU). The latter group embraces all nuclides with mass numbers higher than 92 which are created through successive neutron captures by uranium and its activation products. The TRU mass, on its turn, consists for about 90% of plutonium and for about 10% of the so-called minor actinides (MA), like Np, Am and Cm. Table 1.2 shows the isotopic composition of the plutonium; the listed numbers are used throughout this entire thesis.

World-wide, one can distinguish two main policies concerning the treatment of spent fuel. Countries, like the United States, Canada and Sweden see the plutonium as a constituent of spent fuel which is best committed to intermediate storage along with the intact fuel elements followed by final disposal in deep geological formations. On the other hand,

---

<sup>1</sup>Unless otherwise indicated the data mentioned in this introduction are obtained from [1].

**Table 1.1:** *The composition of spent  $UO_2$  fuel from an LWR with a burnup of 47.5 MWd/kgHM. Also the produced masses of some long-lived nuclides are shown. (Reproduced from p. 11 of [1]).*

Element	Mass (kg/tHM)	Nuclide	Mass (kg/tHM)
U	937.9	$^{93}Zr$	1.0
Np	0.6	$^{99}Tc$	1.1
Pu	11.8	$^{126}Sn$	0.04
Am	0.6	$^{129}I$	0.3
Cm	0.1	$^{135}Cs$	0.6
FP <sup>a</sup>	49.4	$^{237}Np$	0.6

<sup>a</sup> Fission Products

**Table 1.2:** *Isotopic vector of the plutonium from spent LWR fuel with a burnup of 47.5 MWd/kgHM. The isotopes with an odd mass number are the fissile ones. The Pu-vector has been used throughout this entire thesis.*

Isotope	Atom perc.	Half-life (years)
$^{238}Pu$	2.68	$8.8 \cdot 10^1$
$^{239}Pu$	55.58	$2.4 \cdot 10^4$
$^{240}Pu$	23.08	$6.6 \cdot 10^3$
$^{241}Pu$	11.98	$1.4 \cdot 10^1$
$^{242}Pu$	6.68	$3.8 \cdot 10^5$

countries like France, Germany, United Kingdom, Belgium, Switzerland, Russia, Japan and the Netherlands adhere the policy of separating the plutonium from the spent fuel because of some reasons that will be discussed in due course. The countries of the latter group either operate reprocessing plants or have contracts for reprocessing their spent fuel abroad.

As far as Europe is concerned, France and the United Kingdom have been operating reprocessing plants to separate plutonium and uranium from spent fuel since they have embarked on their nuclear programmes. The separation is carried out by the PUREX process, which is an extraction process based on a nitric acid dissolution of the spent fuel and the solvent extraction of U and Pu by tri-butyl-phosphate (TBP). If the yearly available 23 tons of spent fuel from the 1 GW<sub>e</sub> PWR are supplied to the PUREX process, we obtain an outgoing mass stream that consists of 21,800 kg U, 275 kg Pu and 1180 kg MA/FPs. The latter group of minor actinides and fission products is usually regarded as high level radio-active waste and is presently vitrified and conditioned for final disposal. The volume of this vitrified waste is only 20 m<sup>3</sup>. To put this into perspective, this type of waste forms only 0.002<sup>vol%</sup> of the total amount of domestic waste in the UK [2]. Furthermore, it is worthwhile to mention that the reprocessed uranium still contains about one quarter of its

original  $^{235}\text{U}$  content, which is slightly more than that in natural uranium, implying that it can be used as feed material for re-enrichment [3].

The policy to separate the valuable U and Pu from the remaining materials of the spent fuel originated from the envisaged scarcity of the natural uranium resources. However, due to discovery of more natural uranium sites as well as the declined growth rate of world-wide nuclear energy production, and the unforeseen stay-away of fast reactors in the nuclear reactor parks, the prizes of natural uranium decreased and the reprocessed U and Pu were not utilised so that their stocks accumulated. The plutonium stocks have been increasing

**Table 1.3:** *The world plutonium stocks on 31 December 1994, according to [4]. The numbers below exclude the amounts of  $^{241}\text{Pu}$  that have decayed to  $^{241}\text{Am}$ , and the amounts of plutonium in operating power reactors, unless it is contained in MOX fuel.*

Category	Stocks (tons)
<i>Civil plutonium</i>	
In spent reactor fuel	755
Separated in store	118
In fast-reactor fuel cycle	21
In thermal MOX fuel cycle	20
<b>Civil total</b>	<b>914</b>
<i>Military plutonium</i>	
In operational warheads	70
Weapon-grade outside operational warheads	158
Fuel- and Reactor-grade in store	21
<b>Military total</b>	<b>249</b>
<b>Grand total</b>	<b>1160</b>

even more because weapon-grade plutonium ( $>90\%$   $^{239}\text{Pu}$ ) has become available due to the dismantlement of nuclear arms in both the Russian Federation and the USA (START treaties). Table 1.3 lists the estimated world-wide stocks of both civil and military plutonium.

In the last decade, much effort has been made to reduce the growth rate of the plutonium stock by utilising plutonium in existing reactors. This might be considered as a first step towards a stabilisation of the stock and, eventually, towards a decrease of it. To achieve these goals, much research focuses on the development of advanced reactors and advanced fuel concepts able to incinerate plutonium at high rates. At present, there is not a clear single incentive to separate the plutonium and to reuse it in existing or advanced reactors. The strategy is merely based on a diversity of incentives that are to a large extent determined by politics and public acceptance.

It is clear that economic considerations can be excluded as a possible incentive, since

the reprocessing and utilisation of plutonium involve 15 to 20% higher fuel cycle costs than the direct disposal option [5]. Since the fuel cycle costs form only about 15-20% of the overall costs, as far as LWRs are concerned, the cost difference between reprocessing and direct disposal can be considered as insignificant. It is likely that proliferation risks, resource utilisation and environmental impact play more important roles for a country's decision to recycle the plutonium. The fear for proliferation risks forms one of the major incentives to reduce the plutonium stocks. Whether this fear is justified is a point of discussion that is beyond the scope of this text. The incentive of resource utilisation originates from the idea of making the best use of the world's finite energy resources. By utilising plutonium instead of disposing it directly, there will be a lesser demand of enriched uranium and, consequently, a more sparingly use of natural uranium. The incentive to recycle plutonium in relation to environmental impact is based on the significant contribution of plutonium to the long-term potential radiotoxicity source. This will be illuminated in the next section.

## 1.2 Radiotoxicity

Radiotoxicity is a measure for the dose that a human suffers when a certain amount of radioactive nuclides enters the body. The radiotoxicity depends on the activity of the material, the half-life of its constituent nuclides, the type of radiation, the energy of the emitted particles, the way the radionuclides enter the human body (inhalation/ingestion), the organs that are exposed to the radiation and the time that the nuclides stay in different organs (biological half-lives). All these effects are captured in a single quantity:  $e(50)$ , the dose conversion coefficient in units of Sv/Bq, giving the integrated dose over 50 years for the reference human body upon intake of 1 Bq of a specific radionuclide [6]. The dose per ingested mole of a particular radionuclide, denoted henceforth as the molar radiotoxicity in [Sv/mole], can be calculated by multiplying the dose conversion coefficient  $e(50)$  [Sv/Bq] with the activity of a mole of this radionuclide [Bq/mole], which is equal to the decay constant ( $\lambda = \frac{\ln 2}{T_{1/2}}$ ) times the number of Avogadro ( $6.02 \cdot 10^{23}$ ). Hence, the molar radiotoxicity becomes

$$\text{Molar Radiotoxicity [Sv/mole]} = e(50) \text{ [Sv/Bq]} \frac{\ln 2}{T_{1/2}[\text{s}]} 6.02 \cdot 10^{23} \text{ [mole}^{-1}] \quad (1.1)$$

Fig. 1.1 shows a diagram in which the actinides ranging from Th to Cf are positioned against their dose conversion coefficient  $e(50)$  and their half-lives  $T_{1/2}$  in years. The slanting lines are equi-molar-radiotoxicity lines derived from eq. 1.1. Fig. 1.1 shows that the  $e(50)$ -values for all  $\alpha$ -decaying actinides lie between  $4 \cdot 10^{-8}$  and  $8 \cdot 10^{-7}$  Sv/Bq, which reveals that their radiotoxicity values in terms of Sv per Bq do not differ much. However, the half-lives of the nuclides under consideration differ by several orders of magnitude and hence their molar radiotoxicities differ accordingly. In other words, the activity of the actinides determines to a major extent the molar radiotoxicity. Fig. 1.1 shows for example that the  $e(50)$ -values of  $^{235}\text{U}$  and  $^{233}\text{U}$  hardly differ, but as their half-lives differ by more than three orders of magnitude their molar radiotoxicity values differ correspondingly. The  $\beta^\pm$ -decaying nuclides usually have  $e(50)$ -values that are one or more orders of magnitude smaller than the  $\alpha$ -decaying ones. The only  $\beta$ -decaying nuclide present in the half-life domain of fig. 1.1 is  $^{241}\text{Pu}$ ; the remaining  $\beta$ -decaying actinides have half-lives shorter than



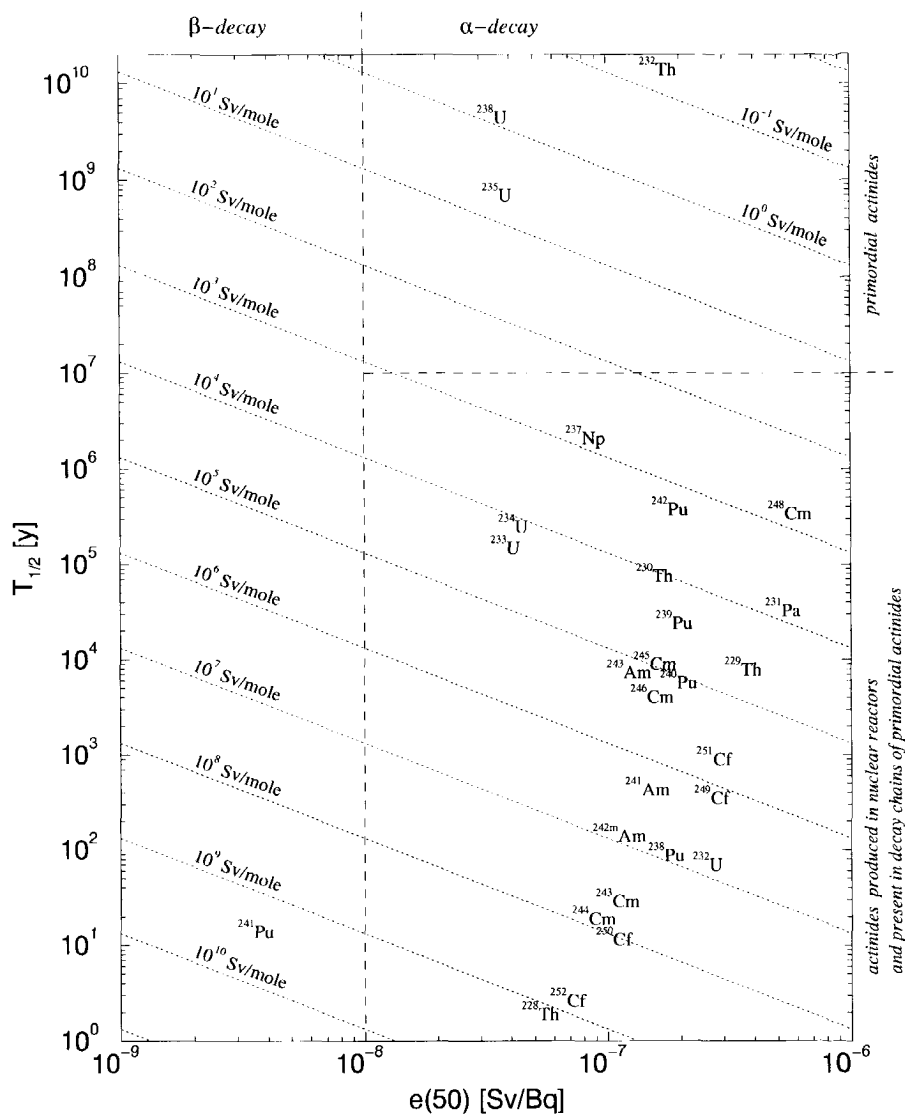


**Figure 1.1:** Diagram showing the radiotoxicity of the actinides ranging from Th to Cf. The vertical axis denotes the half-life in years and the horizontal axis shows the dose conversion coefficient  $e(50)$  in Sv/Bq (for ingestion), according to [6]. The primordial actinides are those formed in terrestrial matter and still present today. The slanting lines connect points of equi-molar radiotoxicity. For example,  $^{235}\text{U}$  and  $^{233}\text{U}$  have similar  $e(50)$ -values, but their molar radiotoxicities in Sv/mole differ by more than three orders of magnitude because of the difference in half-life.

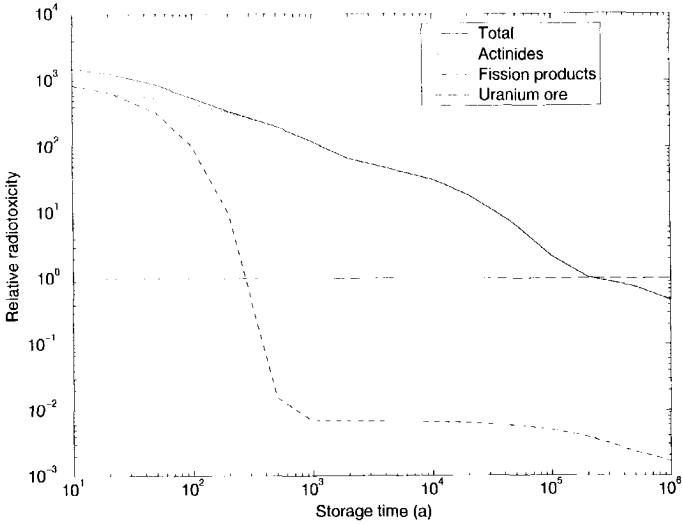
one year.

The horizontal dashed line in fig. 1.1 separates the primordial actinides, i.e.  $^{232}\text{Th}$ ,  $^{235}\text{U}$  and  $^{238}\text{U}$ , from the other  $\alpha$ -decaying actinides. The latter group is composed of actinides that occur in the decay chain of the primordial actinides (e.g.  $^{234}\text{U}$ ,  $^{231}\text{Pa}$ ) and those that are created in nuclear reactors through neutron captures by  $^{235}\text{U}$ ,  $^{238}\text{U}$ ,  $^{232}\text{Th}$  and their activation products. It is clear that the composition of actinides below the horizontal dashed line determines the actinide-radiotoxicity of the spent fuel immediately after discharge. However, as the composition of actinides of the spent fuel changes due to decay its radiotoxicity changes too. This leads to an evolution of the radiotoxicity in the course of time.

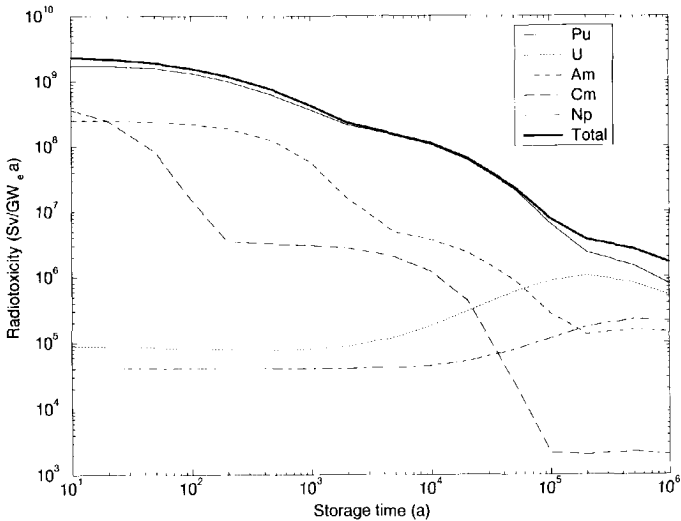
Fig. 1.2 shows the radiotoxicity of both the fission products and the actinides in spent fuel of an LWR with a burnup of 47.5 MWd/kgHM as a function of the storage time. The radiotoxicities are normalised to the radiotoxicity of the ore that was needed to manufacture the fuel. The uranium-line does not indicate a safety limit, but is only included as a reference. If the spent fuel would be admixed with the uranium ore where it originates from, the radiotoxicity of this mixture becomes equal to that of the ore at about 200,000 years. The comparison with the ore only makes sense if one decides to admix the spent fuel with the ore and thus implicitly abandons further utilisation of this mixture. Fig. 1.2 demonstrates that the spent fuel has gained three orders of magnitude in radiotoxicity compared to the involved amount of ore immediately after discharge. In the first ten years of storage the radiotoxicity of the actinides is comparable to that of the fission products. After about 250 years, the radiotoxicity of the fission products becomes negligible compared to that of the actinides.

Fig. 1.3 shows that plutonium dominates the actinide-radiotoxicity up to a storage time of one million years. This clearly illustrates the previously mentioned incentive for the destruction/utilisation of plutonium with the aim to reduce the radiotoxicity. In this view, one should consider the incineration of plutonium as a first approach to a significant reduction of the radiotoxicity of nuclear waste.

Finally, it should be mentioned that the radiotoxicity is only a measure of the *potential* hazard upon ingestion or inhalation. This implies that no dose is suffered by the population as long as the radionuclides are sufficiently isolated from the biosphere. The isolation of nuclear waste in geological repositories have been assessed in several studies. In these studies the radiological risk of nuclear waste for various types of containment, repositories, scenarios (normal evolution and human intrusion) have been calculated. Since these risk analyses are beyond the scope of this thesis we refer to [7], and for a concise over-view to ch. 2.2 of [1].



**Figure 1.2:** Radiotoxicity of both the fission products and the actinides relative to the radiotoxicity of the required ore to manufacture the fuel. The uranium-line does not indicate a safety limit, but is only included as a reference. If the spent fuel would be admixed with the uranium ore where it originates from the radiotoxicity of this mixture becomes equal to that of the ore at about 200,000 years.



**Figure 1.3:** The radiotoxicity per actinide element in spent  $UO_2$ -fuel in units of  $Sv/GW_e a$  as a function of the storage time. Note that plutonium dominates the actinide-radiotoxicity over the entire period of time. Each curve includes the radiotoxicity of the daughters present in the decay chain of the mother nuclides.

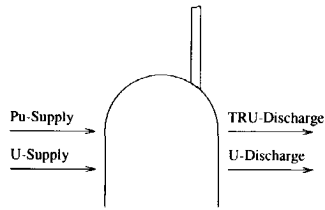


**Figure 1.4:** Mass flows in an arbitrary reactor fuelled with Pu and U. The outward TRU flow stands for transuranics, which consists of plutonium and minor actinides. The mass consumption rate obeys:  $(Pu\text{-supply} + U\text{-Supply}) - (TRU\text{-Discharge} + U\text{-Discharge}) = 375 \text{ kg/GW}_{th}a$ .

### 1.3 Pu-burning in different reactors

To reduce the plutonium stocks or, at least, to reduce their growth rates, plutonium should be used as a reactor fuel. This thesis addresses the burning of plutonium in a pebble-bed type High Temperature Reactor (HTR). Before describing the properties of this reactor and judging its potential as a Pu-burner, we will present a general assessment of Pu-fuelled reactors, which will be done by regarding their mass-balances. On the basis of the assessment in this section the objectives for the pebble-bed HTR as a Pu-burner will be defined and presented in in the next section.

As a logical consequence of their prevalence in the nuclear fuel cycle, LWRs are currently deployed for the utilisation of plutonium. This is realised by replacing a part of the conventional  $UO_2$ -containing fuel assemblies by ones that contain so-called Mixed OXide (MOX) fuel. MOX-fuel is composed of depleted uranium and plutonium. One might say that the plutonium takes over the role that the fissile  $^{235}U$  plays in the  $UO_2$  fuel, although it is not completely fissile but typically consists for only 60% of fissile isotopes. Currently, a limited number of LWRs in France, Belgium, Germany and Switzerland are partially loaded with MOX fuel. Most of these LWRs have an inventory that consists for two thirds of conventional  $UO_2$  assemblies and for one third of MOX assemblies. It is obvious that in the conventional  $UO_2$  assemblies the production of plutonium still goes on, while in the MOX-assemblies a net plutonium consumption takes place. In order to assess<sup>2</sup> the Pu-burning performance of this MOX/ $UO_2$ -fuelled LWR, in particular, and that of an arbitrary (U,Pu)-fuelled reactor, in general, it is useful to regard their actinide mass balances.

Fig. 1.4 depicts the inward and outward actinide mass streams of an arbitrary reactor. Uranium and plutonium are supplied to this reactor, while unused uranium and transuranics are discharged from it. The actinide mass consumption inside the reactor amounts to about  $375 \text{ kg/GW}_{th}a$ . This originates from the fact that every fission generates about 200 MeV and concurrently means one actinide nuclide less. Due to minor variations of both the average actinide mass and the effective energy release per fission (including contributions from capture) for different fuel compositions and reactor types, deviations of the actinide mass consumption of  $375 \text{ kg/GW}_{th}a$  by maximally 5% can occur.

<sup>2</sup>The remaining part of this section is largely based on ref. [8]

The outgoing transuranic mass stream of a (U,Pu)-fuelled reactor, contains besides plutonium isotopes also minor actinides, like Np, Am and Cm. They are produced by successive neutron captures in plutonium and uranium isotopes. Fig. 1.1 shows that most of these minor actinides are at least as radiotoxic as the plutonium isotopes. In order to judge a (U,Pu)-fuelled reactor as a waste incinerator it is, therefore, better to regard the transuranic (TRU) consumption instead of solely the Pu-consumption. It has to be admitted that the TRU-mass consumption itself does not say anything about the radiotoxicity reduction, since it does not give any information on the isotopic composition of the discharged TRU. However, it is a 'solid' quantity which can readily be used for comparison between reactors and is, unlike radiotoxicity, not liable to changing  $\epsilon(50)$ -values due to progress in radiology.

The actinide mass balance for any (U,Pu)-fuelled reactor reads

$$\text{U-Consumption} + \text{TRU-Consumption} \approx 375 \text{ kg/GW}_{\text{th,a}} \quad (1.2)$$

where

$$\text{U-Consumption} = \text{U-supply} - \text{U-discharge} \quad (1.3)$$

$$\text{TRU-Consumption} = \text{Pu-supply} - \text{TRU-discharge} \quad (1.4)$$

Eq. 1.2 reveals that the TRU-Consumption is maximal (i.e. 375 kg/GW<sub>th,a</sub>) if the U-consumption is nil, which is evidently fulfilled when no uranium whatsoever is loaded into the reactor. In literature, the TRU mass consumption is often expressed in terms of kilogrammes per unit of *electric* energy produced. However, since every reactor has a specific electric efficiency, this does not allow the use of a single mass balance for all (U,Pu)-fuelled reactors and thus impedes intercomparison. Moreover, a reactor with a very low efficiency would become an excellent Pu-burner. Expressing the TRU mass consumption in units of kg/GW<sub>th,a</sub> enables a fair comparison and hence has preference.

Besides a high TRU-Consumption rate, a low TRU-Discharge rate is preferred for a Pu-burner as well. This is because of the following:

If a once-through scenario is considered, a low TRU-discharge involves evidently a low TRU-mass that has to be disposed of. If one, on the other hand, considers reprocessing, a low TRU-Discharge rate is preferred since this involves a low mass throughput in the reprocessing trajectory. The separation efficiency for U and Pu that is presently feasible amounts to 99.88%, which implies that the remaining 0.12% ends up in the waste stream together with the fission products and minor actinides. Therefore, a low mass throughput in the reprocessing trajectory results in low losses of plutonium (and minor actinides).

Hereafter, several reactor concepts are assessed on the basis of their *TRU-Consumption* and *TRU-Discharge* characteristics. Other parameters that characterise the Pu burning of a reactor, like the fraction of minor actinides in the discharged TRU and the ability to reprocess the spent fuel are left out of consideration here.

Fig. 1.5 shows the performance of several reactor types fuelled with Pu or with a mixture of U and Pu. The reactors loaded with uranium-free fuel are positioned on the top horizontal line that represents the maximal TRU-Consumption of 375 kg/GW<sub>th,a</sub>. For the reactors that are fuelled with both Pu and U, the U-Consumption equals 375 kg/GW<sub>th,a</sub>

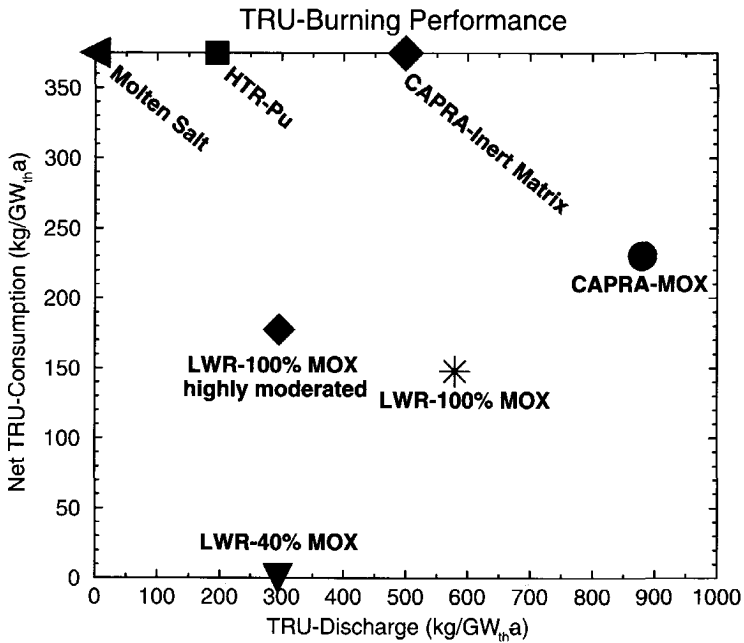


**Figure 1.5:** Mass flows for a number of reactor concepts fuelled with Pu and U. The transuranics (TRU) mass consists of plutonium and the minor actinides.

minus the TRU-Consumption. This corresponds with the vertical distance between the reactor's position in the diagram and the top horizontal line.

As mentioned before, plutonium recycling in LWRs is currently realised by loading both UO<sub>2</sub> and MOX assemblies into the core. In the UO<sub>2</sub> assemblies plutonium is formed due to neutron capture by <sup>238</sup>U and successive decay, whereas in the MOX assemblies a net Pu-consumption takes place. If the core is loaded with MOX assemblies for 40%, the overall TRU-Consumption is nil, while the TRU-Discharge amounts about 295 kg/GW<sub>th,a</sub>. In case of an LWR with a full MOX core [9] the TRU-Consumption and TRU-Discharge read 150 kg/GW<sub>th,a</sub> and 580 kg/GW<sub>th,a</sub>, respectively. For a full MOX core with enhanced moderation the TRU-Consumption increases slightly to 180 kg/GW<sub>th,a</sub>, while the TRU-Discharge reduces considerably to 300 kg/GW<sub>th,a</sub>.

The CAPRA-MOX reactor is a fast burner without breeding blankets and with an initial Pu-content of 45% in the fuel and a Pu-inventory of ~9,000 kg. Its TRU-burning performance is significantly better, whereas the TRU-Discharge of about 880 kg/GW<sub>th,a</sub> is very high (p. 40 of [10]). The CAPRA reactor operated with Pu in an inert matrix, also with an inventory of 9,000 kg Pu, yields the maximal TRU-Consumption of 375 kg/GW<sub>th,a</sub> and a TRU-Discharge of 500 kg/GW<sub>th,a</sub> (p. 21 of [11]).

The Molten Salt Reactor concept with a continuous Pu-feed and on-line fission product removal has been studied in the framework of a PhD-study performed by Bultman

(ch. 4 of [12], and [13]). This reactor concept shows the maximum TRU-Consumption and a zero TRU-Discharge, with disregard of the small losses due to the on-line fission product removal, and therefore seems to be the optimal TRU-burner. However, little is known about the technical feasibility of this concept: expected difficulties are the very high power density of  $\sim 1 \text{ GW/m}^3$ , corrosion by the salt, graphite damage due to high fast fluences and so on. Moreover, the equilibrium nuclide inventory is highly radiotoxic (as an illustration: the  $^{244}\text{Cm}$  content equals  $\sim 10\%$ ) and the reactor physics safety aspects with regard to the approach to equilibrium has to be investigated yet. It is clear that much research has to be done and many technical problems have to be solved before such a concept can become reality. Nevertheless, the Molten Salt transuranics burner remains a promising concept.

This thesis deals with the pebble-bed type High Temperature Reactor as a burner of plutonium. If we, a priori, assume that this reactor can be operated with pure plutonium (U-free) and, moreover, that it can achieve a burnup of  $640 \text{ MWd/kgHM}$ , the maximum TRU-consumption of  $375 \text{ kg/GW}_{\text{th,a}}$  will be attained and the TRU-discharge will amount to about  $215 \text{ kg/GW}_{\text{th,a}}$ .

Reactors fuelled with Th/Pu [14–16] fuel are not shown in fig. 1.4. These systems yield lower TRU-Consumption rates than reactors fuelled with plutonium only, but yield a higher TRU-Consumption rate than (U,Pu)-fuelled reactors. However, this will be at the expense of the formation of radiotoxic isotopes like  $^{232}\text{U}$ ,  $^{233}\text{U}$  and  $^{234}\text{U}$ .

## 1.4 Objectives of this thesis

This thesis deals with the pebble-bed type HTR as a burner of reactor-grade plutonium. The composition of the plutonium that has been used throughout this thesis is the one that is listed in table 1.2. The objectives that were defined for the Pu-burning HTR, read:

1. Maximise the TRU-Consumption (in  $\text{kg/GW}_{\text{th,a}}$ ).
2. Minimise the TRU-Discharge (in  $\text{kg/GW}_{\text{th,a}}$ ).

In the previous section, it was explained that the first objective can simply be achieved if the reactor is fuelled with pure plutonium (no uranium). This gives a TRU-Consumption rate of  $375 \text{ kg/GW}_{\text{th,a}}$ .

Provided that it appears possible to operate the pebble-bed HTR with pure plutonium (no uranium), the second objective can simply be translated as: Maximise the burnup. This can be illustrated by identifying

$$\begin{aligned} \text{Burnup } [\text{GW}_{\text{th,a}}/\text{kg}] &= \frac{1}{\text{Pu-supply } [\text{kg/GW}_{\text{th,a}}]} \\ &= \frac{1}{375 [\text{kg/GW}_{\text{th,a}}] + \text{TRU-discharge } [\text{kg/GW}_{\text{th,a}}]} \end{aligned} \quad (1.5)$$

Eq. 1.5 shows that a minimisation of the TRU-discharge simply corresponds to a maximisation of the burnup.

It is clear that the realisation of both objectives can only be met within the boundary

values of the system. This implies that the design must be such that all process variables and parameters stay within the safety constraints of the system. The constraints used in this study will be presented in section 2.5.

## 1.5 Potential of the pebble-bed HTR as a Pu-burner

To realise the objectives presented in the preceding section the HTR should burn plutonium in the absence of uranium. It is clear that the absence of uranium will have major implications concerning safety, reactivity effects and reprocessing. The advantageous properties of  $^{238}\text{U}$  that are lacking in a uranium-free fuel are, briefly:

- $^{238}\text{U}$  is usually the main contributor to the negative fuel temperature reactivity feedback, also known as the Doppler-effect.
- Uranium enhances the dissolution of spent MOX-fuel in nitric acid of the PUREX process. The lower the U-content in the MOX, the worse the dissolution.
- $^{238}\text{U}$  is a fertile material. Due to neutron capture by  $^{238}\text{U}$  and subsequent decay new  $^{239}\text{Pu}$  is formed. This is of course disadvantageous in terms of Pu-destruction, but is advantageous from the viewpoint of reactivity control during burnup. Thanks to the build-up of  $^{239}\text{Pu}$  a relatively low control worth is required to compensate the reactivity decrease during burnup.
- $^{238}\text{U}$  provides for a negative contribution to the reactivity effect in case of voiding in a MOX-fuelled, liquid-moderated reactor. For a relatively high void fraction in a MOX-fuelled LWR the spectrum tends to that of a fast reactor. If the Pu-content is too high and consequently the  $^{238}\text{U}$  content too low, this leads to an increase of the reactivity which is of course of serious safety concern.

Before judging whether the pebble-bed HTR can cope with the lack of these advantageous  $^{238}\text{U}$  properties, we briefly describe the main features of this reactor:

The pebble-bed HTR is fuelled with graphite spherical fuel elements of 6 cm diameter. Within these pebbles one can distinguish a fuel-free outer shell with a thickness of 0.5 cm and a fuel zone with a diameter of 5 cm in which tens of thousands of tiny coated fuel particles are embedded. The heart of such a coated particle is the fuel kernel, which has a diameter of 200-500  $\mu\text{m}$ . (See the cover of this thesis). More information about the fuel elements will be given in chapter 2. The cylindrical core of the pebble-bed reactor consists of a core cavity that is enclosed by axial graphite reflectors, at the bottom and the top, and by an annular cylindrical graphite reflector. The core cavity is filled with pebbles which constitute the actual pebble-bed.

The pebble-bed HTR has great potential as a uranium-free burner of plutonium because of the following properties:

### • Continuous fuelling

In (U,Pu)-fuelled reactors the depletion of Pu is partially compensated by the formation of new Pu due to neutron capture by  $^{238}\text{U}$  and subsequent decay. This implies that the reactivity in a uranium-free Pu-burner is expected to decrease more rapidly than in a (U,Pu)-fuelled reactor. In most reactors this reactivity decrease is compensated by the withdrawal of control rods and/or by depletion of burnable poisons or soluble boron,



like in LWRs. This has adverse effects from the viewpoint of safety (large amount of excess reactivity is needed) and neutron-economics (the neutrons can better be used for the conversion of non-fissile to fissile nuclides). However, the Pebble-Bed Type HTR is able to circumvent this problem, since it can respond to a decreasing reactivity by continuous (de)fuelling. This is realised by adding fresh pebbles on top of the pebble bed and/or by extracting irradiated ones from the bottom.

- **Solid moderator**

In liquid-moderated reactors, partial or complete voiding of the moderator can occur. If such reactors are operated with a uranium-free fuel, this can lead to a positive reactivity introduction [17]. In case of complete voiding, the spectrum of such a reactor is tending to that of a fast reactor, which leads to an enhanced fission-to-capture ratio of the plutonium isotopes. Since the HTR has a solid moderator and a gaseous coolant, one does not need to worry about such effects.

- **High burnup**

Coated particles dedicated to the burning of plutonium were fabricated and tested in irradiation experiments. With these CPs allegedly high burnups up to 740 MWd/kgHM [18–20] can be achieved. This implies that an incineration of about three quarters of the initial heavy metal content can be realised.

Besides these advantages one can also identify a disadvantage for the HTR as a Pu-burner:

- **Reprocessing difficulties**

The coatings of each fuel particle as well as the graphite matrix in which the CPs are embedded form excellent barriers that prevent the actinides and fission products from migration. This is of course advantageous during reactor operation, but forms a major drawback with respect to reprocessing of the spent Pu-fuel. If reprocessing is nevertheless desirable, the coated particles have to be separated from the graphite matrix and, subsequently, the fuel kernels have to be separated from the coatings. Thereafter, the fuel kernels may follow the same reprocessing route as LWR-fuel. Ref. [21] (see also [22]) proposes some techniques to realise the mentioned separation of the fuel kernels. Since reprocessing of HTR-fuel is rather complex, although technically feasible, the generally adhered strategy is to dispose of the pebbles directly (i.e. once-through).

## 1.6 Outline of this thesis

This thesis deals with the pebble-bed High Temperature Reactor that is fuelled with pure reactor-grade plutonium. The composition of the plutonium that has been used throughout this entire thesis is the one that is listed in table 1.2. Once again, we stress that neither burnable poisons nor fertile materials like  $^{238}\text{U}$  and  $^{232}\text{Th}$  are present in the calculational models throughout this thesis.

This thesis is built up in the following way:

Chapter 2 discusses the general properties of the pebble-bed HTR. Section 2.1 discusses the passive safety features of this reactor, while section 2.2 presents different fuel scenarios

according to which the pebble-bed HTR can be operated. The properties of the pebbles and the CPs are discussed by sections 2.3 and 2.4, respectively. The latter section gives a concise overview of the mechanisms that can lead to coated particle failure. Special attention is paid to the effect of Pu as fuel inside these CPs thereby aiming to indicate which mechanisms are of concern when such CPs are considered as fuel in future reactors. Since sections 2.3 and 2.4 contain detailed background material outside the main scope of this thesis; they might be skipped for reading. In order to guarantee the safety of the pebble-bed HTR there exist some constraints on a number of reactor parameters. Section 2.5 lists the constraints that were imposed to the models that were considered in the framework of this thesis.

Chapter 3 presents the results of unit-cell calculations performed with three code systems. Section 3.2 describes how these code systems work, while section 3.3 presents the results of the calculations. The main objective of this chapter is to compare the calculational results of one particular code system, which is a candidate for the generation of cross sections for a full-core calculation, to those of the other two code systems. In addition to this verification, some reactor physics interpretations of the calculational results are presented. The unit-cell calculations embrace the computation of a number of reactor physics parameters for pebbles with a varying plutonium mass per pebble and with different types of coated particles. For one pebble configuration, these parameters have been calculated for various fuel temperatures and over-all (uniform) temperatures. For that particular pebble configuration, also the results of a two burnup calculations were compared.

Whereas chapter 3 embraces a comparative study, chapter 4 reports the results of a parameter study in which the number of coated particles per pebble as well as the type and size of the CPs have been varied. The effect of different pebble configurations on several reactor physics parameters like the temperature coefficients of reactivity, the delayed neutron fractions and the mean neutron generation time as well as their evolutions during burnup are presented in this chapter. The calculations for this parameter study still refer to an infinite pebble bed or, more precisely, to a 'pebble-cell' with isotropically reflecting boundaries.

On the basis of the results of the cell calculations presented in chapter 4, two pebble configurations were chosen as viable candidates for fuel in a real reactor. These configurations embrace pebbles with either 1 g or 2 g Pu/pebble contained by coated particles with fuel kernel diameters of 220  $\mu\text{m}$ . Chapter 5 presents a conceptual design of a pebble-bed HTR that is operated with pebbles having the mentioned Pu-loadings. This design, which will be designated as the HTR-Pu, is a modified version of the Dutch ACACIA [23] design, which is a small pebble-bed reactor, based on the *Peu-à-Peu* fuelling principle, with a thermal power of 40  $\text{MW}_{\text{th}}$ . The proposed reactor design is only a first try and has not been subject to any optimisation procedures. The calculations are performed by the PANTHERMIX-code system which establishes a coupling between the diffusion code PANTHER and the thermal-hydraulics code THERMIX/DIREKT, which is described in section 5.3. Section 5.4 reports the calculational results during normal operation. This embraces burnup calculations that simulate the continuous fuelling of pebbles on top of the initial pebble bed until the maximum core height is reached. Section 5.5 focuses on the excess reactivities, the control rod requirements and an envisaged start-up procedure of the HTR-Pu, for both Pu-loadings. Finally, section 5.6 shows the calculational results of the

HTR-Pu under off-normal conditions. Several loss-of-cooling scenarios were simulated in order to examine whether the HTR's passive safety features are preserved in case the reactor is loaded with the mentioned Pu-fuels.

Chapter 6 presents the final conclusions of this study.

An important stage in almost any deterministic unit-cell calculation is the generation of shielded fine-group cross sections in the resonance energy range. These computations are often performed by the so-called "Nordheim Integral Method" or sometimes by a method based on "Equivalence Theory". A key-parameter for these shielding calculations is the volume-to-surface ratio of the fuel lump, i.e. the fuel kernel in case of the HTR. However, if the distance between the fuel kernels is small compared to the neutron's mean free path in the graphite, the kernels 'interact' and, hence, the dimension of the fuel kernel becomes effectively larger. This 'fuel shadowing' phenomenon is quantified in the shielding calculations by the Dancoff(-Ginsburg) factor. The average Dancoff factor for a fuel kernel in an HTR pebble depends, amongst others, on the number of CPs per pebble as well as on the size of the fuel kernels. Appendix A presents an analytic expression for the average Dancoff factor of a fuel kernel in an HTR pebble. The Dancoff factors used in the pebble-cell calculations of chapters 3 and 4 were calculated according to this analytic expression.

Appendix B gives the temperature profile across a pebble and derives, on the basis of this profile, the average and effective temperature of the fuel and the graphite.

Appendix C presents a study on the maximisation of the Doppler-effect (i.e. the fuel temperature reactivity feedback). The incentive for performing this maximisation study originated from the expectation that the absence of  $^{238}\text{U}$  would have a weak Doppler-effect as a consequence. Therefore, a generic study was initiated in which the Doppler coefficient was calculated for unit cells with different dimensions but all having the same  $k_{\infty}$ . It was demonstrated that a maximum Doppler coefficient (in absolute sense) can be found at a particular effective dimension of the fuel lump. This has been done for reactor-grade  $\text{PuO}_2$ ,  $\text{UO}_2$  and  $\text{ThO}_2$ . Besides the calculational results an analytic study is presented which explains the results of the calculations and which presents the key-parameters that determine the optimal dimension of the fuel lump. Appendices D and E are auxiliary to appendix C.



## Chapter 2

---

# The Pebble Bed High Temperature Reactor

---

In High Temperature Reactors, helium serves as a coolant and graphite acts both as a structure material and as moderator. The fuel consists of coated particles that are embedded in the graphite of the fuel elements. Two basic concepts of high temperature reactors exist:

- The Modular High Temperature Gas-Cooled Reactor (MHTGR) [24–27], designed by General Atomics. The fuel elements are hexagonal graphite blocks in which fuel rods are inserted. The fuel rods are made of graphite in which coated particles are embedded.
- The pebble-bed High Temperature Reactor (HTR) is fuelled with pebbles of 6 cm diameter, in which tens of thousands CPs are embedded [28]. The founder of this reactor concept is the late Prof. Dr. rer. nat. R. Schulten [29]. Two reactors based on his principle were built, namely the 50 MW<sub>th</sub> AVR [30–32] and the 750 MW<sub>th</sub> THTR-300 [33, 34]. These reactors were successfully operated for a long period of time. On the basis of the experiences with the AVR, KWU (nowadays Siemens) came up with a design called the 200 MW<sub>th</sub> HTR-Modul, whereas BBC/HRB (nowadays ABB) proposed the 250 MW<sub>th</sub> Industriereaktor. As a follow-up of the THTR, BBC/HRB designed the 1390 MW<sub>th</sub> HTR-500.

In this study, we will focus on the pebble-bed type High Temperature Reactor. This reactor has been developed as a reactor type for the production of electricity as well as for the generation of high quality heat. In the beginning of the development, the achievement of a higher thermodynamic efficiency, thanks to higher coolant temperatures, together with the outlook to attain a high degree of utilisation of the fuel received most attention. However, in the course of years other perspectives like process heat utilisation and the accomplishment of systems with particularly favourable safety features became of extreme importance for High Temperature Reactor development.

### 2.1 Passive Safety

During the last two decades of reactor safety development, an increasing amount of attention has been paid to *inherent* and so-called *passive* safety features. "Inherent safety means that the reactor's mechanical and functional design is such that the plant remains in a safe condition on the basis of the laws of nature; these laws ensure that process variables

and parameters remain within safe boundary values in all conceivable circumstances. This implies that no human interference, no triggering signals and no supply of external energy are required to remain in a safe condition. Passive safety features come into operation in the event of an accident without the necessity for switching or triggering operations or supply of external energy." (from [35]). A safe condition in this context means that no unintended release of radioactive materials to the environment takes place. Strictly speaking, this would allow a core melt-down provided that the molten core stays inside the reactor containment and thus does not enter the environment. However, in practice a more tightened definition is employed, which implies that the release of an unacceptable amount of radioactivity from the core is not allowed, even when it stays within the primary circuit. (What is meant with "unacceptable" in this context depends on the directives of the nuclear regulatory authorities.) It should be noted that if the system is fully passively and inherently safe, all safety devices and barriers like the reactor containment have become superfluous.

The pebble-bed HTR has some favourable properties which guarantee a high degree of passive safety. These properties are:

- The fuel is in an excellent way contained by tiny coated particles, which are in fact miniature pressure vessels. The coatings of these particles provide for the retention of fission products up to very high temperatures. In general, an upper limit of 1600 °C for the coated particles is accepted. All the barriers that have to be crossed before fission products can enter the environment are: the oxide fuel kernel itself, the coatings, the graphite matrix, the containment of the primary circuit and, if present, the reactor containment. This multi-barrier concept is also referred to as the defence-in-depth principle.
- Under normal operational conditions, the retention of the CPs is so good that there is only very small release of fission products to the coolant. The very low contamination of the coolant (in the ppm-range) does not cause any corrosion in the primary system.
- The CP-particle fuel offers a high degree of flexibility. By varying the number of CPs per pebble, the moderator-to-fuel ratio can easily be varied. Note that if one changes the moderator-to-fuel ratio in an LWR, by widening the lattice or by changing the dimensions of the pins, one simultaneously changes the cooling properties of the system since in an LWR water acts both as moderator and as coolant. In case of the pebble-bed HTR, a high degree of freedom is available to choose that moderator-to-fuel ratio that gives appropriate temperature coefficients of reactivity. It is needless to say that sufficiently negative temperature coefficients of reactivity are required for a self-controlling nuclear chain reaction and are therefore of paramount importance for the safety of the system.
- The high surface-to-volume ratio of the coated particles in combination with the high heat conductivity of the graphite provides for an efficient heat transfer. This implies, on the one hand, a small temperature difference between the fuel kernels and the graphite matrix and, on the other hand, a small temperature difference between the pebble's center and its surface. These small temperature differences enable relatively high overall pebble temperatures.
- Helium acts as a coolant, which is advantageous because it is chemically inert. Since it does essentially not interact with neutrons it can be considered from the neutronics point of view as inert as well. Moreover, helium can not undergo a phase change, which

implies that uniform cooling is guaranteed. By way of contrast, in a PWR all kinds of two-phase cooling regimes exist (or might occur), which result in different efficiencies for the heat transfer from the fuel to the moderator.

- Graphite acts both as structure material and as moderator. Unlike metals it does not melt at relatively low temperatures but has a sublimation point that is as high as  $\sim 3600\text{ }^{\circ}\text{C}$ .
- A nuclear reactor is in thermal-hydraulic equilibrium if its heat removal equals its heat production. If there occurs an imbalance, for instance due to a loss-of-forced-cooling incident, the design of the reactor has to be such that the temperatures remain below certain limits in order to preserve the integrity of the system and thus to prevent release of radioactivity. Even if the nuclear chain reaction has died out, either due to scram or due to autonomous shut-down, the heat production still goes on because of radioactive decay, which amounts to 5-7% of the fission power in the stationary state. This phenomenon is of major importance as regards reactor safety. One can distinguish two approaches, not excluding each other, to ensure that the temperature remains in an acceptable range in case of a loss-of-forced-cooling incident.
  1. Limit the amount of energy that will be deposited in the core.
  2. Limit the temperature increase due to the amount of energy that is, despite of 1, deposited in the core.

As far as objective 1 is concerned, the difference of the energy production and energy removal represents the amount of energy that will be deposited in the core. Note that the lower limit of the energy *production* is always determined by the decay heat, since this can by no means be turned off. In case of the HTR, the energy production is relatively low because of its low power density, i.e.  $\sim 3\text{ MW/m}^3$ . The lower limit of the heat *removal* is determined by the heat that can be removed by passive means, i.e. heat transfer from the reactor to the surroundings. Inside an HTR heat is transferred toward the reactor boundaries by convection, conduction and radiation. Helium that is still present in the core, which is of course dependent on the type of loss-of-cooling accident, takes care of the heat transport by natural convection. Due to the good heat conductivity of graphite, which moreover increases with increasing temperature, heat can easily be transferred by conduction. Heat transfer inside the pebble bed takes place by conduction via pebble-to-pebble contacts and via radiation across the inter-pebble cavities. Above a temperature of  $1400\text{ }^{\circ}\text{C}$  the heat transfer through the pebble bed is even higher than that of solid block of graphite thanks to the heat transfer by radiation (see fig. 6.45 of [28]). The heat transfer from the reactor vessel to the ambient takes place by both radiation and convection. In case of the HTR, heat transport is realised by air that can flow along the outer surface of the reactor vessel in a passive way (i.e. natural cooling).

As far as objective 2 is concerned, the HTR contains large amounts of graphite. Since graphite has a high specific heat capacity that, moreover, increases with increasing temperature (see fig. 4.31 b of [28]), the energy deposition in the core leads to a relatively small increase of the temperature.

- Because of the continuous supply of pebbles to the core no excess reactivity is necessary to compensate the reactivity loss due to burnup.

## 2.2 Fuel scenarios

The pebble-bed HTR consists of a helium cooled core that is filled with graphite spherical fuel elements (pebbles) with a diameter of 6 cm. In power reactors these pebbles are stochastically stacked, which implies that they occupy about 62% of the core volume [36].

The continuous supply and/or discharge of pebbles enables several fuel scenarios. Besides that, different types of fuel pebbles (e.g. feed and breed pebbles) as well as moderator pebbles can be loaded into the core. One can distinguish three elementary fuel scenarios for the pebble-bed HTR [28]:

- **Multi-pass**

The pebbles travel through the core from the top to the bottom. The pebbles are extracted at the bottom of the core by a discharging machine, after which their fissile content is measured. Once this appears to be sufficient, the pebble is reloaded at the top of the core. This is repeated until the pebble has reached its target burnup. This fuel scenario is envisaged for the 200 MW<sub>th</sub> HTR-Modul; it is also referred to as MEDUL, which is the German acronym for MEhrfachDUrchLauf.

- **OTTO**

In the OTTO-scenario (Once Through Then Out) each pebble travels through the core only once. This scenario was envisaged for the 1390 MW<sub>th</sub> HTR-500 concept.

- **PAP**

PAP is the acronym for the French *Peu à Peu* (little by little), which refers to a core that is continuously *supplied* with pebbles. The reactor starts with an initial pebble bed. During operation pebbles are added on top of the pebble bed until the core is completely filled. Then, all pebbles are discharged and subsequently a new batch can commence. In this scenario, the advantage of a minimum excess reactivity is preserved, while the on-line pebble discharging machine, which showed some problems in the past, can be omitted. In the last decade, several designs of PAP-based HTRs with powers varying between 10 and 80 MW<sub>th</sub> passed by: the GHR-10 [37], GHR-20 [38], PAP-20 [39], PAP-20 H [39, 40], PAP-GT [40–42], PAP-GT Th [41] and the PAP-80 [39]. In general, these designs have relatively low powers and are dedicated to decentralised co-generation of heat and power.

Chapter 5 deals with the reactor physics aspects of a plutonium fuelled HTR that is operated according to the PAP principle.

## 2.3 Pebbles

The cover of this thesis shows a cross section of a fuel pebble. In each fuel pebble [43], thousands of coated fuel particles (CPs) are dispersed in a fuel zone with a diameter of 5 cm. Besides their actual task of generating the desired power, the pebbles have to fulfill a variety of conditions. Primarily, a reliable retention of fission products in the pebbles during both normal and off-normal conditions have to be warranted. Furthermore, the pebbles have to be able to withstand both internal tensions due to temperature gradients and external burdens like a thrust after a free fall. Finally, impurities in the helium coolant may not cause unacceptable corrosion of the pebbles. These demands result in constraints



on the power per pebble, surface temperature of the pebble, the fuel temperature, the burnup and the fast neutron fluence. The constraints that have been used throughout this thesis will be presented in section 2.5. Below, we will discuss in which way the aforementioned parameters will affect the performance of the pebbles and the coated particles, successively.

### 2.3.1 Pebble integrity

The pebble must have a sufficient solidity to be able to withstand all demands during both normal and off-normal operation. The pebbles are subject to tensions due to thermal gradients. Within a pebble, the power density distribution determines temperature profile and thus the temperature gradients. Appendix B solves the temperature profile for a homogeneous power density distribution in the fuel zone of the pebble in case of a temperature-independent heat conduction coefficient. The tensions ( $\sigma^{tens}$ ) both in the radial and the tangential direction are determined by the power density ( $p$ ), the heat conduction coefficient ( $\lambda$ ), the thermal expansion coefficient ( $\alpha$ ), the elasticity modulus ( $E$ ) and the transverse contraction ( $\nu$ ). The maximal radial tension, occurring in the pebble center, and the maximal tangential tension, occurring on the pebble's surface, are both given by (p. 108 of [28])

$$\sigma_{max}^{tens} = \frac{E\alpha p R_o^2}{15\lambda(1-\nu)} \quad [\text{N/m}^2] \quad . \quad (2.1)$$

The minimum value (i.e. at 20 °C) of the permissible stresses for the graphite of the fuel element read  $1 \cdot 10^7$  N/m<sup>2</sup> and  $3.5 \cdot 10^7$  N/m<sup>2</sup> for the tangential (tensile stress) and the radial tensions (pressure), respectively. Adopting  $R_o = 0.03$  m,  $\alpha = 4 \cdot 10^{-6}$  K<sup>-1</sup> (at 1200 °C),  $E = 1.2 \cdot 10^{10}$  N/m<sup>2</sup>,  $\nu = 0.3$  from p. 109 of [28] and assuming  $\lambda = 10$  Wm<sup>-1</sup>K<sup>-1</sup> (conservative: irradiated A3-4 graphite at 250 °C according to [44]) allows a maximum power density  $p$  of  $24 \cdot 10^6$  W/m<sup>3</sup> in the pebble. This implies a boundary value of the power per pebble of 2.7 kW/pebble. In contrast with this result, a limit of 4.5 kW per pebble (for the HTR-M) was given by both ref. [45] (p. 7) and [16] (p. 21). These higher permissible pebble powers are probably based on the following. The highest power per pebble occurs in the fresh pebbles. These pebbles are hardly irradiated, which implies that the graphite has a much higher heat conductivity, viz.  $> 25$  Wm<sup>-1</sup>K<sup>-1</sup> for  $T < 1500$  °C (according to fig. 4.31.a of [28]), which is 2.5 times larger than the previously assumed one and thus allows a maximum power of 6.75 kW/pebble. Furthermore, the mentioned permissible stresses were conservatively estimated (i.e. low). For the purpose of this study we decided to consider the maximally permissible power of 4.5 kW/pebble found in literature as the appropriate one.

## 2.4 Coated particles

The first generation of coated particles were the so-called BISO CPs. Such a CP consists of a fuel kernel with a diameter of 200-600 μm that is surrounded by a porous carbon (PorC) buffer layer (~80 μm thickness) to absorb the fission products and to accommodate kernel swelling and a pyrolytic (PyC) carbon buffer layer with a thickness of ~110 μm that acts as a pressure vessel. The coatings, and to a lesser extent the fuel kernels themselves, provide the primary barrier against fission product release. The BISO coated particle was

improved by adding a SiC coating and another PyC-coating successively, which resulted in the so-called TRISO-coated particle. The properties of the coatings of such a TRISO-CP are listed in table 2.1. The function of the SiC-coating is twofold: it acts as a barrier, particularly against metallic fission products (see fig 6.23 of [28]), and it provides additional mechanical strength to the CP [46]. The TRISO CPs showed a reduction of the  $^{85}\text{Kr}$  release by a factor of 100 compared to the BISO CPs.

In the late 1960s and early 1970s, TRISO CPs dedicated to the burning of plutonium were fabricated and tested in irradiation and heating experiments. The aim was to fabricate a CP with which a high degree of plutonium incineration could be achieved, viz.  $\sim 75\%$  FIMA which corresponds to a burnup of  $\sim 750$  MWd/kgPu. Such a high burnup requires enough space to accommodate kernel swelling and fission products. Two approaches were chosen to meet this requirement. The first involves a dilution of the plutonium kernel with graphite, i.e. the diluted kernel. The second involves a small fuel kernel with a thick porous buffer layer, i.e. the concentrated kernel.

In the calculations of this thesis, coated particles with both concentrated and diluted kernels have been regarded. Table 2.1 lists the specifications of the pebble, the coatings and three kernel types that have been used in the calculational models. Although the coating properties of the diluted and concentrated kernels differ in practice, equal coating properties have been used for all kernels, in the calculational models of this study. The consequences of this simplification are limited because of the following reasons. Firstly, only the size and composition of the *fuel kernel* are important for the resonance shielding calculations and not the coatings. Secondly, the amount of graphite represented by the coatings is very small compared to the total amount of graphite of the pebble, which implies that changes in the coating properties hardly affect the slowing-down properties of the system.

The key nuclides that are of safety concern once released by the fuel elements, are the noble gases  $^{85}\text{Kr}$ ,  $^{133}\text{Xe}$ , the volatile nuclides  $^{131}\text{I}$  and  $^{133}\text{I}$  and the solid-material nuclides  $^{89}\text{Sr}$ ,  $^{90}\text{Sr}$ ,  $^{110m}\text{Ag}$ ,  $^{111}\text{Ag}$ ,  $^{134}\text{Cs}$  and  $^{137}\text{Cs}$ . The migration of these radioactive fission products from the fuel kernels to the helium coolant is primarily determined by a number of processes that are triggered by the following parameters

1. The fraction of as-manufactured defect CPs.
2. The temperatures of fuel kernel, coatings and graphite matrix.
3. The fast fluence ( $> 0.1$  MeV) suffered by the coatings.
4. The burnup.
5. The chemical composition of the fuel, i.e. the carbon-oxygen-heavy metal composition.

The first mentioned source of fission product release can be minimised by removing the particles that do not meet the specified requirements from the manufacturing process. According to [47], the fraction of CPs in the pebbles that has defect as-manufactured SiC-coatings is conservatively estimated as  $< 3 \cdot 10^{-5}$ . The as-manufactured defect particles constitute the main source of release of radioactive nuclides to the graphite and, subsequently, to the coolant. To prevent that during operation more coated particles break and that consequently the release of radiotoxicity increases, a number of reactor parameters

**Table 2.1:** Pebble, coatings and kernel specifications modelled in the calculational models of this thesis.

Pebble				
fuel zone radius	2.5 cm			
pebble radius	3.0 cm			
nuclide density graphite	$8.6456 \cdot 10^{-2} \text{ barn}^{-1} \text{ cm}^{-1}$			
boron density	$1.2518 \cdot 10^{-7} \text{ barn}^{-1} \text{ cm}^{-1}$			
pebble packing fraction	62 %			
Coatings				
coating	thickness ( $\mu\text{m}$ )	Carbon density ( $\text{barn}^{-1} \text{ cm}^{-1}$ )	Boron density ( $\text{barn}^{-1} \text{ cm}^{-1}$ )	Silicon Density ( $\text{barn}^{-1} \text{ cm}^{-1}$ )
PorC	95	$5.5151 \cdot 10^{-2}$	$7.985 \cdot 10^{-8}$	
1 <sup>st</sup> PyC	40	$9.5261 \cdot 10^{-2}$	$1.379 \cdot 10^{-7}$	
SiC	35	$4.8060 \cdot 10^{-2}$	$6.959 \cdot 10^{-8}$	$4.8060 \cdot 10^{-2}$
2 <sup>nd</sup> PyC	40	$9.5261 \cdot 10^{-2}$	$1.379 \cdot 10^{-7}$	
Fuel kernel				
radius ( $\mu\text{m}$ )	type	composition	Pu-mass ( $\mu\text{g}$ )	Pu-density ( $\text{barn}^{-1} \text{ cm}^{-1}$ )
100	<i>concentr.</i>	PuO <sub>2</sub>	38.71	0.023221
110	<i>concentr.</i>	PuO <sub>2</sub>	51.53	0.023221
250	<i>diluted</i>	PuC <sub>20</sub> O <sub>2</sub>	90.15	0.003461

like the temperature, fast fluence and burnup have to be constrained. However, even if all CPs remain intact, a small amount of radionuclides will diffuse through the coatings, the graphite matrix and will eventually end up in the primary circuit. This holds particularly for the noble gases and the volatile elements I and Ag. The process variables of an HTR must be such that these releases stay below certain limits (see tab. 6.3 of [28]).

## 2.4.1 Coated Particle Performance

One can distinguish four main processes that are responsible for the failure of CPs during operation, i.e. non-manufacturing failures. Once the previously mentioned parameters tend to unfavourable values (e.g. high burnup, high fast fluence) the processes leading to CP failures are intensified. The failure of the CPs has a statistical character, which means that not all CPs break down at the same time if a parameter exceeds a certain limit, but instead the *fraction* of broken CPs increases. The four performance-limiting processes that were identified on the basis of information gathered from irradiation and heating experiments

are surveyed below. Special attention is paid to the properties of the Pu-bearing CP in comparison with the conventional UO<sub>2</sub>-CP.

**Pressure vessel failure.**<sup>1</sup> About one half of the fission products are gaseous, which implies that at high burnup, a high pressure will prevail inside a CP. This high pressure exerts a tensile force on the coating. If the coating is thick enough, the tensile stress in the coating does not exceed the maximally permissible one. According to eq. 4.26 of [28], the minimum coating thickness reads

$$s_{min} = \frac{p \cdot r_{ct}}{\sigma_{max}}, \quad (2.2)$$

where  $p$  (N/m<sup>2</sup>) is the pressure inside the CP,  $r_{ct}$  (m) is the inner coating radius and  $\sigma_{max}$  is the maximally permissible tensile stress of the coating, which equals 10<sup>8</sup> N/m<sup>2</sup> for PyC. The pressure can be estimated by means of the ideal-gas equation of state, which reads

$$p = \frac{R n T}{V_G} \approx \frac{R(m_{Pu} \cdot \text{FIMA})T}{V_G A}, \quad (2.3)$$

where  $R = 8.3$  (N·m/K/mole) is the ideal-gas constant,  $n$  (mole) is the number of particles in the gas-state,  $T$  (K) is the gas temperature and  $V_G$  (m<sup>3</sup>) is the volume encapsulated by the inner PyC coating which can accommodate the gaseous fission products. Since about one half of the fission products is gaseous, the molar amount of gas can be approximated as the initial Pu-content ( $m_{Pu}$  in g) times the fissioned fraction of actinides (FIMA) divided by the average mass number of the actinide nuclides (i.e.  $A \approx 239$  for Pu-fuel). Page 110 of [28] presents a calculation of the pressure and the minimum coating thickness that is required to withstand the pressure for a typical UO<sub>2</sub>-CP. The second column of table 2.2 presents the figures of this UO<sub>2</sub>-CP, which shows that for a burnup of 100 MWd/kgHM (i.e. FIMA  $\approx$  0.1) and  $T = 1600$  K, the pressure amounts 200 bar ( $200 \cdot 10^5$  N/m<sup>2</sup>). A coating thickness  $s_{min} \approx 60$   $\mu$ m is required to withstand this pressure.

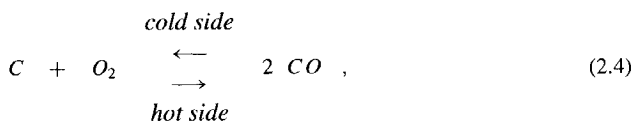
The same exercise has been performed for two Pu-CPs of table 2.2, thereby not aiming to give exact figures but rather providing insight into the order of magnitude of the prevailing pressure in such CPs. The main source of uncertainty for calculating the pressure is the volume available for the gaseous fission products. In the example of [28],  $V_G = 8.8 \cdot 10^{-11}$  m<sup>3</sup>. This is more than the volume of the buffer zone which implies that the fuel kernel itself can also accommodate gaseous fission products. The volumes of both the fuel kernel and the buffer zone constitute an upper limit of the volume available for the containment of gas. With this maximum value, a lower boundary of the pressure can be derived. (It is not clear from literature what the actual available gas volume is). Table 2.2 shows that if three quarters of the Pu-mass is fissioned and, moreover, if the temperature has the off-normal value of 1773 K, the minimum pressure lies in the range from 380 to 490 bar depending on the CP type. The derived minimum thicknesses of the coatings are in that case 150  $\mu$ m for the diluted kernel and 110  $\mu$ m and 45  $\mu$ m for the two concentrated kernels. If the actual available volume for the gaseous fission products appears to be two times smaller, it is clear that the pressures and the required coating thicknesses are twice the mentioned values.

<sup>1</sup>This paragraph is based on the analysis of p. 110 of [28]

Besides the burden of the increasing pressure during burnup, the coatings deteriorate due to the so-called recoil and knock-out mechanisms. The recoil mechanism refers to a highly energetic fission product that, immediately after it is born, penetrates into the coating up to  $\sim 15 \mu\text{m}$ . When, on the other hand, such a fission product knocks away a number of graphite atoms on the coating surface the fission products that are situated in the vicinity of the coating layer can enter the created 'crater'. This is referred to as the knock-out mechanism. The release of fission products by these mechanisms depend on the burnup and are usually rather small.

A stronger contribution to the release of fission products can be ascribed to the fast fluence ( $> 0.1 \text{ MeV}$ ). Fast neutrons cause displacements of atoms in the lattice of the coatings which leads to a deterioration of the coatings and possibly to a break down of the coatings. Fig. 6.11 of [28] shows that the fraction of broken particles, predicted by the computer program PANAMA [48], amounts to 0%, 0.4% and 0.85% for fast fluences of  $0, 5 \cdot 10^{21}$  and  $9 \cdot 10^{21} \text{ n/cm}^2$ , respectively. On the other hand, ref. [49] reports that there is an apparent lack of irradiation damage effects on the high-temperature stability of the SiC material, which is an allegedly surprising observation, given the influence on crystal structure that bombardment of fast neutrons may cause. These observations were based on several irradiation experiments with ultimate loads of 70% FIMA/ $6.3 \cdot 10^{25} \text{ n/cm}^2$  for  $\text{UC}_2$  TRISO particles and 4.1% FIMA/ $11.5 \cdot 10^{25} \text{ n/cm}^2$  for  $\text{ThO}_2$  TRISO particles. Ref. [49] adds that effects of fast fluence may well be present but that they may be overshadowed by the variability in the performance capability of the crystalline SiC layer due to normal variation in processing conditions.

**Kernel migration** Kernel migration or 'amoeba effect' is the result of carbon transport in a thermal gradient leading to an attack on the dense coating layers. At the high-temperature side of the kernel CO-gas is formed, according to the chemical reaction



which pushes the kernel against the coating at its low-temperature side. The kernel migration effect is determined by the burnup, the chemical composition of the kernel, the temperature and temperature gradient across the kernel. Ref. [19] (p. 3-17) reports a good performance for the concentrated Pu-CP fuel with a low oxygen content ( $\text{PuO}_{1.68}$ ) and a poor fuel performance for a higher oxygen content ( $\text{PuO}_{1.81}$ ) which has been ascribed to the kernel migration phenomenon. Currently, research focuses on coated particles with a ZrC-coating instead of a SiC-coating, or a combination of both. These ZrC-containing CPs have several (potential) advantages, of which one is the allegedly good resistance against kernel migration [50].

**SiC thermal dissociation** Thermal dissociation can progress to complete SiC degradation as the temperatures increase beyond  $2200 \text{ }^\circ\text{C}$ . If the design of the reactor is such that the fuel temperature of  $1500\text{-}1600 \text{ }^\circ\text{C}$  is never exceeded, SiC-coating failure due to thermal dissociation is very small. However, thermal decomposition of SiC is the primary

**Table 2.2:** Lower limit of the pressure inside a coated particle ( $p$ ), based on the upper limit for the volume available for the accommodation of gaseous fission products ( $V_G$ ).  $S_{min}$  is the coating thickness that is minimally required to withstand this pressure. These quantities are calculated for one U-bearing CP and three Pu-bearing CPs.

fuel type	UO <sub>2</sub>	PuO <sub>1.8</sub> C <sub>19.5</sub>	PuO <sub>1.6</sub>	PuO <sub>1.68</sub>
source	p. 110 ref. [28]	sample D, tab.XI, ref. [18]	sample T, tab.XI, ref. [18]	p. 3-50 ref. [19]
HM-content ( $\mu\text{g}$ )	330	120	75	36 $\pm$ 5
$r_{fk}$ (m)	$2.0 \cdot 10^{-4}$	$2.75 \cdot 10^{-4}$	$1.35 \cdot 10^{-4}$	$0.9-1.0 \cdot 10^{-4}$
$r_{PyC-t}$ (m)	$3.0 \cdot 10^{-4}$	$3.0 \cdot 10^{-4}$	$2.8 \cdot 10^{-4}$	$1.9-2.2 \cdot 10^{-4}$
envisaged FIMA	10%	75%	75%	75%
$V_{kernel}$ (m <sup>3</sup> )	$3.4 \cdot 10^{-11}$	$8.7 \cdot 10^{-11}$	$1.0 \cdot 10^{-11}$	$0.4 \cdot 10^{-11}$
$V_{buffer}$ (m <sup>3</sup> )	$7.6 \cdot 10^{-11}$	$2.2 \cdot 10^{-11}$	$8.2 \cdot 10^{-11}$	$3.3 \cdot 10^{-11}$
Estimated quantities				
$T$ (K)	1600	1773 <sup>(a)</sup>	1773 <sup>(a)</sup>	1773 <sup>(a)</sup>
$V_G$ (m <sup>3</sup> )	$8.8 \cdot 10^{-11}$	$10.9 \cdot 10^{-11(b)}$	$9.2 \cdot 10^{-11(b)}$	$3.7 \cdot 10^{-11(b)}$
$p$ ( $10^5$ N/m <sup>2</sup> ) eq. 2.3	200	490 <sup>(c)</sup>	380 <sup>(c)</sup>	450 <sup>(c)</sup>
$S_{min}$ ( $\mu\text{m}$ ) eq. 2.2	60	150	110	45

<sup>(a)</sup>Temperature of 1500 °C , which is often used as the limit that may not be exceeded during accidents.

<sup>(b)</sup>This is an upper limit, assuming that the volume of fuel kernel and buffer layer is empty and thus fully available to accommodate gaseous fission products.

<sup>(c)</sup> This is a lower limit corresponding to the upper limit of the available volume for the gaseous fission products mentioned in <sup>(b)</sup>.

mechanism for coating failure and consequent fission product release in the temperature range from 1900 to 2500 °C [49].

**SiC/fission product interactions** Ref. [51] presents an overview of fission products that chemically interact with the SiC layer, resulting in corrosive SiC degradation, which may ultimately lead to failure. The main contributor to the corrosion of SiC is the fission product palladium (Pd) [52]; minor contributions may occur due to reactions with rare earths (in particular Ce and Eu), interactions with CO/O<sub>2</sub> (once the inner PyC-layer is penetrable) and reactions with metallic impurities in the graphite (like Fe, Ni, Co).

Since this thesis deals with Pu CP-fuel, it is useful to compare the Pd-fission yields of <sup>239</sup>Pu and <sup>241</sup>Pu with that of the conventional main fissile isotope <sup>235</sup>U. Table 2.3 lists the mass chain yields of the fission products with mass numbers 105 to 111, retrieved from [53]. All fission products belonging to the mass chains (i.e. the isobars) with mass numbers 105, 106, 107, 108 and 110 end up in a stable or long-lived Pd-isotope after successive  $\beta^-$  decays. The last row of table 2.3 shows that the total yield resulting in a stable or long-lived Pd-isotope is for <sup>239</sup>Pu about 7 times, and for <sup>241</sup>Pu about 13 times larger than that of <sup>235</sup>U.

The  $\beta^-$ -decay chain with mass numbers 109 and 111 end up in <sup>109</sup>Ag and in <sup>111</sup>Cd (via <sup>111</sup>Pd  $\rightarrow$  <sup>111m</sup>Ag  $\rightarrow$  <sup>111</sup>Ag [ $T_{1/2}$  = 7.5 d]  $\rightarrow$  <sup>111</sup>Cd), respectively. These chains are included since

the silver isotopes diffuse relatively easily through the kernel, coatings and matrix (see fig. 6 of [47]). According to table 6.4 of [28],  $^{111}\text{Ag}$  is the main source of activity in the coolant as far as solid fission products are concerned (viz.  $1.1 \cdot 10^{-6} \text{ Ci/m}^3$  for  $T_{He} = 950 \text{ }^\circ\text{C}$  measured in the AVR) and hence is important to maintenance considerations. Table 2.3 reveals that the chain yield with mass number 111 is for  $^{239}\text{Pu}$  16 times and for  $^{241}\text{Pu}$  31 times higher than that of  $^{235}\text{U}$ . Once a Pu-fuelled HTR is designed one should take this into consideration.

Above it was shown that the fractional Pd-yields of both Pu-isotopes are considerable higher than that of  $^{235}\text{U}$ . However, what really matters is the absolute amount of Pd that will be produced within a coated particle. To investigate this we compare a CP with a  $200 \mu\text{m}$ -diameter  $\text{PuO}_2$ -kernel to a conventional  $\text{UO}_2$ -CP of the HTR-M [45]. The fission fractions in an HTR-M under equilibrium conditions read : 0.66, 0.27 and 0.07 for  $^{235}\text{U}$ ,  $^{239}\text{Pu}$  and  $^{241}\text{Pu}$ , respectively (derived from tab. III of [45]). This gives a Pd-yield of 6% per fission. Since the HM-content of the  $\text{UO}_2$ -CP amounts to  $600 \mu\text{g}$  and the exit burnup reads  $80 \text{ MWd/kgHM}$ , this results in a cumulative Pd-production of about  $3 \mu\text{g}$ .

The  $\text{PuO}_2$ -CP has a HM-content of  $39 \mu\text{g}$  and a target burnup of, say,  $700 \text{ MWd/kgHM}$ . Assuming, a priori, that at this burnup 50% of the fissions products originate from  $^{239}\text{Pu}$  and 50% from  $^{241}\text{Pu}$ , gives a Pd-yield of 17%. This corresponds to a cumulative Pd-production of  $5 \mu\text{g}$ . It should be noted, however, that for Pu-CPs with higher mass contents (see tabs. 2.1 and 2.2) the generated Pd-mass per CP will of course be higher. The Pu-bearing CP with the diluted kernel will produce about  $12 \mu\text{g}$  under the same conditions.

Currently, coated particles with ZrC-layers receive much interest, particularly in Japan [54]. The advantages of ZrC are its stability at very high temperatures and its good resistance against corrosion by Pd and other elements. If the aforementioned Pd-production of the Pu-bearing SiC-TRISO-CP would cause difficulties, one might consider to switch over to ZrC-TRISO CPs, where the SiC-layer is replaced by a ZrC-layer. Moreover, other concepts [54] like a CP of which one of the layers has a gradually changing SiC-to-ZrC ratio or a CP with a SiC-ZrC sandwich layer have been developed. However, more irradiation and heating experiments, in particular for a combination of a high burnup, a high fast fluence and high temperatures, have to be carried out to proof a satisfactory fission product retention for such ZrC-CPs.

## 2.4.2 Experiences with irradiations experiments

In the late 1960s and in the early 1970s, six irradiation experiments were performed to test the capability of coated particle fuel with the aim to achieve burnups in excess of  $700 \text{ MWd/kgHM}$ . Table 2.4 gives an overview of these experiments and shows some data obtained from them [27]. Irradiation experiment 6 shows that the coated particle with a  $\text{PuO}_{1.68}$ -kernel of  $195 \pm 5 \mu\text{m}$ -diameter shows a good behaviour. What "good" means in this context is not elucidated in [19]. Fig. 2.1 shows representative cross sections of these high burnup coated particles. The burnups that were achieved in this experiment represent those that are pursued in a Pu-burning HTR. However, the irradiations were performed for relatively low fast fluences, as will be seen later, and for a maximum temperature of only  $1444 \text{ }^\circ\text{C}$ . For  $\text{UO}_2$ -fuel a temperature limit of  $1600 \text{ }^\circ\text{C}$  under off-normal conditions is generally accepted. Due to the lack of information on Pu-CP performance above  $1444 \text{ }^\circ\text{C}$

**Table 2.3:** Mass-chain fission yields of three fissile nuclides. The data from several references, published in [53], were averaged and subsequently rounded to two significant digits.

chain mass number	stable isobar in $\beta^-$ -decay chain	yield (%) <sup>235</sup> U	yield (%) <sup>239</sup> Pu	yield (%) <sup>241</sup> Pu
105	<sup>105</sup> Pd	1.0	5.7	6.0 <sup>a</sup>
106	<sup>106</sup> Pd <sup>106</sup> Ru ( $T_{1/2} = 374$ d)	0.40	4.4	6.1
107	<sup>107</sup> Pd ( $T_{1/2} = 6.5 \cdot 10^6$ y)	0.14	3.2	4.9 <sup>b</sup>
108	<sup>108</sup> Pd	0.057	2.1	3.9 <sup>c</sup>
109	<sup>109</sup> Ag	0.029	2.0	2.9 <sup>d</sup>
110	<sup>110</sup> Pd	0.025	0.63	not av.
111	<sup>111</sup> Cd	0.020 <sup>e</sup>	0.32	0.63 <sup>e</sup>
sum: 105+106+ 107+108+110	Pd-isotopes	1.6	12	>21

<sup>a</sup> cumulative yield up to <sup>105</sup>Rh ( $T_{1/2} = 35$  h)

<sup>b</sup> cumulative yield up to <sup>107</sup>Ru ( $T_{1/2} = 4$  m)

<sup>c</sup> cumulative yield up to <sup>108</sup>Ru ( $T_{1/2} = 4.5$  m)

<sup>d</sup> cumulative yield up to <sup>109</sup>Pd ( $T_{1/2} = 13$  h)

<sup>e</sup> cumulative yield up to <sup>111</sup>Ag ( $T_{1/2} = 7.5$  d)

**Table 2.4:** Overview of Pu-coated particle irradiations experiments performed in the past.

DRAGON tests (late 1960s)		
CP-manufacturing: Belgonucleaire Europe		
	tests 1 to 4	test 5
	R2-reactor Studsvik Sweden	Dragon test reactor
burnup	200-300 MWd/kgHM	747 MWd/kgHM
irradiation temperature	1450-1850 °C	1275 °C
fast fluence ( $E > 0.18$ MeV)	?	$1.5 \cdot 10^{21}$ n/cm <sup>2</sup>
RB <sup>a</sup> ( <sup>85m</sup> Kr)	$5 \cdot 10^{-6}$	$4 \cdot 10^{-5}$
test 6 : Peach Bottom irradiations (early 1970s)		
CP-manufacturing: Oak Ridge National Laboratory		
burnup	737 MWd/kgHM	
irradiation temperature	1444 °C	
fast fluence ( $E > 0.18$ MeV)	$2.2 \cdot 10^{21}$ n/cm <sup>2</sup>	
RB <sup>a</sup> ( <sup>85m</sup> Kr)	?	
performance	PuO <sub>1.68</sub> good, PuO <sub>1.81</sub> poor (amoeba effect)	

<sup>a</sup>RB is defined as the release rate divided by the birth rate.

it is not clear whether the temperature limit of 1600 °C is also applicable to the Pu-CPs.



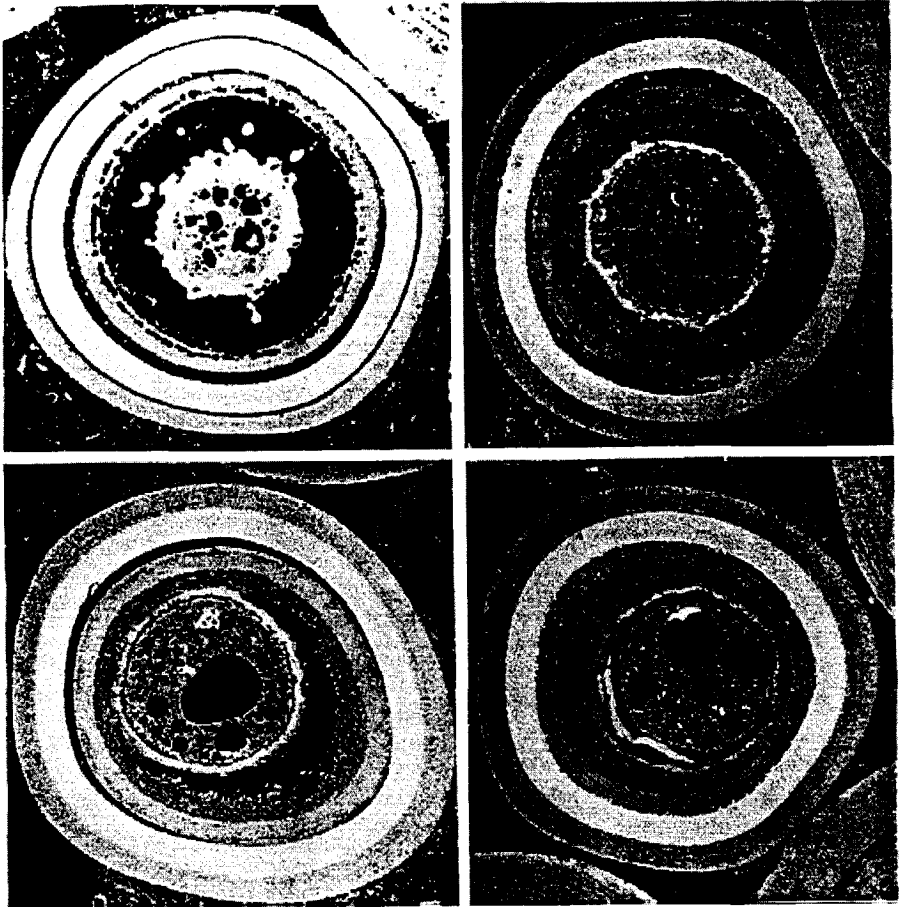


**Figure 2.1:** *Metallographic cross sections of high-burnup Pu coated particles from U.S. Peach Bottom HTGR irradiation test. Reproduced from fig. 3.2.1-2 of ref. [19].*

Moreover, no data on the release/birth-rate ratio of  $^{85m}\text{Kr}$  or other nuclides were present for the  $\text{PuO}_{1.68}$ -kernel in [19]. Since the data do not fully cover the parameter range of interest, the author of this thesis is inclined to propose further irradiation experiments to determine the constraints of plutonium bearing coated particle fuel. In addition, it might be worthwhile to develop ZrC-based coated particles dedicated to the burning of plutonium, because ZrC possesses an excellent stability at high temperatures and, moreover, shows strong resistance against Pd-attack and kernel migration.

## 2.5 Constraints assumed in this study

This thesis deals with the conceptual design of a Pu-burning pebble-bed HTR with the aim to fulfill the objectives presented in sec. 1.4 as good as possible. This can of course only be done within the constraints of the system. These constraints are such that the integrity of the pebbles and the coated particles are preserved under any circumstances and that consequently no unacceptable amounts of radiotoxicity can enter the primary system. In the preceding section it was mentioned that the constraints for the Pu-bearing CPs with regard to the maximally permissible temperature and burnup are not completely clear. In this thesis we presume that the maximally allowable temperature during off-normal operation equals the maximum temperature achieved in experiment 6 of table 2.4, namely 1444 °C. This is very conservative since our temperature limit refers to a temperature occurring only for a limited period of time during off-normal conditions, while the temperature of 1444 °C of irradiation experiment 6 refers to an elongated period of time during which the irradiation of the CPs took place. Furthermore, we presume that the maximum temperature during normal operation may not exceed 1250 °C. Irradiation experiments with *Pu-bearing* CPs have provided data for fast fluences up to  $2.2 \cdot 10^{21}$  n/cm<sup>2</sup> only (see table 2.4). However, since we expect that the Pu-CPs should be able to withstand much higher fast fluences we presume a constraint of  $8 \cdot 10^{21}$  n/cm<sup>2</sup>. Table 2.5 surveys the constraints that will be obeyed for the design of the Pu-burning HTR.

**Table 2.5:** Constraints for the Pu-burning HTR assumed in this thesis.

Maximum burnup	740 MWd/kgHM
Max. fuel temperature (normal conditions)	1250 °C
Max. fuel temperature (off-normal conditions)	1444 °C
Max. fast fluence ( $E > 0.1$ MeV)	$8 \cdot 10^{21}$ n/cm <sup>2</sup>
Max. power per pebble	4.5 kW

# Chapter 3

---

## Unit-cell calculations

---

This chapter<sup>1</sup> describes the results of unit-cell calculations for plutonium fuelled pebbles of the High Temperature Gas-cooled Reactor carried out with the code systems WIMS, SCALE and MCNP. The main objective of this chapter is to compare the calculational results of the WIMS code, which was candidate for the generation of nuclear data for the full-core calculations of chapter 5, to those obtained with SCALE and MCNP. In addition to that, some reactor physics interpretations of the calculational results are presented. These constitute an introduction of the extensive reactor physics analyses of chapter 4.

This chapter starts with the description of the mentioned codes systems. Thereafter, the results of calculations are presented. The calculations embrace the following: The  $k_{\infty}$  and spectral parameters, especially introduced for the plutonium fuel, have been calculated, for pebbles with 1 and 2 g Pu per pebble in combination with different types of coated particles. For one pebble geometry, the mentioned parameters have been calculated for various fuel temperatures and over-all (uniform) temperatures. For this particular geometry, burnup calculations have been carried out with WIMS and SCALE/ORIGEN-S.

A very important stage in the unit-cell calculations of both SCALE and WIMS is the generation of shielding fine-group cross sections in the resonance range. The self-shielding depends on the so-called Dancoff-factor. Section 3.2.2 presents a graph which shows the average Dancoff factor for a fuel kernel of an HTR pebble as a function of the number of CPs per pebble. The curves in this graph are based on an analytical formula. Appendix A presents the derivation of this formula.

### 3.1 Specifications of pebbles and coated particles

The upper-part of table 2.1 on page 23 shows the size and nuclide densities of the pebble, that are used in the calculations. The graphite density refers to the matrix material between the CPs and to the material of the pebble shell. The boron (19.8%  $^{10}\text{B}$ ) in the graphite of the calculational model accounts for the presence of various impurities in the graphite [36]. The packing fraction is defined as the volume of the pebble divided by the sum of the

---

<sup>1</sup>This chapter is based on chapters 3, 4 and 5 of ref. [55]

volumes of the pebble and the void. We recall that the fuel composition is given by table 1.2 on page 2.

## 3.2 Code descriptions

### 3.2.1 WIMS

**Library** The calculations with WIMS7b are performed with an adapted version of the 172 groups 1997-library (w97dg172v1.dat). The adapted version is equal to the original version except that the cross-section data of  $^{238}\text{Pu}$ ,  $^{241}\text{Pu}$  and  $^{242}\text{Pu}$ , as well as all Am and Cm-isotopes are replaced. The original library contains for these nuclides resonance integrals at infinite dilution and zero temperature only. Moreover, the thermal data are only present for room temperature. Since it is expected that the mentioned isotopes play an important role in uranium-free fuel, an appropriate resonance treatment might be required for them. This holds in particular for increasing burnup values, because then the contribution of the mentioned nuclides to the total absorption rate increases, whereas that of  $^{239}\text{Pu}$  and  $^{240}\text{Pu}$  decreases. The new cross-section data of  $^{238}\text{Pu}$ ,  $^{241}\text{Pu}$ ,  $^{242}\text{Pu}$ , the Am and Cm-isotopes are listed as a function of  $\sigma_p$  and  $T$ . The temperatures ( $T$ ) read 293.6, 700, 1250 and 2000 K, and the  $\sigma_p$ -values read  $10^2$ ,  $10^3$ ,  $10^4$ ,  $2 \cdot 10^4$ ,  $10^5$ ,  $10^6$ , and  $10^9$  barn. The data were obtained in the following way:

For each nuclide and for all mentioned ( $\sigma_p$ ,  $T$ )-combinations, cross sections sets were generated by the code package SCALE-4. Each calculation is based on an infinite homogeneous medium in which the nuclide of interest is mixed with hydrogen with a ratio that corresponds to a particular  $\sigma_p$ -value. Each SCALE calculation comprises a BONAMI-S [56] and a NITAWL-II [57] calculation, which take care of the unresolved resonance treatment by the Bondarenko method and the resolved resonance treatment by the Nordheim Integral Method, respectively. The calculations were performed with the EIJ2-XMAS 172-group library [58] (version March 95), which is just like the WIMS library based on the JEF2.2 library. Each SCALE calculation results for each nuclide in a set of AMPX-working libraries. The WIMS library tool WILITO [59] translates all libraries into WIMS format, after which all sets belonging to one nuclide are lumped. Subsequently, WILITO replaces the existing cross-section set of this nuclide by the new 'lumped' set.

**Calculational Method** It is impossible to model a spherical geometry containing grains with the WIMS-code. Therefore, an equivalent cylindrical cell containing grains has been used as an approximation. The validity of this approximation has been tested for the LEUPRO-1  $\text{UO}_2$  fuel in [60]. To this end, two MCNP calculations with both a spherical geometry and an equivalent cylindrical geometry were carried out. It was shown that the  $k_\infty$ 's were in agreement within an accuracy of 0.07%, whereas the spectral parameters showed deviations of maximally 3%. As far as these parameters are concerned the equivalent cylindrical model seems an acceptable approximation.

The spherical pebble is translated into an equivalent infinitely long cylinder by conservation of the mean chord length of the fuel zone. As the mean chord length of a convex body is given by  $4 \times \text{volume/surface}$  [61], that of the fuel zone of a pebble reads  $\frac{10}{3}$  cm.

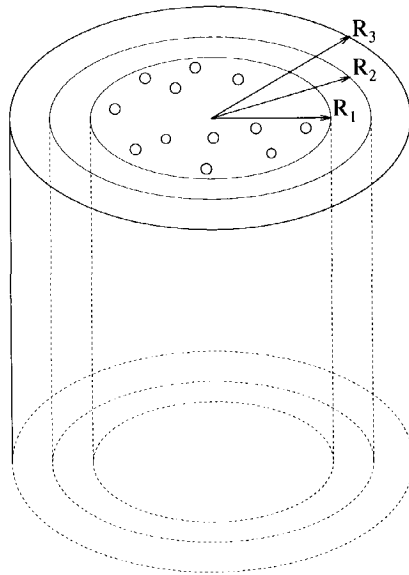


**Figure 3.1:** *Equivalent cylindrical model used by the module WPROCOL of the WIMS code system. The outer radius of the fuel zone is given by  $R_1 = 1.66667$  cm, based on the equivalence of the chord length of the spherical fuel zone. The outer radius of the graphite annulus ( $R_2 = 2.1909$  cm) and the outer radius ( $R_3 = 2.7824$  cm) of the void region are based on volume-ratio conservation.*

This chord length corresponds to a radius of  $\frac{5}{3}$  cm for the fuel zone of an infinite cylinder. The outer radii of the annular cylindrical shells, that correspond to the pebble shell and inter-pebble void are based on volume-ratio conservation and are therefore equal to 2.1909 and 2.7824 cm, respectively. The described annular cylindrical model, of which the inner zone contains the coated particles, is used by the WIMS-module WPROCOL to generate collision probabilities that are used for both the resonance calculations and the flux calculations (WPIP) later on. The resonance calculations are performed by the sequence WPRES-WPROCOL-WRES. Here, WPRES sets up a new interface containing subgroup cross sections that have been obtained by fitting the library resonance integrals. In case the original library is used, the subgroup treatment is performed for  $^{239}\text{Pu}$  and  $^{240}\text{Pu}$  only, since these are the only nuclides in the fuel that have temperature and  $\sigma_p$ -dependent resonance data. In case of the adapted version of the library, the subgroup treatment is extended with the nuclides  $^{241}\text{Pu}$  and  $^{242}\text{Pu}$ . Due to restrictions of the WPRES-module no more than 4 resonance absorbers can be treated. Subsequently, WPROCOL evaluates the collision probabilities for the subgroup cross sections in the mentioned cylindrical geometry. Then, WRES uses the collision probabilities to calculate the subgroup fluxes and an appropriately weighted broad group resonance cross section [62, 63]. Before the mentioned subgroup method is applied to  $^{239}\text{Pu}$ ,  $^{240}\text{Pu}$ ,  $^{241}\text{Pu}$  and  $^{242}\text{Pu}$ , WHEAD carries out the resonance shielding for all resonance absorbers, in an approximate way. This approximate calculation is based on equivalence theory and is in our case applied to a slab geometry. WHEAD calculates a potential scatter cross section ( $\sigma_p$ ) appropriate to the slab geometry and interpolates in a table of resonance integrals as a function of  $\sigma_p$  and  $T$ . The

slab geometry is constructed in such a way that the effective mean chord length of the inner layer of the slab (i.e. two times the width of the layer) is equal to the effective mean chord length of a fuel kernel ( $\bar{l}_F$ ). The effective mean chord length reads

$$\bar{l}_F = \bar{l}_F \left( \frac{1}{\mathcal{A}} + \frac{C}{1-C} \right) , \quad (3.1)$$

which originates from eq. D.6. Here,  $\mathcal{A}$  is the so-called Bell factor, that originates from a modification of Wigner's rational approximation for the first-flight escape probability. The Bell factor has the fixed value of 1.16, which is identical to the default value used by WHEAD. Furthermore,  $C$  is the average Dancoff factor for the fuel kernel, accounting for 'fuel shadowing' between kernels. This Dancoff factor was given by a formula (eq. A.29) that was derived by analytic means. Appendix A (see also ref. [64]) presents the derivation of this formula. Moreover, section 3.2.2 presents the Dancoff factor by graphical means. The mean chord length of the fuel kernel  $\bar{l}_F$  is equal to  $\frac{4}{3}$  times the radius of the fuel kernel. The width of the fuel layer in WHEAD becomes equal to  $\bar{l}_F/2$ . Since the fuel layer width of the slab is an *effective* one, which means that it is already 'Bell and Dancoff-corrected', the Bell and Dancoff factor supplied to the WHEAD module are set to 1 and 0, respectively (i.e. BELL=1.0 and DANCOFF=0.0).

### 3.2.2 The Dancoff factor

An important stage in the unit-cell calculations of both WIMS and SCALE is the generation of shielded fine-group cross sections in the resonance energy range. To this end, SCALE uses the so-called "Nordheim Integral Method", while WIMS uses a method based on "Equivalence Theory". A key-parameter for these shielding calculations is the volume-to-surface ratio of the fuel lump, i.e. the fuel kernel in case of the HTR. If the distance between the fuel kernels is small compared to a neutron's mean free path in the graphite in between the kernels, the kernels 'interact' and, hence, the volume-to-surface of the fuel kernel becomes effectively larger. This 'fuel shadowing' phenomenon is quantified by the Dancoff(-Ginsburg) factor. Appendix A presents an analytic expression for the average Dancoff factor of a fuel kernel in a HTR pebble. The Dancoff factors used in the cell calculations of chapters 3 and 4 were based on eq. A.29. Fig. 3.2 shows the average Dancoff factor for a fuel kernel in an HTR pebble as a function of the number of CPs per pebble with the size of the fuel kernel as a parameter.

### 3.2.3 SCALE

The SCALE-calculation involves a double heterogeneous cell-calculation, which is illustrated in fig. 3.3. First, a calculation on grain level ('grain-cell' calculation) is performed and thereafter another one on pebble level ('pebble-cell' calculation) is performed. The grain-cell calculation embraces the following. First, the codes BONAMI-S and NITAWL-II process shielded group cross sections, using the 172-group EIJ2-XMAS library based on JEF2.2. BONAMI-S performs the resonance shielding for the unresolved resonances, whereas NITAWL-II does the same for the resolved resonances by the Nordheim Integral Method. Both codes use an externally calculated Dancoff factor, given by eq. A.29. (This Dancoff factor is identical to the one used for the calculation of the effective chord length

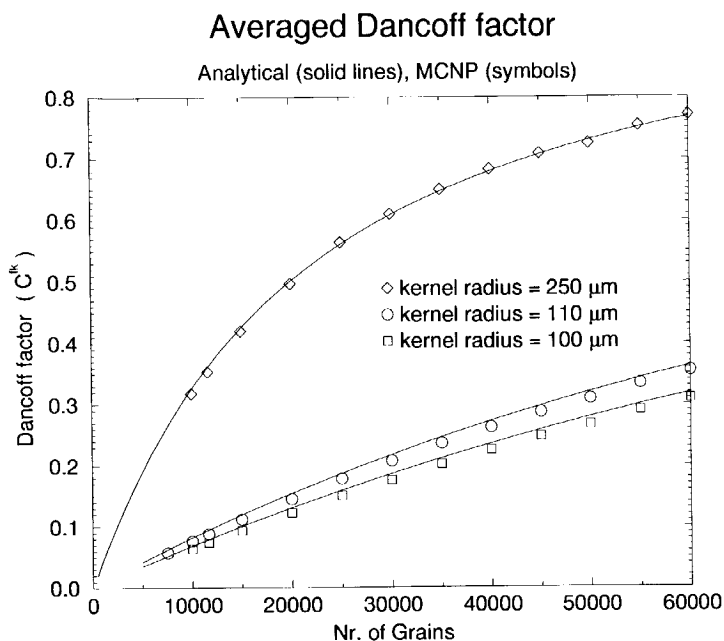


**Figure 3.2:** *The average fuel-kernel Dancoff-factor as a function of the number of coated particles (grains) in the fuel zone, with the fuel kernel radius as a parameter.*

of the fuel layer in the slab geometry of WIMS' module WHEAD). Thereafter, the one-dimensional discrete ordinate code XSDRNPM [65] uses the shielded group cross sections and solves the eigenvalue equation in radial coordinates. The grain cell has a spherical annular geometry. It consists of the kernel, surrounded by a spherical shell containing the four coatings in a homogenised sense, a shell containing the inter-granular matrix material, as well as a shell containing the pebble shell and the inter-pebble void. The volume ratios between the various spherical shells in this grain cell are the same as in the real pebble bed. After the spatial flux calculation performed by XSDRNPM, the cross sections of the inner three zones are weighted (so-called inner-cell weighting), but not collapsed.

These weighted cross sections are passed on to a second XSDRNPM calculation. This calculation is based on the pebble cell, which comprises a fuel zone (containing the weighted cross sections of the grain-cell calculation) with a radius of 2.5 cm, a pebble shell with an outer radius of 3 cm and an outer shell with an outer radius of  $3/(\text{packing fraction})^{1/3}$  cm. The last shell contains the inter-pebble void and hence its volume depends on the packing fraction of the pebbles. The outer spherical boundaries of both the grain cell and the pebble cell are isotropically reflecting. The  $k_{\infty}$  and the spectral parameters are calculated on pebble level.

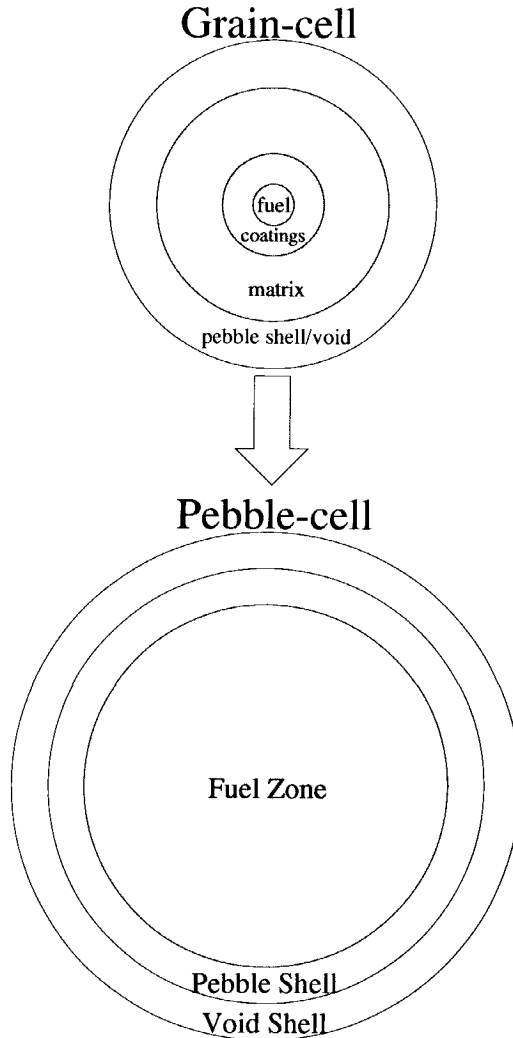


**Figure 3.3:** The two-step approach of SCALE: The upper-part is a schematic drawing of the grain cell, whereas the lower-part depicts the pebble cell. The grain cell consists of the fuel kernel, a shell containing the homogenised coatings, a shell representing the inter-granular matrix and a shell representing the pebble-shell plus void region. The inner region has the actual size of the kernel and the other regions are based on volume-ratio conservation. The cross-section data of the inner three regions are weighted with the inner-cell weighting option in SCALE. These data (grey area) are passed on to the inner region of the pebble cell. The pebble cell consists of the fuel zone, the pebble-shell and a shell representing the void in between the pebbles. Their outer radii read 2.5, 3.0 and 3.0/(packing fraction)<sup>1/3</sup> cm, respectively.



### 3.2.4 MCNP4B

The Monte Carlo Code MCNP4B [66] has been used in conjunction with the continuous-energy cross section library EJ2-MCNP [67]. This library is also based on the JEF2.2 evaluation, which makes a reliable comparison between the results of the three code systems possible. Fig. 3.4 shows the model used for the MCNP calculations. It is composed of the fuel zone, the pebble shell and a void shell, with outer radii of 2.5, 3 and  $3/(\text{packing fraction})^{1/3}$  cm, respectively. The outer boundary is isotropically reflecting, which seems expedient for a stochastically stacked pebble bed. Until so far, this spherical three-region cell resembles the SCALE pebble cell. However, while the fuel zone of SCALE's pebble cell is homogeneous and containing weighted cross sections originating from the grain cell, the fuel zone of the MCNP configuration is modelled explicitly. It contains a rectangular lattice of cubic unit cells, of which each consists of a fuel kernel and four surrounding coating layers.

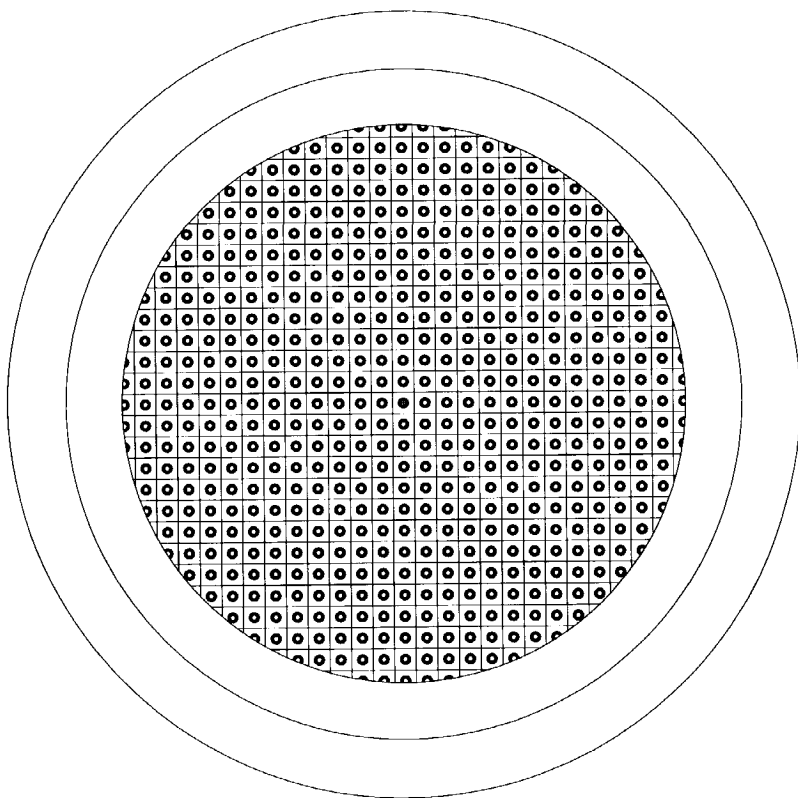


**Figure 3.4:** Cross section through the midplane of the double heterogeneous MCNP-model of the pebble. It is composed of the 5-cm-diam fuel zone, containing a rectangular lattice of cubic unit cells, the 0.5 cm graphite shell and the outer void shell. The outer spherical boundary is isotropically reflecting.

### 3.3 Results of calculations

The calculations have been performed for different pebble parameters and for different temperatures. Subsection 3.3.1 presents the calculational results of six cases. These cases differ with respect to the plutonium mass per pebble and the coated particle type. For these calculations the temperature is kept constant at 600 K, uniformly over the pebble. Subsection 3.3.2 presents the calculational results of one particular pebble geometry with varying temperatures. Parameters that have been calculated are also the  $k_{\infty}$  and spectral parameters based on the reaction rates of  $^{235}\text{U}$  and  $^{238}\text{U}$  become useless. Hence, a new set of spectral parameters based on  $^{239}\text{Pu}$  and  $^{240}\text{Pu}$ , which are the main nuclides, has been introduced. Table 3.1 shows the new spectral parameters, which are defined analogously to the existing ones. For all calculations the boundary between the epithermal and thermal energy range is positioned at 0.625 eV. This implies that the important resonance of  $^{240}\text{Pu}$  at 1 eV lies just in the epithermal energy range, while the strong 0.3-eV resonance of  $^{239}\text{Pu}$  is located in the thermal range.

**Table 3.1:** Definition of the spectral parameters

$\rho^{40}$	= ratio epithermal-to-thermal $^{240}\text{Pu}$ captures
$\delta^{49}$	= ratio epithermal-to-thermal $^{239}\text{Pu}$ fissions
$\delta^{40}$	= ratio $^{240}\text{Pu}$ fissions to $^{239}\text{Pu}$ fissions
$C^{\dagger}$	= ratio $^{240}\text{Pu}$ captures to $^{239}\text{Pu}$ fissions

#### 3.3.1 Variation of pebble parameters

The  $k_{\infty}$ -values and the spectral parameters are calculated for six cases. These cases can be divided into two groups: Case 1 to 3 deal with 2 gram plutonium per pebble, while cases 4 to 6 deal with 1 gram per pebble. For all cases the temperature is 600 K uniformly over the pebble. Table 3.2 shows several parameters for the different cases. Case 3 and 6 refer to the diluted fuel kernel with a radius of 250  $\mu\text{m}$ , while the other cases refer to the concentrated kernels with radii of either 100 or 110  $\mu\text{m}$  (see table 2.1). The outer-right column shows the atomic moderator-to-fuel ratio, defined as C-atoms/Pu-atoms in the pebble. For a given Pu-mass per pebble these values do not deviate with more than 0.3% between the cases. This implies that the coated particles only occupy a small volume of the pebble. The Dancoff factors used by SCALE and WIMS were calculated analytically [64]. Table 3.3 shows the results of the calculations for the six cases.

**Conclusions concerning calculational results** Let the MCNP4B results be the reference ones. The MCNP  $k_{\infty}$ -values have standard deviations of less than 0.2%. All parameters calculated with both WIMS and SCALE lie within two times the standard deviation of the reference  $k_{\infty}$ -values. For SCALE, the exceptions are:  $k_{\infty}$ (case 6),  $\rho^{40}$ (case 1,4,5,6),  $\delta^{49}$ (case 1,3) and  $C^{\dagger}$ (case 4). For WIMS these are:  $k_{\infty}$ (case 6),  $\rho^{40}$ (case 4),  $\delta^{49}$ (case 1). This reveals that WIMS performs slightly better than SCALE. The maximum deviations from the reference results read 0.4%, 5%, 2%, 1% and 2% for  $k_{\infty}$ ,  $\rho^{40}$ ,  $\delta^{49}$ ,  $\delta^{40}$  and  $C^{\dagger}$ , respectively.

**Table 3.2:** The various cases for which the calculations have been performed. Cases 1 to 3 involve 2 grams plutonium per pebble, and cases 4 to 6 involve 1 gram per pebble. The Dancoff factors are used by the code systems WIMS and SCALE.

CASE	fuel	Pu-mass (gram/ pebble)	CPs per pebble	kernel radius (cm)	Dancoff- factor	C-atoms/ Pu-atoms
1	PuO <sub>2</sub>	2	51659	0.010	0.287	1928
2	PuO <sub>2</sub>	2	38812	0.011	0.267	1931
3	PuC <sub>20</sub> O <sub>2</sub>	2	22183	0.025	0.530	1920
4	PuO <sub>2</sub>	1	25829	0.010	0.164	3875
5	PuO <sub>2</sub>	1	19406	0.011	0.151	3877
6	PuC <sub>20</sub> O <sub>2</sub>	1	11092	0.025	0.350	3866

**Table 3.3:** The  $k_{\infty}$ -values and spectral parameters for the different cases. The temperature is for all cases 600 K and is uniform over the entire pebble. The definitions of the spectral parameters are given in table 3.1.

CASE	CODE	$k_{\infty}$	$\rho^{40}$	$\delta^{49}$ (10 <sup>-1</sup> )	$\delta^{40}$ (10 <sup>-3</sup> )	$C^+$ (10 <sup>-1</sup> )
1	WIMS7b	1.235	9.54	3.13	3.03	8.53
	SCALE-4	1.234	9.43	3.13	3.04	8.47
	MCNP4B	1.233±0.001	9.60±0.04	3.17±0.01	3.05±0.01	8.50±0.03
2	WIMS7b	1.248	9.11	3.07	3.01	8.26
	SCALE-4	1.247	9.01	3.08	3.02	8.21
	MCNP4B	1.247±0.002	9.13±0.07	3.10±0.02	3.03±0.02	8.26±0.05
3	WIMS7b	1.124	13.8	3.63	3.28	11.13
	SCALE-4	1.125	13.7	3.67	3.32	11.04
	MCNP4B	1.127±0.002	13.7±0.1	3.61±0.02	3.30±0.02	10.99±0.06
4	WIMS7b	1.405	4.84	1.27	1.43	5.47
	SCALE-4	1.405	4.77	1.28	1.44	5.45
	MCNP4B	1.403±0.002	4.99±0.04	1.28±0.01	1.45±0.01	5.55±0.04
5	WIMS7b	1.416	4.60	1.26	1.43	5.29
	SCALE-4	1.417	4.54	1.26	1.44	5.27
	MCNP4B	1.418±0.002	4.63±0.04	1.27±0.01	1.45±0.01	5.30±0.04
6	WIMS7b	1.291	7.50	1.42	1.50	7.50
	SCALE-4	1.292	7.38	1.43	1.51	7.45
	MCNP4B	1.296±0.002	7.51±0.05	1.42±0.01	1.50±0.01	7.45±0.04

**Conclusions concerning reactor physics** Comparing cases 1 with 4, 2 with 5 and 3 with 6, reveals that those with a higher plutonium mass per pebble yield a lower  $k_{\infty}$ . This leads one to suspect that all configurations are under-moderated, which is indeed confirmed by ref. [68]. The parameter  $\delta^{49}$  is higher for the cases with a 2 gr Pu loading than for those with the 1 gr Pu loadings, which is caused by a harder spectrum. For the 2 gr Pu/pebble cases  $\delta^{49}$  is of the order of 0.3, which means that about one fourth of the <sup>239</sup>Pu-fissions takes place in the epithermal energy range. As the order of magnitude of  $\delta^{40}$  is only 10<sup>-3</sup>, the contribution of <sup>240</sup>Pu to the total fission rate (i.e. mainly fast fission of <sup>240</sup>Pu) is small.

The MCNP cases referring to 1 gram plutonium per pebble show, in ascending order,  $k_{\infty}$ -values of 1.127, 1.233 to 1.247 for cases 3, 1 and 2, respectively. For the two-gram cases these read 1.296, 1.403, 1.418 for cases 6, 4 and 5, respectively. The increase of  $k_{\infty}$  is accompanied by a decrease of the parameters  $\rho^{40}$  and  $C^{\dagger}$ . This can be understood as follows:

The resonance absorption is determined by both the moderator-to-fuel ratio and the resonance integral. It increases if the moderator-to-fuel is lowered and/or if the resonance integral is increased. As mentioned before, the moderator-to-fuel ratio hardly varies between cases with the same Pu mass loading (see table 3.2). The resonance integral, on the other hand, does vary. According to the narrow resonance theory, the parameter that determines the self-shielding for a heterogeneous system (pages 432-435 of [69]) reads  $\frac{1}{N_A \bar{l}_F}$ . Here,  $N_A$  is the atomic density in  $\text{barn}^{-1}\text{cm}^{-1}$  of the resonance nuclide of interest and  $\bar{l}_F$  the effective mean chord length in cm, given by eq. 3.1. The higher this parameter, the lower the self-shielding, and hence the higher the resonance integral. Table 3.4 lists the self-shielding parameter for  $^{240}\text{Pu}$ . This illustrates that for case 3, i.e. the one with

**Table 3.4:** The parameter  $1/(N_A \bar{l}_F)$  for three cases, corresponding to three coated particle types. The listed parameter determines the self-shielding for the fuel kernel. It is also known as the microscopic escape cross section. The higher the microscopic escape cross section is, the higher the resonance integral of a particular resonance absorber.

CASE	kernel	$1/(N_A \bar{l}_F)$
3	'diluted' 500 $\mu\text{m}$ diameter	$1.89 \cdot 10^4$ barn
1	'concentrated' 200 $\mu\text{m}$ diameter	$1.11 \cdot 10^4$ barn
2	'concentrated' 220 $\mu\text{m}$ diameter	$1.04 \cdot 10^4$ barn

the diluted 250  $\mu\text{m}$ -radius kernel, the self-shielding is low, implying that the resonance absorption of  $^{240}\text{Pu}$  is relatively large. This is in agreement with the relatively large values of  $\rho^{40}$  and  $C^{\dagger}$ . An increase of the  $^{240}\text{Pu}$  resonance absorption leads, at the one hand, to a lower  $k_{\infty}$  and, at the other, to a slower decrease of  $k_{\infty}$  during burnup. The latter is due to a higher conversion rate from  $^{240}\text{Pu}$  to  $^{241}\text{Pu}$ , which was demonstrated in [68].

### 3.3.2 Variation of temperature

For case 5 of table 3.3, the  $k_{\infty}$ -values and spectral parameters were calculated as a function of the fuel temperature and as a function of the uniform-temperature. The WIMS calculations were done with the adapted library. In section 3.3.3 the differences between the original and the adapted library with respect to the fuel temperature reactivity effect will be shown.

**Variation of the uniform temperature** Table 3.5 shows the results for the variation of the temperature in a uniform sense, which means that all materials of the pebble have the same temperature. This uniform temperature is mainly a choice to be able to perform a calculational comparison. Under normal operational conditions, the temperature difference of a fuel kernel and the ambient graphite is of the order of 1 K (see appendix B). Moreover,

there is a temperature gradient in a power generating pebble. For an HTR-M the maximum temperature difference between centre and surface of the pebble amounts to 189 K (see page 12 of [45]). Appendix B discusses the consequences of the uniform-temperature-profile assumption.

In Table 3.5, no MCNP results are listed for the uniform temperatures of 900 and 1500 K. This is due to a lack of appropriate graphite thermal cross-section data for the mentioned temperatures, and the inability to interpolate between temperatures of the available graphite thermal matrices. Table 3.5 reveals that the parameters calculated with SCALE and WIMS lie within two times the standard deviation of the MCNP results.

**Table 3.5:** The  $k_{\infty}$ -values and spectral parameters for CASE 5 at different temperatures. The temperatures are uniform over the entire pebble. No appropriate cross-section data were available for the MCNP calculations at the uniform temperatures of 900 and 1500 K. The definitions of the spectral parameters are given in table 3.1.

$T_{uni}$ (K)	CODE	$k_{\infty}$	$\rho^{40}$	$\delta^{49}$ ( $10^{-1}$ )	$\delta^{40}$ ( $10^{-3}$ )	$C^+$ ( $10^{-1}$ )
293	WIMS7b	1.446	3.86	1.23	1.41	5.13
	SCALE-4	1.447	3.80	1.23	1.42	5.11
	MCNP4B	1.444±0.002	3.85±0.03	1.24±0.01	1.43±0.01	5.13±0.03
600	WIMS7b	1.416	4.60	1.26	1.43	5.29
	SCALE-4	1.417	4.54	1.26	1.44	5.27
	MCNP4B	1.418±0.002	4.63±0.04	1.27±0.01	1.45±0.01	5.30±0.04
900	WIMS7b	1.384	5.51	1.29	1.45	5.53
	SCALE-4	1.384	5.45	1.29	1.46	5.50
	MCNP4B			not available		
1200	WIMS7b	1.349	6.36	1.34	1.48	5.96
	SCALE-4	1.349	6.32	1.34	1.49	5.91
	MCNP4B	1.350±0.001	6.44±0.03	1.35±0.01	1.49±0.01	5.96±0.03
1500	WIMS7b	1.306	7.28	1.41	1.53	6.64
	SCALE-4	1.306	7.28	1.41	1.53	6.58
	MCNP4B			not available		

**Variation of the fuel temperature** Table 3.6 shows the results in case of variation of the fuel temperature only. During these calculations the temperatures of coatings, matrix material, pebble shell and void remain at 293 K. The resulting temperature combinations are of course unlikely in an operating reactor, but are studied to give insight into the Doppler effect. Table 3.6 reveals that the parameters calculated with SCALE and WIMS lie within two times the standard deviation of the MCNP results. For SCALE the exceptions are  $\delta^{49}(T_F=600,1500 \text{ K})$  and  $\delta^{49}(T_F=1500 \text{ K})$ . For WIMS these are  $\delta^{49}(T_F=1500 \text{ K})$  and  $\delta^{40}(T_F=1500 \text{ K})$ . The maximal deviations of these parameters from the reference ones are 2%.

**Temperature reactivity coefficients** Table 3.7 shows the reactivity changes due to temperature changes expressed in the form  $\frac{\Delta \ln k_{\infty}}{\Delta T}$ . This quantity is chosen since it is the finite difference analogy of  $\frac{d \ln k_{\infty}}{dT} = \frac{1}{k_{\infty}} \frac{dk_{\infty}}{dT}$ , which is the appropriate expression for the temperature coefficient of reactivity in case of infinite lattices [70]. The temperature coefficients were derived from the numbers in tables 3.5 and 3.6. Since the temperature intervals are

**Table 3.6:** The  $k_{\infty}$ -values and spectral parameters for CASE 5 at different fuel temperatures. In this table the temperature of coatings, matrix material and void remains 293.6 K, whereas the temperature of the fuel kernel ( $T_F$ ) varies. The definitions of the spectral parameters are given in table 3.1.

$T_F$ (K)	CODE	$k_{\infty}$	$\rho^{40}$	$\delta^{49}$ ( $10^{-1}$ )	$\delta^{40}$ ( $10^{-3}$ )	$C^+$ ( $10^{-1}$ )
293	WIMS7b	1.446	3.86	1.23	1.41	5.13
	SCALE-4	1.447	3.80	1.23	1.42	5.11
	MCNP4B	1.444±0.002	3.85±0.03	1.24±0.01	1.43±0.01	5.13±0.03
600	WIMS7b	1.436	4.01	1.25	1.43	5.29
	SCALE-4	1.436	3.95	1.25	1.43	5.26
	MCNP4B	1.435±0.002	4.03±0.03	1.26±0.01	1.43±0.01	5.28±0.03
900	WIMS7b	1.426	4.14	1.26	1.44	5.43
	SCALE-4	1.427	4.09	1.26	1.45	5.40
	MCNP4B	1.428±0.002	4.13±0.03	1.25±0.01	1.44±0.01	5.38±0.04
1200	WIMS7b	1.419	4.26	1.27	1.45	5.55
	SCALE-4	1.419	4.22	1.27	1.46	5.52
	MCNP4B	1.421±0.002	4.25±0.04	1.28±0.01	1.47±0.01	5.50±0.04
1500	WIMS7b	1.412	4.37	1.282	1.464	5.66
	SCALE-4	1.412	4.35	1.278	1.470	5.64
	MCNP4B	1.412±0.001	4.43±0.02	1.284±0.003	1.477±0.003	5.66±0.02

very large, it only gives an estimation of the temperature coefficient of reactivity. However, for the comparison of the results this forms no obstacle. Table 3.7 demonstrates that the MCNP 'finite difference' temperature coefficients have error-margins of about 30%. The WIMS and SCALE results differ from each other by less than 5%. The left-half of the table shows the reactivity decrease due to a Doppler broadening of the resonances of the nuclides in the fuel. The right-half of table 3.7 involves a combined effect: Both the Doppler effect and the reactivity effect due to a change of the moderator temperature. Table 3.7 shows that the Doppler effect becomes weaker with increasing temperatures, while the combined effect (i.e. moderator and fuel temperature reactivity effects) becomes stronger. Moreover, the combined effect is much stronger than the Doppler effect. One should note that the reactivity defect caused by the uniform temperature increase from room temperature to say 1200 K is rather sizable ( $\Delta\rho \approx -0.05$ ), which is about twice the maximum value of the xenon reactivity defect (see page 572 of [69]). The reactivity effect due to a change of the uniform temperature will be discussed in more detail in section 3.3.3.

### 3.3.3 Burnup calculation

For case 5 of table 3.3 burnup calculations with both WIMS and SCALE/ ORIGIN-S were performed. For the WIMS code, the burnup was done internally by the module WBRNUP. The burnup for the SCALE code was performed by the point-depletion code ORIGIN-S [71]. NRG's codes system OCTOPUS [72] takes care of the interfacing between the SCALE spectrum calculation and the burnup code ORIGIN-S. In the spectrum calculation 17 actinides and 23 fission products were explicitly taken into account. A pseudo nuclide with a fine-group cross section set represents all nuclides present in the fuel that are not explicitly included in the spectrum calculation. The cross section of this pseudo nuclide is

**Table 3.7:** The (finite-difference) temperature coefficients of reactivity for CASE 5. The left-half of the table involves temperature increases for the fuel kernel, while the other materials of the pebble remain at the temperature of 293.6 K. The numbers are derived from table 3.6. The right-half of the table involves temperature increases of the uniform temperature. The numbers are derived from table 3.5.

$\Delta T_F$ (K)	CODE	$\frac{\Delta \ln(k_{\infty})}{\Delta T_F}$ (pcm/K)	$\Delta T_{uniform}$ (K)	CODE	$\frac{\Delta \ln(k_{\infty})}{\Delta T_{uniform}}$ (pcm/K)
293→600	WIMS7b	-2.4	293→600	WIMS7b	-6.8
	SCALE-4	-2.4		SCALE-4	-6.8
	MCNP4B	-2.1±0.5		MCNP4B	-6.0±0.5
600→900	WIMS7b	-2.2	600→900	WIMS7b	-7.8
	SCALE-4	-2.1		SCALE-4	-7.7
	MCNP4B	-1.7±0.5		MCNP4B	not av.
900→1200	WIMS7b	-1.8	900→1200	WIMS7b	-8.6
	SCALE-4	-1.9		SCALE-4	-8.6
	MCNP4B	-1.6±0.5		MCNP4B	not av.
1200→1500	WIMS7b	-1.6	1200→1500	WIMS7b	-10.7
	SCALE-4	-1.7		SCALE-4	-10.8
	MCNP4B	-2.2±0.4		MCNP4B	not av.
			600→1200	WIMS7b	-8.2
				SCALE-4	-8.0
				MCNP4B	-8.9±0.3

composed of cross-section data from the ECNAF data library [73]. This library contains cross-section data for over more than 750 nuclides, mainly based on the JEF2.2 data file.

The burnup was performed at a uniform temperature of 900 K, which will be called the historical temperature hereafter. The number of cycles and the length of each cycle used in the burnup calculations were the same for WIMS and SCALE. For each cycle some branching calculations were performed in which the temperature was varied. In these branches the differences between the branching- $k_{\infty}$ 's and the historical- $k_{\infty}$  were calculated.

**Nuclide densities and  $k_{\infty}$  as a function of burnup** Fig. 3.5 shows the plutonium nuclide densities as a function of burnup, both calculated with WIMS and SCALE/ORIGEN-S. The burnup is performed at a constant power density of 3 W/cm<sup>3</sup>, corresponding to 547 W per pebble. The differences between the curves are caused by discrepancies in the energy production figures of WIMS and SCALE/ORIGEN-S. WIMS uses for the fissionable nuclides an effective energy release per fission, which includes the contribution from captures. This capture contribution is an averaged number accounting for captures in all materials present in a typical thermal reactor. The effective energy releases per fission used by WIMS read 210.0 and 212.9 MeV for <sup>239</sup>Pu and <sup>241</sup>Pu, respectively. The OCTOPUS code system uses, on the other hand, energy releases taken from the JEF2.2 library for fission and capture, separately. The energy releases for fission and capture of the nuclides <sup>239</sup>Pu, <sup>240</sup>Pu and <sup>241</sup>Pu, read 199.9 and 6.53, 195.0 and 5.24, and 201.7 and 6.31 MeV, respectively. At Begin of Life (BOL) the contributions of <sup>239</sup>Pu and <sup>241</sup>Pu to the fission rate read 82% and 18%, respectively. This means that the effective energy release in the WIMS calculation equals 0.82×210.0+0.18×212.9=210.5 MeV. It has been derived that the energy release

per fission in the SCALE/ORIGEN-S calculations yields for the same fuel at BOL only 206.9 MeV, which is almost 2% lower than that of WIMS. This means that the fission rate in the SCALE/ORIGEN-S calculation is higher, since for the generation of a certain amount of energy, more nuclides have to be fissioned. The discrepancies between the two curves become larger with increasing burnup. This is due to the following:

The total amount of actinides in a pebble decreases linearly with burnup, which means that the decrease of the actinide mass is constant. However, due to burnup with constant power, the fractional decrease of actinide mass becomes larger with increasing burnup. The following example illustrates this: From 0 to 100 MWd/kgHM the actinide mass reduces with about 10%, whereas from 600 to 700 MWd/kgHM the actinide mass reduces with almost 30%. This means that the differences in energy production per fission lead at higher burnup values to larger deviations in nuclide densities.

Obviously, the differences in nuclide densities lead to differences in  $k_{\infty}$ . Fig. 3.6 shows the difference in the historical- $k_{\infty}$  for WIMS (square symbols) and SCALE / ORIGEN-S (filled circular symbols). The differences in  $k_{\infty}$  amount to 5% and 25% at burnups of 600 and 700 MWd/kgHM, respectively. In order to verify that the differences are due to discrepancies in energy releases, we did another SCALE/ORIGEN-S calculation, but now ORIGEN-S was forced to use the energy yields of WIMS. The curve with the open circular symbols in fig. 3.6 corresponds to this calculation. The maximum difference in  $k_{\infty}$  between this calculation and the WIMS calculation is only 0.0035 (i.e. 0.4%) at 700 MWd/kgHM.

The energy yields per fission of WIMS are approximate figures (at least for HTRs), since they include the energy from capture independently of the actual capture rates of the various material present in the system. We are therefore inclined to think that the burnup with SCALE/ORIGEN-S is, at least for uranium-free fuels, to be preferred. Another option could be to adapt the effective energy yields in the WIMS library appropriate to the type of fuel and configuration.



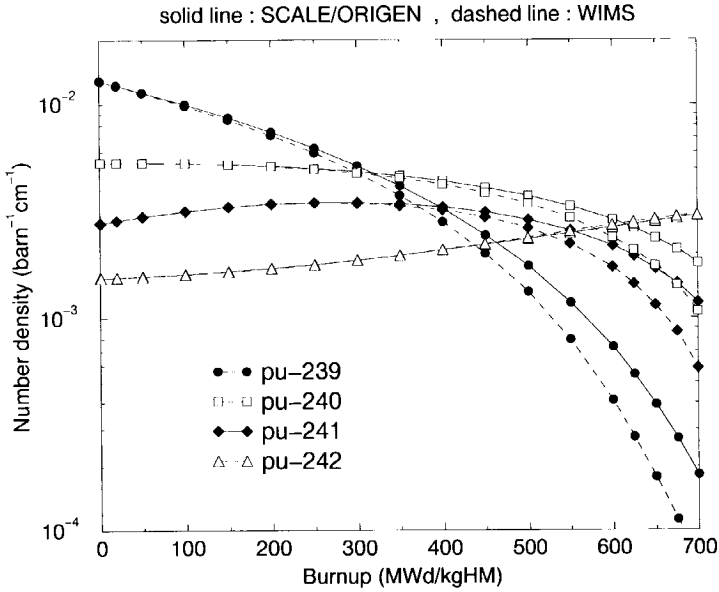


**Figure 3.5:** *Pu-densities as a function of burnup, calculated with both SCALE/ORIGEN-S (solid curves) and WIMS (dashed curves).*

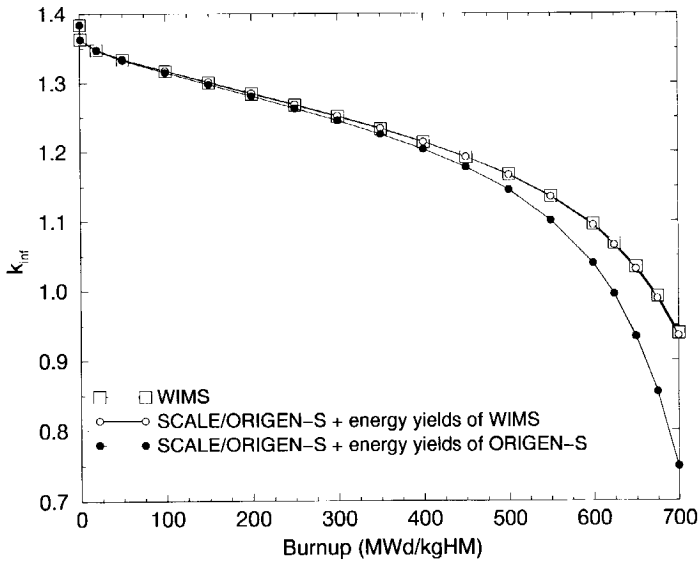


**Figure 3.6:**  $k_{\infty}$  as a function of burnup. The calculations are done with WIMS, SCALE/ORIGEN-S in combination with energy-yield data of WIMS, and SCALE/ORIGEN-S in combination with energy-yield data of ORIGEN-S itself. The burnup is performed at constant power. (CASE 5 of table 3.2;  $T_{\text{ini}} = 900 \text{ K}$ ).

**Branches involving a change of fuel temperature** Fig. 3.7 shows the  $\Delta k_{\infty}$ -values for branches in which only the fuel temperature has been altered. In all calculations the moderator temperature remains at 900 K, whereas the fuel temperature is varied from 900 K to 300, 600, 1200 and 1500 K. Obviously, the cases in which the fuel temperature is lower than the moderator temperature are unlikely to occur in practice, but they are included to illustrate the Doppler effect. The following can be inferred from fig. 3.7:

- An increase of the fuel temperature leads for all burnup values to a reactivity decrease.
- The burnup and branching calculations have been performed, at the one hand, by WIMS with both the original and the adapted 172 groups library, and, at the other with SCALE/ORIGEN-S. For the WIMS calculation, the adapted library exhibits higher  $|\Delta k_{\infty}|$ -values than those of the original library. This is mainly due to the fact that in the adapted version the thermal cross sections and resonance integrals of  $^{242}\text{Pu}$  are tabulated for more than one temperature. Contrarily to the original library, this nuclide, as well as others, is now treated properly. In our fuel,  $^{240}\text{Pu}$  is the main contributor to the Doppler effect and  $^{242}\text{Pu}$  is the second. At BOL their contributions read  $90 \pm 2\%$  and  $8 \pm 2\%$ , whereas at a burnup of 700 MWd/kgHM these read  $76 \pm 5\%$  and  $22 \pm 3\%$ , respectively. The  $|\Delta k_{\infty}|$ -values of the WIMS calculations with the original and adapted library differ from those of the SCALE calculation by maximally 33% and 8%, respectively. The differences between the WIMS calculation with the *adapted* library and the SCALE calculation are probably due to the fact that the *thermal* cross sections in the WIMS library can only be tabulated for one  $\sigma_p$ -value, which means that they are independent of the density of the nuclide of interest.

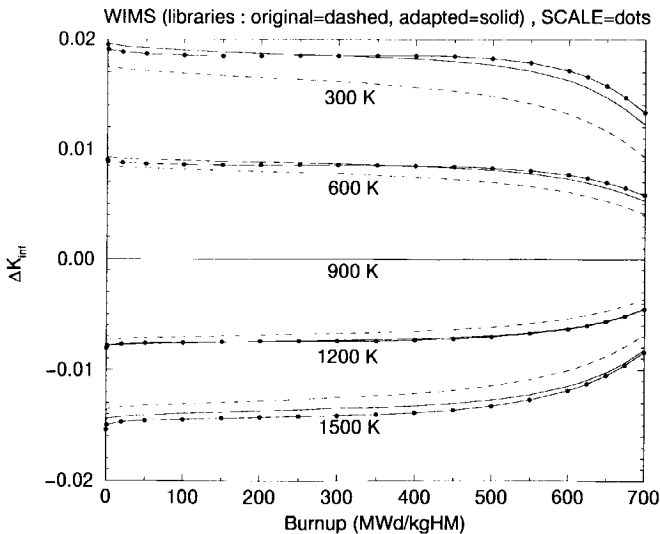


**Figure 3.7:** Differences between branching- $k_{\infty}$  and the historical- $k_{\infty}$  as a function of burnup. In the branches, the fuel temperature has been altered. The calculations were done with SCALE / ORIGEN-S and WIMS (original and adapted library).

## Chapter 4

---

# Reactor physics of plutonium fuelled pebbles

---

In the previous chapter, the results of unit-cell calculations performed by WIMS were compared to those performed by SCALE and MCNP. For the purpose of that comparative study a limited number of reactor physics parameters were studied for a limited number of pebble configurations. In this chapter<sup>1</sup>, we present the results of an extensive parameter study as regards plutonium fuelled pebbles thereby putting the emphasis on the reactor physics. Unless otherwise indicated, the calculations were performed with the WIMS code. The specifications of the calculational models that have been used, read

Plutonium specifications	:	table 1.2 on page 2.
Material specifications (pebbles and coated particles)	:	table 2.1 on page 23.
Dancoff factor as a function of nr. of CPs and kernel size	:	eq. A.29 on page 170.

### 4.1 Parameter study

Table 4.1 shows both the parameters that have been varied in the calculational model (input parameters) and the reactor physics parameters that have been calculated (output parameters). Below, both the input and output parameters will be discussed briefly.

The coated particle type refers to the concentrated 200- $\mu\text{m}$ -diam, the concentrated 220- $\mu\text{m}$ -diam kernel or the diluted 500- $\mu\text{m}$ -diam kernel as mentioned in table 2.1. The fuel temperature refers to the fuel kernels, whereas the moderator temperature refers to the coatings and the graphite of the pebble. The 'historical' temperature denotes the overall-temperature ( $T_M = T_F$ ) with which the burnup calculation is carried out, i.e. the 'irradiation temperature'.

The multiplication factor for an infinite medium or for a unit cell with white boundary conditions, presented in the form of the four-factor formula, reads

$$k_{\infty} = \eta \cdot f \cdot p \cdot \epsilon \quad (4.1)$$

---

<sup>1</sup>This chapter is largely based on refs. [68] and [74].

Table 4.1: Parameters involved in the parameter study.

Varied Parameters	
Parameter	Range
A) Plutonium mass per pebble	0.01 – 4 g
B) Coated particle type	concentrated 220- $\mu$ m-diam kernel concentrated 200- $\mu$ m-diam kernel diluted 500- $\mu$ m-diam kernel
C) Fuel temperature ( $T_F$ )	300 – 1800 K
D) Moderator temperature ( $T_M$ )	300 – 1800 K
E) Burnup	0 – 700 MWd/kgHM
F) The 'historical' temperature or irradiation temperature	900 – 1500 K
Calculated Parameters	
1) Infinite multiplication factor,	$k_\infty$
2) Factors of four-factor formula,	$\eta, f, p, \epsilon$
3) Spectral parameters,	$\rho^{40}, \delta^{49}, \delta^{40}, C^+$
4) The uniform-temperature coefficient of reactivity,	UTC ( $K^{-1}$ )
5) The moderator temperature coefficient of reactivity,	MTC ( $K^{-1}$ )
6) The fuel temperature coefficient of reactivity,	FTC ( $K^{-1}$ )
7) Neutron mean generation time,	$\Lambda$ (s)
8) Effective delayed neutron fraction,	$\beta_{eff}$
9) Nuclide densities	
10) Fast fluence ( $E > 0.1$ MeV)	

in which

$$\eta = \frac{\sum_F (\nu \Sigma_f)_{th} \Phi_{th}}{\sum_F (\Sigma_a)_{th} \Phi_{th}}, \quad f = \frac{\sum_F (\Sigma_a)_{th} \Phi_{th}}{\sum_Z (\Sigma_a)_{th} \Phi_{th}}, \quad p = \frac{\sum_Z (\Sigma_a)_{th} \Phi_{th}}{\sum_Z (\Sigma_a) \Phi}, \quad \epsilon = \frac{\sum_F (\nu \Sigma_f) \Phi}{\sum_F (\nu \Sigma_f)_{th} \Phi_{th}}, \quad (4.2)$$

where

- $\eta$  is the number of neutrons produced per thermal neutron absorbed in the fuel;
- $f$  is the thermal utilisation factor, defined as the number of thermal neutrons absorbed in the fuel divided by the total number of thermal neutrons absorbed;
- $p$  is the number of thermal neutrons absorbed divided by the total number of neutrons absorbed (because most of the nonthermal absorption takes place in the resonances  $p$  is called the resonance escape probability);
- $\epsilon$  is the nonthermal fission factor, defined as the total number of neutrons produced by both thermal and nonthermal fissions divided by the number of neutrons produced by thermal fissions.

Here,  $\nu$  is the number of neutrons released per fission,  $\Sigma_f$  and  $\Sigma_a$  are the macroscopic cross sections for fission and absorption, respectively ( $\Sigma_a = \Sigma_f + \Sigma_\gamma - \Sigma_{n,2n} - 2\Sigma_{n,3n}$ ), and  $\Phi$  and  $\Phi_{th}$  are the total and thermal fluxes, respectively. The index  $Z$  indicates summation over all zones,  $F$  over the fuel zones. In this study, the cut-off energy that separates the thermal from the nonthermal energy range is located at 0.625 eV. This means that the lowest lying resonance of  $^{240}\text{Pu}$  at 1 eV, lies just in the nonthermal energy range, while the

**Table 4.2:** Different parameters for a Pu-loading of 1 g/pebble.

Type	Diameter ( $\mu\text{m}$ )	Nr. of CPs per pebble	C-to-Pu ratio
<i>Concentrated</i>	200	25829	3811
<i>Concentrated</i>	220	19406	3813
<i>Diluted</i>	500	11092	3801

0.3-eV resonance of  $^{239}\text{Pu}$  lies in the thermal range.

The appropriate definition of the temperature coefficient of reactivity in an infinite system, or in a unit cell with reflecting boundaries, reads [75]

$$TC = \frac{1}{k_{\infty}} \frac{dk_{\infty}}{dT} . \quad (4.3)$$

Inserting eq. 4.1 into eq. 4.3 yields

$$\frac{1}{k_{\infty}} \frac{dk_{\infty}}{dT} = \frac{1}{\eta} \frac{d\eta}{dT} + \frac{1}{f} \frac{df}{dT} + \frac{1}{\epsilon} \frac{d\epsilon}{dT} + \frac{1}{p} \frac{dp}{dT} . \quad (4.4)$$

In section 4.2.2, the temperature coefficients of reactivity will be analysed by means of eq. 4.4. The FTC, MTC and UTC stand for the fuel temperature, the moderator temperature and the uniform-temperature coefficient of reactivity. The latter coefficient refers to a change of the overall-temperature ( $T_f = T_M$ ), i.e. the same temperatures for fuel kernels, coatings and graphite.

The spectral parameters are defined in table 3.1. The factors of the four-factor formula as well as the neutron mean generation time and the effective delayed neutron fraction were calculated with the VAREX code [76–78].

Table 4.1 shows that the parameters A to F constitute a six-dimensional parameter space. Hence, the quantities 1) to 10) of table 4.1 are in fact functions of six variables. To be restrictive, the mentioned quantities are not calculated for all combinations of the parameters; e.g.  $k_{\infty}$  for a wide parameter range, while  $\Lambda$  and  $\beta_{eff}$  only for a limited one. It is clear that the plutonium mass per pebble determines the moderator-to-fuel ratio (i.e. atomic C-to-Pu ratio). Table 4.2 shows that, for a given plutonium mass per pebble, the number and the size of the coated particles hardly influences the moderator-to-fuel ratio, which implies that the coated particles occupy only a very small part of the pebble volume.

The presentation of the results of the parameter study are split up into two sections. Section 4.2 presents the reactor physics parameters of the fresh fuel, implying that the six-dimensional parameter space is in fact reduced to four dimensions because the burnup (param. E of table 4.1) and the historical- $T_{uni}$  (param. F of table 4.1) are meaningless. Section 4.3 focuses on the reactor physics parameters during burnup.

## 4.2 Reactor Physics Parameters of Fresh Fuel

### 4.2.1 Infinite multiplication factor, spectral parameters, 4 factor formula

Fig. 4.1 shows the  $k_{\infty}$  as a function of the plutonium mass per pebble for three types of coated particles. The maxima of the curves lie in the range from 0.1 to 0.2 g Pu/pebble.

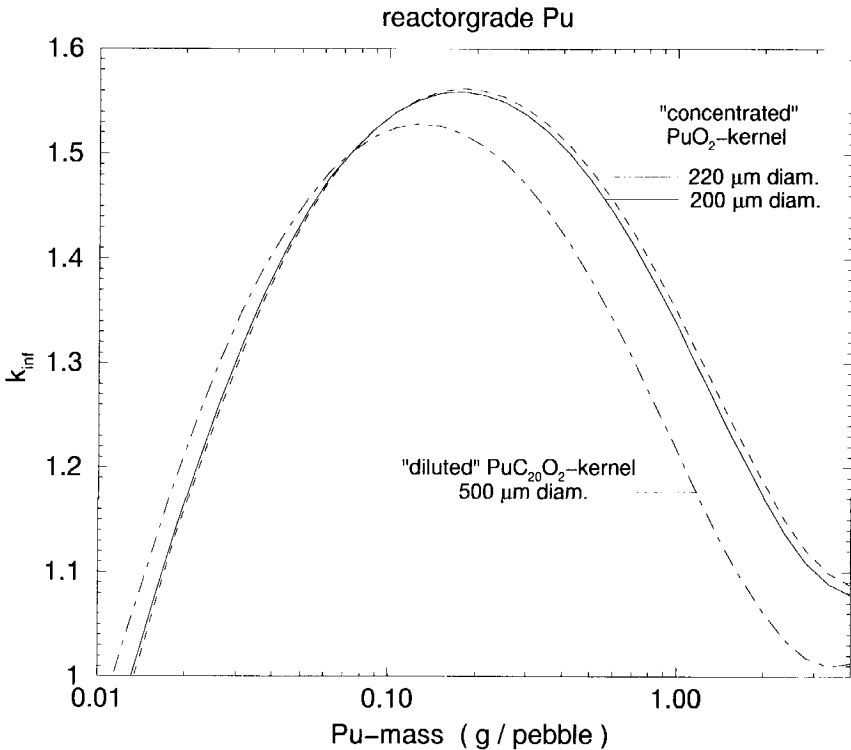


**Figure 4.1:**  $k_{\infty}$  as a function of the plutonium mass per pebble for three types of coated particles. ( $T_{uni} = 1200\text{ K}$ ,  $0\text{ MWd/kgHM}$ ).

Left of such a maximum the system is over-moderated and right of it the system is under-moderated. An over-moderated system implies that the addition of moderator material will lead to a decrease of the  $k_{\infty}$ , while the opposite holds for an under-moderated system. If we compare the under-moderated wings of the  $k_{\infty}$ -curves, we see that the concentrated 220- $\mu\text{m}$ -diam kernel yields a higher  $k_{\infty}$  than its 200- $\mu\text{m}$ -diam counterpart, while the 200- $\mu\text{m}$ -diam kernel yields a considerably higher  $k_{\infty}$  than the diluted 500- $\mu\text{m}$ -diam kernel. The opposite holds for the over-moderated wings of the  $k_{\infty}$ -curves. Both effects will be explained hereafter.

Fig. 4.2 shows the normalised fluxes of both the fuel kernel and the inter-pebble voids, for the under-moderated case of 1 g Pu/pebble and for the over-moderated case of 0.0625 g Pu/pebble. The vertical dotted lines indicate flux depressions in the fuel due to absorption

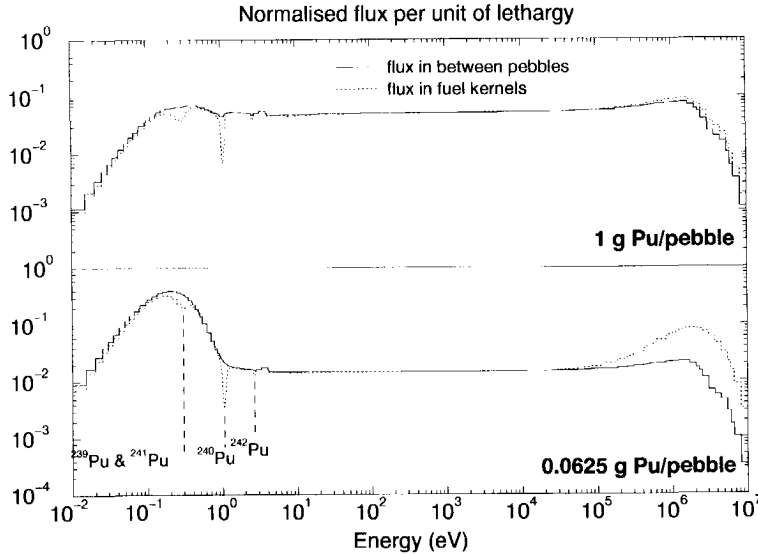


**Figure 4.2:** Flux per unit lethargy in a fuel kernel and in the intra-pebble cavities, for Pu-loadings of 0.0625 g/pebble and 1 g/pebble. The vertical lines indicate flux depressions due to absorption by the 0.3-eV resonance of  $^{239}\text{Pu}$  and the 0.27-eV resonance of  $^{241}\text{Pu}$  as well as the 1-eV resonance of  $^{240}\text{Pu}$  and the 2.7-eV resonance of  $^{242}\text{Pu}$ . The Pu-loading of 1 g/pebble shows a much harder spectrum than that of 0.0625 g/pebble. ( $T_{\text{uni}} = 1200\text{ K}$ , concentrated 220- $\mu\text{m}$ -diam kernel, 0 MWd/kgHM).

by the 0.3-eV resonance of  $^{239}\text{Pu}$  and the 0.27-eV resonance of  $^{241}\text{Pu}$  as well as the 1-eV resonance of  $^{240}\text{Pu}$  and the 2.7-eV resonance of  $^{242}\text{Pu}$ . The Pu-loading of 1 g/pebble shows a much harder spectrum than that of 0.0625 g/pebble. In this relatively hard spectrum, about one tenth of the  $^{239}\text{Pu}$  fissions takes place in the nonthermal ( $E > 0.625\text{ eV}$ ) energy range (see  $\delta^{49}$  in table 3.5).

Fig. 4.3 shows the factors of the four-factor formula as a function of the plutonium mass per pebble for the three CP types. The factors were defined according to eq. 4.2. Fig. 4.3 gives the expected result that  $\eta$ , the number of neutron produced per thermal absorption in the fuel, hardly varies with the Pu-loading. The other parameters, however, vary strongly with the Pu-loading. The thermal utilisation factor  $f$  approaches unity with increasing Pu-loading. This indicates a decrease of the parasitic absorption by the moderator; if  $f = 1$  the absorption by graphite vanishes. The differences in the thermal utilisation factor for different coated particles can be ascribed to a change of self-shielding. The concentrated 220- $\mu\text{m}$ -diam kernel yields a slightly higher degree of self-shielding than its 200- $\mu\text{m}$ -diam counterpart, whereas the 200- $\mu\text{m}$ -diam kernel yields a much higher degree of self-shielding than the diluted 500- $\mu\text{m}$ -diam kernel (see also table 3.4). A higher degree of self-shielding involves a stronger thermal flux depression or, in other words, a higher thermal disadvantage factor (e.g., see p. 402 of ref. [69]) and thus a lower thermal utilisation factor.

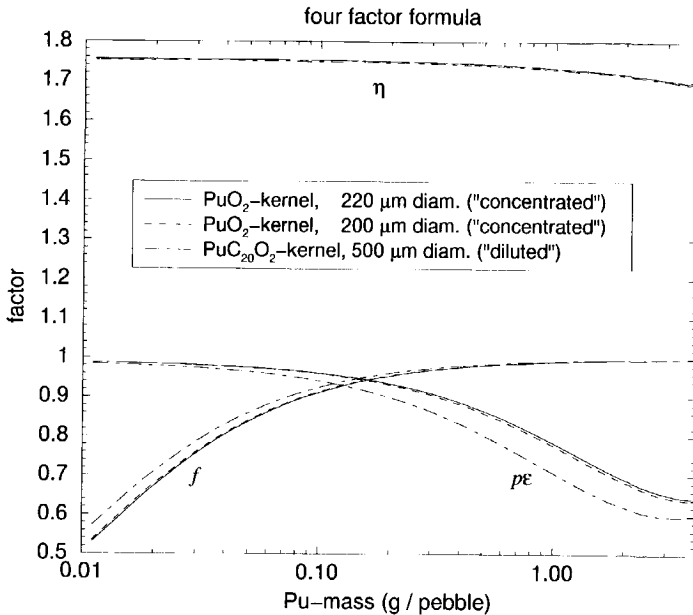


**Figure 4.3:** The factors of the four-factor formula as a function of the plutonium mass per pebble for three types of coated particles. ( $T_{mi} = 1200\text{ K}$ ,  $0\text{ MWd/kgHM}$ ).

The resonance escape probability  $p$  tends to unity if the plutonium mass per pebble decreases (increasing moderator-to-fuel ratio). The nonthermal fission factor  $\epsilon$  is equal to 1.01, 1.03 and 1.43 for Pu-loadings of 0.02, 0.2 and 2 g Pu/pebble, respectively. The high  $\epsilon$  value of the latter Pu-loading can be attributed to an increase of the resonance fission of  $^{239}\text{Pu}$  and  $^{241}\text{Pu}$  rather than to fast fission ( $> 0.1\text{ MeV}$ ) of even Pu-isotopes. (On the contrary, the deviation of  $\epsilon$  from unity in the case of uranium fuel is usually due to fast fission of  $^{238}\text{U}$ ). Fig. 4.3 shows that, despite of the high  $\epsilon$ -values, the product  $\epsilon p$  stays below unity and, moreover, decreases with increasing Pu-loading. The discrepancies between the  $\epsilon p$ -curves of different coated particles is again due to differences in self-shielding. The increasing degree of self-shielding for the 500- $\mu\text{m}$ -diam, the 200- $\mu\text{m}$ -diam and the 220- $\mu\text{m}$ -diam kernel, successively, implies decreasing resonance integrals and hence, for a given moderator-to-fuel ratio, lower resonance absorption rates and consequently a lower  $\epsilon p$ -value. A decrease of self-shielding (e.g., by using a diluted 500- $\mu\text{m}$ -diam kernel instead of a concentrated 220- $\mu\text{m}$ -diam kernel) causes for all resonance absorbers an increase of the nonthermal absorption rate. However, the higher the ratio of the resonance integral to the thermal cross section of a particular nuclide is, the more sensitive the absorption rate to a change of self-shielding is. This can be illuminated by the following data:



Nonthermal-to-thermal absorption rates. (1 g Pu/pebble; $T_{uniform} = 1200$ K)		
	concentrated 220- $\mu$ m-diam kernel	diluted 500- $\mu$ m-diam kernel
$^{239}\text{Pu}$	0.136	0.155
$^{240}\text{Pu}$	6.36	10.4

These numbers demonstrate that, for a given Pu-loading, the use of diluted CPs instead of concentrated ones (i.e. reduction of self-shielding) mainly leads to an increase of the absorption rate of  $^{240}\text{Pu}$ . This is due to the high nonthermal-to-thermal absorption rate ratio of  $^{240}\text{Pu}$ , which originates from the high ratio of the resonance integral to the thermal cross section.

Fig. 4.4 shows the spectral parameters (see table 3.1) as a function of the plutonium mass per pebble, for three CP types. The increasing  $\rho^{40}$  indicates an increase of the nonthermal-

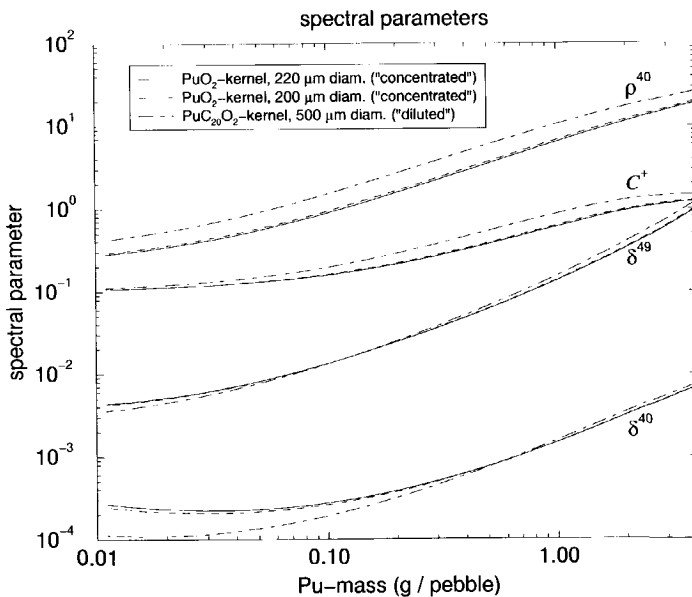


**Figure 4.4:** Spectral parameters as a function of the plutonium mass per pebble for three types of coated particles. The definitions of the spectral parameters are given by table 3.1 on page 38. ( $T_{uni} = 1200$  K, 0 MWd/kgHM).

to-thermal capture rate of  $^{240}\text{Pu}$ . Note the difference between the  $\rho^{40}$ -curves of different CPs. The increasing  $C^+$  demonstrates the increase of the  $^{240}\text{Pu}$ -capture to  $^{239}\text{Pu}$ -fission rate with increasing Pu-mass. This reveals that the Pu-loading determines the conversion of  $^{240}\text{Pu}$  to  $^{241}\text{Pu}$  and hence the  $k_{\infty}$ -evolution during burnup. The increasing  $\delta^{49}$  illustrates the increase of the nonthermal-to-thermal  $^{239}\text{Pu}$  fission rate due to a hardening of the spectrum with increasing Pu-loading. Furthermore, the ratio of  $^{240}\text{Pu}$ -fissions to  $^{239}\text{Pu}$ -fissions ( $\delta^{40}$ ) remains below 1%.

## 4.2.2 Temperature coefficients of reactivity

In this section, we present the temperature coefficients of plutonium bearing pebbles with zero burnup. Since the kernel of a coated particle has a high surface-to-volume ratio, an effective heat transfer from the fuel to moderator is realised. This means that there is only a small temperature difference between the kernel and the surrounding graphite, namely  $\sim 1$  K. Since the temperature of the kernels and the graphite are almost equal, this allows us, in view of reactivity feed-back effects, to consider a uniform-temperature coefficient of reactivity (UTC). Although the temperature difference between a kernel and the ambient graphite is negligible, the temperature profile across the pebble is such that the average temperature of the kernels is higher than the average temperature of the graphite. Note, in this respect, that almost half of the graphite is contained by the outer fuel-free pebble shell, where the temperature is of course lower than in the fuel zone. Appendix B shows that the difference of the average fuel temperature and the average moderator temperature obeys

$$T_{fuel}^{ave} - T_{Peb}^{ave} = 3.935 \cdot 10^{-3} \left( \frac{P}{\lambda} \right), \quad (4.5)$$

where  $T_{fuel}^{ave}$  and  $T_{Peb}^{ave}$  are the average temperature of the fuel and the moderator, respectively, and where  $P$  [W] is the pebble power and  $\lambda$  [ $\text{W}\cdot\text{cm}^{-1}\cdot\text{K}^{-1}$ ] is the heat conductivity coefficient of graphite. For  $P = 547$  W (corresponding to the nominal power density of  $3 \text{ W}/\text{cm}^3$ ) and the conservative (i.e. low)  $\lambda = 0.06 \text{ W}\cdot\text{cm}^{-1}\cdot\text{K}^{-1}$ , the temperature difference becomes 36 K. Assuming that the fuel temperature coefficient equals  $-5 \text{ pcm}/\text{K}$ , the uniform-temperature assumption of the pebble yields a multiplication factor that is  $\sim 0.2\%$  higher than that of a pebble for which the temperature difference between fuel zone and the entire pebble is explicitly accounted for.

Figures 4.5 and 4.6 show the UTC as a function of the Pu-loading with the uniform-temperature ( $T_{uni}$ ) as a parameter. The graphs reveal that Pu-loadings of more than  $0.2 \text{ g Pu}/\text{pebble}$  yield negative UTCs for the entire temperature range. Pu-loadings of less than  $0.2 \text{ g Pu}/\text{pebble}$  yield a positive UTC for a low  $T_{uni}$  and a negative one for a high  $T_{uni}$ . This behaviour will be discussed in depth in section 4.4. To see which contribution comes from the fuel and which from the moderator, the FTC and the MTC have been calculated separately. Fig. 4.7 shows the FTC, MTC and the UTC as a function of the plutonium mass per pebble, for ( $T_{uni} = 1150 \text{ K}$ , concentr.  $220\text{-}\mu\text{m}$ -diam kernel). This reveals that the MTC is much stronger than the FTC. The MTC lies between  $-7$  and  $+16 \text{ pcm}/\text{K}$ , while the FTC lies between  $-3$  and  $+0.2 \text{ pcm}/\text{K}$ . Furthermore, the MTC has a minimum at about  $1 \text{ g Pu}/\text{pebble}$ , while the FTC at  $3 \text{ g Pu}/\text{pebble}$ , which results in a minimum UTC between  $1$  and  $2 \text{ g Pu}/\text{pebble}$ .

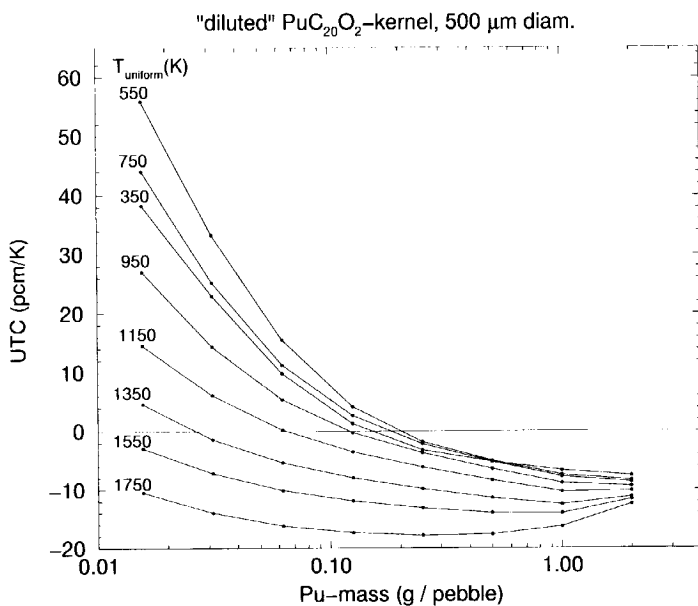


**Figure 4.5:** The uniform-temperature coefficient of reactivity (UTC) as a function of the plutonium mass per pebble with the uniform-temperature ( $T_{uni}$ ) as a parameter. (Diluted 500- $\mu\text{m}$ -diam kernel, 0 MWd/kgHM).

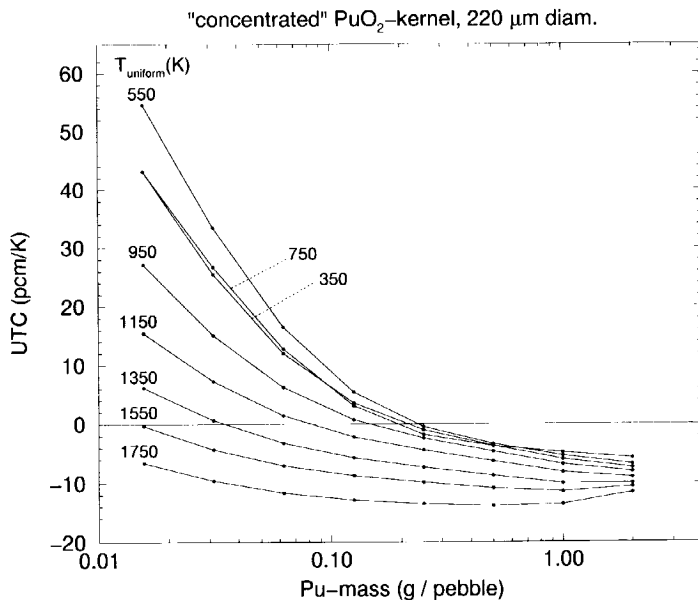


**Figure 4.6:** The uniform-temperature coefficient of reactivity (UTC) as a function of the plutonium mass per pebble with the uniform-temperature ( $T_{uni}$ ) as a parameter. (Concentrated 220- $\mu\text{m}$ -diam kernel, 0 MWd/kgHM).

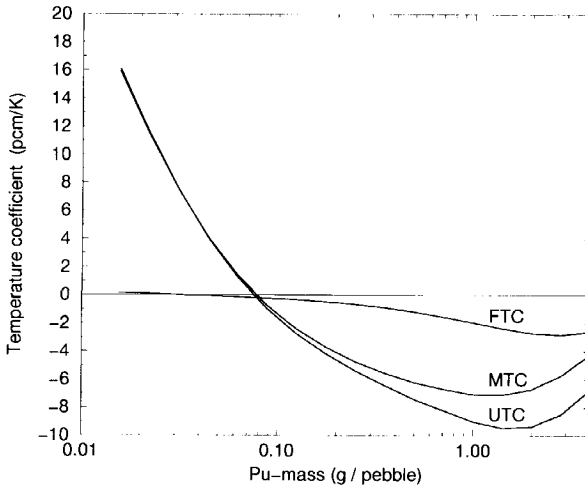


**Figure 4.7:** The fuel temperature coefficient (FTC), the moderator temperature coefficient (MTC) and the uniform-temperature coefficient (UTC) as a function of the plutonium mass per pebble. ( $T_{uni} = 1150$  K, concentrated 220- $\mu$ m-diam kernel, 0 MWd/kgHM).

## Maximisation of the Doppler effect

In the early stage of this study, difficulties were envisaged in achieving a sufficiently negative Doppler coefficient in the case of pebbles that contain pure plutonium. It was believed that the absence of  $^{238}\text{U}$  would lead to a very weak Doppler effect. To obtain nevertheless a high Doppler coefficient a generic study was initiated, with the aim, on the one hand, to get insight into the physics and, on the other hand, to maximise the Doppler effect.

The maximisation of the Doppler effect was studied on the basis of a simple spherical two-region white-boundary unit cell. The inner region of this unit cell (radius  $r_F$ ) contains the fuel, whereas the outer spherical shell (outer radius  $r_M$ ) contains the moderator, namely graphite. By varying both  $r_F$  and  $r_M$  the Doppler coefficient can be varied. However, if one reduces  $r_M$  at a constant  $r_F$ , provided that the system is under-moderated, the increase of the Doppler coefficient (in absolute sense) is accompanied by a decrease of the moderator-to-fuel ratio and thus causes a decrease of the multiplication factor of the system. To obtain a maximum Doppler effect (i.e. a minimum Doppler coefficient) without a change of the reactivity, the  $r_F$  and  $r_M$  were therefore varied in such a way that  $k_\infty$  remained equal. In other words, the Doppler effect was maximised under the constraint of a constant  $k_\infty$ . It turned out that, for a given  $k_\infty$ , a maximum Doppler effect is present at a particular  $N_A \bar{l}_F$ , where  $N_A$  is the number density of the main resonance absorber and  $\bar{l}_F$  is the so-called *Dancoff-corrected mean chord length* of the fuel lump (see eq. 3.1). An analysis on the basis of the Narrow Resonance Infinite Mass (NRIM) theory pointed out that the  $N_A \bar{l}_F$  at which the Doppler coefficient is maximal, is determined to a large extent by the resonance parameters of the resonance with the highest infinite-dilution resonance integral ( $I_\infty$ ), which is usually the one that is positioned at the lowest energy. One might say that for neutrons with an energy that is equal to the resonance energy of this particular resonance, the optimal size of the lump is such that the absorber is 'grey', i.e. between a 'white' and a 'black' absorber.

Appendix C presents a thorough analysis of the maximisation of the Doppler coefficient. This study also appeared as refs. [79–81]. The analyses and calculations were done for reactor-grade  $\text{PuO}_2$  (see table 1.2),  $\text{UO}_2$  and  $\text{ThO}_2$ . The optimal  $N_A \bar{l}_F$ -values that were found read  $(1.6 \pm 0.7) \cdot 10^{-2}$ ,  $(1.3 \pm 0.3) \cdot 10^{-3}$  and  $(3.8 \pm 0.5) \cdot 10^{-5} \text{ barn}^{-1}$  for  $^{232}\text{Th}$ ,  $^{238}\text{U}$  and  $^{240}\text{Pu}$ , respectively. This implies that a  $\text{UO}_2$ -kernel like in an HTR-M, with  $N_{\text{U}238} = 0.02 \text{ barn}^{-1} \cdot \text{cm}^{-1}$ ,  $r_F = 0.025 \text{ cm}$  and a Dancoff factor ( $C$ ) of 0.36, yields  $N_A \bar{l}_F = 1 \cdot 10^{-3}$  and hence coincides with the optimal one. This means that  $\text{UO}_2$  coated particle fuel provides for the highest Doppler coefficient for a given  $k_\infty$  thanks to the optimal size of the kernels.

Fig. 4.8 shows the Doppler coefficient as a function of  $\bar{l}_F$  with  $k_\infty$  as a parameter for the plutonium fuel. The maximum Doppler effect is found for  $\bar{l}_F = (6.5 \pm 0.5) \cdot 10^{-3} \text{ cm}$ , which is in agreement with the aforementioned optimal- $N_A \bar{l}_F$  because the number density of the key resonance absorber,  $^{240}\text{Pu}$ , equals  $N_{\text{Pu}240} = 5.36 \cdot 10^{-3} \text{ barn}^{-1} \cdot \text{cm}^{-1}$ . Note that,  $N_A \bar{l}_F$  reads  $5.3 \cdot 10^{-5}$ ,  $9.0 \cdot 10^{-5}$  and  $9.6 \cdot 10^{-5} \text{ barn}^{-1}$  for the concentrated 220- $\mu\text{m}$ -diam kernel, the concentrated 200- $\mu\text{m}$ -diam kernel and the diluted 500- $\mu\text{m}$ -diam kernel, mentioned in table 2.1. Hence, the  $N_A \bar{l}_F$ -values of the coated particles under consideration are 1.4 to 2.5 times greater than the optimal value. However, during burnup  $^{240}\text{Pu}$  will be

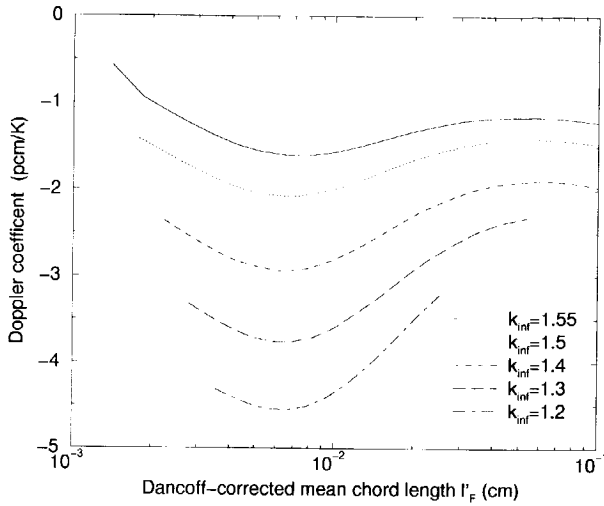


**Figure 4.8:** The Doppler coefficient as a function of the Dancoff-corrected mean chord length with  $k_{\infty}$  as a parameter. This graph refers to an undermoderated two-region white-boundary unit cell with a fuel zone (radius  $r_F$ ) and a moderator (i.e. graphite) shell (outer radius  $r_M$ ). The fuel zone contains  $\text{PuO}_2$ -fuel of which the  $\text{Pu}$ -composition is given by table 1.2.

depleted (i.e.  $N_A$  will decrease), which means that the  $N_A \bar{l}_F$ -values will get closer to the optimal value.

### 4.2.3 Kinetic parameters

Fig. 4.9 shows the kinetic parameters as a function of the Pu-loading for the fresh fuel. A curve fitting procedure has pointed out that

$$\Lambda = 1.217 \cdot 10^{-4} m_{Pu}^{-0.983}, \quad (4.6)$$

where  $\Lambda$  [s] is the mean generation time and  $m_{Pu}$  is the plutonium mass per pebble [g]. The relative difference between the fit, given by eq. 4.6, and the calculational results amounts to maximally 30%. Furthermore, fig. 4.9 shows that the effective delayed neutron fraction (i.e.  $\beta_{eff}$  calculated with VAREX [77]) increases only very slightly with increasing Pu-loading, indicating an increase of the fractional fission rate of  $^{241}\text{Pu}$  ( $\beta = 0.55\%$ ) at the cost of a decrease of the fractional fission rate of  $^{239}\text{Pu}$  ( $\beta = 0.22\%$ ).

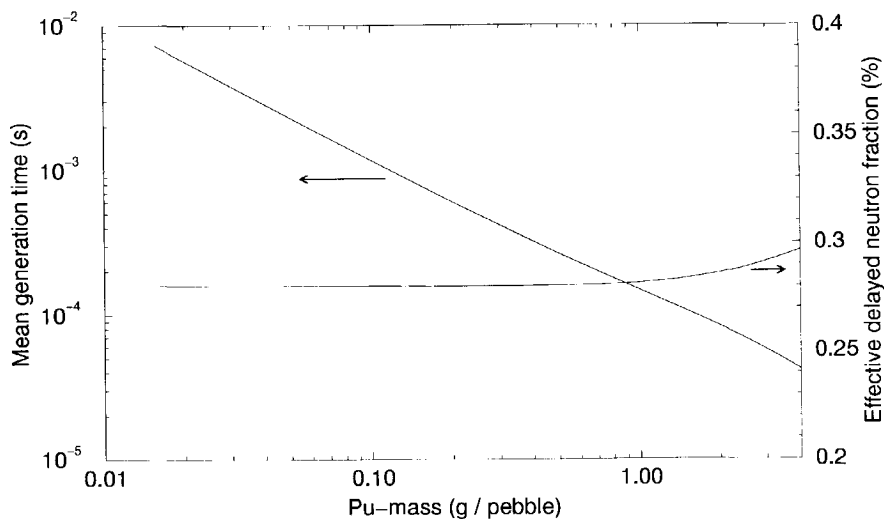


**Figure 4.9:** The neutron mean generation time and the delayed neutron fraction as a function of the plutonium mass per pebble. ( $T_{uni} = 1200$  K, concentrated 220- $\mu\text{m}$ -diam kernel, 0 MWd/kgHM).

### 4.3 Reactor Physics Parameters during Burnup

As discussed in section 4.2.1, both the Pu-loading and the type of coated particles affect the isotopic composition and  $k_{\infty}$  during burnup. To understand the  $k_{\infty}$ -evolutions presented in this section, one should bear in mind the following relations:

$$\left. \begin{array}{l} \text{An increase of the plutonium mass per pebble} \\ \text{A decrease of self-shielding of the fuel} \end{array} \right\} \text{involve:} \quad (4.7)$$

- A decrease of the resonance escape probability ( $p$ ), indicating an increase of the ratio of the nonthermal-to-total absorption rate.
- An increase of the nonthermal fission factor ( $\epsilon$ ), indicating a relative increase of the fission rate in the nonthermal range (mainly resonance fission of  $^{239}\text{Pu}$  and  $^{241}\text{Pu}$ ).
- A decrease of  $\epsilon p$ .
- An increase of the thermal utilisation factor ( $f$ ), indicating a decrease of the parasitic absorption by graphite. A higher  $f$  also implies that more neutrons are available for the conversion from even to odd Pu-isotopes which causes a relatively slow decrease of  $k_{\infty}$  with burnup.
- A higher  $C^{\ddagger}$ , indicating an increase of the  $^{240}\text{Pu}$ -capture rate to  $^{239}\text{Pu}$ -fission rate. This has the following consequences:
  - 1) A lower  $k_{\infty}$  at zero burnup for under-moderated systems.
  - 2) A faster conversion from  $^{240}\text{Pu}$  to  $^{241}\text{Pu}$ , causing a slower decrease, or even increase, of  $k_{\infty}$  during burnup.

A decrease of self-shielding of the fuel (i.e. an increase of dilution) is established by the use of different coated particles. The sequence of coated particles with concentrated 220- $\mu\text{m}$ -diam kernels, concentrated 200- $\mu\text{m}$ -diam kernels and diluted 500- $\mu\text{m}$ -diam kernels, successively, represents a decreasing order of self-shielding. (See also table 3.4).

#### 4.3.1 Nuclide Composition during Burnup

The above mentioned relations, as far as the  $^{240}\text{Pu}$ -to- $^{241}\text{Pu}$  conversion rate is concerned, are corroborated by figs. 4.10 and 4.11. Fig. 4.10 illustrates the high  $^{240}\text{Pu}$ -to- $^{241}\text{Pu}$  conversion rate of the under-moderated case with a Pu-loading of 1 g/pebble compared to the over-moderated case with a Pu-loading of 0.0625 g/pebble. Fig. 4.11 shows the isotopic composition as a function of the burnup for the concentrated 220- $\mu\text{m}$ -diam kernel and the diluted 500- $\mu\text{m}$ -diam kernel both referring to 1 g Pu/pebble. The fuel with the diluted 500- $\mu\text{m}$ -diam kernels shows a faster  $^{240}\text{Pu}$ -to- $^{241}\text{Pu}$  conversion than its concentrated 220- $\mu\text{m}$ -diam kernel counterpart.

Obviously, the mentioned differences in  $^{240}\text{Pu}$ -to- $^{241}\text{Pu}$  conversion rates have consequences for the relative fission rates of  $^{239}\text{Pu}$  and  $^{241}\text{Pu}$ . Fig. 4.12 shows the relative fission rates of  $^{239}\text{Pu}$  and  $^{241}\text{Pu}$  as a function of burnup for both 0.0625 g and 1 g Pu/pebble. The under-moderated system of 1 g Pu/pebble shows initially a faster increase of the  $^{241}\text{Pu}$  fission fraction, which is caused by a higher conversion rate from  $^{240}\text{Pu}$  to  $^{241}\text{Pu}$ .



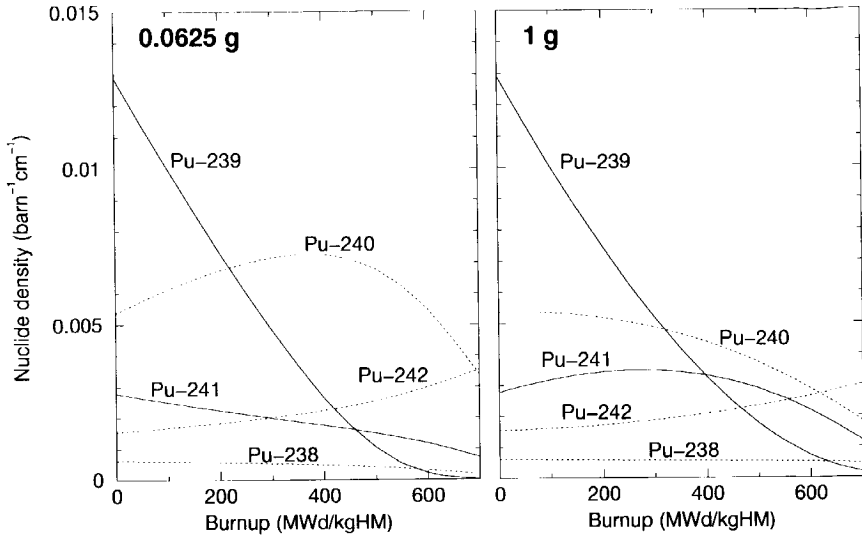


**Figure 4.10:** Number densities of the plutonium isotopes in the kernels as a function of the burnup, for Pu-loadings of 0.0625 and 1 g Pu/pebble. Burnup at constant power density of  $3 \text{ W}\cdot\text{cm}^{-3}$ . (historical- $T_{\text{uni}} = 900 \text{ K}$ , concentrated  $220\text{-}\mu\text{m}$ -diam kernel).

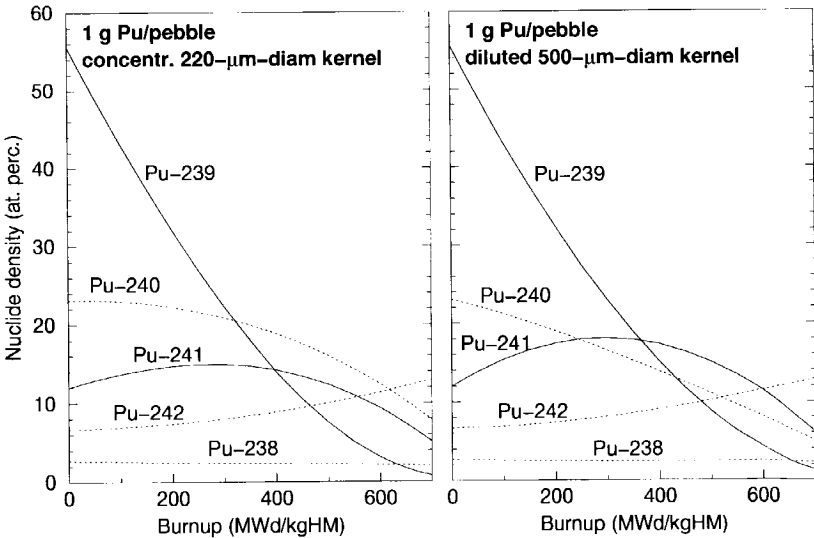


**Figure 4.11:** Fractional number densities of the plutonium isotopes as a function of the burnup, for the both the concentrated  $220\text{-}\mu\text{m}$ -diam kernel and the diluted  $500\text{-}\mu\text{m}$ -diam kernel. Burnup at constant power density of  $3 \text{ W}\cdot\text{cm}^{-3}$ . (historical- $T_{\text{uni}} = 900 \text{ K}$ , 1 g Pu/pebble).

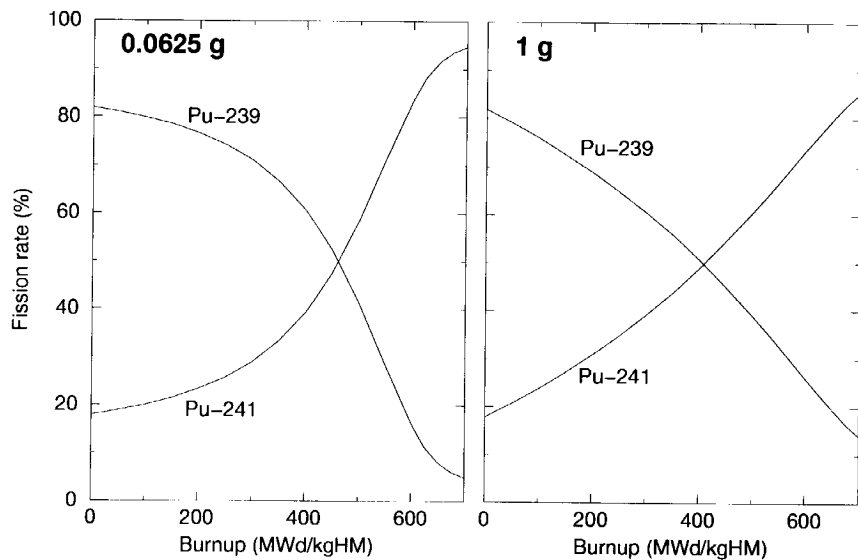


**Figure 4.12:** Contributions of  $^{239}\text{Pu}$  and  $^{241}\text{Pu}$  to the total fission rate as a function of burnup for the over-moderated system with 0.0625 g Pu/pebble and the under-moderated system with 1 g Pu/pebble. The under-moderated system shows initially a faster increase of the  $^{241}\text{Pu}$  fission fraction, which is caused by a higher conversion rate from  $^{240}\text{Pu}$  to  $^{241}\text{Pu}$ .

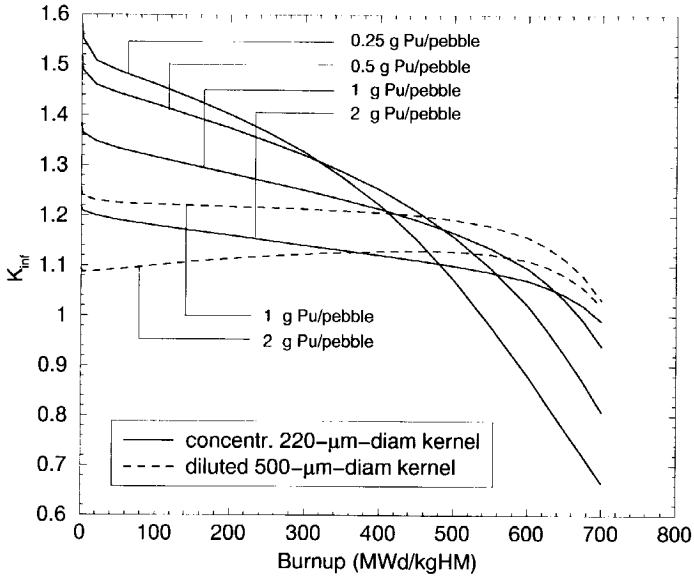
### 4.3.2 The Infinite Multiplication Factor during Burnup

It is clear that different evolutions of nuclide compositions due to different Pu-loadings or types of coated particles also lead to different  $k_{\infty}$ -evolutions. Fig. 4.13 shows the  $k_{\infty}$  as a function of the burnup with the Pu-loading as a parameter. This is done for, on the one hand, the 220- $\mu\text{m}$ -diam kernel the under-moderated systems with  $2^{(1-n)}$  g Pu/pebble where  $n = 0, 1, 2$  and  $3$  and, on the other, for the diluted 500- $\mu\text{m}$ -diam kernel with  $1$  and  $2$  g Pu/pebble. For the mentioned configurations the following trend can be observed. An increase of the Pu-loading causes on the one hand a lower initial  $k_{\infty}$  and on the other hand a slower decrease of the  $k_{\infty}$  with burnup. We recall that this is due to an increase of the resonance absorption rate and since the resonance absorption is dominated by  $^{240}\text{Pu}$  this leads a faster conversion of  $^{240}\text{Pu}$  to  $^{241}\text{Pu}$ . The use of diluted 500- $\mu\text{m}$ -diam kernels instead of concentrated 220- $\mu\text{m}$ -diam kernels also leads to a lower initial  $k_{\infty}$  and a less steep slope of the  $k_{\infty}$ -curve. The Pu-loading of  $2$  g/pebble in conjunction with the diluted 500- $\mu\text{m}$ -diam kernels even leads to an increase of  $k_{\infty}$  with burnup! One might say that  $^{240}\text{Pu}$  acts as a burnable poison whose depletion rate is determined by the resonance absorption rate, where the resonance absorption rate, on its turn, is determined by the plutonium mass per pebble and the type of the coated particles.

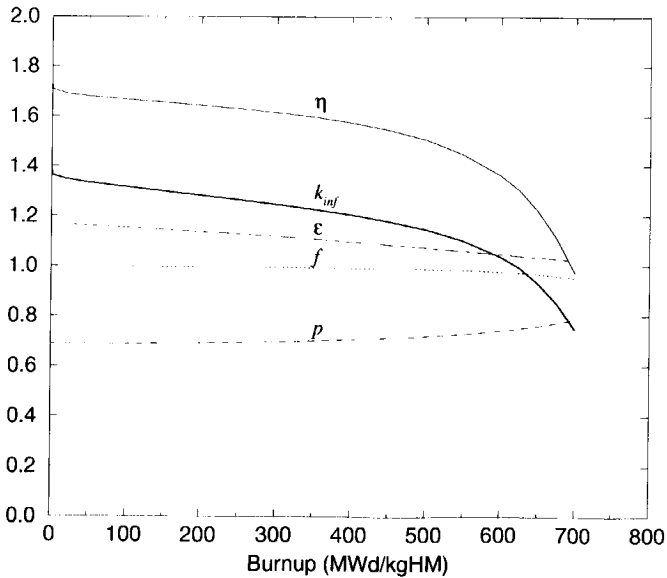
The over-moderated cases, not shown in fig. 4.13, have much stronger decreasing  $k_{\infty}$  with increasing burnup which is due to the parasitic absorption by graphite (i.e. a low thermal utilisation factor  $f$ ). The parasitic absorption implies that less neutrons are left for the conversion from even to odd Pu-isotopes. The following example illustrates this: The over-moderated case of  $0.03125$  g/pebble exhibits a decrease of the  $k_{\infty}$  from  $1.26$  at  $0$  MWd/kgHM to  $0.71$  at  $400$  MWd/kgHM, while the under-moderated case of  $2$  g/pebble shows for the same burnup interval a decrease of  $k_{\infty}$  from  $1.21$  to  $1.12$  only. The  $k_{\infty}$ -curves of the over-moderated cases will be presented in section 4.4.3.

Fig. 4.13 shows that, in particular, the  $k_{\infty}$ -curves with a high Pu-loading decrease relatively fast beyond a burnup of  $\sim 600$  MWd/kgHM. This can be ascribed to a decrease of  $\eta$ , which is illustrated by fig. 4.13. Note that the thermal utilisation factor  $f$  remains close to unity during burnup, indicating that the parasitic absorption by graphite stays low<sup>2</sup>, and that the nonthermal fission factor  $\epsilon$  decreases while the resonance escape probability  $p$  increases with increasing burnup. This can be ascribed to an increase of the moderator-to-fuel ratio due to the depletion of actinide nuclides. Before  $\sim 600$  MWd/kgHM, the  $\eta$ -curve decreases slowly compared to the  $\eta$ -curve of a conventional LWR. The average decrease of  $\eta$  per MWd/kgHM in a  $\text{UO}_2$ -fuelled PWR reads  $0.0074$  per MWd/kgHM [84], while the decrease of  $\eta$  in fig. 4.14 equals only  $\sim 0.0011$  per MWd/kgHM. This is caused by the high initial fissile-to-fertile Pu-isotopes ratio of  $\sim 67\%$  in combination with the relatively high even-to-odd Pu-isotopes conversion during burnup. Beyond  $\sim 600$  MWd/kgHM, the macroscopic cross sections of  $^{238}\text{Pu}$ ,  $^{240}\text{Pu}$  and  $^{241}\text{Am}$  become relatively important, which causes a decrease of the fission-to-capture ratio and thus a decrease of  $\eta$ .

<sup>2</sup>This has a low  $^{14}\text{C}$  production [22, 82, 83] as a beneficial side effect.



**Figure 4.13:**  $k_{\infty}$  as a function of the burnup with the plutonium mass per pebble as a parameter. (Concentr. 220- $\mu\text{m}$ -diam kernel and diluted 500- $\mu\text{m}$ -diam kernel, historical- $T_{uni} = 900\text{ K}$ , under-moderated Pu-loadings only).



**Figure 4.14:** Factors of the 4-factor formula as a function of burnup. (Concentrated 220- $\mu\text{m}$ -diam kernel, 1 g Pu/pebble).

### 4.3.3 Kinetic Parameters during Burnup

Fig. 4.15 shows the effective delayed neutron fraction and the neutron mean generation time as a function of the burnup, respectively. The curves refer to 1, 2 and 3 g Pu/pebble. The increase of the mean generation time ( $\Lambda$ ) is caused by an increase of the moderator-to-actinide ratio with increasing burnup. Note that  $\Lambda < 2$  milliseconds. The effective delayed neutron fraction ( $\beta_{eff}$ ) increases due to a gradual shift from a situation in which  $^{239}\text{Pu}$  with  $\beta = 0.22\%$  dominates the fission rate to a situation in which  $^{241}\text{Pu}$  with  $\beta = 0.55\%$  dominates the fission rate. This is illustrated by fig. 4.12.

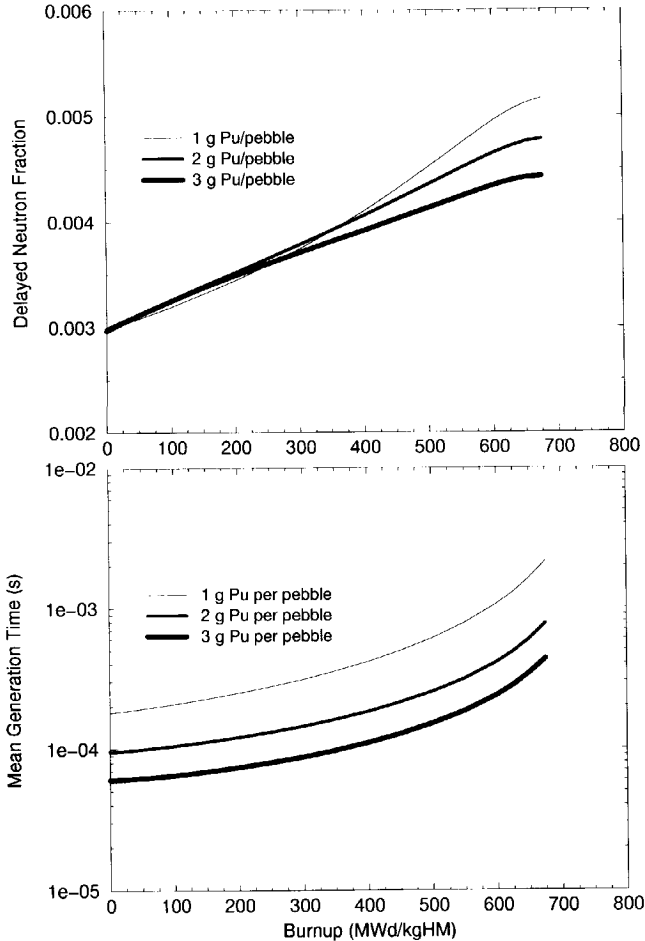


**Figure 4.15:** The effective delayed neutron fraction (top) and the neutron mean generation time (bottom) as a function of the burnup with plutonium mass per pebble as a parameter. (Concentrated 220- $\mu\text{m}$ -diam kernels,  $T_{ini} = 900\text{ K}$ ).

#### 4.3.4 Influence of the historical temperature

Parameter F of table 4.1 is the so-called historical uniform-temperature (historical- $T_{uni}$ ). This parameter refers to the temperature with which the burnup calculations are performed (i.e. the irradiation temperature). The influence of the historical- $T_{uni}$  on the evolution of  $k_{\infty}$  is only studied superficially. Fig. 4.16 shows  $k_{\infty}$  as a function of the uniform-temperature (i.e. 'branching' temperatures) with the burnup as a parameter for two historical- $T_{uni}$ 's, namely 900 K and 1500 K. Obviously, the two curves referring to 1 MWd/kgHM nearly coincide. Furthermore, the decrease of  $k_{\infty}$  with burnup is much slower for historical- $T_{uni} = 1500$  K than for historical- $T_{uni} = 900$  K. Table 3.5 shows that a higher uniform-temperature involves a lower initial  $k_{\infty}$  and a higher  $C^{\dagger}$ . The latter means a higher ratio of the  $^{240}\text{Pu}$ -capture to  $^{239}\text{Pu}$ -fission rate, which implies a slower decrease of  $k_{\infty}$  with burnup.

The above demonstrates that the historical-temperature is an interesting tool to enhance the burnup. It is clear that in a Pu-fuelled reactor the irradiation temperature can be adjusted by varying the ratios of the helium inlet temperature, the helium mass flow and the reactor power.

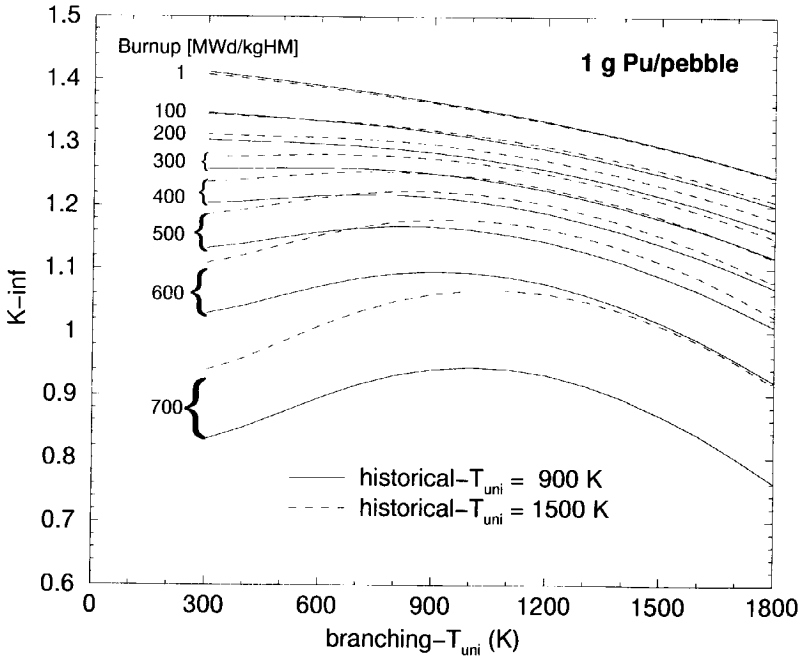


**Figure 4.16:**  $k_{\infty}$  as a function of the uniform-temperature (i.e. 'branching' temperatures) with the burnup in MWd/kgHM as a parameter, for the historical- $T_{uni}$  of 900 K and 1500 K. (1 g Pu/pebble, concentrated 220- $\mu\text{m}$ -diam kernel).

### 4.3.5 Fast fluence

Fast neutrons cause displacements of atoms, which leads to a deterioration of the coatings and possibly to a complete coated particle break down. The longer the coated particles are exposed to a fast flux ( $> 0.1$  MeV), the higher the probability is that failure will occur. As the irradiation time increases linearly with the plutonium mass per pebble, the fast fluence will do so as well, because the power density and thus the fast neutron source are assumed to be constant.

Table 4.3 shows the thermal, epi-thermal and fast fluences at a burnup of 700 MWd/kgHM for three Pu-loadings. The fast fluence is nearly proportional with the plutonium mass per pebble. The deviation from the linear dependence between the plutonium mass and the fast fluence can be ascribed to the fact that the results stem from  $k_{\infty}$ -calculations, which implies that for the solution of the eigenvalue equation the fast spectrum is reduced by a factor  $1/k_{\infty}$ . Since the listed figures refer to under-moderated cases, a higher plutonium mass corresponds with a lower  $k_{\infty}$ , which implies a lower reduction of the fast flux with increasing plutonium mass.

In the case of 3 g Pu/pebble, the fast fluence exceeds the premise of a maximal fast fluence of  $8 \cdot 10^{21}$  n/cm<sup>2</sup>. This indicates that there is an upper boundary for the plutonium mass per pebble. As mentioned in chapter 2, irradiation experiments providing data for a combination of a high fast fluence, a high temperature and a high burnup are necessary to judge whether the Pu-CP performance under these circumstances is satisfactory.

In addition, table 4.3 shows that the thermal fluence decreases with increasing plutonium mass per pebble. This phenomenon can be attributed to the increased contribution of epithermal fissions with increasing plutonium mass per pebble. This is corroborated by the  $\delta^{49}$ -curve of fig. 4.4.

**Table 4.3:** Fluences at 700 MWd/kgHM for three Pu-loadings.

Pu-loading (g/pebble)	Fluences ( $10^{21}$ n/cm <sup>2</sup> ) at 700 MWd/kgHM		
	Thermal ( $E < 0.625$ eV)	Epi-thermal ( $0.625$ eV $< E < 10^5$ eV)	Fast ( $E > 10^5$ eV)
1	4.4	7.0	2.8
2	3.2	15.1	6.7
3	2.7	22.4	9.9

## 4.4 Temperature reactivity effects

### 4.4.1 Abstract

This section<sup>3</sup> presents the temperature reactivity effects occurring in a pebble-bed type High Temperature gas-cooled Reactor fuelled with reactor-grade plutonium without uranium and without any burnable poisons. Burnup calculations are performed for pebbles loaded with various amounts of plutonium per pebble. During burnup, branching calculations are carried out to calculate  $k_\infty$  as a function of the uniform temperature. For a high plutonium mass per pebble and low burnup values,  $k_\infty$  decreases with uniform temperature, which indicates a negative uniform temperature coefficient of reactivity (UTC). However, for a low plutonium mass per pebble as well as for a high plutonium mass per pebble in combination with high burnup,  $k_\infty$  is maximal at a particular uniform temperature. Below this temperature, the UTC is positive while above this temperature it is negative. Branching calculations with a varying moderator temperature show almost the same behaviour, which indicates that the contribution of the fuel temperature plays a minor role for the mentioned effect. To understand the reactivity effect, the moderator temperature coefficient (MTC) is investigated by two methods. In the first method, changes in reaction rates of individual nuclides and their corresponding contributions to the MTC are calculated, whereas in the second method the four-factor formula has been used. For the fresh fuel cases, the positive coefficient at low temperature is due to a positive coefficient for the thermal utilisation factor. For high moderator temperatures, the coefficient for the resonance escape probability renders the moderator temperature coefficient negative. This trend is basically caused by the shift of the high-energy tail of the Maxwell-spectrum towards the 1-eV resonance of  $^{240}\text{Pu}$ , and towards the resonances of  $^{241}\text{Pu}$ , which leads to an increase of the capture-to-fission ratio.

### 4.4.2 Historical back-ground

Among the important properties in determining the safety characteristics of a nuclear reactor are its temperature coefficients of reactivity. Both a change of the fuel temperature and a change of the moderator temperature lead to a change in reactivity. An increase of the fuel temperature causes a broadening of the resonances, which leads to a reduction of self-shielding and therefore to an increase of resonance absorption. This mechanism, known as the Doppler effect, is prompt since it occurs simultaneously with the dissipation of kinetic energy of the fission products. The moderator-temperature effect, on the other hand, is somewhat delayed since heat must flow from the fuel to the moderator before the moderator temperature changes. An increase of the moderator temperature, keeping the density constant, leads to a shift of the Maxwell spectrum to higher energies. In the thermal energy range cross sections behave basically as  $1/v$ . If one assumes that a cross section behaves exactly as  $\sigma(E) \sim 1/\sqrt{E}$  and that the spectrum is perfectly Maxwellian, the one-group cross section becomes  $\bar{\sigma} = \int \sigma(E)\phi_M(T, E)dE / \int \phi_M(T, E)dE \sim 1/\sqrt{T}$ , where  $\phi_M(T, E)$  is the Maxwell spectrum (see e.g. p. 383 of [69]). If both the neutron production and absorption cross sections would fall off with temperature as  $1/\sqrt{T}$ , the ratio of the

<sup>3</sup>Section 4.4 is largely based on ref. [74]



total neutron production rate and the total absorption rate (i.e.  $k_{\infty}$ ) would remain constant, and this would not lead to a change of reactivity. However, many heavy nuclides have resonances in the thermal energy range, which cause deviations from the  $1/v$ -behaviour. Fig. 4.17 shows the cross sections of a number of nuclides, normalised to their  $1/v$ -limits. Fig. 4.17 reveals that the capture cross section of graphite does not deviate from the

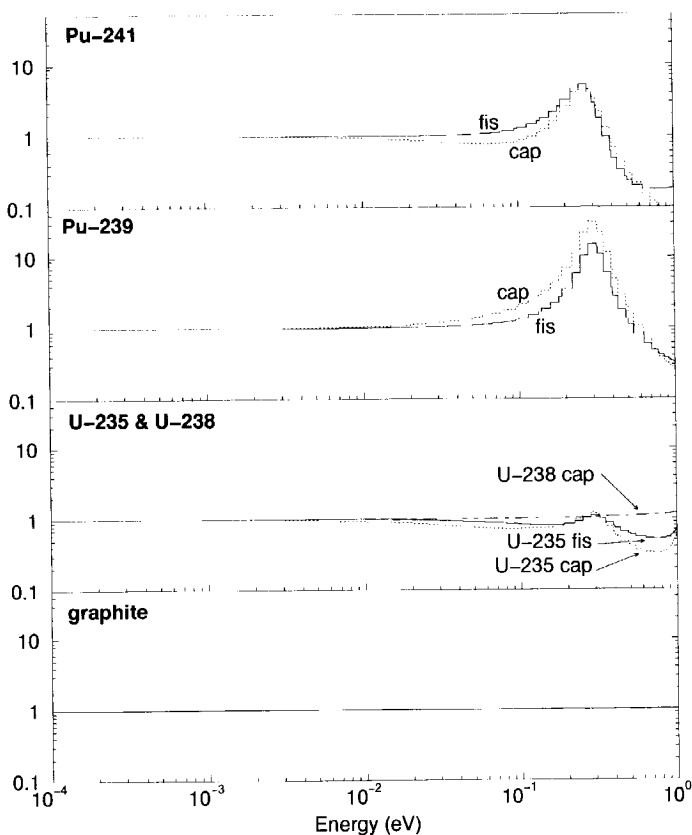


**Figure 4.17:** Cross sections of  $^{241}\text{Pu}$ ,  $^{239}\text{Pu}$ ,  $^{235}\text{U}$ ,  $^{238}\text{U}$  and graphite, normalised to their  $1/v$ -limit, as a function of energy.

$1/v$ -shape, while the  $^{235}\text{U}$  cross sections do due to a tiny resonance at 0.29 eV [85]. The dot-dashed curve of  $^{238}\text{U}$  hardly deviates from the  $1/v$ -shape, while the cross sections of  $^{239}\text{Pu}$  and  $^{241}\text{Pu}$  show strong deviations due to their pronounced resonances at 0.30 eV and 0.26 eV, respectively. Note that the capture-to-fission ratio of  $^{239}\text{Pu}$  is higher at the resonance energy than in its low-energy wing.

As early as in the 1950s it was found that the formation of  $^{239}\text{Pu}$  in the Calder Hall reactors (fuelled with natural uranium and moderated with graphite) caused a positive moderator-temperature coefficient, yet at a burnup of 0.8 MWd/kgHM (p. 578 ff of [86]).

The shift of the thermal neutron spectrum with temperature in the presence of  $^{239}\text{Pu}$  appeared to cause two reactivity effects acting in opposite directions. On the one hand, the capture-to-fission ratio of the thermal-group constants of  $^{239}\text{Pu}$  increased due to the shift of the Maxwell spectrum towards the 0.3 eV resonance of  $^{239}\text{Pu}$ . This led to a decrease of the average number of neutrons per thermal neutron absorbed in the fuel (i.e.  $\frac{d\eta}{dT_M} < 0$ ), which resulted in a negative reactivity contribution. On the other hand, the shift of the Maxwell spectrum towards higher energies caused an increase of the thermal utilisation factor (i.e.  $\frac{df}{dT_M} > 0$ ), which led to a positive contribution. This means that the ratio of the thermal absorption rate in the fuel to the thermal absorption rate in the moderator increases with increasing temperature. At a burnup of 0.8 MWd/kgHM, the second effect dominated in the strongly moderated Calder Hall reactor, which resulted in a net positive reactivity effect.

Nowadays, new fuel concepts such as plutonium in inert matrices and plutonium in coated particles are investigated and being developed. It is clear that in such fuels, temperature reactivity effects like the precedingly described effect due to  $^{239}\text{Pu}$  may occur. Besides that, other plutonium isotopes with their own characteristic thermal resonances, will contribute to the behaviour of the temperature coefficients of reactivity, too.

This section discusses the temperature coefficients of the pebble bed type High Temperature gas-cooled Reactor fuelled with reactor-grade plutonium. The pebbles are uranium-free and do not contain any burnable poisons.

#### 4.4.3 Temperature reactivity effects during burnup

Branching calculations have been performed at burnup values of 0, 100, 200, ..., 700 MWd/kgHM. In these branches, the uniform temperature ( $T_u$ ), the moderator temperature ( $T_M$ ) and the fuel temperature ( $T_f$ ) were separately altered from 300 to 1800 K with steps of 100 K. In case of a changing fuel temperature, the moderator temperature (coatings and graphite) was kept at 900 K; in case of a changing moderator temperature, the fuel temperature was kept at 900 K. The calculations were done for coated particles with both diluted 500- $\mu\text{m}$ -diam kernels and concentrated 220- $\mu\text{m}$ -diam kernels.

Fig. 4.18 and 4.19 show the  $k_\infty$  as a function of the plutonium mass per pebble with the burnup as a parameter, for coated particles with the diluted 500  $\mu\text{m}$ -diam kernel and the concentrated 220  $\mu\text{m}$ -diam kernel, respectively.

Each  $k_\infty$ -value with  $T_u = 1200$  K on the (0 MWd/kgHM)-curves in fig. 4.18 corresponds to a point on the  $k_\infty$ -curve of the diluted 500- $\mu\text{m}$ -diam kernel in fig. 4.1. Analogously, each point with  $T_u = 1200$  K on (0 MWd/kgHM)-curves in fig. 4.19 corresponds to a point on the  $k_\infty$ -curve of the concentrated 220  $\mu\text{m}$ -diam kernel in fig. 4.1.

Fig. 4.19 shows that the cases (0.25 g Pu; 0 MWd/kgHM), (0.5 g Pu; 0 MWd/kgHM), (1 g Pu; 0, 100, 200 MWd/kgHM) and (2 g Pu; 0, 100, ..., 500 MWd/kgHM) have  $k_\infty(T_u)$ -curves with a negative slope, which signifies negative uniform temperature coefficients (UTCs) for the entire temperature range.

The remaining curves have a maximum denoted by a dot. It is clear that the uniform

temperature coefficient (UTC) is positive left of such a maximum and negative at the opposite side. For similar uranium-free fuels, UTCs that decrease from a positive to a negative value with increasing uniform temperature were also reported by ref. [87]. The positions of the maxima (i.e. the uniform temperature for which  $UTC = 0$ ) decrease with increasing Pu-loading. For 0.015625 g Pu/pebble, the maxima lie between 1450 and 1650 K; for 2 g Pu/pebble these lie between 650 and 950 K. The difference between the maximum- $k_{\infty}$  and  $k_{\infty}$  at a uniform temperature of 300 K decreases with increasing Pu-loading. For the (0.015265 g; 0 MWd/kgHM)-case,  $k_{\infty}^{max} - k_{\infty}(300 \text{ K}) = 1.08 - 0.75 = 0.33$ , which is equal to a reactivity increase of about  $\Delta\rho = (k_{\infty}(300 \text{ K}))^{-1} - (k_{\infty}^{max})^{-1} = 0.4$ . The total delayed neutron fraction of the fuel, calculated as the  $(\nu\Sigma_f)$ -weighted average of the delayed neutron fractions of  $^{239}\text{Pu}$  ( $\beta = 0.23\%$ ) and  $^{241}\text{Pu}$  ( $\beta = 0.55\%$ ), is equal to 0.3 % in this case, which means that the reactivity Difference of 0.4 corresponds to about +130 \$ !

In order to find out to which degree the moderator temperature contributes to the uniform temperature effect, the moderator temperature has been separately changed in the branching calculations. Fig. 4.20 shows that the  $k_{\infty}(T_M)$ -curves are only slightly distorted compared to the  $k_{\infty}(T_u)$ -curves of fig. 4.19, which demonstrates that the moderator temperature reactivity effect is the main component of the uniform temperature reactivity effect. The differences between the  $k_{\infty}(T_M)$ -curves of fig. 4.20 and the  $k_{\infty}(T_u)$ -curves of fig. 4.19 increase with increasing Pu-loading per pebble, indicating that the fuel temperature contribution to the uniform temperature reactivity effect increases with increasing Pu-loading. The maximum difference equals  $k_{\infty}(T_M) - k_{\infty}(T_u) = 0.025$ , for the case of (2 g Pu; 0 MWd/kgHM).

The reactivity effect due to a changing fuel temperature will be discussed in section 4.4.5.

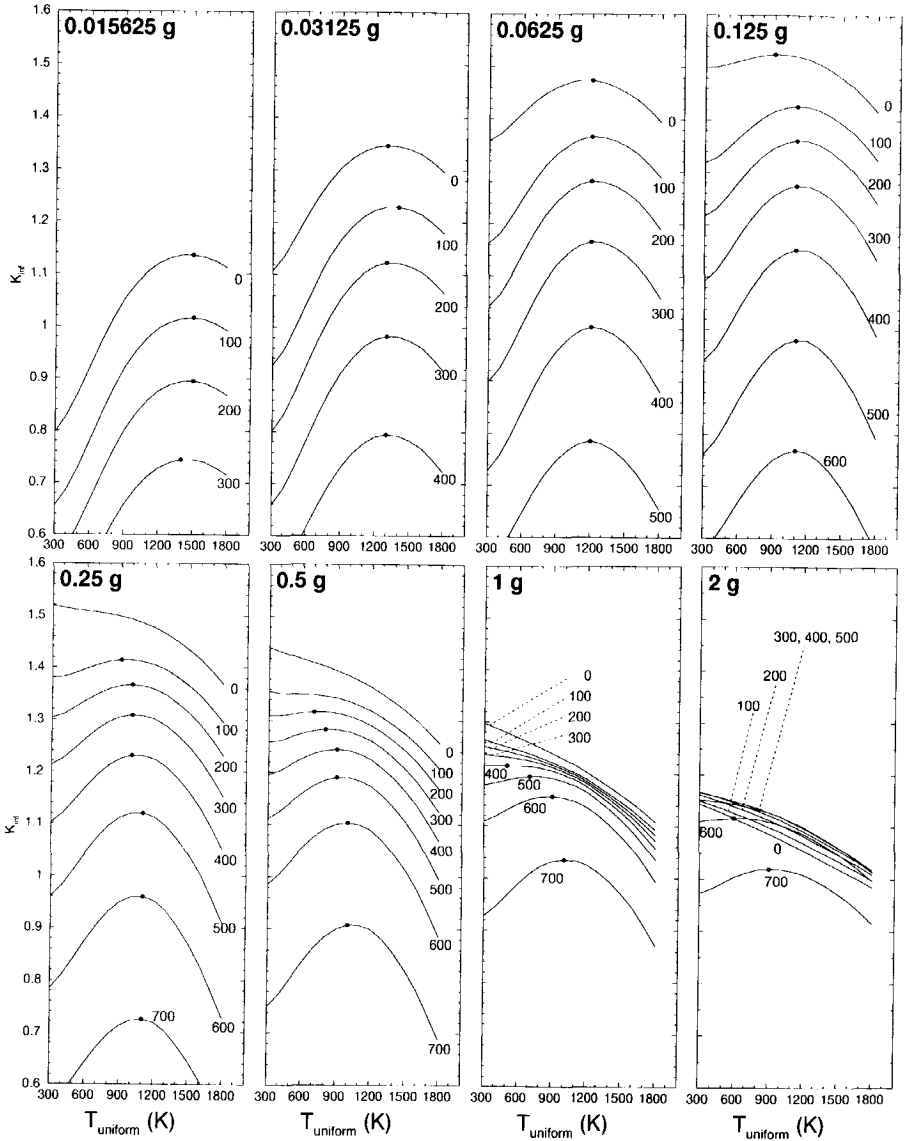


**Figure 1.18:**  $k_{\infty}$  as a function of the uniform temperature with the burnup in MWd/kgHM as parameter. The Pu-loadings of  $2^{(1-n)}$  g/pebble with  $n = 0, 1, \dots, 7$  are indicated in the corners of the graphs. The graphs refer to coated particles with diluted kernels of  $500 \mu\text{m}$  diameter. The dots denote the maxima of the curves. Notice that  $k_{\infty}$  increases with burnup in the case of 2 g Pu/pebble.

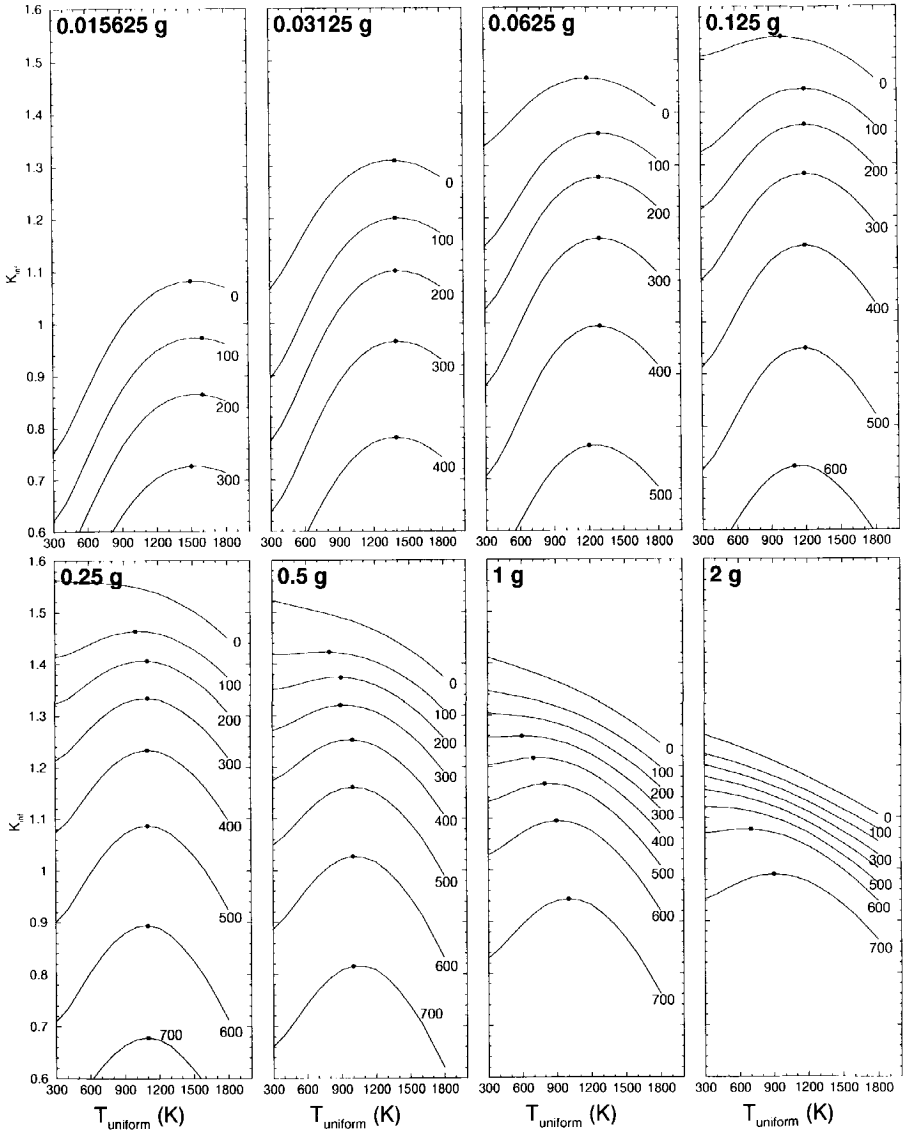


**Figure 4.19:**  $k_{\infty}$  as a function of the uniform temperature with the burnup in MWd/kgHM as parameter. The Pu-loadings of  $2^{(1-n)}$  g/pebble with  $n = 0, 1, \dots, 7$  are indicated in the corners of the graphs. The graphs refer to coated particles with concentrated kernels of  $220 \mu\text{m}$  diameter. The dots denote the maxima of the curves.

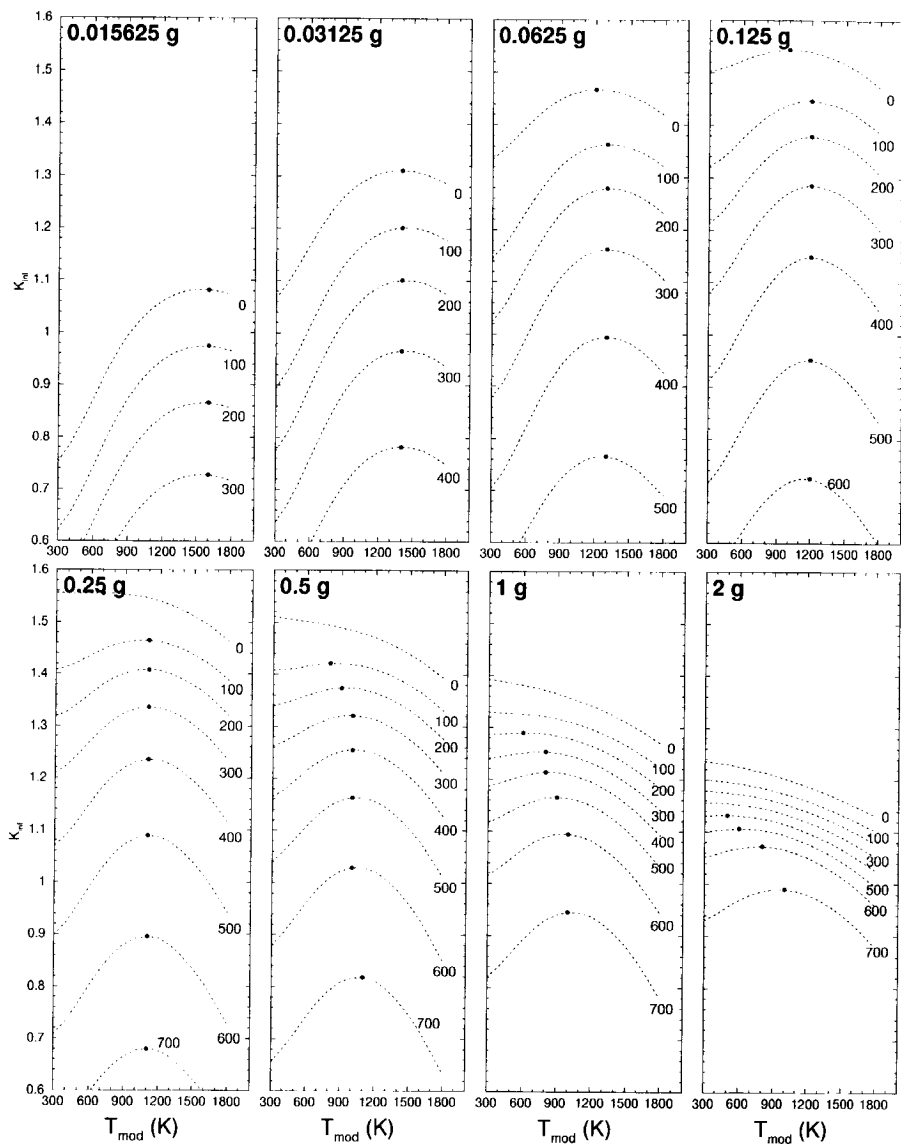


**Figure 4.20:**  $k_{\infty}$  as a function of the moderator temperature with the burnup in MWd/kgHM as parameter. The Pu-loadings of  $2^{(1-n)}$  g/pebble with  $n = 0, 1, \dots, 7$  are indicated in the corners of the graphs. The graphs refer to coated particles with concentrated kernels of  $220 \mu\text{m}$  diameter. The dots denote the maxima of the curves.

#### 4.4.4 Analysis of the moderator temperature coefficients

The  $k_{\infty}(T_M)$ -data, presented in section 4.4.3, were used for the calculation of the moderator temperature coefficient. We recall that temperature coefficient of reactivity in an infinite system (or in a unit cell with reflecting boundaries) is given by eq. 4.3, in which  $T = T_M$  yields the moderator temperature coefficient.

We analysed the MTC on the basis of two methods. The first method calculates changes in reaction rates of individual nuclides and their corresponding contributions to the MTC, as a function of the moderator temperature. The second method is based on the four factor formula, which means that the MTC is expressed in terms of temperature derivatives of the factors of the four-factor formula.

##### Analysis of the MTC by regarding changes in reaction rates

The infinite multiplication factor of an arbitrary multi-zone system reads

$$k_{\infty} = \frac{P}{A} , \quad (4.8)$$

where  $P$  is the neutron-production rate due to fission, given by

$$P = \sum_i^{nucs} P_i = \sum_i^{nucs} \sum_z^{zones} N_{i,z} (\nu\sigma_f)_{i,z} \phi_z V_z , \quad (4.9)$$

and where  $A$  is the total absorption rate, given by

$$A = \sum_i^{nucs} A_i = \sum_i^{nucs} \sum_z^{zones} N_{i,z} (\sigma_a)_{i,z} \phi_z V_z . \quad (4.10)$$

Here, the one-group reactions rates are given as summations over zones  $z$  and nuclides  $i$ . The number density of nuclide  $i$  in zone  $z$  equals  $N_{i,z}$ , the flux in zone  $z$  equals  $\phi_z$ , the volume of zone  $z$  equals  $V_z$ , and  $(\nu\sigma_f)_{i,z}$  and  $(\sigma_a)_{i,z}$  are the microscopic cross sections of nuclide  $i$  in zone  $z$  for neutron-production and absorption, respectively. Inserting eq. 4.8 in eq. 4.3 yields

$$MTC = \frac{1}{P} \frac{dP}{dT_M} - \frac{1}{A} \frac{dA}{dT_M} = \sum_i^{nucs} contr_i , \quad (4.11)$$

where the contribution of nuclide  $i$  to the temperature coefficient of reactivity reads

$$contr_i = \frac{1}{P} \frac{dP_i}{dT_M} - \frac{1}{A} \frac{dA_i}{dT_M} , \quad (4.12)$$

in which the total reaction rate for absorption of nuclide  $i$ , summed over all zones, is given by

$$A_i = \sum_z^{zones} N_{i,z} (\sigma_a)_{i,z} \phi_z V_z , \quad (4.13)$$

and where the neutron production rate is defined analogously. Eq. 4.12 shows that the contribution of a nuclide  $i$  is negative if

$$\frac{1}{P} \frac{dP_i}{dT_M} < \frac{1}{A} \frac{dA_i}{dT_M} , \quad (4.14)$$

which means the relative contribution to the total production rate is smaller than the relative contribution to the total absorption rate.

Fig. 4.21 shows the MTC as well as the contributions of several nuclides to the MTC as a function of the moderator temperature, for Pu-loadings of 0.0625 g and 1 g/pebble, at burnup values of 0, 200, 400 and 600 MWd/kgHM. It can be observed that the MTC varies strongly with moderator temperature. In order to illustrate this we mention that the over-moderated case of 0.0625 g Pu/pebble yields  $-11 < \text{MTC} < +17$  (pcm/K) for 0 MWd/kgHM, and  $-25 < \text{MTC} < +60$  (pcm/K) for 400 MWd/kgHM, in the range of  $300 \text{ K} < T_M < 1800 \text{ K}$ . The under-moderated case of 1 g Pu/pebble yields, in the same temperature range,  $-12 < \text{MTC} < -2$  (pcm/K) for 0 MWd/kgHM, and  $-21 < \text{MTC} < +7$  (pcm/K) for 400 MWd/kgHM.

The intersections of the MTC-curves (thick solid curves) with the horizontal axis ( $\text{MTC}=0$ ) correspond with the maxima of the  $k_\infty$ -curves in fig. 4.20. The contributions of graphite (dotted curve),  $^{239}\text{Pu}$  (dashed),  $^{240}\text{Pu}$  (dotted curve with squares),  $^{241}\text{Pu}$  (x-symbols) and  $^{135}\text{Xe}$  (thin solid) were calculated according to eq. 4.12. The contribution of the remaining nuclides is represented by the solid curve with circular symbols.

Fig. 4.21 reveals that graphite and  $^{135}\text{Xe}$  always yield positive contributions to the MTC, which become stronger with decreasing Pu-loading (i.e. increasing moderator-to-fuel ratio). A shift of the Maxwell spectrum as a result of a temperature increase seems to cause a decrease of absorption for both graphite and  $^{135}\text{Xe}$ . The contribution of  $^{239}\text{Pu}$  shifts towards positive values with decreasing Pu-loading and with increasing burnup. The upper-half of fig. 4.21, referring to 0.0625 g Pu/pebble, shows that for zero burnup important positive contributions to the MTC are due to graphite and  $^{239}\text{Pu}$ . For high temperatures, the negative contributions due to  $^{240}\text{Pu}$  and  $^{241}\text{Pu}$  dominate, which renders the MTC negative.

### Analysis of the MTC through the four-factor formula

Inserting eq. 4.1 in eq. 4.3 yields for the MTC

$$\frac{1}{k_\infty} \frac{dk_\infty}{dT_M} = \frac{1}{\eta} \frac{d\eta}{dT_M} + \frac{1}{f} \frac{df}{dT_M} + \frac{1}{p} \frac{dp}{dT_M} + \frac{1}{\epsilon} \frac{d\epsilon}{dT_M}. \quad (4.15)$$

The MTC and the coefficients at the RHS of eq. 4.15 are plotted as function of the moderator temperature in fig. 4.22, again for the over-moderated case of 0.0625 g Pu/pebble and for the under-moderated case of 1 g Pu/pebble. We will discuss the coefficients of the four factors, successively.

- The magnitude and sign of the coefficient for the neutron production per thermally absorbed neutron in the fuel,  $\frac{1}{\eta} \frac{d\eta}{dT_M}$ , depends on both the moderator temperature and burnup. At zero burnup, the thermal absorption rate in the fuel is for about 80% determined by  $^{239}\text{Pu}$ . In that case an increase of the moderator temperature involves a shift of the Maxwell spectrum towards the 0.3-eV resonance of  $^{239}\text{Pu}$ . Fig. 4.17 shows that the capture-to-fission ratio is lower in the resonance than at low energies. The shift of the Maxwell spectrum causes an increase of the capture-to-fission ratio, which involves a negative  $\frac{1}{\eta} \frac{d\eta}{dT_M}$ . However, with increasing burnup the fractional thermal absorption rate of  $^{239}\text{Pu}$  decreases, while that of  $^{241}\text{Pu}$  increases. At 200 MWd/kgHM these read 70% and 30%, respectively. A shift of the Maxwell spectrum to higher energies in the



presence of the thermal resonances of  $^{239}\text{Pu}$  and  $^{241}\text{Pu}$  (depicted in fig. 4.17), leads to a positive  $\frac{1}{\eta} \frac{d\eta}{dT_M}$  at low temperatures, and to a negative  $\frac{1}{\eta} \frac{d\eta}{dT_M}$  at high temperatures.

- The coefficient for the thermal utilisation factor  $\frac{1}{f} \frac{df}{dT_M}$  is positive in all cases. This implies that a shift of the Maxwell spectrum to higher energies with increasing moderator temperature leads to an increased ratio of the thermal absorption rate in the fuel to the thermal absorption rate in the moderator, which is due to the thermal resonances of  $^{239}\text{Pu}$  and  $^{241}\text{Pu}$ . This effect becomes stronger with increasing moderator-to-fuel ratio.
- The coefficient for the resonance escape probability  $\frac{1}{p} \frac{dp}{dT_M}$  is always negative, which implies that the nonthermal-to-thermal absorption rate (averaged over all zones) increases with increasing moderator temperature. At high temperatures, the  $\frac{1}{p} \frac{dp}{dT_M}$ -curve of fig. 4.22 corresponds to a major extent with the  $^{240}\text{Pu}$  and  $^{241}\text{Pu}$  curves of fig. 4.21. The decrease of  $p$  with increasing moderator temperature involves an increase of the  $^{240}\text{Pu}$ -capture rate and an increase of the capture-to-fission rate of  $^{241}\text{Pu}$ . This is due to a shift of the high-energy tail of the Maxwell spectrum in the nonthermal energy range, where the presence of the 1-eV resonance of  $^{240}\text{Pu}$  and the resonances of  $^{241}\text{Pu}$  provide for an increased nonthermal absorption rate.
- The coefficient for the nonthermal fission factor  $\frac{1}{\epsilon} \frac{d\epsilon}{dT_M}$  is negative at high burnups and low temperatures. Then, both the nonthermal and thermal fission rate increase, but the fractional increase of the nonthermal fission rate is smaller than the fractional increase of the thermal fission rate. For high enough temperatures a fractional decrease of the thermal fission rate and a fractional increase of the nonthermal fission rate can be observed, which leads of course to a positive  $\frac{1}{\epsilon} \frac{d\epsilon}{dT_M}$ .

Fig. 4.22 demonstrates in which way the coefficients of the four factor formula constitute the MTC. At zero burnup,  $\frac{1}{f} \frac{df}{dT_M}$  is basically responsible for the positive MTC at low temperatures, while the negative  $\frac{1}{p} \frac{dp}{dT_M}$  provides for a negative MTC at high temperatures. With increasing burnup,  $\frac{1}{\eta} \frac{d\eta}{dT_M}$  becomes positive for a large interval of the temperature range, which gives rise to an even stronger positive MTC.

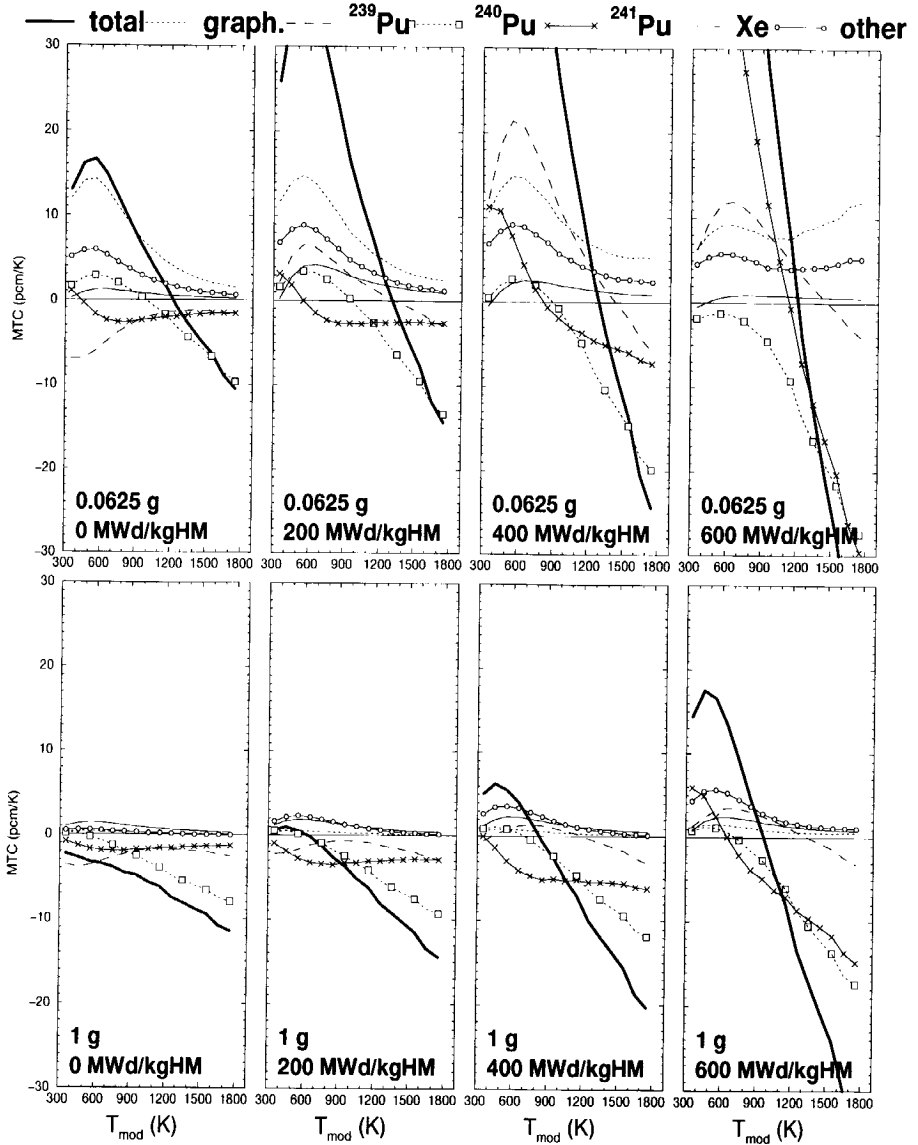


**Figure 4.21:** Contribution of several nuclides to the MTC as a function of the moderator temperature for 0.0625 and 1 g Pebble, and for burnups of 0, 200, 400, 600 MWd/kgHM. The thick, solid curve represents the total value of the MTC. The graphs refer to coated particles with concentrated kernels of 220  $\mu\text{m}$  diameter.

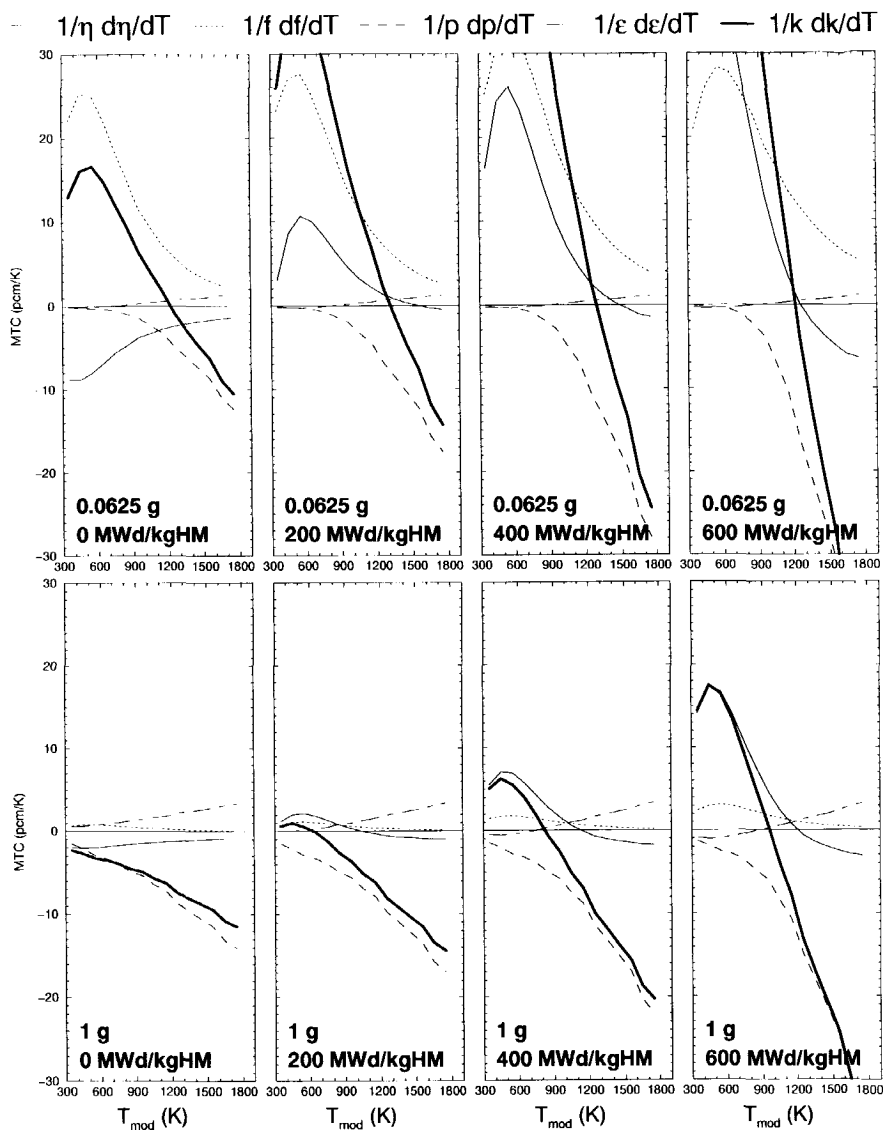


**Figure 4.22:** Analysis of the MTC by means of the four-factor formula, for 0.0625 and 1 g Pu/pebble, and for burnups of 0, 200, 400, 600 MWd/kgHM. The graphs refer to coated particles with concentrated kernels of 220  $\mu\text{m}$  diameter.

#### 4.4.5 The fuel temperature coefficient of reactivity

Since the fuel temperature effect is much weaker than the moderator temperature effect, it is presented in the form of fuel temperature coefficients (FTCs) rather than  $k_{\infty}(T_F)$ -curves. Fig. 4.23 shows the FTC as function of the fuel temperature with the Pu-loading per pebble as parameter, for burnups of 0 and 600 MWd/kgHM. The local minima at about 650 K are most probably caused by inaccuracies occurring when WIMS interpolates with respect to the temperature in the table of resonance integrals.

Fig. 4.23 shows that the FTC becomes weaker with decreasing Pu-loading per pebble, i.e. with increasing moderator-to-fuel ratio. Moreover, the magnitude of the FTC decreases with increasing fuel temperature. For fuel temperatures between 300 K and 1800 K the FTC is always less negative than  $-4$  pcm/K. The FTC hardly changes during burnup, viz. less than 1 pcm/K from 0 to 600 MWd/kgHM.

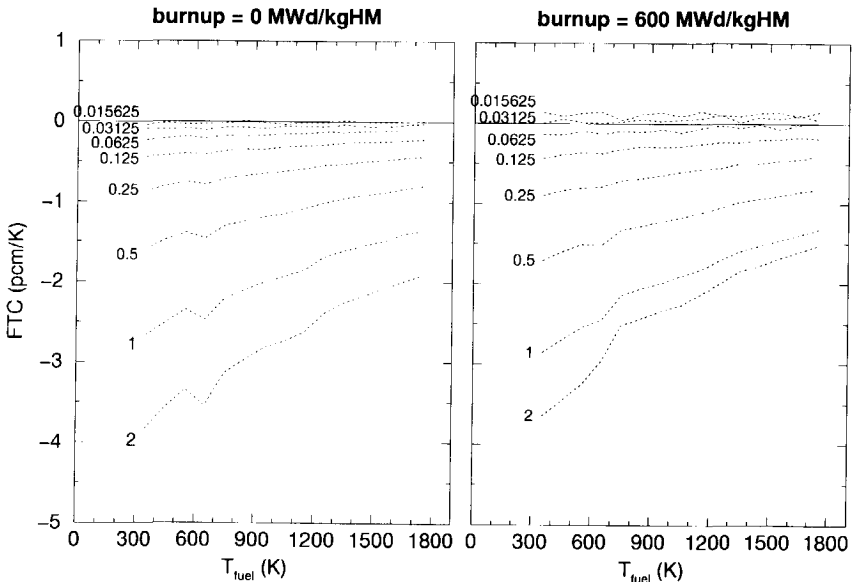


**Figure 4.23:** The FTC as a function of the fuel temperature, with the Pu-loading (g/pebble) as a parameter, for burnups of 0 and 600 MWd/kgHM. The graphs refer to coated particles with concentrated kernels of 220  $\mu\text{m}$  diameter.

#### 4.4.6 Considerations with regard to reactor operation

It is clear that the reactivity coefficients presented in the preceding sections will cause a start-up and stability behaviour that differs from what we are used to in more conventional reactor types. Below, we will give an example to illustrate this, thereby not aiming to present a complete and thorough analysis, since this is considered to be a subject for further investigations.

Usually, the negative reactivity introduced when the reactor is brought from the cold to the nominal hot state, is compensated through the (partial) withdrawal of control rods. However, if we consider a Pu-fuelled pebble-bed HTR with a positive uniform temperature coefficient, a temperature increase from, say, 300 K to the nominal operating temperature will result in a positive reactivity introduction. This can be illustrated by considering a bare configuration (no reflectors) of fresh pebbles with 0.125 g Pu per pebble. Fig. 4.19 demonstrates that  $k_{\infty}$  increases from 1.506 at 300 K to 1.543 at 1000 K, and then decreases to 1.464 at 1800 K. Let us assume that the neutrons of this system have a temperature-independent nonleakage probability of 0.65. This implies that the reactivity can be calculated as  $\rho = (k_{eff} - 1)/k_{eff}$  with  $k_{eff} = 0.65 \cdot k_{\infty}$ . The reactivity values calculated in this way are depicted as "+"-symbols in fig. 4.24. The curve shows that the reactivity behaves nicely as a second-order function for  $T > T_0$ .

Fig. 4.24 shows that the reactor is subcritical ( $\rho = -0.024$ ) in the cold state of  $T_u = 300$  K. If the reactor is heated by pumping high-temperature helium through the pebble bed (i.e. nonnuclear heating), it becomes critical at  $T_0 = 800$  K. At this temperature, the system finds itself in an instable equilibrium and has to be operated through active control. When the active control of the system ceases for one or another reason, a *negative* reactivity disturbance will lead to a power decrease and consequently to a temperature decrease. This renders the reactivity even more negative and leads eventually to an autonomous shutdown of the reactor. On the other hand, a *positive* reactivity disturbance causes an increase in power, accompanied by an increase of the uniform temperature and hence leads to a positive reactivity introduction, which causes the power to increase even more, and so on. However, when the temperature passes  $T_1$  the reactivity changes sign which causes a negative feed-back of the power. The system will eventually settle down (perhaps after some damped oscillations) at temperature  $T_1$  and at an equilibrium power that provides for a balance between heat production and removal.

Section 4.4.7 treats a special case of the described transient by analytic means, where the model reactor suffers, in addition to the failure of the control devices, a complete loss of cooling.

The above mentioned system of 0.125 g Pu/pebble is characterised by a parabola-like  $k_{\infty}(T_u)$ -curve. Systems from 0.25 to 2 g Pu/pebble, however, show a decreasing  $k_{\infty}(T_u)$ -curve and only for high burnups a parabola-like curve (see fig. 4.19). In realistic pebble-bed HTRs, there will be a temperature profile across the core and, moreover, pebbles with various burnups will be present. (In multi-pass systems, pebbles with different degrees of burnup are mixed, while in so-called *Peu-à-Peu* systems, where the pebble bed is continuously fuelled by adding fresh pebbles on top, there is an axial burnup gradient.) This

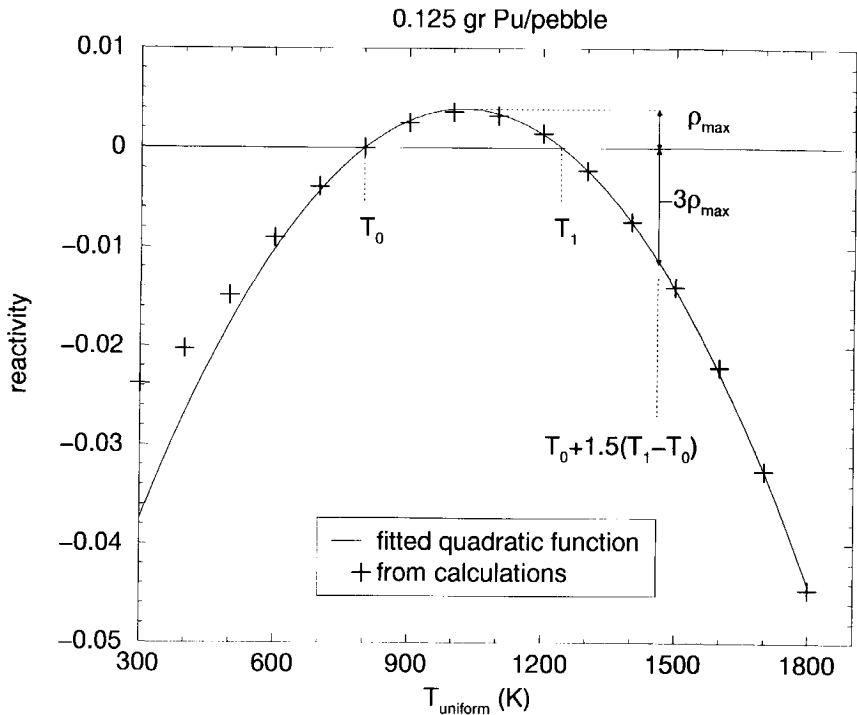


**Figure 4.24:** The reactivity of a bare core, with a homogeneous temperature distribution, consisting of fresh pebbles with 0.125 g Pu/pebble contained by coated particles with concentrated 220  $\mu\text{m}$ -diam kernels. A temperature-independent nonleakage probability of 0.65 is assumed so that  $\rho = (k_{\text{eff}} - 1)/k_{\text{eff}}$  with  $k_{\text{eff}} = 0.65 \cdot k_{\infty}$ . The '+'-symbols are the reactivity values that were calculated from the  $k_{\infty}(T_u)$ -data from fig. 4.19 (zero burnup). The curve is obtained via a fit with a 2<sup>nd</sup>-order function. At  $T_0 = 800$  K the reactor finds itself in an instable equilibrium.

implies that the reactivity of such a reactor can not be described simply as a function of temperature, but has to be calculated by solving the eigenvalue equation (transport or diffusion) for the full core, using cross sections that vary locally with burnup and temperature. Moreover, an HTR has relatively small 'neutronic' dimensions (the ratio of core radius to migration length is relatively small), which means that the reflectors contribute significantly to the slowing-down process. This implies, at least for slow temperature changes, that the positive temperature coefficient of the reflectors might play an important role too.

#### 4.4.7 Autonomous reactor shutdown from an instable equilibrium after complete loss of cooling

In view of inherent or passive safety, a reactor should be able to endure a loss of cooling without achieving too high temperatures, even in case of failure of active control systems.

This can be realised if the reactor shuts itself down due to a negative temperature feedback of reactivity. Refs. [88, 89] gave an analysis of a Loss Of Cooling Without Scram (LOCWS) on the basis of a space-independent reactor model, where the reactivity was presented as a linear function of the temperature. It was shown that if a *complete* loss of cooling is assumed and, moreover, if xenon and decay heat dynamics are neglected, the amount of energy deposited during the transient can be calculated analytically. Consequently, the asymptotic temperature increase can be derived from the produced energy and the reactor's heat capacity.

Below, we will carry out the same exercise, but now for a point-reactor having a temperature feedback of reactivity that corresponds to an HTR with 0.125 g Pu/pebble. Fig. 4.24 shows that for  $T > T_0$  the reactivity can nicely be fitted by a quadratic function of the temperature, which reads

$$\rho(T) = -\frac{4\rho_{max}}{(T_1 - T_0)^2} (T - T_0)(T - T_1) , \quad (4.16)$$

where the parameters  $T_0 = 800$  K,  $T_1 = 1240$  K and  $\rho_{max} = 0.0039$  are depicted in fig. 4.24. Before the transient commences, the reactor finds itself in the instable equilibrium at  $T = T_0$ , where  $\rho(T_0) = 0$  and  $\frac{d\rho}{dT}(T_0) > 0$ . During the transient the temperature increases and the system becomes supercritical which has a power excursion as a consequence. At  $T = (T_0 + T_1)/2$  the reactivity is maximal and amounts to 0.0039, which corresponds to prompt-criticality since  $\beta = 0.3\%$ . For  $T > T_1$  the system becomes subcritical, which causes the power to decrease again.

The dynamics of the point-reactor will be described by the conventional point-kinetic equations in combination with a lumped parameter equation for the heat transport (also known as Newton's law of cooling, see e.g. p. 262 of [69]):

$$\frac{dP}{dt} = \frac{\rho - \beta}{\Lambda} P + \sum_i \lambda_i C_i , \quad (4.17)$$

$$\frac{dC_i}{dt} = \frac{\beta_i}{\Lambda} P - \lambda_i C_i , \quad (4.18)$$

$$C \frac{dT}{dt} = P - h(T - T_c) , \quad (4.19)$$

where

- $P$  = fission power (W)
- $\beta$  = effective delayed neutron fraction
- $\beta_i$  = effective delayed neutron fraction of the  $i$ 'th group of delayed neutron emitters
- $\Lambda$  = neutron generation time (s)
- $C_i$  = delayed neutron emitter population (in power units) (W)
- $C$  = heat capacity of reactor (J/K)
- $\lambda_i$  = decay constant of the  $i$ 'th group of delayed neutron emitters ( $s^{-1}$ )
- $h$  = overall heat transfer coefficient (W/K)
- $T$  = pebble-bed temperature (K)
- $T_c$  = effective coolant temperature (K)

At  $t = 0$  a complete loss of cooling is assumed ( $h = 0$ ), which means that the core heats up

adiabatically. Eq. 4.19 shows that the temperature in that case can be expressed as

$$T(t) = T_0 + \frac{1}{C} \int_0^t P(\tau) d\tau, \quad (4.20)$$

where it has been taken into account that the temperature equals  $T_0$  at  $t = 0$ . Inserting eq. 4.20 in eq. 4.16 and subsequently summing eq. 4.17 and eqs. 4.18, yields

$$\frac{dP}{dt} + \sum_i \frac{dC_i}{dt} = -\frac{4\rho_{max}}{\Lambda C^2(T_1 - T_0)^2} \left\{ \int_0^t P(\tau) d\tau \right\} \left\{ \int_0^t P(\tau) d\tau - C(T_1 - T_0) \right\} P(t). \quad (4.21)$$

Integrating this equation from time zero to time infinity and taking into account the equilibrium conditions for the delayed neutron emitters, yields

$$E_\infty^2 \left( E_\infty - \frac{3}{2} C(T_1 - T_0) \right) = \frac{3C^2(T_1 - T_0)^2}{4\rho_{max}} \left( \Lambda + \sum_i \frac{\beta_i}{\lambda_i} \right) P_0, \quad (4.22)$$

where  $P_0$  is the reactor power before the transient and  $E_\infty = \int_0^\infty P(\tau) d\tau$ , i.e. the total energy produced during the transient. For the asymptotic temperature increase  $\Delta T (\equiv T_\infty - T_0)$  we obtain

$$\Delta T^2 \left( \Delta T - \frac{3}{2} (T_1 - T_0) \right) = \frac{3(T_1 - T_0)^2}{4\rho_{max}} \left( \Lambda + \sum_i \frac{\beta_i}{\lambda_i} \right) \frac{P_0}{C}, \quad (4.23)$$

which reveals that the ratio of the nominal power to the heat capacity, the kinetic parameter  $\beta/\lambda$  ( $\Lambda$  is negligible) and  $\frac{\rho_{max}}{(T_1 - T_0)^2}$  are the relevant parameters for safety.

Eqs. 4.22 and 4.23 reveal that there are lower limits for the produced energy and for the asymptotic temperature, and a corresponding upper limit for the shutdown reactivity, that read

$$E_\infty \geq \frac{3}{2} C(T_1 - T_0), \quad (4.24)$$

$$\Delta T \geq \frac{3}{2} (T_1 - T_0), \quad (4.25)$$

$$\rho_\infty \leq -3 \rho_{max}. \quad (4.26)$$

These quantities become equal to their boundary values if  $P_0 = 0$ . The boundary values for the asymptotic temperature (i.e.  $T_0 + \frac{3}{2}(T_1 - T_0)$ ) and reactivity ( $-3\rho_{max}$ ) are depicted in fig. 4.24. In the zero-power case ( $P_0 = 0$ ), we obtain for our model HTR an asymptotic temperature of  $T_\infty = 1460$  K and a shutdown reactivity of  $\rho = -0.0117$ . On the other hand, adopting from ref. [89] typical HTR parameters that read  $P = 200$  MW and  $C = 100$  MJ/K, and having  $\sum_i \beta_i/\lambda_i = 0.038$  s and  $\Lambda = 9 \cdot 10^{-4}$  s for the plutonium fuel, makes the RHS of eq. 4.23 equal to  $2.83 \cdot 10^6$  K<sup>3</sup> and hence yields an asymptotic temperature that is only slightly higher, namely  $T_\infty = 1466$  K =  $1193$  °C. This temperature is well below the presumed limit of  $1444$  °C for Pu-bearing CPs as listed in table 2.5.

#### 4.4.8 Conclusions as concerns temperature reactivity effects

For pebbles with  $2^{(1-n)}$  gr Pu/pebble with  $n = 0, 1, \dots, 7$  burnup calculations were performed. At burnup values of 0, 100, 200, ..., 700 MWd/kgHM branching calculations



were carried out. In these branches the uniform temperature ( $T_u$ ), the moderator temperature ( $T_M$ ) and the fuel temperature ( $T_F$ ) were separately varied from 300 to 1800 K with steps of 100 K.

The main result of these calculations reads:

- For cases with different Pu loadings and different burnup values,  $k_\infty(T_u)$ -curves with a single maximum were found. These curves correspond to uniform-temperature coefficients (UTCs) that decrease with increasing uniform temperature ( $T_u$ ) from a positive to a negative value.

In addition to that, other phenomena that could be observed, are:

- Only the under-moderated cases of (0.25 g Pu; 0 MWd/kgHM), (0.5 g Pu; 0 MWd/kgHM), (1 g Pu; 0, 100, 200 MWd/kgHM) and (2 g Pu; 0, 100, ..., 500 MWd/kgHM) yield a UTC that is negative for the entire temperature range (fig. 4.19).
- The positions of maxima of the  $k_\infty(T_u)$ -curves decrease with increasing Pu-loading (fig. 4.19).
- The difference between the reactivity at  $T_u = 300$  K and the maximum reactivity, signifying a reactivity surplus, can amount to +130 \$.
- The moderator temperature coefficient (MTC) is in general much larger than the fuel temperature coefficient. The MTC can vary strongly with moderator temperature. For example, a Pu-loading of 0.0625 g Pu/pebble yields  $-11 < \text{MTC} < +17$  (pcm/K) at a burnup of 0 MWd/kgHM, and  $-25 < \text{MTC} < +60$  (pcm/K) at a burnup of 400 MWd/kgHM within the temperature range of  $300 \text{ K} < T_M < 1800 \text{ K}$ .
- At zero burnup,  $\frac{1}{\beta} \frac{df}{dT_M}$  is basically responsible for the positive MTC at low temperatures, while the negative  $\frac{1}{\rho} \frac{d\rho}{dT_M}$  provides for a negative MTC at high temperatures. With increasing burnup,  $\frac{1}{\eta} \frac{d\eta}{dT_M}$  becomes positive for a large temperature interval, which gives rise to an even stronger positive MTC.
- The negative MTC at high moderator temperatures can be attributed to an increased absorption of neutrons by the 1-eV resonance of  $^{240}\text{Pu}$  and to an increase of the capture-to-fission ratio of  $^{241}\text{Pu}$  with increasing temperature.
- The fuel temperature coefficient becomes less negative with increasing fuel temperature and with increasing Pu-loading. The FTC is smaller (in absolute sense) than -4 pcm/K. It does not change by more than 1 pcm/K, within the burnup range of 0 to 600 MWd/kgHM.

## 4.5 Conclusions

Inherent safety requires that the temperature in an HTR should not exceed the maximally allowable value under any conceivable circumstances. This should happen on the basis of the laws of nature, implying that no human interference or supply of external energy is needed to remain below this temperature. (See also section 2.1). Strictly speaking, a temperature coefficient that decreases from a positive value to a negative value with increasing temperature does not mean beforehand that the inherent safety of the system is violated. Section 4.4.7 illustrates by means of a simple space-independent model that the temperature of a hypothetical reactor, with a temperature coefficient that decreases from a positive

value to a negative one with increasing temperature, stays below the maximally permissible temperature in the case that the reactor suffers a complete loss of cooling. However, the presented analysis of such a reactor is rather academic; from the practical point of view a negative temperature coefficient of reactivity over the entire temperature range is required.

The strongly under-moderated pebble configurations with 1 and 2 g Pu/pebble show negative uniform-temperature coefficients over the entire temperature range, up to a high burnup. Therefore, these configurations seem viable candidates as fuel for a reactor. However, a negative temperature coefficient itself does not guarantee that the temperature stays within safe limits under any conceivable situations. To ensure that the temperature remains below the maximally permissible values and thus demonstrating the reactor's inherent safety, extensive transient studies are compulsory. Chapter 5 describes the properties of a pebble-bed type HTR that is fuelled with pebbles of 1 and 2 g Pu/pebble. To verify whether this design is inherent safe under certain loss-of-cooling scenarios detailed dynamic studies will be performed.

# Chapter 5

---

## Core Calculations

---

In the preceding part of this thesis, the results of cell calculations have been presented. These calculations embrace a variety of cases, viz. several Pu-mass loadings per pebble and different types of CPs. The most promising cases were selected for full core calculations. It has been shown that strongly under-moderated systems, with Pu mass loadings of 1 to 2 g per pebble, yield negative moderator temperature coefficients over a broad temperature range. Only for high burnup values and low temperatures, the moderator temperature coefficient can become positive. Moreover, these systems yield  $k_{\infty}$ -evolutions for which a reasonable burnup, say up to 600 MWd/kgHM, seems feasible. These findings lead to the choice to regard only Pu-loadings of 1 and 2 g/pebble in the full core calculations. As far as the type of CP is concerned, systems with 2 g Pu/pebble contained by *diluted* CPs yield a  $k_{\infty}$  that increases with increasing burnup, while systems with the same amount of Pu but contained by *concentrated* CPs yield a decreasing  $k_{\infty}$  with increasing burnup. Since the latter  $k_{\infty}$ -evolution seems most practical in view of the fuel scenario that will be applied, the *concentrated* CPs were selected for the full-core calculations. In order to restrict ourselves, the *concentrated* CP with a 220  $\mu\text{m}$  diameter kernel was regarded only.

It should be noted that the described properties of the fuel were obtained from calculations based on an infinite system or, more precisely, on a unit cell with a reflecting boundary. Whether similar properties occur in a finite reactor with graphite reflectors remains to be seen, since leakage and enhanced moderation by the reflectors will affect the system.

The reactor concept and fuel scenario for a plutonium burning HTR (HTR-Pu) were adopted from the conceptual design of a small  $\text{UO}_2$ -fuelled HTR, which was introduced in the framework of a Dutch nuclear programme. This programme embraces the development of a modular HTR based on proven technology and dedicated to the co-generation of heat and power. The latest design of the Dutch HTR is called ACACIA (AdvanCed Atomic Cogenerator for Industrial Applications [23]), which is a 40  $\text{MW}_{\text{th}}$  reactor that is coupled to a direct-cycle, closed-loop, helium power turbine [90]. The ACACIA core concept is primarily based on the PAP20 design of Forschungszentrum Jülich [42, 91]. The reactivity decrease during operation is compensated by continuously adding fresh fuel pebbles on top of the pebble bed. At Begin Of Life (BOL), only the lower part of the core is occupied by the pebble bed, and at End Of Life (EOL) the core is completely filled with pebbles. At

EOL the core is discharged and thereafter a new batch will commence. The described fuel scenario is referred to as the PAP principle, which is the acronym for the French *Peu à Peu* (little by little).

At NRG, full core calculations have been performed for the ACACIA reactor [92] with the PANTHERMIX [93] code combination. The PANTHERMIX code combination was used for the full core calculations on the HTR-Pu, too. The properties of the code system will be explained in the course of the text.

Some important reactor parameters of the HTR-Pu (*viz.* thermal reactor power, helium in- and outlet temperature, helium inlet pressure and helium mass flow) were adopted from the ACACIA design. It should be stressed that these properties constitute only a first try, since no optimisation with respect to any parameter whatsoever has occurred yet. The approach in this early stage of the conceptual design of the HTR-Pu is to keep things as simple as possible. This means for instance that the use of burnable poison in the reflectors or in the pebbles was discarded and that a fuel scenario with more than one type of pebbles was avoided.

This study deals with the neutronics and thermal-hydraulics of the core and does not regard the energy conversion system. Nevertheless, we pose that a direct cycle, like in the ACACIA design [90, 94], has preference. Apart from the argument of a high efficiency ( $\varepsilon \approx 40\%$ ) due to the gas turbine in conjunction with the Brayton cycle there is a safety related reason. Since the mentioned Pu-loadings of 1 and 2 g/pebble form strongly under-moderated systems, water ingress into the core will cause a positive reactivity introduction [95, 96]. The ACACIA-design involves a Closed Cycle Gas Turbine (CCGT) system, with an intermediate helium circuit and a ternary system in which steam is produced [23, 97]. The purpose of the intermediate helium loop is to avoid ingress of water in the primary system. The intermediate loop is kept at a high pressure so that in case of a leak helium flows into the primary loop or into the steam circuit.

## 5.1 Reactor characteristics

Table 5.1 lists the main characteristics of the plutonium burning HTR. As mentioned before, the reactor power, helium pressures and helium temperature were adopted from the ACACIA conceptual design. The main difference between the HTR-Pu and ACACIA is the core volume. All dimensions in the radial direction were multiplied by a factor of 1.2, giving a core radius of 1.5 m, while the core height was increased from 4.5 m to 7.2 m. This has a longer batch time as a consequence, which means that the pebbles stay in the core for a longer time. Since in this case the fuel is exposed to a higher fluence, an enhanced burnup is expected.

Fig. 5.1 shows the geometry of the HTR-Pu. The initial core consists of a pebble bed with a height of 1.2 m and a cavity with a height of 6 m. The core is surrounded by radial and axial graphite reflectors.

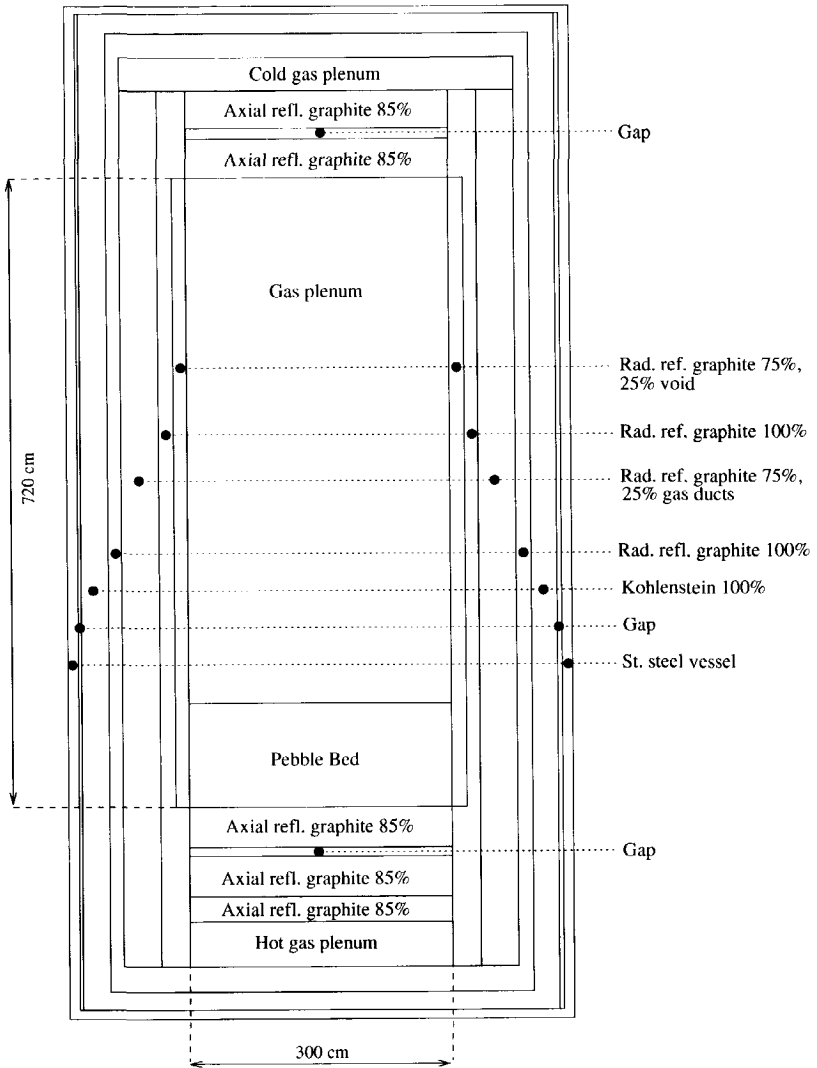


**Figure 5.1:** *Geometry of the HTR-Pu.*

**Table 5.1:** Main characteristics of the 40 MW<sub>th</sub> HTR Pu-burner

Thermal power [MW <sub>th</sub> ]	40.0
Heat leakage [MW <sub>th</sub> ]	0.6
Core radius [m]	1.5
Core height [m]	7.2
Pressure vessel height [m]	11.55
Pressure vessel inner radius [m]	2.77
Pressure vessel thickness [m]	0.12
Helium inlet temperature [°C]	495
Helium outlet temperature [°C]	800
Helium mass flow [kg/s]	25
Primary pressure [bar]	23.2
Maximum pressure loss over core [bar]	0.2
Pebble packing fraction	0.62

## 5.2 Nuclear data generation

The full core calculations were carried out with the PANTHERMIX code combination. PANTHERMIX combines the general purpose modular reactor code PANTHER and the HTR thermal hydraulics code THERMIX/DIREKT. PANTHER requires a nuclear data base containing nuclear data for all reactor materials, depending on irradiation, temperature, xenon density, etc.. The WIMS7B code was selected to generate such a database.

### 5.2.1 Pseudo reactor calculations with WIMS

The WIMS calculations involve two separate pseudo two-dimensional reactor models. The first model is a slab geometry, which is designated as the axial pseudo reactor. The geometry in the axial direction is modelled explicitly, while the geometry in the radial direction is taken into account by imposing a radial buckling.

The second model is a cylindrical geometry, which is designated as the radial pseudo reactor. This one is modelled explicitly in the radial direction while the geometry in the axial direction is taken into account by imposing an axial buckling.

Each reactor calculation starts with the generation of fine-group cross sections for the pebble bed with the adapted 172 group "1997" library as described in section 3.2.1. Fig. 5.2 shows the flow chart of the data generation for the purpose of PANTHER. The calculational steps of the pseudo axial reactor run are explicitly shown, while the supply of WIMS interface files of the radial run is only depicted by the parallelepiped. The structure of the radial reactor run is the same as the axial one, except that the WTHES(EUS) module is replaced by the WPROCOL module. Both pseudo reactor calculations start with calculations of fluxes and fine-group cross sections for the pebble bed by the following sequence: WHEAD (gets nuclear data from library and performs resonance shielding using equivalence theory), WPRES (prepares subgroup cross sections for <sup>239</sup>Pu, <sup>240</sup>Pu, <sup>241</sup>Pu and <sup>241</sup>Pu for the calculation of collision probabilities), WPROCOL (calculates collision prob-

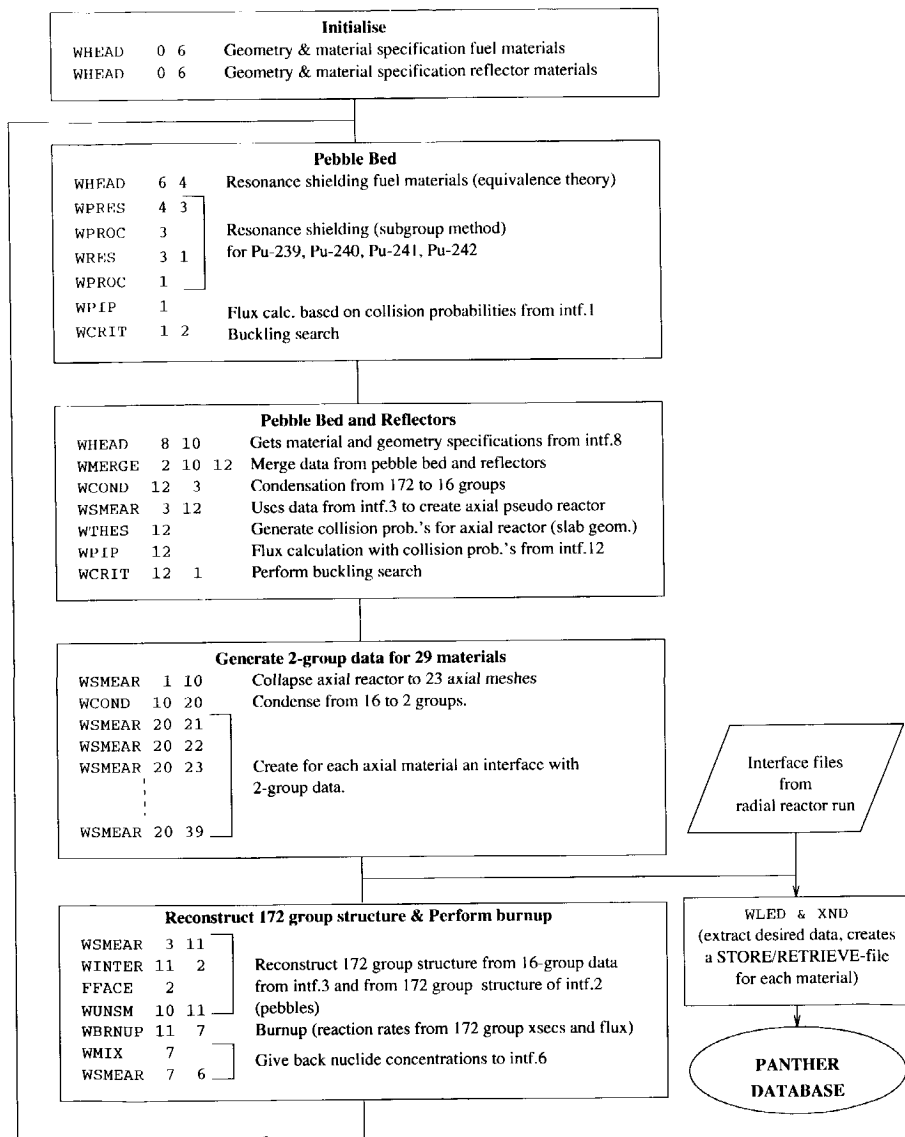


**Figure 5.2:** Flow chart of the pseudo axial reactor calculation. The structure of the pseudo radial reactor run is the same, except that WTHES(EUS) is replaced by the module WPROCOL that generates collision probabilities for the cylindrical geometry. The numbers after each module name indicate the read and written interface files ("intf."). The modules WLED and XND use the interface files with 2-group data of both the radial and axial run. They combine the data to generate a STORE/RETRIEVE (SR) file for each material. All SR-files constitute the PANTHER database.

abilities for grains in an annular cylindrical geometry), WRES (calculates group averaged resonance cross sections by the subgroup method), WPROCOL (reads macroscopic cross section and calculates again collision probabilities), WPIP (calculates 172 groups fluxes from collision probabilities and scatter cross section matrices). Subsection 3.2.1 gives a more detailed description of the preceding. After this calculation the data of the pebble bed are joined with those of the reflectors (WMERGE) and the cross sections are condensed to 16 groups (WCOND). WTHES(EUS) generates collision probabilities for all zones of the pseudo radial reactor, whereas WPROCOL does the same for the cylindrical geometry of the radial pseudo reactor. The collision probabilities are used for flux calculations by the module WPIP. The 16 group data of the complete pseudo reactor are smeared for a number of regions and condensed to two energy groups (energy boundary at 2.1 eV). The two-group data are stored on interface files from which the desired data will be extracted for the purpose of PANTHER's nuclear data base. After the flux calculation in the pseudo reactor geometry, the fine-group fluxes and cross sections are reconstructed by the module WUNSMEAR [98]. The new fine-group data have the same broad group dependence as the 16 groups data. However, within each broad group the fine-group structure from the previously mentioned WPIP-run is imported. The obtained fine-group data are passed on to the module WBRNUP, which performs the burnup for the fuel zone of the pseudo reactor. Finally, the calculated nuclide densities are given back to an interface file with which the complete calculation is repeated.

Two-group data is generated for 27 burnup steps up to 750 MWd/kgHM. The 'historical' temperature for which the burnup was performed equals 800 °C (i.e. average graphite temperature). The temperature of the fuel kernels was calculated according to eq. B.28. In order to attain temperature-dependent data for the fuel at a certain burnup, some branching calculations were done. In these branchings, the temperature of the pebbles was varied between room temperature and 1500 °C by 15 steps. In other branchings, the Xe-level was set to zero in order to obtain nuclear data in the absence of xenon. For each ("pseudo reactor", "burnup step" and "branching")-combination a WIMS interface file, containing two-group data for the entire pseudo reactor, is stored.



## 5.2.2 Providing data for PANTHER

The module WLED extracts from all interface files the desired information, and sets up a library consisting of so-called flat-files labelled by material name, number of the WIMS-run, burnup index and branching index. For instance, the flat-file "AXFUEL1.R.1.C.1.B.0" refers to the material AXFUEL1, which is the bottom layer of the pebble bed, of the first WIMS-run ("R.1"), of the first burnup cycle "C.1" and of branching "B.0" which is the main or so-called historical branch. These flat-files are not only created for fuel zones, but also for reflector zones.

The program XND (eXternal Nuclear Data function) collects all flat-files of the same material, subsequently filters and calculates the desired nuclear data and translates this into the Store/Retrieve (SR) format for the purpose of PANTHER. In this way, a SR-file is obtained for each material containing nuclear data as a function of burnup, temperature and zero or nominal Xe. The data for the axial bottom and top layer of the pebble bed are taken from the axial pseudo reactor run, while the data for the remaining part of the pebble bed is taken from the radial reactor run. For solving the two-group diffusion equation and performing burnup, PANTHER requires a set of 13 parameters. This set comprises the parameter "SCATTER", which is the down-scatter cross section accounting for scattering from the fast to the thermal group, as well as, for both groups, the radial diffusion coefficient "DR" (i.e.  $D_r$ ), the axial diffusion coefficient "DZ" (i.e.  $D_z$ ), the macroscopic absorption cross section "ABS", the macroscopic fission cross section "FIS", the macroscopic neutron production cross section "NUF" (i.e.  $\nu\Sigma^f$ ) and the power cross section "POWER" (i.e.  $\sum_i E_i \Sigma_i^f$  where the summation extends over all fissionable isotopes and where  $E_i$  is the energy yield per fission of nuclide  $i$ ).

## 5.2.3 Data generation for the purpose of time-dependent solutions in PANTHER

For the solution of the time-dependent diffusion equation other parameters, like the inverse neutron speed ( $1/v$ ) and the delayed neutron fractions, are calculated by means of the data from the WIMS interface files too. As XND appeared to calculate the delayed neutron fractions ( $\beta_{dg}$ 's) erroneously, they were calculated externally. This was done according to the formula that XND is supposed to use, published in the XND-chapter of the PANTHER manual [99], using the six-group delayed neutron data as recommended by [100]. The delayed neutron fractions for energy group  $g$  and delayed group  $dg$  were calculated according to

$$\beta_{g,dg} = \frac{\sum_i^{isotopes} v_{i,dg}^D \Sigma_{i,g}^f \Phi_g}{\sum_i^{isotopes} (\nu\Sigma^f)_{i,g} \Phi_g}, \quad (5.1)$$

where  $v_{i,dg}^D$  is the delayed neutron yield of isotope  $i$  in delayed group  $dg$ ,  $\Sigma_{i,g}^f$  is the macroscopic fission cross section of isotope  $i$  in group  $g$ ,  $(\nu\Sigma^f)_{i,g}$  the total neutron production cross section and  $\Phi_g$  is the flux in group  $g$ . We recall the delayed neutron yields of the main fissile isotopes in our fuel. Table 5.2 shows the decay constants  $\lambda$  and delayed neutron yields for each delayed group. Assuming total neutron yields of 2.865 for  $^{239}\text{Pu}$  and 2.932 for  $^{241}\text{Pu}$ , the delayed neutron fractions ( $\beta^{tot}$ ) become 0.22% and 0.55%, respectively.

**Table 5.2:** Decay constants and delayed neutron yields (neutrons/fission) for the main fissile isotopes, from [100].

Del. group	1	2	3	4	5	6	Total
$\lambda$ ( $s^{-1}$ )	0.0127	0.0320	0.128	0.304	1.35	3.63	
$\nu^D$ ( $^{239}\text{Pu}$ )	0.00023	0.00196	0.00097	0.00234	0.00070	0.00015	0.00635
$\nu^D$ ( $^{241}\text{Pu}$ )	0.00019	0.00413	0.00151	0.00655	0.00310	0.00051	0.01599

### 5.3 Neutronic and thermal-hydraulic core calculations with PANTHERMIX

The core calculations have been performed by the combined code system PANTHER-THERMIX/DIREKT (PANTHERMIX). Fig. 5.3 shows the flow chart of PANTHERMIX. The diffusion code PANTHER calculates the flux and power distribution for a given temperature profile. The power distribution is passed on to the thermal-hydraulics code THERMIX/DIREKT, which calculates for the given power distribution a temperature profile. The temperature profile is transferred to PANTHER again, from which the procedure is repeated until certain convergence criteria are met.

The cylindrical structure of the HTR is treated with an R-Z geometry in THERMIX/DIREKT. Since PANTHER does not have the possibility of using an R-Z geometry, the cylindrical geometry is approximated by a 3-D Hex-Z structure. In the axial direction, the meshes of both codes are constructed in such a way that they coincide. However, in the radial direction the geometries of the two codes are coupled through associating a set of hexagonal channels in the PANTHER model with a cylindrical ring of the same area in THERMIX/DIREKT. The word channel in this context should not be confused with a fuel bundle or something like that but must be interpreted as a term that refers the collection of hexagonal mesh volumes with the same  $(x, y)$ -coordinates in the calculational model. Fig. 5.4 shows that the THERMIX/DIREKT model is composed of 18 cylindrical rings that are associated with 18 sets of hexagonal channels of the PANTHER model. The THERMIX/DIREKT rings and the PANTHER hexagonal channels with thermal-hydraulic indices 1 to 10 constitute the core, whereas those indexed by 11 to 18 constitute the radial reflectors. The total power generated by all PANTHER hexagons with thermal-hydraulic index  $i$  in axial layer  $j$  is preserved when transferred to THERMIX/DIREKT.

Hereafter, both codes will be discussed separately.

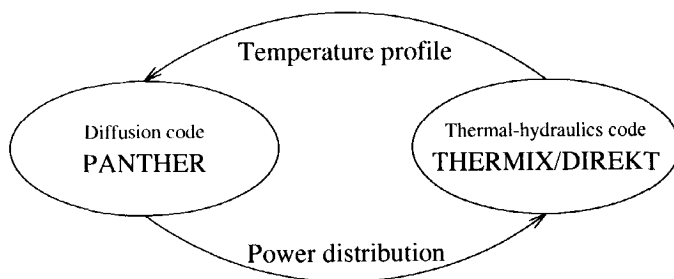


**Figure 5.3:** *The PANTHER-THERMIX/DIREKT interaction. The power distribution refers to the nuclear power only, implying that heat deposition by gamma's and fast neutrons in the reflectors is neglected.*

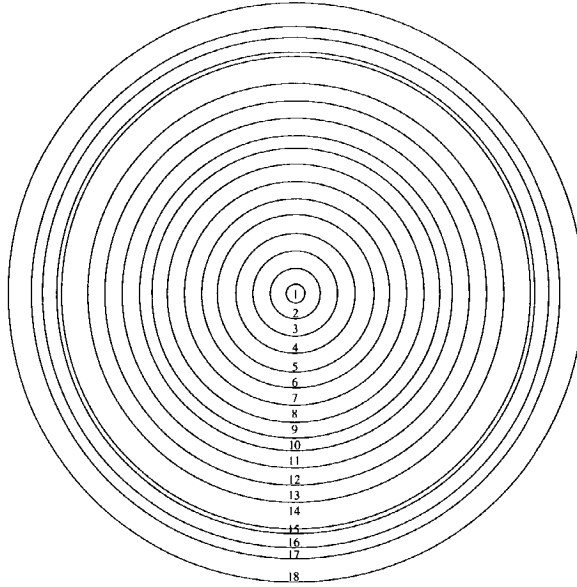
### 5.3.1 PANTHER

As mentioned before the cylindrical structure of the HTR is approximated by a 3-D Hex-Z structure in PANTHER. The validity of this approximation was tested in the framework of an MHTGR benchmark as described by ref. [101] (p. 84). First of all, the results of the PANTHER code were compared with those of the diffusion module SNAP of the WIMS code package, where an MHTGR was modelled with an Hex-Z geometry. Both codes were in excellent agreement, viz. differences in  $k_{eff}$  of less than 1 pcm. The results of the SNAP calculation with the Hex-Z model were compared to those of a SNAP calculation with an R-Z model, in which all material volumes were preserved. The agreement between the calculated  $k_{eff}$  for the Hex-Z and R-Z geometry was found to be quite close, viz. maximally 0.8% for the hexagons with sides of 10 cm. From this it was concluded that a cylindrical structure like an HTR can be approximated for neutronics purposes by a Hex-Z geometry. The HTR-Pu is modelled by 253 core channels, 576 reflector channels, 60 core Z-layers, 13 bottom reflector Z-layers and 11 top reflector Z-layers. Each hexagonal volume in the core has a side of 10.4 cm and a height of 12 cm.

#### Modelling the reactor

Each mesh volume in the PANTHER model contains a certain material that corresponds with a set of nuclear constants. For the solution of the steady-state diffusion equation PANTHER requires the previously mentioned set of 13 parameters, viz. "SCATTER", and, for both energy groups, "DR", "DZ", "ABS", "FIS", "NUF" and "POWER". These nuclear constants are generated by the PANTHER function *Constants Generation* through interpolation from a library of nuclear constants listed by material and tabulated against a number of dependencies. Besides the previously mentioned dependencies (temperature, burnup etc.) the nuclear data of the HTR-Pu is tabulated against the dependency "ROD-TYPE" which can adopt either the value "RODDED" or "UNRODDED". This dependency is normally used for a material whose nuclear constants depend on the presence or absence of a control rod. In case of a PWR assembly in which the control rod is partially inserted, the nuclear constants of the lower-part of the assembly correspond to the "UNRODDED" state, while those of the upper-part correspond to the "RODDED" state. The HTR-Pu

ANNULAR CYLINDRICAL GEOMETRY IN THERMIX/DIREKT



HEXAGON STRUCTURE IN PANTHER

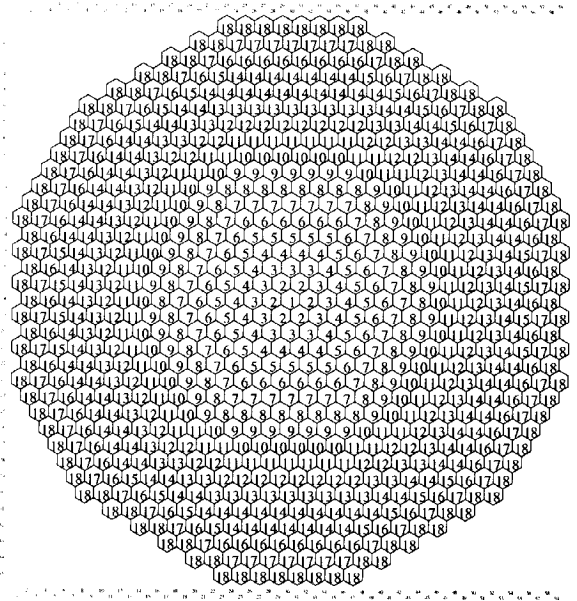


**Figure 5.4:** Coupling of the thermal-hydraulic mesh of THERMIX/DIREKT to the hexagon structure in PANTHER, based on volume conservation. An Annulus of the THERMIX/DIREKT-model corresponds to a set of hexagonal 'channels' with the same index in the PANTHER-model. Indices 1 to 10 refer to the core, while 11 to 18 refer to the reflectors.

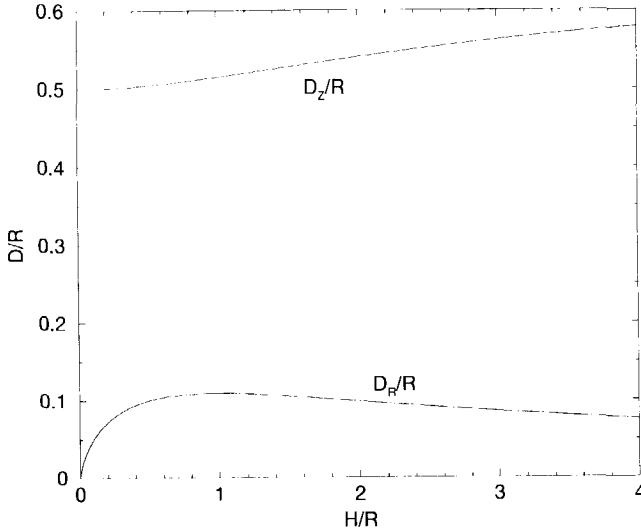


**Figure 5.5:** Normalised radial and axial diffusion constants as a function of  $H/R$  according to the equations of Gerwin and Scherer [102]. Here,  $H$  is the the height of the core cavity and  $R$  is the radius of the core.

model makes use of this principle in the following way. The "UNRODDED" state corresponds to that part of the core that is occupied by pebbles (i.e. the pebble bed), whereas the "RODDED" part corresponds to the core cavity. The height of the pebble bed in the PANTHER model can be enlarged continuously by withdrawing a notional bank of rods present in all channels of the core. The node that embraces the "rod tip" has nuclear constants that are flux-volume weighted averages of the "RODDED" and "UNRODDED" nuclear constants. Keeping temperatures and irradiations constant, the reactor can be made critical by performing a bank search, which represents an adjustment of the pebble-bed height.

### Treatment of core cavity with diffusion theory

Since PANTHER uses diffusion theory, difficulties are to be expected when treating the core cavity. Gerwin and Scherer [102] came up with a method that treats the cavity as a diffusion region with effective anisotropic diffusion constants ( $D_r$  and  $D_z$ ) and zero reaction cross sections. Fig. 5.5 shows the axial and radial diffusion coefficients ( $D_z$  and  $D_r$ ) normalised to the core radius ( $R$ ) as a function of  $H/R$ , where  $H$  is the cavity height. During burnup, the core remains critical by adding pebbles on top of the pebble bed. Obviously, the increase of the pebble-bed height involves a decrease of the cavity height. In the PANTHER model the effective diffusion constants of the core cavity are continuously recalculated with changing cavity height.

### Treatment of decay heat

The mesh power in the PANTHER model is calculated as the sum of the prompt power and the decay power. The decay power originates from the energy releases due to the decay of fission products, and their daughters, to stable elements. In the HTR-Pu PANTHER model the decay heat kinetics are described by 32 pseudo fission products with stable daughters. The pseudo fission product yields and decay constants were retrieved from 33-groups sets published by Tasaka *et al.* [103] (groups 22 and 23 were lumped in order to prevent negative yields). The pseudo fission product yields for both  $^{239}\text{Pu}$ ,  $^{240}\text{Pu}$  and  $^{241}\text{Pu}$  were taken into account. The decay heat kinetics obey the following equations

$$\frac{dP_{dj}}{dt} = \left( \sum_n a_{j,n} E_n \Sigma_{f,n} \right) \Phi - \lambda_j P_{dj}, \quad (5.2)$$

where

- $P_{dj}$  = decay power density of  $j$ 'th group of pseudo fission products ( $\text{W}/\text{m}^3$ )
- $n$  = index for nuclides (i.e.  $^{239}\text{Pu}$ ,  $^{240}\text{Pu}$  and  $^{241}\text{Pu}$ )
- $a_{j,n}$  = yield of  $j$ 'th group of pseudo fission products for fissile nuclide with index  $n$  ( $\text{s}^{-1}$ )
- $E_n$  = prompt energy release per fission (including contribution from capture) for the fissile nuclide with index  $n$  (J)
- $\lambda_j$  = decay constant of  $j$ 'th group of pseudo fission products ( $\text{s}^{-1}$ )
- $\Sigma_{f,n}$  = macroscopic fission cross section of fissile nuclide with index  $n$  ( $\text{m}^{-1}$ )
- $\Phi$  = flux (neutrons/ $\text{m}^2/\text{s}$ )

Note that the total decay heat power density can be obtained through a summation over all decay heat groups, i.e.  $P_d = \sum_{j=1}^{32} P_{dj}$  and that the total prompt power density ( $\text{W}/\text{m}^3$ ) reads

$$P_f = \sum_n E_n \Sigma_{f,n} \Phi. \quad (5.3)$$

In equilibrium, i.e. each pseudo fission product decay rate cancels its production rate, the time derivatives in each group  $j$  of eq. 5.2 can be set to zero. Assuming furthermore that there exists only one fissile nuclide (either  $^{239}\text{Pu}$ ,  $^{240}\text{Pu}$  or  $^{241}\text{Pu}$ ), eqs. 5.2 and 5.3 yield

$$\frac{P_d}{P_f} = \sum_{j=1}^{32} \frac{a_j}{\lambda_{dj}}, \quad (5.4)$$

which represents the decay-to-prompt power ratio. This ratio amounts to 0.056 for  $^{239}\text{Pu}$ , 0.062 for  $^{240}\text{Pu}$  and 0.070 for  $^{241}\text{Pu}$ . By way of comparison,  $^{235}\text{U}$  yields 0.072, which shows that the contribution of the decay power to the total power is somewhat smaller in plutonium fuelled systems. This seems advantageous with respect to decay heat removal, regardless whether this is after an intentional, active reactor shut-down or after an autonomous shut-down, e.g. triggered by a negative temperature coefficient in combination with a temperature increase due to a loss-of-cooling event. Fig. 5.6 shows the build-up of the total decay power, normalised to the total prompt power, as a function of the operation time. At time  $t = 0$ , the system switches from a zero power level to a constant prompt power level  $P_f$ . The curves in fig. 5.6 have been obtained through analytical integration of

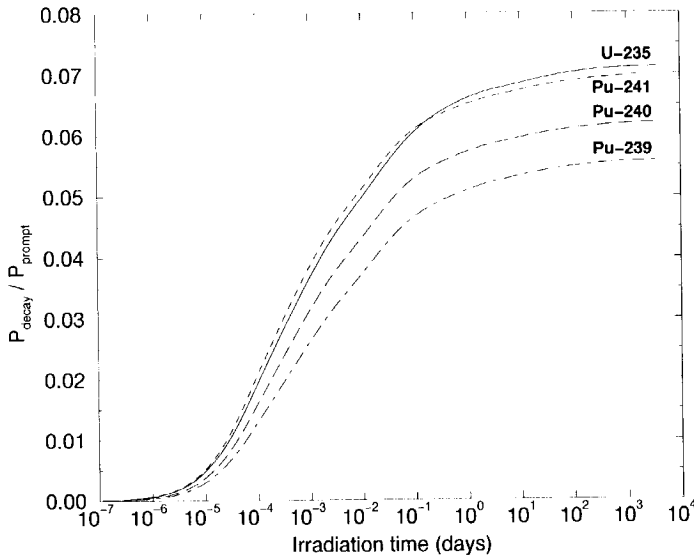


**Figure 5.6:** Decay-to-prompt power ratio as a function of time. At time  $t = 0$  the reactor is instantaneously switched from zero power to a constant prompt power level. (based on the 33-groups decay-heat data sets of Tasaka et al. [103])

eq. 5.2 for each decay heat group. Fig. 5.6 shows that after one day of operation the decay powers have already reached about 90% of their equilibrium values. Each curve of fig. 5.6 is based on a system with a single fissile nuclide. However, the fission rate in the HTR-Pu is determined by both  $^{239}\text{Pu}$  and  $^{241}\text{Pu}$  (81.5% by  $^{239}\text{Pu}$  and 18.2% by  $^{241}\text{Pu}$  at 0 MWd/kgHM ; 24.2% by  $^{239}\text{Pu}$  and 73.6% by  $^{241}\text{Pu}$  at 750 MWd/kgHM), which means that the build-up of the decay power lies between the curves of  $^{239}\text{Pu}$  and  $^{241}\text{Pu}$  in fig. 5.6.

### 5.3.2 THERMIX/DIREKT

The THERMIX/DIREKT [44] code is an improved version of the thermal-hydraulic code system THERMIX/KONVEK which was developed in the 1980s by the "Institut für Reaktorentwicklung" (nowadays ISR) of Forschungszentrum Jülich. The code system consisted of the programmes THERMIX (heat conduction and heat radiation applied to solid materials) and KONVEK (gas flow and heat transfer in void regions), and was suitable for the thermal-hydraulic simulation of high temperature reactors under normal operational conditions, as well as, for slow transients in high temperature reactors. However, as the code system appeared to have convergence problems when calculating gas velocities in the core cavity in case of nearly vanishing mass flows (natural convection), the existing iterative solution procedures for the pressure distribution and the gas-temperature distribution, were replaced by direct solution procedures (matrix elimination), which resulted in the DIREKT code.

The THERMIX/DIREKT code calculates the temperature distributions for the solid materials as well as for the gas from the nuclear power distribution supplied by PANTHER (see fig. 5.3). The obtained temperature distribution is transferred to PANTHER, which uses it to determine temperature-dependent cross sections. THERMIX/DIREKT uses an R-Z geometry, where the mesh in the radial direction corresponds to sets of hexagonal channels in the PANTHER model (see fig. 5.4) and where the Z mesh of the reactor is similar to that of PANTHER. The THERMIX mesh is composed of 16 Z-layers for the bottom reflector, 60 Z-layers of 12 cm for the core and 14 for the top-reflector, and of 21 mesh points in the radial direction. The DIREKT mesh is equal to that of THERMIX, except that three axial layers at the top and three at the bottom as well as the four outer radial meshes are stripped away. These meshes are not required for DIREKT, since they do not contain any gas.

Below, a concise overview of the calculational method of the THERMIX/DIREKT code is presented. Special attention is paid to options and parameters that were used in our model. However, for a more detailed description we refer to the THERMIX/DIREKT manual [44] as well as [104–106].

## THERMIX

THERMIX solves the heat conduction equation for the solid materials in the R-Z mesh. The mesh points are covered by all kind of material compositions. Each composition has its own (temperature-dependent) heat conductivity coefficient and specific heat capacity. In our model, the pebble bed is modelled as a homogeneous material, where an effective heat conductivity coefficient given by Zehner and Schlünder [44, 107] was used. This effective heat conductivity coefficient equals  $1 - \sqrt{1 - \epsilon_v}$  times the effective heat conductivity of the void plus  $\sqrt{1 - \epsilon_v}$  times the effective heat conductivity of the solid material, where  $\epsilon_v$  denotes the pebble bed void fraction (i.e. 0.38). The effective heat conductivity coefficient of the void is a function of the heat conductivity of the gas ( $\lambda_{gas}$ ) and a term which accounts for the heat transport through radiation ( $\lambda_{rad}$ ). The effective heat conductivity coefficient of the solid material is a function of  $\lambda_{rad}$ ,  $\lambda_{gas}$  and  $\lambda_{graph}$  and the so-called "Abflachung" (i.e. flattening of the pebble)  $a$ . The latter parameter, hard-coded in the THERMIX as 0.016 (dimensionless), accounts for the fact that the contact surface between the pebbles is not zero as it is if they would behave as exact 'mathematical' spheres. The  $\lambda_{graph}$  used in the calculational model was the one for irradiated A3-4 graphite [44], which signifies conservatism because of its relatively low value.

The boundary conditions imposed to the system embrace, on the one hand, a zero temperature gradient for meshes with  $R = 0$  and, on the other hand, fixed temperatures for the outer meshes that represent the air outside the reactor vessel, i.e. the ambient. Heat transport along the normal vector  $\hat{n}$  on the outer surface of the reactor vessel is given by Newton's relation

$$\lambda(T) \frac{\partial T}{\partial \hat{n}} = \alpha_H (T_{boundary} - T_{ambient}), \quad (5.5)$$

where  $T$  is the temperature,  $\lambda(T)$  is the heat conductivity coefficient for the material of the outer boundary (in our case the reactor vessel),  $\alpha_H$  is the heat transfer coefficient,  $T_{boundary}$  is the temperature of the boundary (vessel) and  $T_{ambient}$  is the fixed ambient temperature of 293 K. An  $\alpha_H \rightarrow 0$  signifies an adiabatic boundary condition which means that there is no



heat transfer from the boundary to the surroundings. In case of a complete loss-of-cooling incident this would imply that all heat accumulates in the reactor, since neither heat will be removed by the gas stream nor heat can leak away to the surroundings. In our model  $\alpha_H = 10 \text{ W m}^{-2} \text{ K}^{-1}$ , which results in a heat leakage of about 0.6 MW under normal operational conditions, i.e. 1.5% of the total thermal power.

## DIREKT

The DIREKT code solves time-dependent versions of the continuity equation (conservation of mass), the equation of motion (conservation of momentum) and the energy equation (conservation of energy) for the gas containing part of the mesh. These equations are solved in the following way. Firstly, the pressure field and thereby the mass flow field are calculated for a given gas temperature distribution through a combination of the continuity equation and the equation of motion. Secondly, the gas-temperature distribution is calculated for the precedingly determined pressure and mass flow fields by means of the energy equation. The distributions of gas temperature, pressure and mass flow are then brought into conformity with each other through outer iterations over these two steps. The interaction between the gas temperatures of DIREKT and the solid-state temperatures of THERMIX is established through a heat transfer term in the energy balance of DIREKT (p. 7 of [44]). This term reads

$$Q_H = \alpha_H^{sg} \cdot F_V \cdot (T_{solid} - T_{gas}), \quad (5.6)$$

where  $Q_H$  is the heat transferred per mesh volume from the solid material to the gas,  $F_V$  is the effective heat exchanging surface of the solid material per mesh volume,  $T_{solid}$  is the surface temperature of the solid material,  $T_{gas}$  is the gas temperature and  $\alpha_H^{sg}$  is the heat transfer coefficient from the solid material to the gas. The latter coefficient is derived from empirical Nusselt laws as functions of the local gas flow (Appendix C of [106]), both for the pebble bed and for gas conducting pipes.

The main boundary conditions that are imposed (under normal operation) to the system are a mass flow source of 25 kg/s at the helium inlet and consequently a mass flow sink of -25 kg/s at the helium outlet, a helium inlet temperature of 495 °C and a pressure outlet of 23 bar.

## 5.4 Calculational results regarding normal reactor operation.

This section presents the calculational results for the continuous operation of the HTR-Pu with the properties listed in table 5.1. As mentioned before, the core calculations were done for Pu-loadings of 1 and 2 g per pebble. Table 5.3 shows some important results for both Pu-loadings. As both Pu-loadings yield under-moderated systems, the lower Pu-loading of one gram per pebble yields a higher  $k_\infty$  at Begin Of Life (BOL). This means that a smaller pebble bed volume and hence a lower pebble-bed height is required to obtain a critical configuration. The calculations were ceased when the pebble-bed height reached 6.8 m, which corresponds to a core-cavity height of 0.4 m. Fig. 5.7 shows the pebble-bed height

**Table 5.3:** Two fuel loadings for the "Peu-à-Peu" HTR Pu-burner.

		1 gram/pebble	2 gram/pebble
Initial Pebble Bed Height	[m]	0.97	1.30
Final Pebble Bed Height	[m]	6.80	6.80
Batch time	[a]	11	22.8
HM inventory at BOL	[kg]	38	100
HM inventory at EOL	[kg]	96	182
Minor Actinides	[kg]	18	36
Am	[kg]	11	21
Cm	[kg]	7	15
Average burnup at EOL	[MWd/kgHM]	622	643
Maximum burnup at EOL	[MWd/kgHM]	721	740
Maximum xenon worth	[%]	2.2	1.6
Maximum power density	[W cm <sup>-3</sup> ]	11	9.2

as a function of operation time, expressed in Full Power Years (FPY), for both Pu-loadings. A reference burnup calculation with constant diffusion coefficients ( $D_r = 0.625$  m and  $D_c = 0.125$  m) showed a pebble-bed height that was 1% lower at BOL and 0.03% lower at EOL.

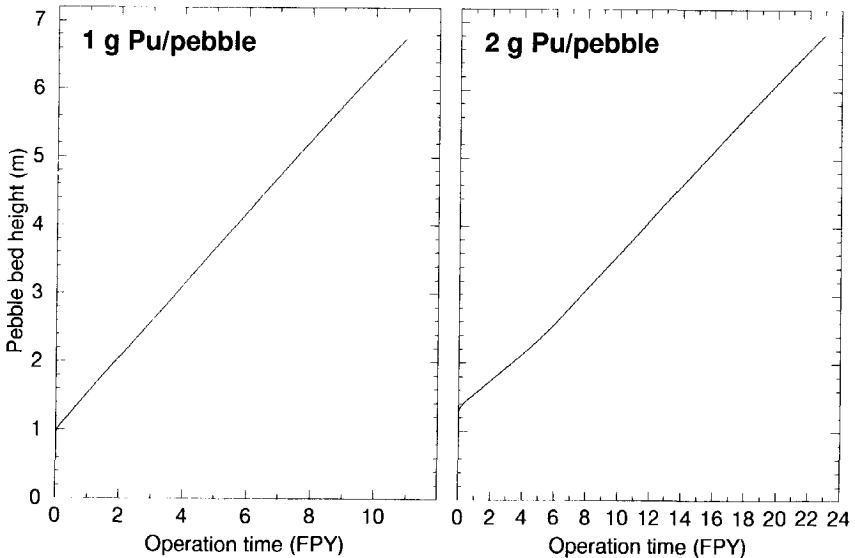


**Figure 5.7:** Height of the pebble bed as a function of the operation time, for the HTR-Pu with 1 and 2 g Pu/pebble. The virtual kink in the '2 g'-curve is most probably due to the swing-over over the axial power profile between 2 and 8 years of operation, as depicted in fig. 5.13.

### 5.4.1 Burnup

The batch time (i.e. the time from start-up to the time at which the pebble bed reaches the height of 6.8 m) is for the case of 1 gram/pebble 11 years. The Pu-loading of 2 g has obviously twice the amount of fuel per pebble and thus twice the amount of potentially available energy. Since the '2 g'-reactor attains a higher average burnup compared to the '1 g' reactor, its batch time becomes more than twice that of the '1 g'-reactor. The energy releases per fission mentioned in subsection 3.3.3 yield a relation between burnup in MWd/kgHM and Fissions per Initial Metal Atom (FIMA) that reads

$$\text{FIMA [\%]} = 0.1016 \cdot \text{BURNUP [MWd/kgHM]}, \quad (5.7)$$

which was obtained by linear regression. It shows that if all actinides would be fissioned (i.e. FIMA=100%) the burnup amounts to 984 MWd/kgHM. Furthermore, eq. 5.7 shows that the average burnup at EOL of 622 MWd/kgHM for the '1 g'-reactor and that of 643 MWd/kgHM for the '2 g'-reactor correspond to average FIMA values of 63.2% and 65.3%, respectively. The maximum burnups of 721 MWd/kgHM and 740 MWd/kgHM correspond to FIMA values of 73.2% and 75%, respectively. We recall that the capability of the CPs to attain burnups up to 740 MWd/kgHM while maintaining coating integrity has been demonstrated amongst others in the Peach Bottom irradiation tests (see p. 3-17 of [19]). Fig. 5.8 shows the maximum and average burnup as a function of the operation time for both both Pu-loadings. The average burnup indicates the burnup averaged over the entire pebble bed, whereas the maximum burnup refers to a mesh volume somewhere in the core at which the maximum burnup is found at time  $t$ . Fig. 5.9 shows the local burnup in the R-Z plane of the '1 g'-reactor at three points in time. At EOL, the largest part of the reactor (from 0 to 5.3 m) contains pebbles that have reached a burnup >600 MWd/kgHM, while the remaining part (from 5.3 m to 6.8 m) contains pebbles with burnups between 0 and 600 MWd/kgHM. The fuel pebbles of the first category are useless for a next fuel batch, but those of the second category might be used for the initial pebble bed of the next batch. This could be a subject for further investigations.

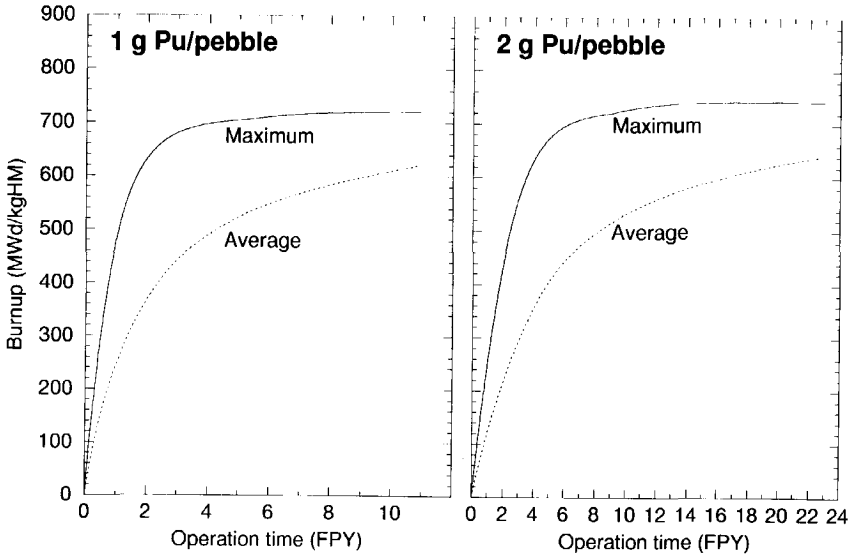
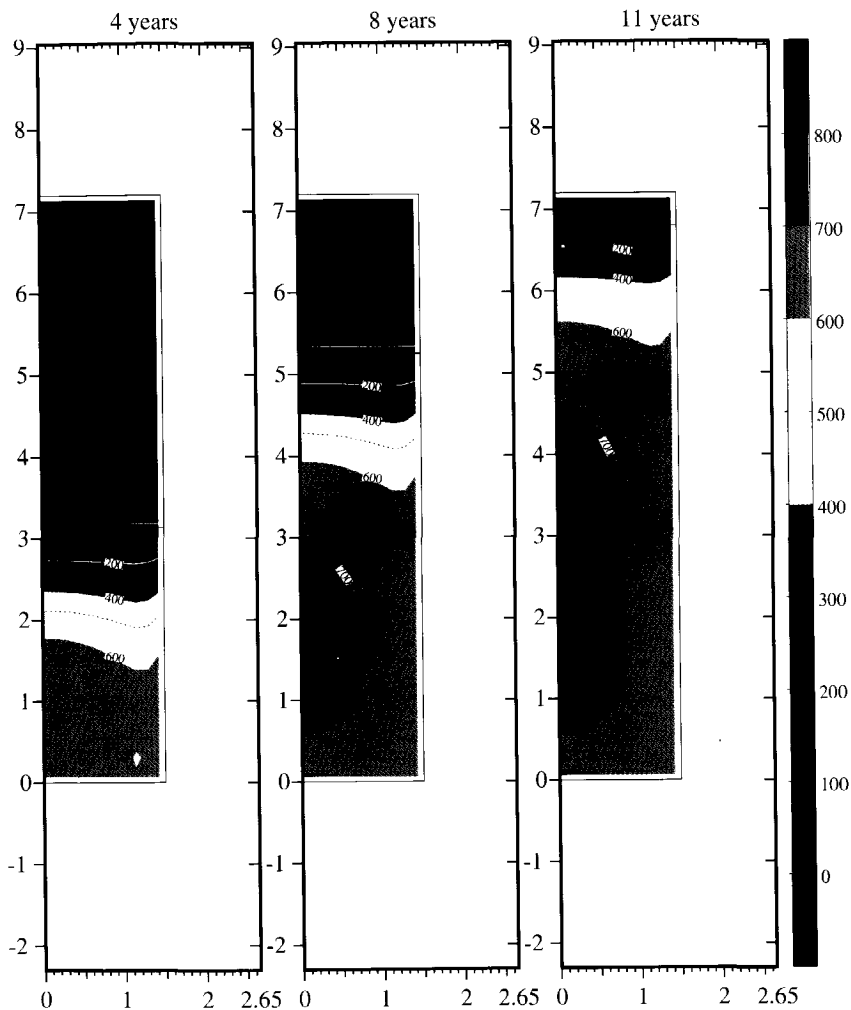


Figure 5.8: Maximum and average burnup as a function of the operation time, for the HTR-Pu with 1 and 2 g Pu/pebble.

## 5.4.2 Delayed neutrons

In the HTR-Pu, more than 97% of the fissions comes from  $^{239}\text{Pu}$  and  $^{241}\text{Pu}$ . For a fresh pebble, about 80% of the fissions are due to  $^{239}\text{Pu}$ , and about 20% of them are due to  $^{241}\text{Pu}$ . During burnup, the relative fission rate of  $^{241}\text{Pu}$  increases, while that of  $^{239}\text{Pu}$  decreases. At a burnup of about 675 MWd/kgHM, the relative fission rates of  $^{239}\text{Pu}$  and  $^{241}\text{Pu}$  are 13.5% and 85.8%, respectively. Beyond this burnup, the relative fission rate of  $^{239}\text{Pu}$  increases again, while that of  $^{241}\text{Pu}$  decreases. As both nuclides have different delayed neutron fractions ( $\beta = 0.22\%$  for  $^{239}\text{Pu}$ ;  $\beta = 0.55\%$  for  $^{241}\text{Pu}$ ), the total delayed neutron fraction (the  $\nu\Sigma_j$ -weighted average) varies with burnup. From 0 to 675 MWd/kgHM,  $\beta$  increases from 0.27% to 0.51%; for higher burnup values  $\beta$  decreases again. Fig. 5.10 shows the local delayed neutron fractions in the '1 g'-reactor at three points in time. The darkest shaded area corresponds with  $0.5\% < \beta < 0.55\%$ . Note that at 8 and 11 years this area largely coincides with the burnup interval of 600-700 MWd/kgHM in fig. 5.9. The burnup interval of 700-800 MWd/kgHM corresponds to a large extent with the  $\beta$ -interval of 0.45-0.50%, while the burnups between 500 and 600 MWd/kgHM also yield  $\beta$ 's in the 0.45-0.50% interval.

## Burnup (MWd/kgHM)



**Figure 5.9:** The local burnup in the '1 g'-reactor at three points in time. The maximum burnup amounts to 720 MWd/kgHM (see fig. 5.8).

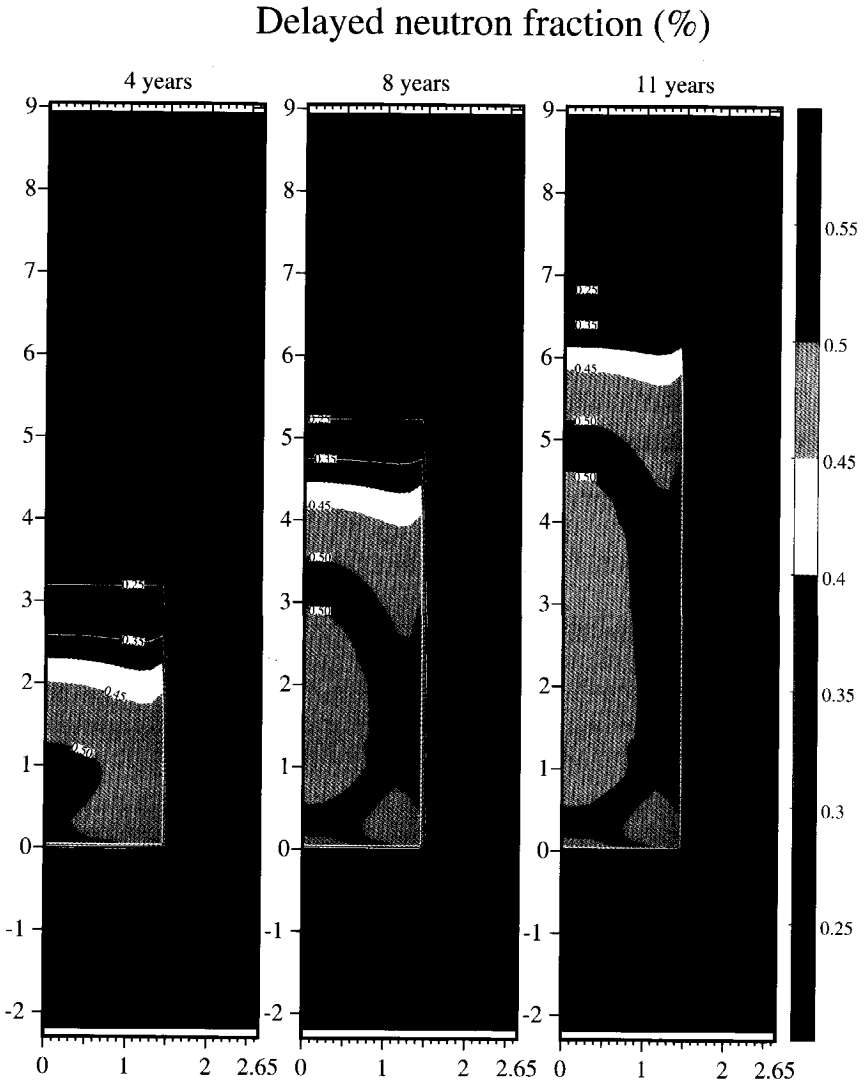


**Figure 5.10:** The local delayed neutron fraction ( $\beta$  in %) in the '1 g'-reactor at three points in time. The  $\beta$  increases from 0.27% at 0 MWd/kgHM to 0.51% at 675 MWd/kgHM, and decreases for higher burnup values. The  $\beta$  is calculated as the  $\nu\Sigma_f$ -weighted average of the  $\beta$  of  $^{239}\text{Pu}$  (0.22%) and that of  $^{241}\text{Pu}$  (0.55%).

### 5.4.3 Power density

During reactor operation, the integrity of the fuel elements should be warranted under all conceivable conditions. This means that the power generated in the pebble may not cause any thermal tensions (in both the tangential and radial direction) that exceed the maximally permissible ones ([28] p. 107 ff). According to p. 7 of [45] this results in a maximum power per pebble of 4.5 kW. As we have a stochastically packed pebble bed with a pebble fraction of 62%, this power corresponds with a power density of  $24.7 \text{ W/cm}^3$ . Fig. 5.11 shows that the maximum power densities of  $11 \text{ W/cm}^3$  for the '1 g'-reactor and  $9 \text{ W/cm}^3$  for the '2 g'-reactor stay well below the maximally allowed power density during the full period of operation. At BOL, the maximum power densities are obtained for the pebbles that are adjacent to the bottom reflector, which is illustrated for the '1 g'-reactor in fig. 5.12. As the bottom reflector provides for an enhanced neutron thermalisation (also coming into expression by a thermal flux peak in the reflector as will be seen later), most power is generated in the axial layer that is adjacent to the bottom reflector. Fig. 5.13 shows the axial power profile of the '1 g'-reactor in the course of operation. At BOL, the axial core layer with a thickness of 12 cm generates nearly 8 MW. In the first two years of operation the power profile changes rapidly, but beyond that period it stays more or less the same while it moves along with the top of the pebble bed. Between one and two years of operation, the 'active' core breaks away, so to speak, from the bottom reflector, which is also illustrated by the twist in the curve of the maximum power density in fig. 5.11. When the pebble-bed height increases the influence of the top reflector becomes increasingly perceptible, which leads to a gradual steepening of the power profile as depicted in fig. 5.13 and an increase of the maximum power density as illustrated by fig. 5.11.

#### Explanation of the sawtoothed curves

The sawtooth shape of the curves in fig. 5.11 can be ascribed to the discrete character of PANTHER's mesh in the axial direction. When the maximum power density is plotted as a function of the pebble-bed height it can be seen that the period of the sawtooth curve equals 12 cm, i.e. the axial mesh width. Physically, the maximum power density occurs in the pebble-bed's axial plane that is adjacent to the core cavity. In the calculational model, the axial position of this plane is imposed by the rod-tip position as described in sec. 5.3.1. The calculated power density is obtained through dividing the mesh power by the mesh volume. If the rod tip is just in a new axial mesh, this mesh has a lower power density than the neighbouring axial mesh below. However, if the rod tip is at about three quarters of the mesh, the calculated power density occurs in the top mesh and, moreover, increases with increasing pebble-bed height. The increasing parts of the sawtooth curve in fig. 5.11 refer therefore to the axial top mesh, that embraces the rod tip, while the decreasing parts refer to the mesh below this mesh.

### 5.4.4 Thermal-hydraulic properties

In respect of inherent or so-called passive safety, the power density must be such that for all operation and accident conditions the after-heat can be transferred to the environment by conduction, irradiation and natural convection, in such a way that the temperature never

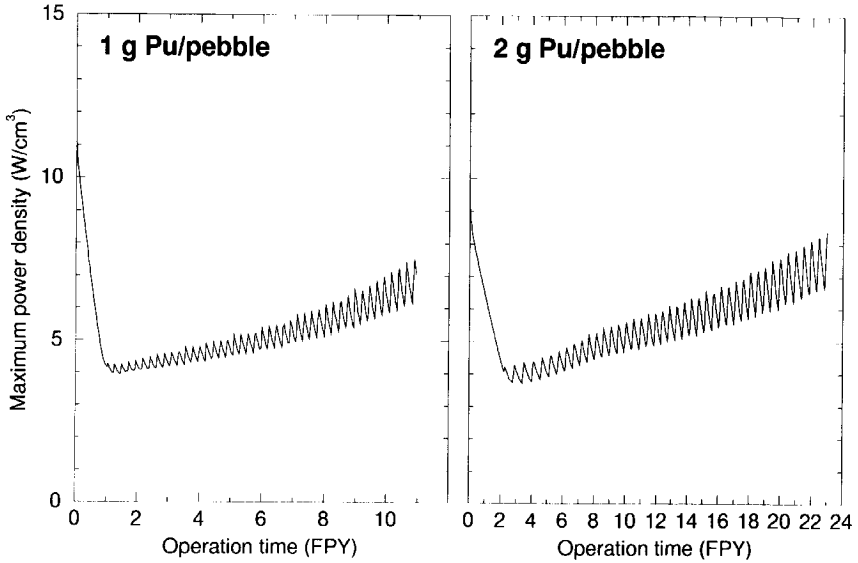


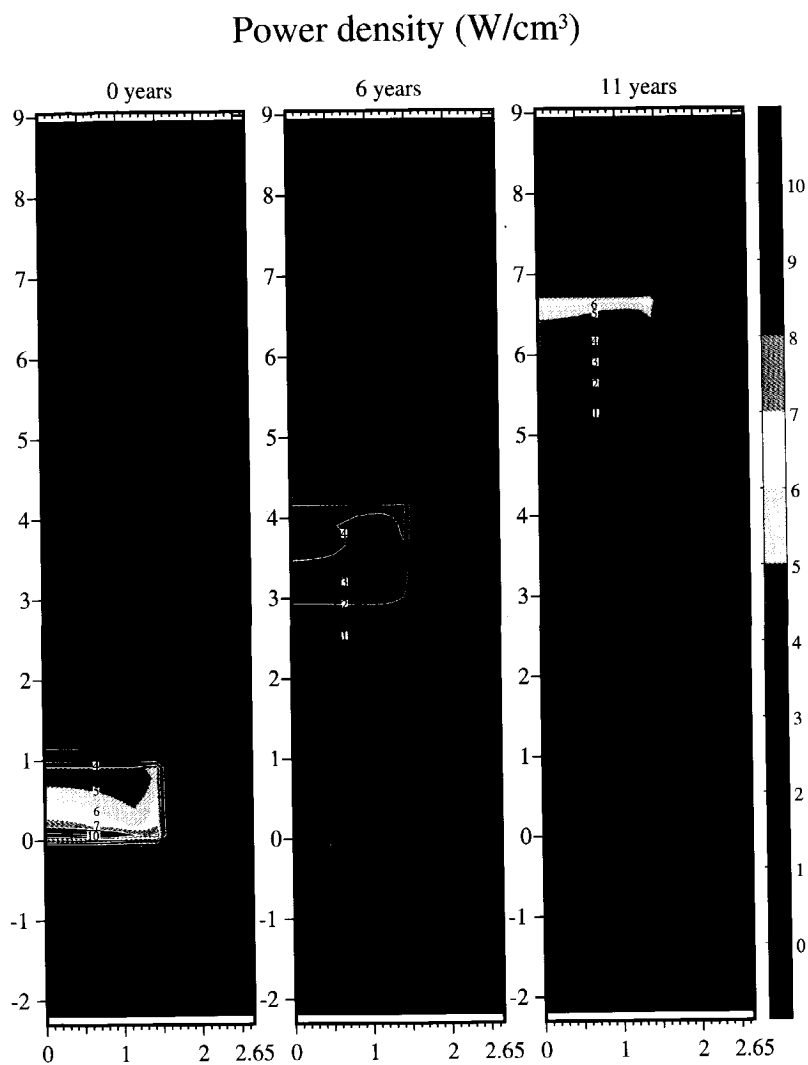
**Figure 5.11:** *The maximum power density as a function of the operation time, for the HTR-Pu with 1 and 2 g Pu/pebble.*

exceeds the temperature limit for the fuel elements. Nowadays, it is generally accepted ([28] p. 268) that no worth mentioning release of fission products from the pebbles is expected if the fuel temperature of the TRISO coated particles does not exceed 1600 °C (see also [47]). This holds for UO<sub>2</sub> bearing coated particles, but whether this holds for Pu-bearing CPs too is not clear yet. Section 2.5 reports that data about the performance of Pu-bearing CPs with high burnup values (737 MWd/kgHM) were only available for temperatures up to 1444 °C. To be conservative we presumed therefore a temperature limit for the Pu-CPs of 1444 °C (see table 2.5).

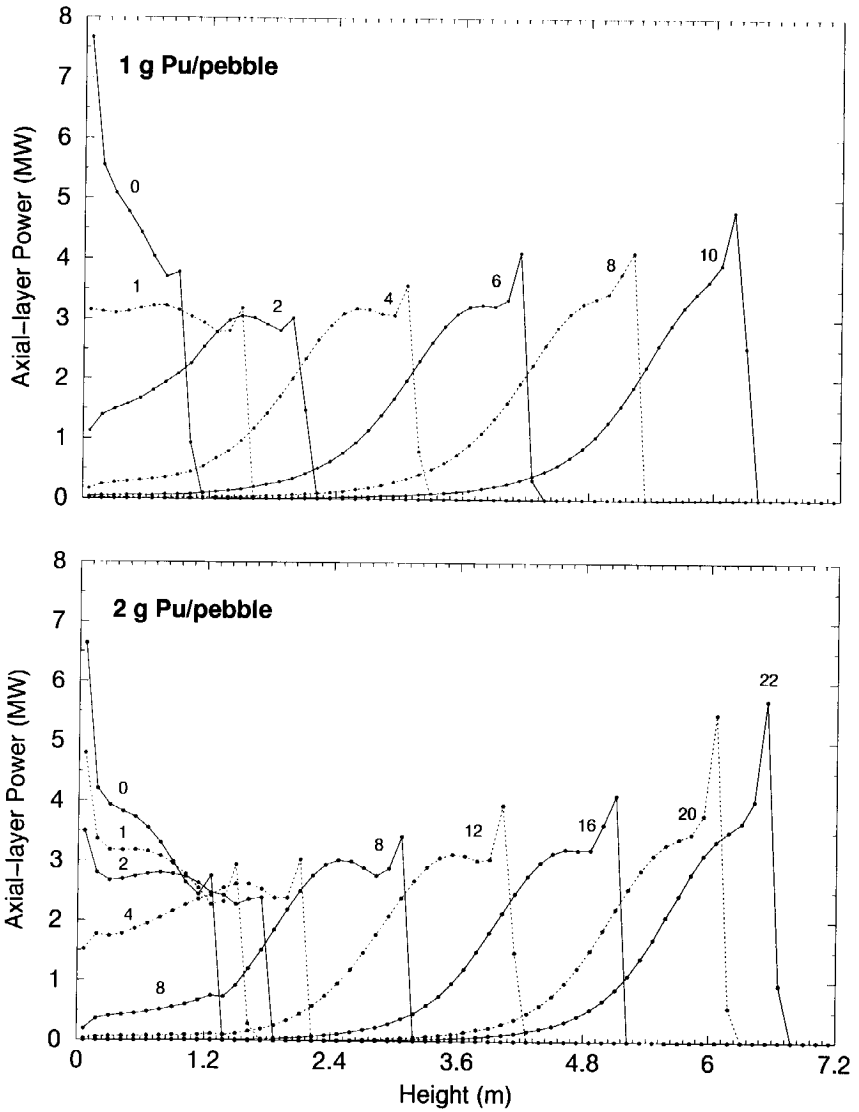
Fig. 5.14 shows that fuel temperatures read maximally 990 °C for the '1 g'-reactor and 940 °C for the '2 g'-reactor, which is well below the limit of 1444 °C. Fig. 5.15 shows for the '1 g'-reactor that the maximum temperature at BOL can be found just above the bottom reflector. The solid-material temperatures in the gas spaces are due to solid-material traces in the calculational model. The radial temperature profile of the pebble bed originates from a local peak in the power density close to the reflectors, which is visible in fig. 5.12 at 6 years of operation, in combination with the over-all temperature gradient due to the hot, power generating, part of the pebble bed next to the relatively cold reflectors.

Fig. 5.16 shows the corresponding helium temperatures. The gas source of 25 kg/s is positioned at the bottom of the vertical duct, from which the helium flows with an initial temperature of 495 °C in the upward direction. At the top, the flow is bended, after which the gas flows from the top of the core to the bottom. The gas heats up in the power generating part of the pebble bed. It is worthwhile to note that the helium gas is in thermal





**Figure 5.12:** The local power density ( $\text{W}/\text{cm}^3$ ) in the  $^1\text{g}^1$ -reactor at three points in time. The maximal power density of  $11.2 \text{ W}/\text{cm}^3$  occurs at  $t = 0$  in the  $z$ -layer adjacent to the bottom reflector.



**Figure 5.13:** The power (MW) generated in each z-layer of 12 cm thickness as a function of the axial position, with the operation time in full-power years as a parameter. Compare the power profiles to the R-Z contour plots of fig. 5.12. After  $\sim 1$  FPY for 1 g Pu/pebble and after 4-8 FPYs for 2 g Pu/pebble, the active core starts to 'break away' from the thermalising influence of the bottom reflector. Thereafter, the power profile remains about the same and translates with increasing pebble-bed height. However, the power profile gradually steepens up when the pebble bed approaches the top reflector. See also fig. 5.11.

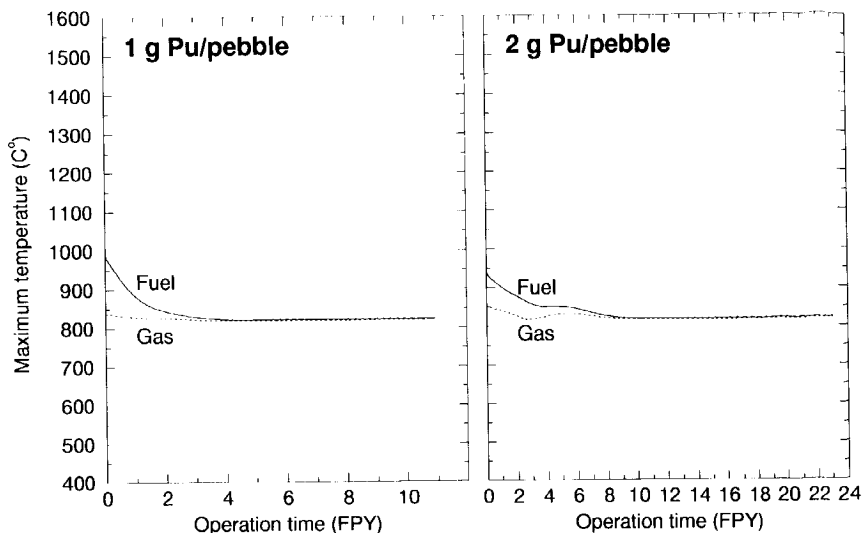


**Figure 5.14:** The maximum temperature of the fuel and the gas as a function of the operation time, for the HTR-Pu with 1 and 2 g Pu/pebble.

equilibrium with the solid material in that parts of the pebble bed where the power density is practically zero. The snapshots at 6 and 11 years of operation of figs. 5.15 and 5.16 illustrate this: the temperatures of the helium and the fuel match in the lower part of the pebble bed. The helium temperature at the outlet, which is below the bottom reflector, amounts to 800 °C .

### 5.4.5 Temperature and power coefficients of reactivity

During the reactor calculations, temperature coefficients of reactivity (for both the core and the reflector) and the power coefficient of reactivity were calculated. The temperature coefficients are defined as

$$\alpha = \frac{\partial \rho}{\partial T} \approx \frac{-\frac{1}{k_{eff}^{pert}} + \frac{1}{k_{eff}^{nom}}}{T^{pert} - T^{nom}} \quad [\text{K}^{-1}] \quad , \quad (5.8)$$

where  $k_{eff}^{nom}$  is the effective multiplication factor at nominal conditions (which is of course close to unity), while  $k_{eff}^{pert}$  is the perturbed one, and  $\Delta T = T^{pert} - T^{nom}$  is the temperature increase. If eq. 5.8 is used for the computation of the pebble-bed temperature coefficient, the temperature refers to the uniform-temperature, which implies that the temperature of the CPs and the graphite are simultaneously altered. The  $k_{eff}^{pert}$  is obtained from an eigenvalue calculation in which the temperatures of all meshes, either of the pebble bed or of the reflectors, were increased by  $\Delta T = 50$  °C , while all other quantities (xenon etc.) were kept equal.

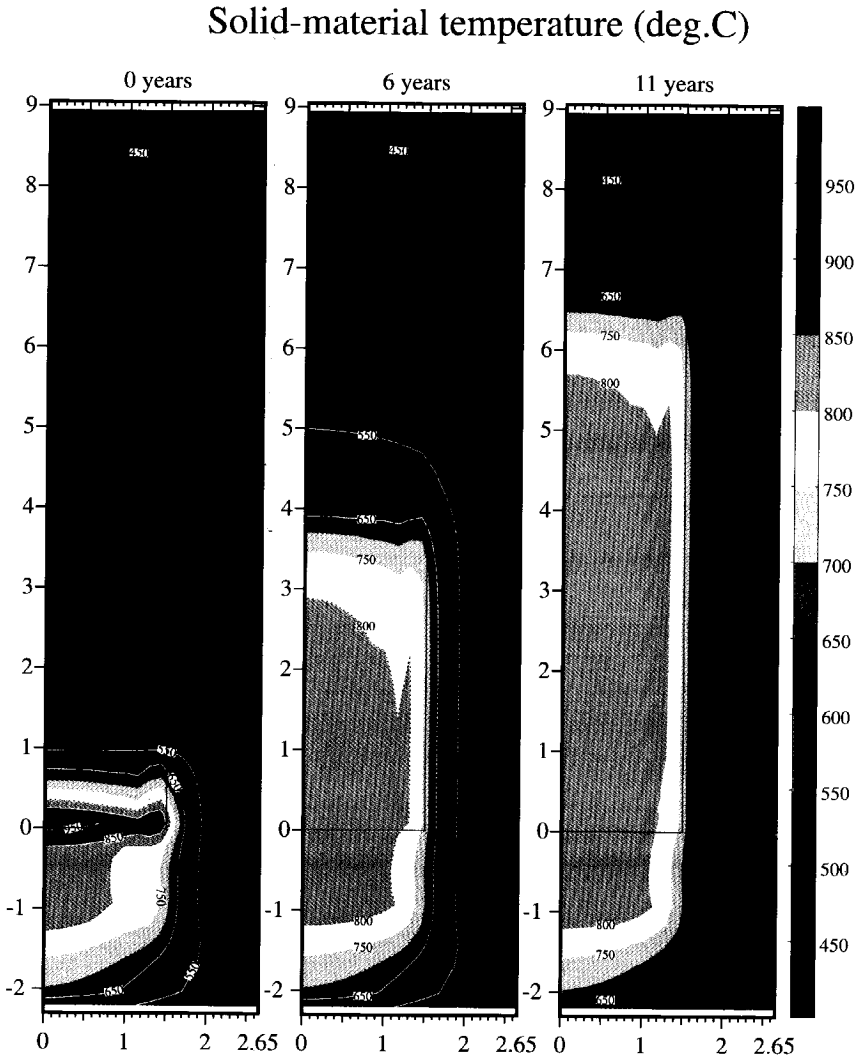


**Figure 5.15:** The temperature of all solid materials in the '1 g'-reactor at three points in time. The temperatures in the gas spaces are due to solid-material traces in the calculational model. The maximum temperature of 990 °C occurs in the core layer adjacent to the bottom reflector at  $t = 0$  (compare to fig. 5.14). Furthermore, note that the pebbles which do not generate any significant power, are in thermal equilibrium with the coolant. For example, the pebbles at the core bottom at  $t = 11$  years have the same temperature as the helium, i.e. 800 °C

## Helium temperature (deg.C)

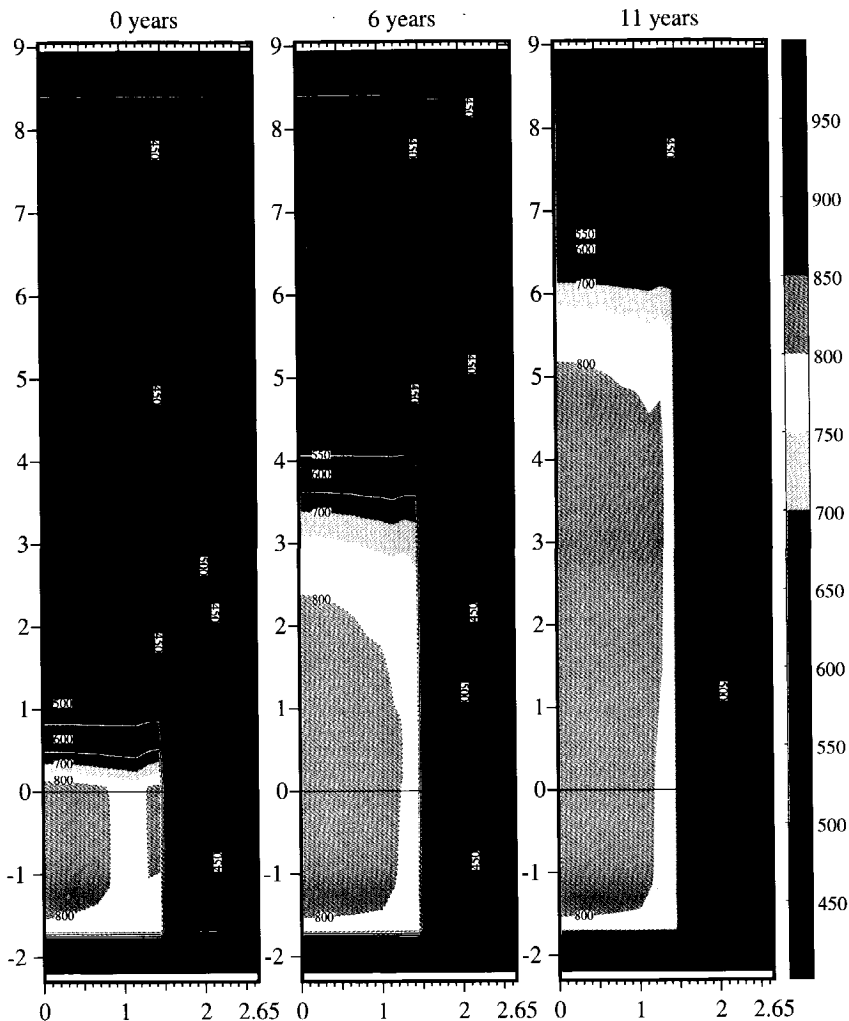


**Figure 5.16:** The helium temperature of the '1 g'-reactor at three points in time. The helium inlet temperature is 495 °C and the outlet temperature is 800 °C . The helium inlet is positioned at the bottom of the vertical duct; the helium flows from the bottom of the duct to the top. Thereafter, it flows from the top of the core, through the pebble bed to the outlet, beneath the bottom reflector.

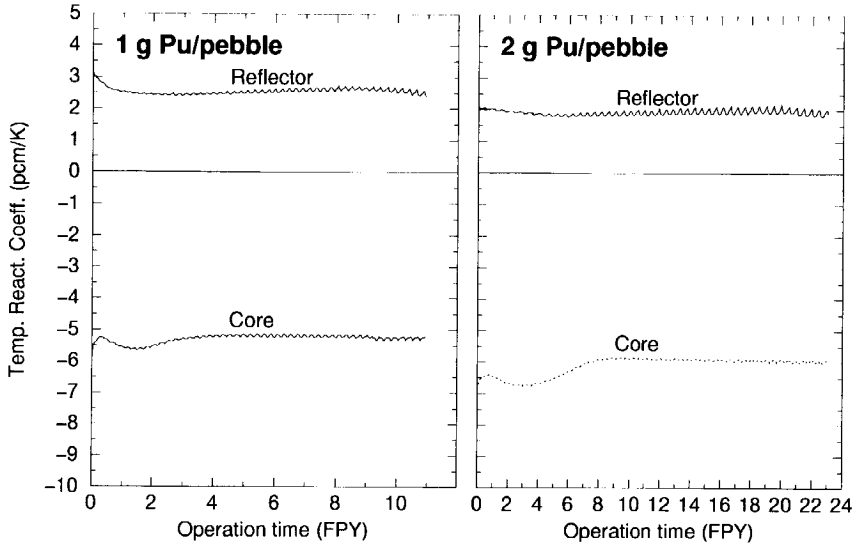


**Figure 5.17:** The temperature coefficients of reactivity for the core and the reflectors as a function of the operation time, for the HTR-Pu with 1 and 2 g Pu/pebble. The definition of the temperature coefficients is given by eq. 5.8.

The power coefficient was calculated as

$$\alpha_P = \frac{d\rho}{dP} \approx \frac{-\frac{1}{k_{eff}^{pert}} + \frac{1}{k_{eff}^{nom}}}{P^{pert} - P^{nom}} \quad [W^{-1}] \quad (5.9)$$

In the calculations, the fractional change of the power was 5%, which gives  $P^{pert} = 42$  MW. The perturbed  $k_{eff}$  was calculated for a new neutronic/thermal-hydraulic equilibrium, implying that flux, power distribution and temperature profile were recalculated, while the xenon distribution remained unaltered.

Fig. 5.17 shows that the temperature coefficients of the reflector are for both reactor configurations positive. If the temperature of the reflectors increases the thermal absorption rate of the graphite decreases, while the scattering rate does not change. This is due to the fact that the absorption cross section of graphite behaves as  $1/v$ , which leads to a decrease of the effective thermal-group cross section for absorption if the Maxwell spectrum shifts to higher energies, while the energy-independent scattering cross section remains constant. This implies that the probability for a neutron of being absorbed in the reflector decreases, while consequently the probability of being scattered back into the core increases with increasing reflector temperature.

As far as the temperature coefficients of the core are concerned, the '2 g'-reactor shows a slightly stronger negative coefficient because of the harder spectrum (see also fig. 4.19). Fig. 5.18 shows the power coefficient of reactivity according to eq. 5.9 (in units of pcm/MW) for both Pu-loadings.

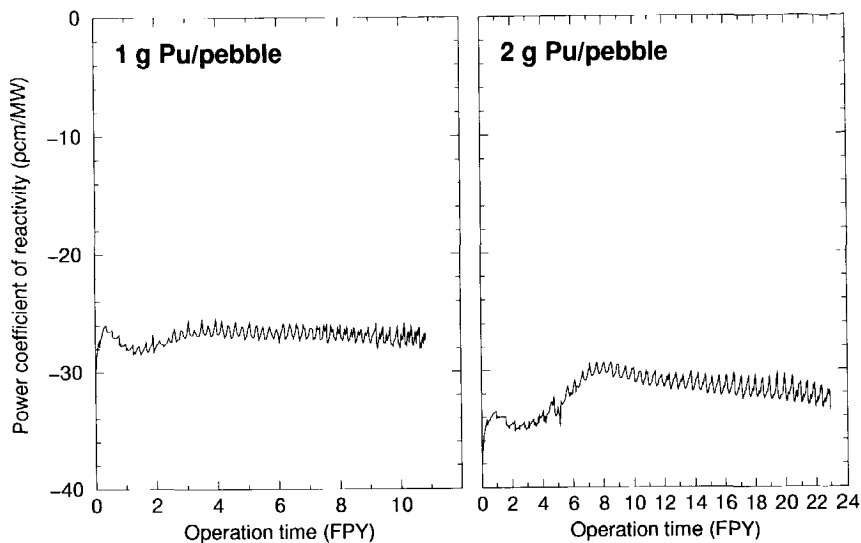


**Figure 5.18:** The power coefficients of reactivity (defined by eq. 5.9) as a function of the operation time, for the HTR-Pu with 1 and 2 g Pu/pebble.

#### 5.4.6 Flux

Figs. 5.19 and 5.20 show the thermal ( $0 < E < 2.1$  eV) and the nonthermal ( $E > 2.1$  eV) flux, respectively. Fig. 5.19 shows a huge thermal flux peak in the bottom reflector at BOL, a somewhat smaller one in the top reflector at EOL and at all times one in the radial reflector. Furthermore, note that the maximum of the thermal flux in the pebble bed at 6 and 11 years do not coincide with the maximum power density of fig. 5.12. This is due to the axial burnup gradient; at the top, the fresh pebbles require a lower flux to obtain a certain power density than the pebbles with a higher burnup below them. The maximum total flux (i.e. thermal + nonthermal) is depicted in fig. 5.21. Since a pebble of the '2 g'-reactor contains twice the amount of Pu compared to that of the '1 g'-reactor, a two times lower total flux is expected to obtain the same power density. However, since the microscopic fission cross sections are smaller for the '2 g'-reactor, due to the harder spectrum, the maximum total flux is somewhat higher than half that of the '1 g'-reactor.

### Thermal flux (n/cm<sup>2</sup>/sec)

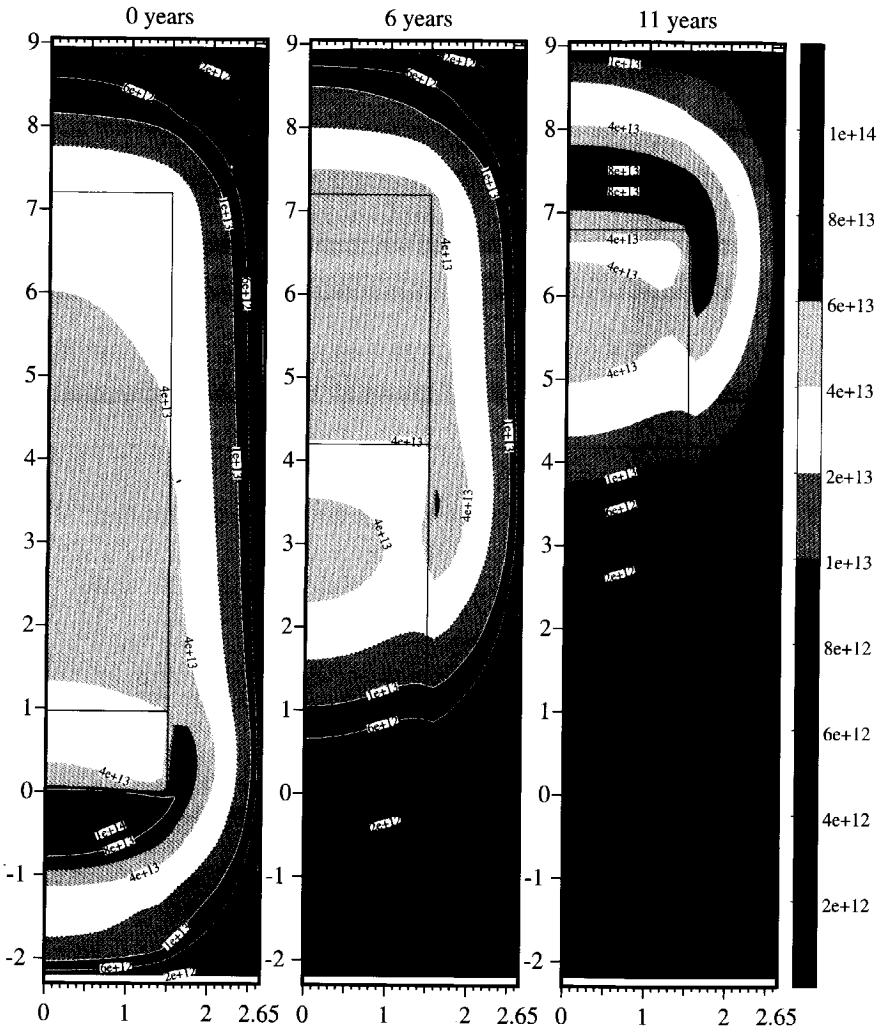


**Figure 5.19:** The thermal flux ( $\text{cm}^{-2}\text{s}^{-1}$ ) of the '1 g'-reactor at three points in time. The energy boundary between the thermal and nonthermal range lies at 2.1 eV. The maximal thermal flux of  $1.5 \cdot 10^{14} \text{ cm}^{-2}\text{s}^{-1}$  occurs in the bottom reflector at  $t = 0$ .



## Nonthermal flux (n/cm<sup>2</sup>/sec)

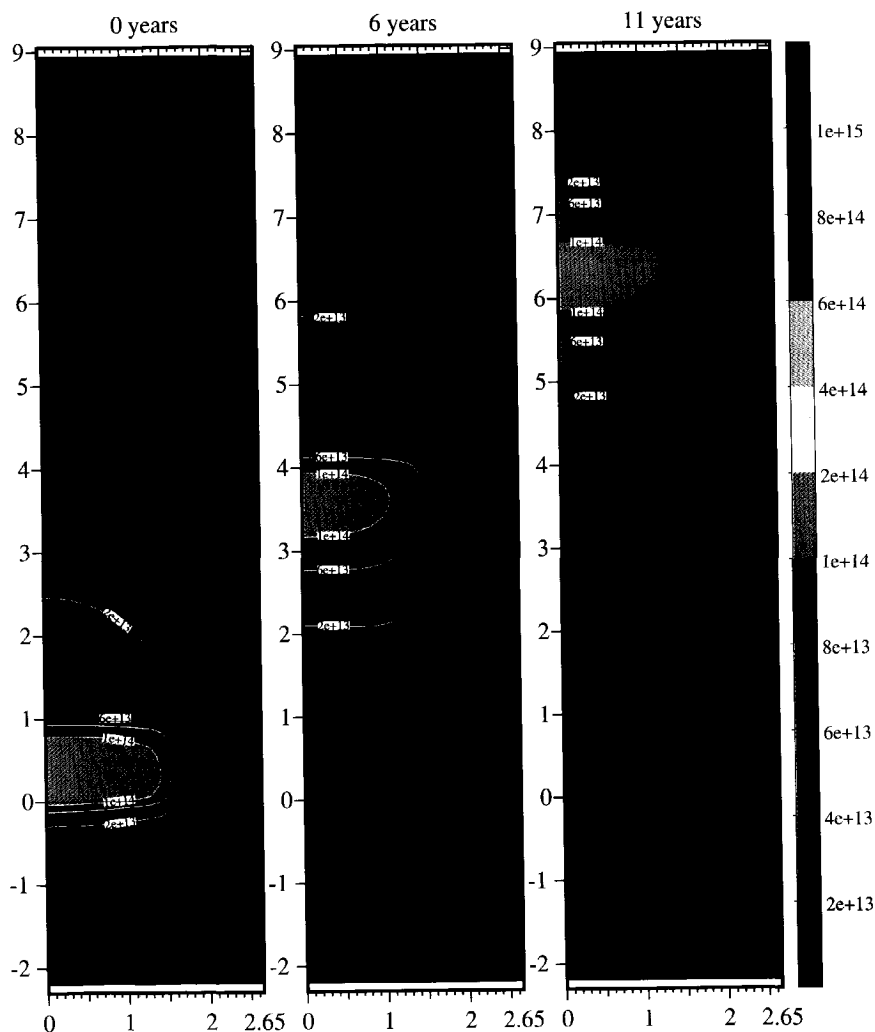


**Figure 5.20:** The nonthermal flux ( $\text{cm}^{-2}\text{s}^{-1}$ ) of the '1 g'-reactor at three points in time. The energy boundary between the thermal and nonthermal range lies at 2.1 eV. The nonthermal flux does not exceed  $2 \cdot 10^{14} \text{ cm}^{-2}\text{s}^{-1}$ .

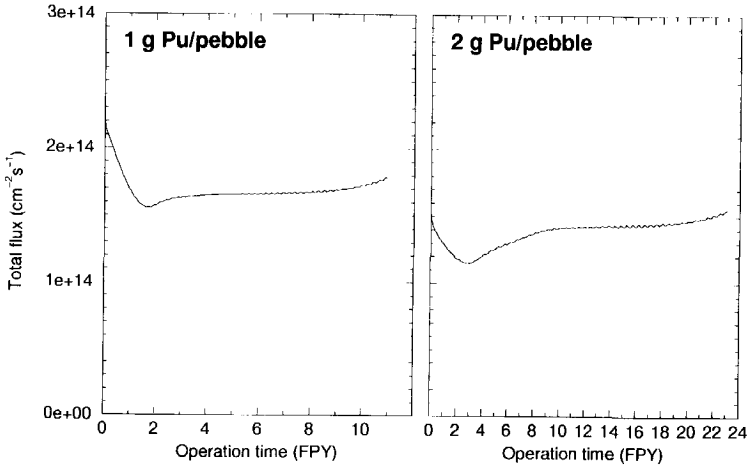


Figure 5.21: The maximum total flux as a function of the operation time, for the HTR-Pu with 1 and 2 g Pu/pebble.

### 5.4.7 Xenon

Fig. 5.22 and 5.23 show the equilibrium xenon density (averaged per mesh volume) and the Xe-worth, respectively. The xenon worth was calculated as

$$\Delta\rho_{Xe} = [k_{eff}(nom. Xe)]^{-1} - [k_{eff}(zero Xe)]^{-1}, \quad (5.10)$$

where  $k_{eff}(nom. Xe)$  and  $k_{eff}(zero Xe)$  are the effective multiplication factors under nominal conditions and under the condition in which xenon is set to zero, respectively. Despite of having a higher xenon density, the 2 g'-reactor shows a Xe-worth that is much lower than that of the 1 g'-reactor. This is caused by the lower thermal microscopic absorption cross section of  $^{135}\text{Xe}$  due to the harder spectrum and a lower total flux.

It is useful to compare the calculated Xe-worths of, say, the BOL and EOL cores of both Pu-loadings to some well-known analytical expressions that are valid for a space-independent reactor model. Before doing so, we introduce the following parameters:

- $\gamma_I$  = effective fission product yield for  $^{135}\text{I}$ ;
- $\gamma_X$  = effective fission product yield for  $^{135}\text{Xe}$ ;
- $\lambda_I$  = decay time constant for  $^{135}\text{I}$  ( $\lambda_I = 2.912 \cdot 10^{-5} [\text{s}^{-1}]$ );
- $\lambda_X$  = decay time constant for  $^{135}\text{Xe}$  ( $\lambda_X = 2.118 \cdot 10^{-5} [\text{s}^{-1}]$ );
- $\sigma_a^X$  = one-group microscopic absorption cross section of  $^{135}\text{Xe}$  [ $\text{cm}^2$ ];
- $\Phi$  = one-group flux [ $\text{cm}^{-2}\text{s}^{-1}$ ];
- $\nu$  = average neutron yield per fission.

According to eq. 15-16 of [69] the Xe-worth can be expressed as

$$\Delta\rho_{Xe} \approx k_{\infty} \frac{\gamma_I + \gamma_X}{\nu} \left\{ 1 - \left( 1 + \frac{\sigma_a^X \Phi}{\lambda_X} \right)^{-1} \right\}. \quad (5.11)$$

Eq. 5.11 shows that for  $\Phi \rightarrow \infty$  one obtains the maximum Xe-worth which reads  $\Delta\rho_{Xe}^{max} \approx \frac{k_{\infty}}{\beta} (\gamma_I + \gamma_X)$ . This means that the Xe-worth relative to its maximum value can be expressed as

$$\Delta\rho_{Xe} / \Delta\rho_{Xe}^{max} \approx 1 - \left(1 + \frac{\sigma_a^X \Phi}{\lambda_X}\right)^{-1} \quad (5.12)$$

From this it is clear that  $\sigma_a^X \Phi / \lambda_X$  is the key parameter. It indicates the competition between the disappearance rate of  $^{135}\text{Xe}$  through neutron capture on the one hand and through decay on the other. If  $\sigma_a^X \Phi / \lambda_X \rightarrow \infty$  each  $^{135}\text{Xe}$  nuclide is converted to  $^{136}\text{Xe}$  through neutron capture; if  $\sigma_a^X \Phi / \lambda_X \rightarrow 0$  each  $^{135}\text{Xe}$  nuclide decays to  $^{135}\text{Cs}$ . The  $\sigma_a^X \Phi / \lambda_X$ 's are computed in the full-core calculations. Its maximum value, occurring somewhere in the pebble bed, is listed in table 5.4. If it is inserted in eq. 5.12 one attains an upper boundary of the fractional Xe-worth  $\Delta\rho_{Xe} / \Delta\rho_{Xe}^{max}$ . Table 5.4 clearly shows the difference between the '1 g' and '2 g' Pu-loadings.

Another interesting parameter is the time at which the xenon concentration reaches its maximum after an abrupt shutdown of the reactor, henceforth denoted by  $t_{Xe-max}$ . Such a rapid shutdown occurs for instance in a loss-of-cooling incident in which a combination of a negative temperature coefficient and a temperature increase provide for enough negative reactivity to cease the chain reaction. Such incidents will be discussed thoroughly in section 5.6. By combining eqs. 15-15 and 15-25 of [69] one attains an expression for  $t_{Xe-max}$  which reads

$$t_{Xe-max} = \frac{1}{\lambda_I - \lambda_X} \left\{ \ln[\lambda_I / \lambda_X] - \ln \left[ 1 + \frac{(\lambda_I / \lambda_X - 1)(1 + \gamma_X / \gamma_I)}{1 + \sigma_a^X \Phi / \lambda_X} \right] \right\} \quad (5.13)$$

This expression is valid for a point-reactor. It shows that for  $\Phi \rightarrow \infty$ , one obtains  $t_{Xe-max} = \ln(\lambda_I / \lambda_X) / (\lambda_I - \lambda_X) = 11.1$  hr. Eq. 5.13 has been employed to determine an upper boundary for  $t_{Xe-max}$  in case of our HTR-Pu. To this end, the maximum  $\sigma_a^X \Phi / \lambda_X$  and the minimum  $\gamma_X / \gamma_I$  were computed in the full-core calculations and successively inserted in eq. 5.13. Table 5.4 shows that the  $t_{Xe-max}$ 's are short compared to common experiences in xenon dynamics. This is caused by the relatively low  $\sigma_a^X \Phi / \lambda_X$ -values, which can be attributed to the fact that fuel is made of plutonium instead of enriched uranium. The ratio of the Xe-capture rate to the fission rate is for a given flux lower for Pu-fuels than for U-fuels due to the 3-4 times higher thermal fission cross sections of the fissile Pu-isotopes compared to  $^{235}\text{U}$ . The lower  $\gamma_X / \gamma_I$ -ratio of the EOL-cores in table 5.4 are due to an increased contribution of  $^{241}\text{Pu}$  to the fission rate. A lower  $\gamma_X / \gamma_I$ -ratio has a longer  $t_{Xe-max}$  as a consequence, but is of less importance than the magnitude of the  $\sigma_a^X \Phi / \lambda_X$ -parameter.

**Table 5.4:** Xe-data obtained from both the full-core calculations and two analytical expressions.

	according to:	1 g Pu/pebble		2 g Pu/pebble	
		BOL	EOL	BOL	EOL
$\Delta\rho_{Xe}(\%)$	full-core calc.	2.0	2.2	1.0	1.6
$\sigma_a^X \Phi / \lambda_X$ (maximum in pebble bed)	full-core calc.	2.5	3.5	0.94	1.7
$\gamma_X / \gamma_I$ (minimum in pebble bed)	full-core calc.	0.113	0.047	0.114	0.058
$\Delta\rho_{Xe} / \Delta\rho_{Xe}^{max}$ (upper boundary)	eq. 5.12	0.71	0.78	0.48	0.63
$t_{Xe-max}$ (hr) (upper boundary)	eq. 5.13	7.1	8.2	4.3	6.4

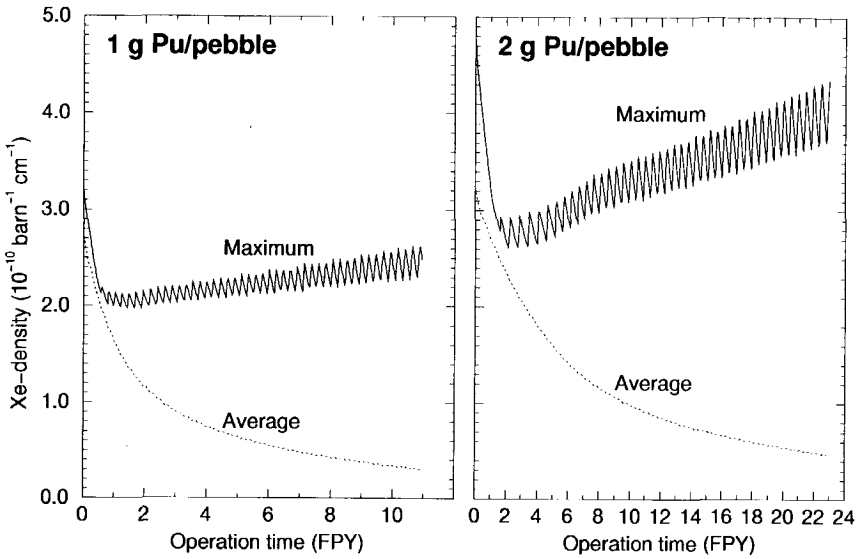


Figure 5.22: The xenon nuclide density in the pebble bed as a function of the operation time, for the HTR-Pu with 1 and 2 g Pu/pebble.

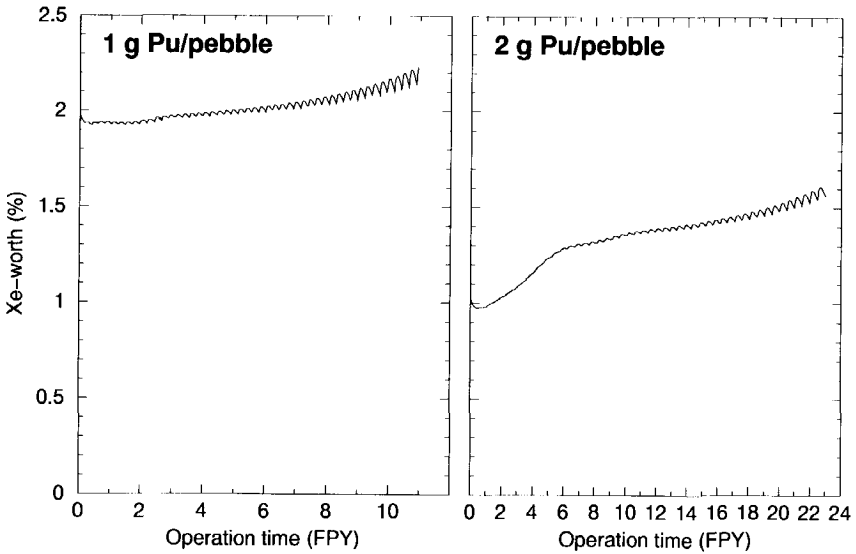


Figure 5.23: The xenon worth as a function of the operation time, for the HTR-Pu with 1 and 2 g Pu/pebble.

## 5.5 Start-up and shut-down of the HTR-Pu

In this section, we present a brief discussion on the start-up and shut-down features of the HTR-Pu. To this end, we focus on the reactivity evolution during a particular start-up procedure. In addition, the temperature defect, the power defect and the xenon defect are given for the Pu-loadings of 1 and 2 g/pebble, both at BOL and EOL.

These defects are defined as the difference of the reactivity of one reactor state with that of another state. Table 5.6 lists the properties of four states at which the HTR-Pu can find it self and three corresponding reactivity defects. Note that a *positive* temperature

**Table 5.5:** Definition of four reactor states and the corresponding reactivity defects calculated as the difference in reactivity between two successive reactor states.

Reactor states	
CZP	Cold Zero Power : Zero power, zero xenon, reactor temperature equals 20 °C .
HZP	Hot Zero Power : Zero power, zero xenon, He-inlet temperature and core temperature: 495 °C .
HFP-(zero Xe)	Hot Full Power (zero xenon) : Thermal power equals 40 MW, zero xenon, nominal temperature profile.
HFP-(nom. Xe)	Hot Full Power (nominal xenon) : Thermal power equals 40 MW, xenon at nominal/equilibrium concentration, nominal temperature profile.
Reactivity defects	
Defect:	Reactivity difference:
Temperature	CZP - HZP.
Power	HZP - HFP-(zero Xe).
Xenon	HFP-(zero Xe) - HFP-(nom. Xe).

defect corresponds, according to its definition in table 5.5, to a *decrease* in reactivity when the reactor makes the transition from CZP to HZP. For the HTR-Pu, this defect as well as the others are listed in table 5.6. During the calculations, the pebble-bed height was fixed. For each (Pu-loading/core)-combination this height is given by table 5.3; each height is such that the system is critical in the HFP-(nom. Xe) state. The (2 g, BOL)-case shows the familiar result of a positive temperature defect, signifying a reactivity decrease when the reactor is heated from 20 °C to 495 °C , while the other cases show negative values. To understand this, the temperature defect has been split up into a contribution of the pebble bed and that of the reflectors. Table 5.6 reveals that the contribution of the reflectors is always negative, which indicates an increase of the reactivity when the temperature of the reflectors increases. An increase of the reflector temperature results in a shift of the Maxwell spectrum to higher energies. Since the absorption cross section of the graphite

**Table 5.6:** Reactivity defects for the Pu-loadings of 1 and 2 g per pebble, for the cores at BOL and EOL. The pebble-bed height is such that the system is critical in the HFP-(nom. xenon) state.

Pu-loading	1 g Pu/pebble		2 g Pu/pebble	
	BOL	EOL	BOL	EOL
Core				
Temperature defect (%)	<b>-0.8</b>	<b>-4.4</b>	<b>0.6</b>	<b>-2.7</b>
Pebble Bed (%)	1.9	-2.3	2.5	-1.0
Reflectors (%)	-2.7	-2.0	-1.9	-1.6
Power defect (%)	<b>1.1</b>	<b>0.2</b>	<b>1.4</b>	<b>0.8</b>
Xenon defect (%)	<b>2.0</b>	<b>2.2</b>	<b>1.0</b>	<b>1.6</b>

behaves as  $1/v$  while its scattering cross section is constant, a shift of the Maxwell spectrum leads to a decrease of the absorption-to-scattering ratio. This implies that the probability for a neutron to re-enter the core increases, which leads of course to an increase in reactivity. The contribution of the pebble bed is positive for both BOL-cores. Since the reflector contribution of the (1 g, BOL)-case is greater, in absolute sense, than the one of the pebble bed, a negative net temperature defect is found.

The EOL-cores of both Pu-loadings show negative contributions from the pebble bed, which is due to the following. At EOL, large parts of the core have reached very high burnup values. Fig. 4.19 shows that the combination of a high burnup and a low uniform-temperature is responsible for an increasing  $k_{eff}$  with increasing uniform-temperature. Apparently, the positive uniform-temperature reactivity feed-back of the large 'high-burnup' part of the core outweighs the negative reactivity feed-back of the smaller 'low-burnup' part of the core. Note that the described phenomenon occurs if the temperature, with a homogeneous distribution across the pebble bed, increases from 20 to 495 °C .

When the reactor is brought from HZP to HFP, the average temperature of the system increases even more. Moreover, the temperature profile is not homogeneous anymore; the temperature of the pebble bed becomes higher than that of the reflectors. The power transition from 0 to 40 MW<sub>th</sub> leads in all cases to a reactivity decrease and hence yields a positive power defect. Obviously, the xenon defects are positive, too. These are quantitatively in agreement with fig. 5.23. Section 5.4.7 gives an explanation of the differences between the Xe-defects of the various Pu-loadings and cores.

Each defect refers solely to the reactivity difference between two states and does not give any information about the reactivity change during the transition from one state to another. Therefore, we investigated the  $k_{eff}$ -evolution between successive states of a particular start-up procedure. This envisaged start-up procedure is analogous to that of PWR, which implies that it consists of two stages. The first stage involves the transition from CZP to HZP. In case of the HTR-Pu the heating of the core might be established by pumping helium through the pebble bed. The helium flow could be realised by using the gas turbine as a blower, which in that case is consuming electricity instead of producing it. To see whether this is really feasible further research is required. Once the core is 'hot', the second stage commences. This stage embraces the generation of power through

**Table 5.7:** Maximum excess reactivities occurring during start-up of the HTR-Pu.

Pu-loading	1 g Pu/pebble		2 g Pu/pebble	
	BOL	EOL	BOL	EOL
Core				
Max. excess reactivity (%)	3.1	2.8	3.0	2.4
Max. excess reactivity (\$)	11.1	7.3	10.6	6.2

the insertion of reactivity until the power reaches its nominal value of 40 MW<sub>th</sub>. This can be realised either by withdrawing control rods or by adding pebbles on top of the pebble bed.

For the purpose of this concise study, we only regard the precedingly described start-up procedure thereby stressing that other start-up procedures may not be excluded in advance. Furthermore, we assume that pebble-bed height is fixed during start-up and that the reactor is controlled by moving control rods instead of by adding pebbles to the core.

Fig. 5.24 shows the  $k_{eff}$ -evolution for the four cases. The graphs on the left correspond to the first stage of the start-up, while those on the right correspond to the second stage. The parameter along the horizontal axes of the graphs of the first stage is the helium temperature at the inlet ( $T_{He-inlet}$ ). In this stage, the pebble bed and the reflectors are in thermal equilibrium with the helium, implying that pebble-bed and reflector temperatures are equal to that of the helium-inlet. The curves of fig. 5.24 show the excess- $k_{eff}$ , which indicates the deviation from  $k_{eff} = 1$  that holds for the (HFP, nom Xe)-state. In practice, the deviation of  $k_{eff}$  from unity is of course compensated by control rods. Furthermore, note that the excess reactivity is given by  $(k_{eff} - 1)/k_{eff}$ .

In order to bring or to keep the reactor in a subcritical state whenever necessary, the control rod worth should be greater than the maximum reactivity occurring during start-up. The maximum reactivity of the (2 g, BOL)-case occurs in the CZP-state;  $k_{eff}$  decreases from CZP to HZP as well as from HZP to HFP. In this case, the control worth should therefore be greater than the sum of all defects, i.e. temperature + power + xenon defect. In both the (1 g, BOL)-case and the (2 g, EOL)-case, the maximum reactivity occurs in the HZP-state, while in the (1 g, EOL)-case the maximum reactivity occurs if the thermal power equals about 15 MW<sub>th</sub> (zero xenon). The (1 g, EOL)-curve shows a maximum at 15 MW<sub>th</sub>, signifying a positive power coefficient of reactivity below this power. What this means for the stability of the reactor when operated at low power as well as for the start-up needs to be investigated in future studies. Table 5.7 shows the maximum reactivities of all cases.

It is clear that the maximum reactivities listed in table 5.7 impose the lower boundary of the total control rod worth required to make the reactor subcritical whenever necessary. It should be noted that the total control rod worth of the HTR-Pu is considerably smaller than those of other thermal reactors. Table 14-1 of [69] lists total control-rod worths that read 17% for a BWR, 7% for a PWR and 16% for the MHTGR with prismatic-block fuel (fixed core). Note that these figures do not include control worths of soluble and burnable poisons. The weakly positive or even negative temperature defect allows a relatively small control worth for the HTR-Pu. More important, however, is the fact that the HTR-Pu is

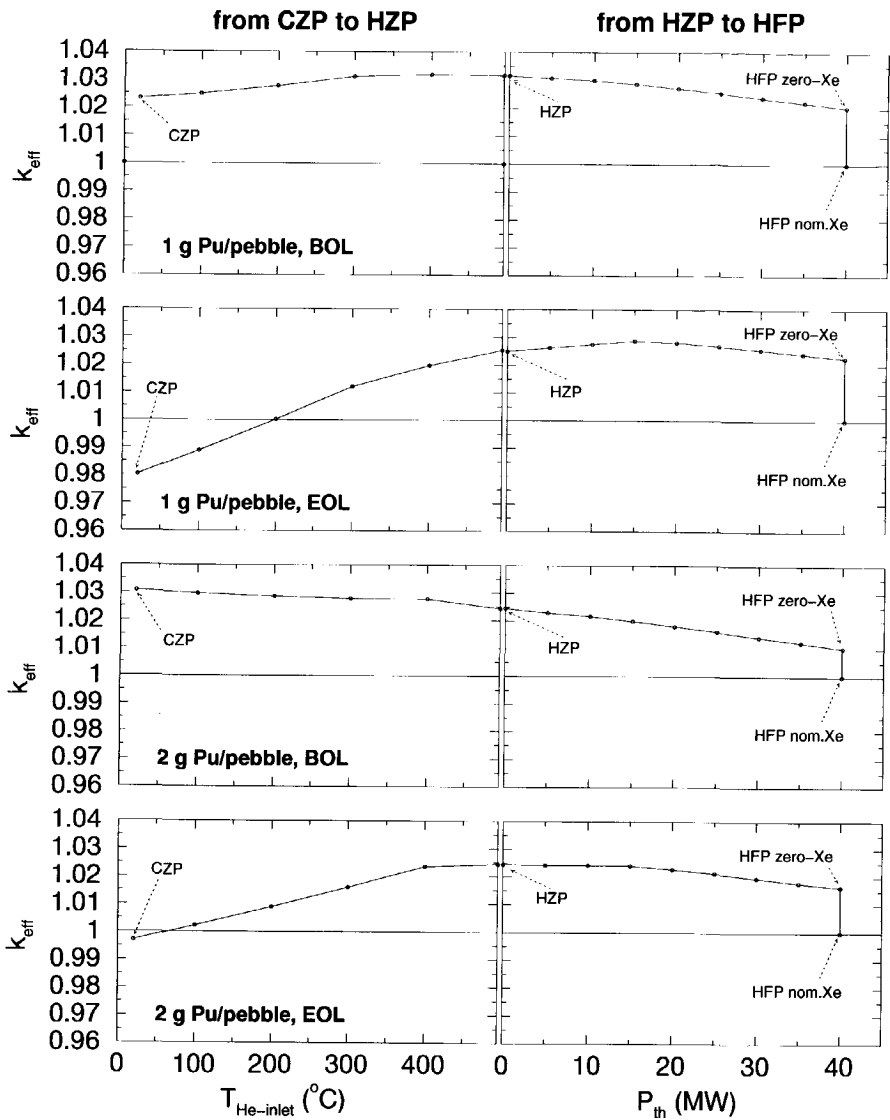


**Figure 5.24:** Reactivity effects for Pu-loadings of 1 and 2 g/pebble, both for the BOL and the EOL core. The graphs on the left side show the  $k_{eff}$ -evolution if the reactor is brought from CZP to HZP. The graphs on the right side show the  $k_{eff}$ -evolution if the reactor is brought from HZP to HFP-(zero Xe), and subsequently to HFP-(nom. Xe). The definitions of the mentioned reactor states are given by table 5.5.



continuously fuelled, which obviates the need for large control worths to compensate the reactivity decrease during burnup.

In conclusion, both Pu-loadings show negative temperature defects for the EOL-cores. This is advantageous in view of having a low total control rod worth, but seems a major drawback for the start-up as far as *nuclear* heat-up is concerned. Note that, in PWRs, nuclear heat-up from room temperature is also not allowed because of a positive temperature coefficient at low temperatures, (p. 37 of [108]). For the HTR-Pu, the loading of 2 g Pu/pebble has preference because it shows a decreasing reactivity with increasing power during the HZP-HFP trajectory for both the BOL-core and the EOL-core.

The reflectors are responsible for a negative contribution to the temperature defect, which is due to a positive reflector-temperature coefficient. This reflector-temperature coefficient might be rendered negative by inserting resonance absorbers in the reflectors. These absorbers should have low-lying resonances that provide for an increased resonance absorption when the Maxwell spectrum shifts to higher energies with increasing reflector temperature. Candidates for these resonance absorbers are  $^{99}\text{Tc}$  and  $^{167}\text{Er}$ , perhaps contained in coated particles that are embedded in graphite rods which can be inserted in cylindrical cavities in the reflectors.

In order to obtain a total (reflectors + pebble-bed) temperature defect that is zero or (slightly) positive, the reflector-temperature defect needs to be equal to or greater than -1.9% for the (1 g, BOL)-case, +2.3% for the (1 g, EOL)-case, +1.0% for the (2 g, EOL)-case. Note that the (2 g, BOL)-case already has a positive total temperature defect.

Another option to attain a positive total temperature defect is to use pebbles with more than 2 g Pu/pebble. It is likely that then a more negative temperature coefficient and thus a more positive pebble-bed temperature defect will be attained. However, in order to realise a positive *total* temperature defect (i.e. pebble-bed and reflectors together) the positive pebble-bed temperature defect should outweigh the negative reflector temperature defect, also in the case of the EOL-cores. However, higher Pu-loadings will have higher fast fluences at the exit burnup as a consequence. (see p. 67). This might pose problems as regards the preservation of the integrity of the CPs.

It is needless to say that an extensive start-up study, in particular with respect to the heating of the core by the gas turbine, has to be performed in a follow-up phase of the HTR-Pu design.

## 5.6 The HTR-Pu under loss-of-cooling conditions

In view of inherent or so-called passive safety, the HTR-Pu should be able to endure a loss-of-cooling event without exceeding too high fuel temperatures, even in case of failure of active control systems. Computational results of such events referring to  $\text{UO}_2$  fuelled HTRs can be found in refs. [28] (ch. 6), [39, 41, 45, 50, 109]. A loss-of-cooling event was simulated with the German AVR reactor [110, 111] in the 1970s. This experiment convincingly demonstrated that passive cooling mechanisms like radiation and natural convection can provide for sufficient decay heat removal so that the temperature is kept below the maximally allowed one.

For  $\text{UO}_2$  systems it is generally accepted ([28] p. 268) that the temperature of fuel particles with TRISO coatings should not exceed  $1600\text{ }^\circ\text{C}$  under any conditions. Whether this holds for plutonium oxide kernels with TRISO coatings too, is not clear yet. Ref. [19] (p. 3-17) reports that  $\text{PuO}_{1.68}$  fuel showed good performance after a peak burnup of  $737\text{ MWd/kgHM}$  and a peak temperature of  $1444\text{ }^\circ\text{C}$ , but does not give any information of fuel behaviour at  $1600\text{ }^\circ\text{C}$  or higher temperatures. To give an answer to this question, further irradiation experiments are required. Due to the lack of data we presume for the time being a temperature limit of  $1444\text{ }^\circ\text{C}$  for our Pu-fuel.

Section 5.6.3 presents the calculational results referring to the behaviour of the HTR-Pu under loss-of-cooling conditions. The calculations embrace two Pu-loadings (1 and 2 g Pu/pebble), two cores (BOL and EOL) and two loss-of-cooling scenarios, which yields eight different combinations in total. The BOL-core refers to the zero-burnup pebble bed with a relatively small volume (low heat capacity) in combination with a large core cavity offering much space for natural convection, while the EOL-core refers to a pebble bed with a height of 6.8 m, signifying a large heat capacity, in combination with a small core cavity offering limited possibilities for natural convection. The BOL-core corresponds to a core in which xenon and decay heat are set equal to their equilibrium values (conservatism); the EOL-core refers to the actual core after 11 and 23 full-power years of operation in case of the Pu-loading of 1 and 2 g/pebble, respectively.

Each transient calculation simulates 100 hours of real reactor time, which involves about 10,000 successive neutronic/thermal-hydraulic coupled calculations. Below, the loss-of-cooling scenarios are described and the calculational results are presented, subsequently. Thereafter, the results are interpreted by means of a space-independent reactor model.

### 5.6.1 Definition of loss-of-cooling scenarios

Table 5.8 presents the definitions of the two loss-of-cooling scenarios that were considered. The evolutions of the helium mass flow and pressure are in fact changing boundary conditions imposed to the DIREKT-part of the thermal-hydraulic code. It should be noted that the interaction with the energy conversion system is not accounted for, which implies that the loss-of-cooling scenarios of table 5.8 are only presumptions. The Loss Of Flow Incident (LOFI) involves a loss of helium mass flow and is associated with a trip of the turbine. Since the compressor is attached to the same shaft as the turbine, the helium pressure

of 23 bar prevailing in the core can no longer be sustained. The pressures in the core, on the one hand, and in the energy conversion system, on the other, will balance out at a new equilibrium pressure, which is estimated to be 20 bar [112]. The Loss Of Coolant Incident (LOCI) involves, besides the drop of flow, a complete drop of the pressure. This scenario is associated with a complete rupture of the manifold pipe that connects the reactor and the energy conversion system (a so-called guillotine-break). In this situation helium flows out of the system until its pressure is equal to that of the surroundings. In the calculational model of the LOCI, air ingress is left out of consideration.

**Table 5.8:** Definitions of the loss-of-cooling scenarios

LOFI	Loss Of Flow Incident Linear helium mass flow decrease from 25 to 0.01 kg/s in 30 s. Linear pressure drop from 23 to 20 bar in 30 s.
LOCI	Loss Of Coolant Incident Linear helium mass flow decrease from 25 to 0.01 kg/s in 30 s. Linear pressure drop from 23 to 1 bar in 30 s.

## 5.6.2 Reactor-physics description of the transients

Below, we will describe the main reactor-physics phenomena that occur during a typical loss-of-cooling transient by means of fig. 5.25. Although this figure refers to the LOCI at BOL of the '2 g'-reactor, the general behaviour of the curves are representative for all transient cases. Some characteristic transient-parameters (namely,  $t_{\rho_{min}}$ ,  $\rho_{min}$ ,  $\rho_{max}$ ,  $t_{crit}$ ,  $P_{f,crit}$ ,  $P_{f,max}$ ,  $\Delta T_{max}$ ) are for the ('2 g'/LOCI/BOL)-case depicted in fig. 5.25; their values are listed in table 5.9 in section 5.6.3.

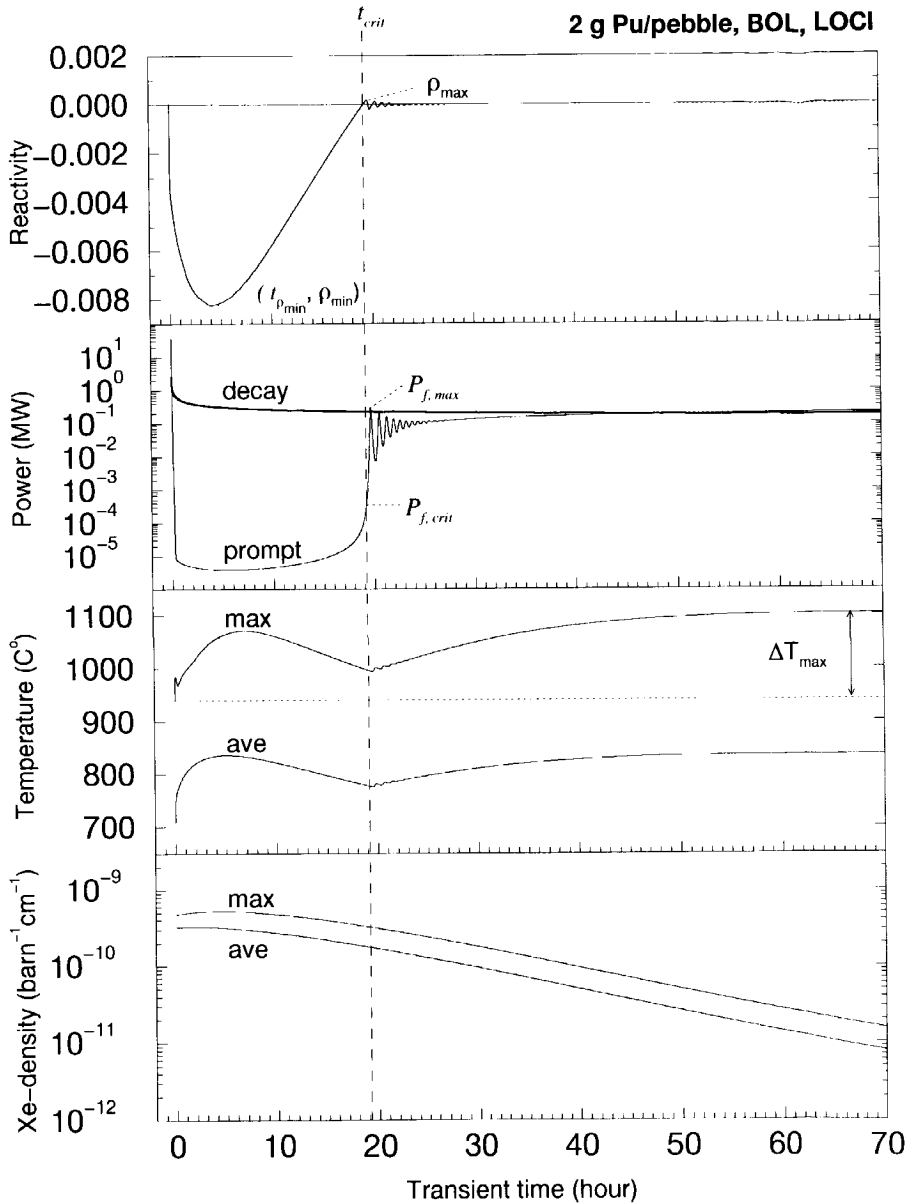
The transient commences when, at time zero, the helium mass flow and pressure start to decrease. As the mass flow decreases, less heat can be removed from the pebble bed, which leads to higher core temperatures. Since the temperature coefficient of the core is negative (see fig. 5.17), the temperature increase has a decrease of the reactivity as a consequence, which leads to a decrease of the fission power. The decrease of the fission power leads on its turn to a xenon build-up, which renders the reactivity even more negative. The maximum Xe-density reaches a maximum at about 4 hours, after which it decreases (note the logarithmic vertical scale for the Xe-density in fig. 5.25). This is in agreement with the  $t_{Xe=max}$  listed in table 5.4. The negative reactivity introduced by both the temperature increase and the xenon build-up causes a fast decrease of the direct fission power (prompt power). At a transient time of about 2 min, the prompt power is as low as the decay power; at  $t \approx 8$  min the prompt power is reduced by a factor of 1000 and at  $t \approx 15$  min the prompt power is reduced by a factor of  $10^6$ , which implies that the direct fission power has become comparable to the power of an ordinary light bulb!

Fig. 5.25 shows that both the average and maximum core temperatures increase relatively fast in the first three minutes. A closer look reveals that the maximum temperature

(positioned somewhere in the core) decreases between  $t \sim 3$  min and  $t \sim 20$  min, while the average temperature keeps increasing. This is due to a re-distribution of the heat in the core; the temperature profile flattens when the power decreases. After  $t \sim 20$  min, the average and maximum temperature increase again simultaneously.

In the subcritical period of  $0 < t < t_{crit}$ , heat production due to prompt power and, more important, decay power over-compensates the heat removal by passive means, i.e. heat conduction, convection and radiation to the surroundings. At  $t \approx 7$  hours, heat production and removal are in balance (restricting ourselves to the mesh volume that refers to the maximum temperature). Thereafter, heat removal becomes stronger than production, which leads to a decreasing (maximum) temperature. This is caused by the higher temperature difference between the core and the ambient and by the slowly decreasing total power. It is worthwhile to mention that if the total power (decay plus prompt) were constant, the temperature would simply increase to an asymptotic value, at which heat removal and production are in equilibrium. Since in our case the power decreases with time, (fast in the beginning and thereafter slowly, illustrated by fig. 5.25), the temperature curve does not increase to an asymptotic value but shows a maximum.

Both the decreasing temperature and the decreasing Xe-density render the reactivity less negative. At  $t_{crit}$ , the temperature and xenon values are such that recriticality occurs. The power at that very moment equals  $P_{f,crit}$ . After  $t_{crit}$ , the reactivity exhibits some damped oscillations and correspondingly a series of power surges occurs. The oscillations with a period of  $\sim 0.5$  hr are triggered by the negative temperature reactivity feedback, which is implicitly confirmed by the weak ripples in the temperature-curves in fig. 5.25. The amplitude of the first surge is denoted by  $P_{f,max}$  (prompt power); it is roughly proportional to the reactivity ramp rate  $\frac{d\rho}{dt}$  at  $t_{crit}$  [89]. The maximum reactivity (i.e. the height of the first maximum of  $\rho(t)$ ) is denoted by  $\rho_{max}$ . Eventually, the fission power settles down at a new equilibrium with a temperature-xenon combination at which the reactor is critical. The difference between the maximum temperature at time zero and its asymptotic value (i.e. the equilibrium- $T_{max}$  for the reactor under passive cooling conditions) is depicted as  $\Delta T_{max}$  in fig. 5.25.



**Figure 5.25:** Various parameters as a function of the transient time, in case of a LOCI at BOL for the '2 g'-reactor.

### 5.6.3 Computational results of loss-of-cooling incidents

Table 5.9 lists a variety of parameters that have been calculated for each transient. The meaning of the transient-parameters  $t_{\rho_{min}}$ ,  $\rho_{min}$ ,  $\rho_{max}$ ,  $t_{crit}$ ,  $P_{f,crit}$ ,  $P_{f,max}$ ,  $\Delta T_{max}$  were given in the preceding section and are, moreover, depicted in fig. 5.25. The parameters referring to eqs. 5.14-5.18 in the lower five rows of table 5.9 will be treated in section 5.6.4.

Figs. 5.26-5.31 show for both Pu-loadings the reactivity, the prompt power, the maximum Xe-density and the maximum fuel temperature as a function of the transient time, respectively. Fig. 5.26 and 5.27 show that the minimum reactivity values of the '1 g'-reactor are in general stronger negative than those of the '2 g'-reactor (see also  $\rho_{min}$ -values in table 5.9). This is mainly due to the stronger Xe-worths of the '1 g'-reactor. The points in time at which the Xe-density reaches its maximum value ( $t_{Xe=max}$ ) are in agreement with the calculated upper-boundaries presented in table 5.4 on page 119. The maximum reactivities, occurring after recriticality, lie between +15 and +35 pcm (see  $\rho_{max}$  in table 5.9). Noting the delayed neutron fractions in table 5.9, this implies that the system stays well below prompt-criticality. Furthermore, note that the approach to recriticality is fairly slow:  $\frac{d\rho}{dt}(t_{crit})$  of table 5.9 lies between 57 and 124 pcm/hr.

An important conclusion that can be drawn from figs. 5.26-5.31 is that for a given core (either BOL or EOL) recriticality occurs earlier for the LOFI than for the LOCI-case, which is due to the following. In the LOFI-case helium under high pressure is still prevailing in the core (pressure drop of 23→20 bar, only), which means that heat can be transported by natural convection in the core cavity much more effectively than in the LOCI-case (He-pressure equals 1 bar). The enhanced heat removal means a faster temperature decrease during the subcritical period of the transient, causing the recriticality to occur earlier. Compare in this respect also temperature-curves of a LOCI to that of a LOFI for a particular core in the subcritical period (figs. 5.30-5.31). (E.g. LOCI vs. LOFI difference of the BOL-core of the '2 g'-reactor). In the space-independent reactor model of Van Dam [89] the degree to which heat can be removed (by passive means) is captured by an effective heat transfer coefficient  $h$  (W/K), whose definition is deferred until section 5.6.4. Table 5.9 shows that the  $h$ 's of the LOFIs are always larger than their LOCI-counterparts.

The differences between the BOL and EOL reactivity curves for a given transient (either LOCI or LOFI) reveal that the BOL core reaches recriticality earlier than the EOL core. This is due to the smaller core volume and its corresponding smaller heat capacity, which implies that the thermal time constant of the system is smaller (see eq. 32 of [89]). Xenon can be excluded as the driving mechanism, since the time at which the Xe-density becomes equal to the nominal equilibrium Xe-density ( $t_{Xe=Xe(0)}$ ) is, unlike  $t_{crit}$ , shorter for the EOL core than for the BOL core.

In conclusion, a combination of a large heat removal rate and a small heat storage capability (LOFI/BOL-case) yields a short time to attain recriticality (low  $t_{crit}$ ) and vice versa (LOCI/EOL-case).

**Table 5.9:** *Calculational results of the transients. The numbers in the five lowest rows are based on eqs. 5.14-5.18, while all the other ones are obtained from the PANTHERMIX calculations.*

Pu-loadings core	1 gram/pebble				2 gram/pebble				
	BOL		EOL		BOL		EOL		
$\beta$ [ $10^{-3}$ ]	2.80		3.86		2.83		3.88		
$\beta/\lambda$ [ $10^{-2}$ s]	3.84		4.76		3.86		4.78		
$\Delta\rho_{Xe}$ [%]	2.0		2.2		1.0		1.6		
$T_{max}(0 \text{ hr})$ [ $^{\circ}\text{C}$ ]	990		820		940		820		
scenario	LOCI	LOFI	LOCI	LOFI	LOCI	LOFI	LOCI	LOFI	
$t_{\rho min}$ [hr]	4.9	3.4	6.1	5.1	4.0	2.5	5.8	4.3	
$t_{crit}$ [hr]	19.8	14.3	23.7	19.9	19.2	11.1	22.5	15.9	
$t_{Xe-max}$ [hr]	7.1	7.1	6.3	6.3	4.3	4.3	4.2	4.2	
$t_{Xe=Xe(0)}$ [hr]	20.0	19.9	16.7	16.7	10.0	10.0	9.7	9.7	
$P_{f,crit}$ [W]	270	260	220	220	337	372	230	264	
$P_{f,max}$ [MW]	0.474	0.554	0.905	1.054	0.272	0.407	0.432	0.604	
$P_{tot,max}$ [MW]	0.60	0.81	1.1	1.3	0.42	0.67	0.66	0.85	
$\rho_{min}$ [pcm]	-1300	-1000	-1600	-1300	-820	-670	-1100	-820	
$\rho_{max}$ [pcm]	+25	+30	+31	+35	+15	+22	+25	+28	
$\frac{d\rho}{dt}(t_{crit})$ [pcm/hr]	93	124	101	104	57	85	65	80	
$\Delta T_{max}(0 \rightarrow 100 \text{ hr})$ [ $^{\circ}\text{C}$ ]	266	261	445	447	156	154	384	391	
$E_f(0 \rightarrow t_{crit})$ [fps]	38	39	45	45	43	40	45	45	
$P_{tot}(100 \text{ hr})$ [MW]	0.45	0.7	0.44	0.55	0.36	0.55	0.36	0.51	
$T_{osc}$ [hr]	0.41	0.34	0.51	0.35	0.54	0.46	0.55	0.43	
$h$ [W/K]	eq. 5.14	370	550	350	430	330	500	300	410
$-\alpha$ [pcm/K]	eq. 5.15	-8	-8	-5	-5	-7	-7	-4	-4
$P_{f,crit}$ [W]	eq. 5.16	230	250	170	200	300	330	200	260
$C/\alpha$ [MJ/pcm]	eq. 5.17	2.5	2.1	3.9	4.3	2.6	2.5	3.2	3.5
$C/\alpha$ [MJ/pcm]	eq. 5.18	2.4	2.4	2.6	2.7	2.9	2.7	3.2	3.5

- $\beta/\lambda$   $\sum_i \beta_i/\lambda_i$ , where  $\beta_i$  is the  $\nu \Sigma_f \Phi$ -weighted core averaged delayed neutron fraction of the  $i$ 'th delayed group and  $\lambda_i$  ( $s^{-1}$ ) is the time constant of that group;
- $\beta$  total delayed neutron fraction (i.e.  $\sum_i \beta_i$ );
- $\Delta\rho_{Xe}$  Xe-worth according to eq. 5.10;
- $T_{max}(0 \text{ hr})$  the maximum fuel temperature before the transient starts;
- $t_{\rho min}$  time at which minimum reactivity is found;
- $t_{crit}$  time at which recriticality occurs;
- $t_{Xe=max}$  time at which the max-Xe density is maximal;
- $t_{Xe=Xe(0)}$  time at which the max-Xe density becomes equal to its value at  $t = 0$ ;
- $P_{f,crit}$  fission power at  $t_{crit}$ ;
- $P_{f,max}$  maximum fission power occurring in the first power surge;
- $P_{tot,max}$  maximum total (decay + prompt) power occurring in the first power surge;
- $\rho_{min}$  minimum reactivity occurring at  $t_{\rho min}$ ;
- $\rho_{max}$  maximum reactivity (occurring after  $t_{crit}$ );
- $P_{tot,max}$  the maximum total (prompt plus decay) power of the first power surge;
- $\frac{d\rho}{dt}(t_{crit})$  reactivity ramp rate at  $t_{crit}$ ;
- $\Delta T_{max}(0 \rightarrow 100 \text{ hr})$  the difference between  $T_{max}$  at  $t = 0$  and at  $t = 100$  hr;
- $E_f(0 \rightarrow t_{crit})$  prompt power integrated from  $t = 0$  to  $t_{crit}$  (full-power seconds);
- $P_{tot}(100 \text{ hr})$  the total (prompt plus decay) power at  $t = 100$  hours;
- $T_{osc}$  the period of the power oscillations.

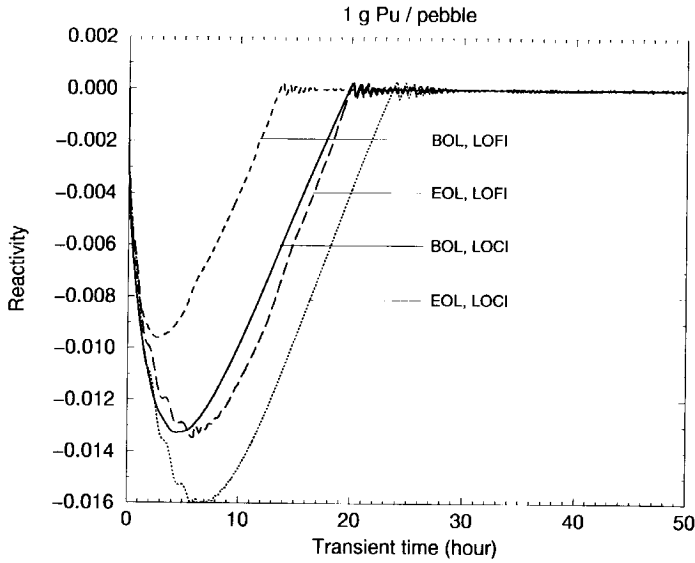


**Figure 5.26:** The reactivity during the first 50 hours of the transient, for the '1 g'-reactor. The curves refer to two cores (BOL and EOL) and two loss-of-cooling scenarios (LOCI and LOFI, defined in table 5.8).

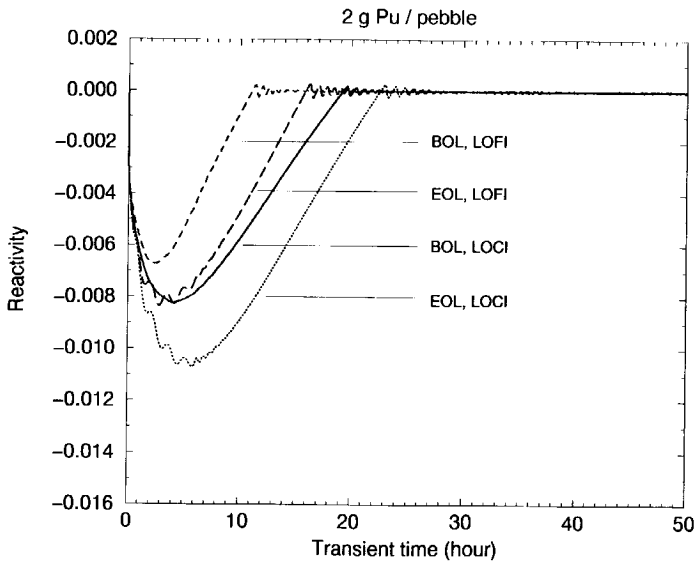


**Figure 5.27:** The reactivity during the first 50 hours of the transient, for the '2 g'-reactor. The curves refer to two cores (BOL and EOL) and two loss-of-cooling scenarios (LOCI and LOFI, defined in table 5.8).



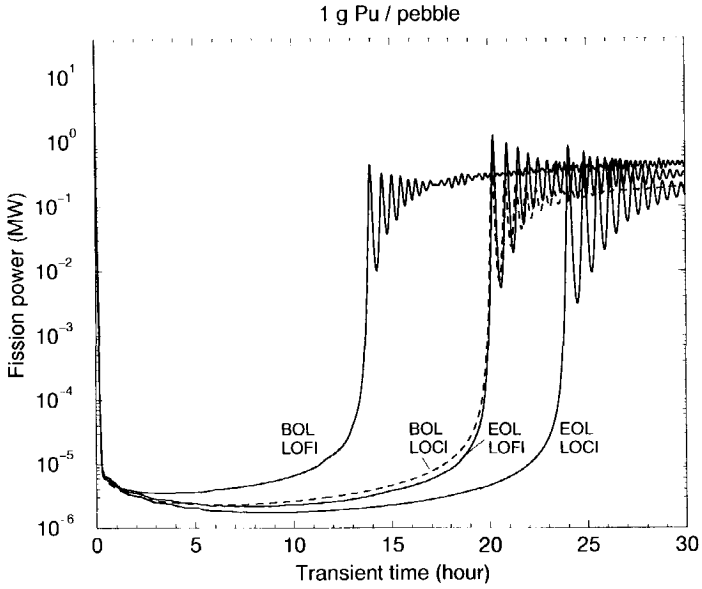


**Figure 5.28:** The fission power during the first 30 hours of the transient, for the '1 g'-reactor. The curves refer to two cores (BOL and EOL) and two loss-of-cooling scenarios (LOCI and LOFI, defined in table 5.8).

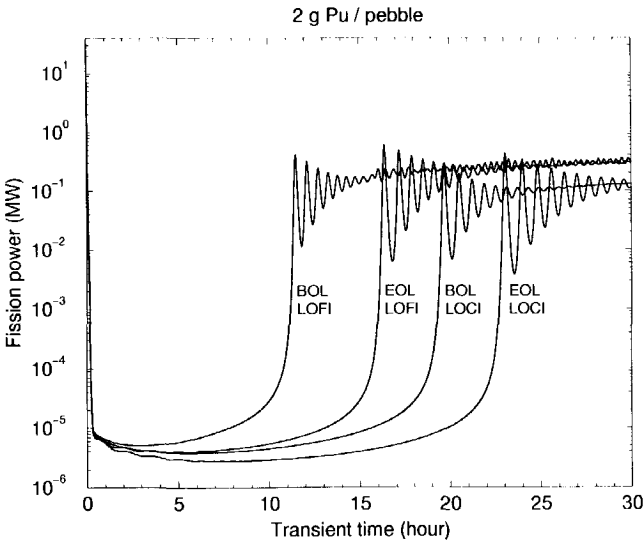


**Figure 5.29:** The fission power during the first 30 hours of the transient, for the '2 g'-reactor. The curves refer to two cores (BOL and EOL) and two loss-of-cooling scenarios (LOCI and LOFI, defined in table 5.8).

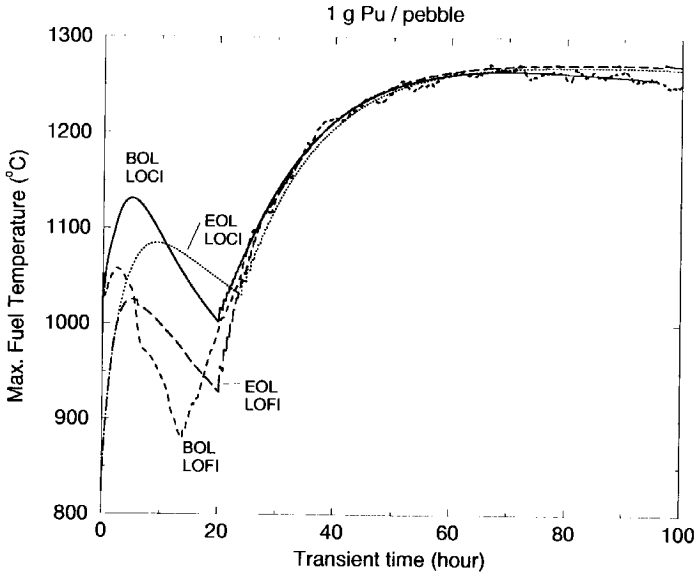


**Figure 5.30:** The maximum fuel temperature as a function of the transient time for the '1 g'-reactor. The curves refer to two cores (BOL and EOL) and two loss-of-cooling scenarios (LOCI and LOFI, defined in table 5.8).

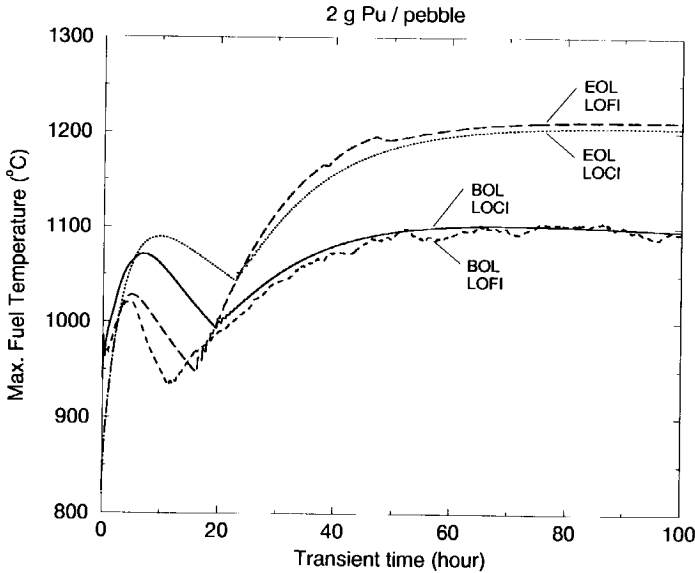


**Figure 5.31:** The maximum fuel temperature as a function of the transient time for the '2 g'-reactor. The curves refer to two cores (BOL and EOL) and two loss-of-cooling scenarios (LOCI and LOFI, defined in table 5.8).

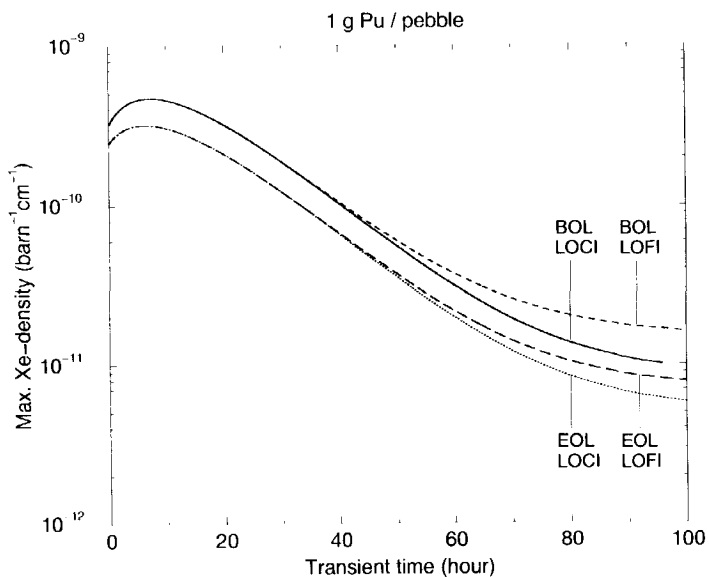


**Figure 5.32:** The (mesh-averaged) maximum xenon density as a function of the transient time for the '1 g'-reactor. The curves refer to two cores (BOL and EOL) and two loss-of-cooling scenarios (LOCI and LOFI, defined in table 5.8).

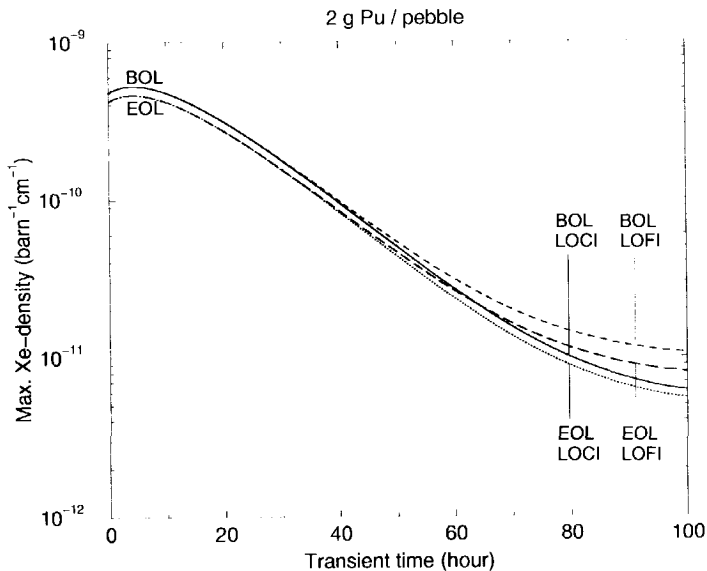


**Figure 5.33:** The (mesh-averaged) maximum xenon density as a function of the transient time for the '2 g'-reactor. The curves refer to two cores (BOL and EOL) and two loss-of-cooling scenarios (LOCI and LOFI, defined in table 5.8).

### 5.6.4 Comparison with point-reactor model

In a publication of Van Dam [89], a space-independent reactor model was used to analyse the fundamental physical aspects of a loss-of-cooling incident. The model equations were implemented in a computer code to simulate a typical loss-of-cooling incident. In addition, a number of analytical expressions were derived which provide for the physical understanding of the dominating phenomena and which reveal the parameters that govern these phenomena. In this section, we quantify some of the parameters of the point-reactor model on the basis of the PANTHERMIX-calculational results. The point-reactor parameters, like heat capacity and heat transfer coefficient, will be obtained through inserting some computed PANTHERMIX-parameters (e.g. temperature, power) in Van Dam's analytical expressions. The aim thereby is not to attain exact values for these parameters, but rather to get insight into their order of magnitude and to see how they differ in the various cases. Eqs. 5.14-5.18 show the point-reactor parameters that were considered and the equations from which they were retrieved. The obtained parameters are listed at the bottom of table 5.9.

ref. [89]

formula

$$- \quad h = \frac{P_{tot}(100 \text{ hr})}{T_{max}(100 \text{ hr})} \quad (5.14)$$

$$- \quad \alpha = \frac{\Delta\rho_{Xe}}{\Delta T(0 \rightarrow 100 \text{ hr})} \quad (5.15)$$

$$18 \quad P_{f,crit} = Q \left( \frac{2}{\pi} \frac{\beta}{\lambda} \frac{d\rho}{dt}(t_{crit}) \right)^{-1/2} \quad (5.16)$$

$$25 \quad C/\alpha = \left( \frac{d\rho}{dt}(t_{crit}) \right)^{-1} \left( \frac{P_{f,max} - P_{f,crit}}{\ln(P_{f,max}) - \ln(P_{f,crit})} \right) \quad (5.17)$$

$$36 \quad C/\alpha \approx \frac{P_0}{(\beta/\lambda)} \left( \frac{T_{osc}}{2\pi} \right)^2 \quad (5.18)$$

Hereafter, these equations will be discussed subsequently.

#### Point-reactor model

The dynamic equations of the reactor model of [89] consist of a combination of the conventional point kinetics equations, the dynamic equations for fission product decay heat, equations for  $^{135}\text{I}$  and  $^{135}\text{Xe}$  kinetics, an equation for heat transfer via Newton cooling and a linear temperature and xenon feedback for the reactivity. We recall the latter two equations, respectively:

$$C \frac{dT}{dt} = P_f + P_d - hT, \quad (5.19)$$

$$\rho = -\alpha(T - T_0) - \xi(X - X_0), \quad (5.20)$$

where

- $C$  = heat capacity of reactor (J/K)
- $T$  = reactor temperature (K)
- $T_0$  = nominal reactor temperature (K)
- $P_f$  = direct fission power (W)
- $P_d$  = decay power (W)
- $h$  = overall heat transfer coefficient (W/K)
- $-\alpha$  = temperature coefficient of reactivity ( $K^{-1}$ )
- $X$  =  $^{135}\text{Xe}$  nuclide density ( $m^{-3}$ )
- $X_0$  = equilibrium  $^{135}\text{Xe}$  nuclide density ( $m^{-3}$ )
- $-\xi$  =  $^{135}\text{Xe}$  coefficient of reactivity ( $m^3$ )

### Point-reactor heat transfer coefficient

Setting the time-derivative of eq. 5.19 to zero, shows that the equilibrium total power ( $P_{tot} = P_f + P_d$ ) is related to the equilibrium temperature by the heat transfer coefficient  $h$ . At 100 hours after the beginning of each transient a new equilibrium under passive cooling conditions is attained. Eq. 5.14 shows the heat transfer coefficient  $h$  as a function of the equilibrium total power and the equilibrium temperature. Here, the temperature of point-reactor is associated with the maximum temperature of the full-core calculations. The  $T_{max}(100 \text{ hr})$  in eq. 5.14 equals  $T_{max}(0 \text{ hr}) + \Delta T_{max}(0 \rightarrow 100 \text{ hr})$  listed in table 5.9. The heat transfer coefficients in passive-cooling mode  $h$ , calculated according to eq. 5.14, are listed in table 5.9. Table 5.9 shows that for each Pu-loading/core combination the heat transfer coefficient of the LOFI is always higher than that of the LOCI. This is due to the enhanced heat removal by natural convection when the helium in the core is still under high pressure (LOFI: 20 bar, while LOCI: 1 bar only). The heat transfer coefficients of the LOFIs are maximally 50% higher than those of the LOCI.

### Estimation of the point-reactor temperature reactivity coefficient

At a transient time of 100 hours the passively cooled system is in equilibrium ( $\rho = 0$ ) with the  $T_{max}(100 \text{ hr})$  and  $X_e(100 \text{ hr})$ . Eq. 5.20 shows that the temperature reactivity coefficient of the point-reactor can be estimated as

$$\alpha = \frac{-\xi(X(100 \text{ hr}) - X_0)}{\Delta T(0 \rightarrow 100 \text{ hr})} \quad (5.21)$$

Figs. 5.30-5.31 show that  $X(100 \text{ hr}) < 10X_0$ , which implies that neglecting  $X(100 \text{ hr})$  in eq. 5.21 leads to an overestimation of  $\alpha$  of maximally  $\sim 10\%$ . Neglecting  $X(100 \text{ hr})$  in eq. 5.21 and identifying  $\xi X_0$  as the Xe-worth ( $\Delta\rho_{Xe}$ ), gives eq. 5.15.

### Analytic expression of the fission power at first criticality

During the subcritical transient period ( $0 < t < t_{crit}$ ) the fission power is determined by the strength of an inherent neutron source in the core. In a real HTR-Pu such a neutron source

would originate from spontaneous fissions (mainly due to even Pu-isotopes) and from  $(\alpha, n)$ -reactions with oxygen (mainly due to  $^{238}\text{Pu}$  because of its short half-life). However, implementation of an inherent neutron source that simulates the aforementioned processes in the calculational model appeared impossible until so far. Instead, an inherent neutron source was artificially created by modelling a seventh delayed neutron group with a very small yield ( $\beta_{dq7} = 1 \cdot 10^{-9}$ ) and a small decay constant ( $\lambda_{dq7} = 1 \cdot 10^{-5} \text{ s}^{-1}$ ;  $T_{1/2} = 19.3 \text{ h}$ ). The aim of this artificial neutron source is to prevent numerical instabilities in the subcritical period. The fact that it does not represent the real neutron source is not very harmful, because the total power in the subcritical period is almost fully determined by the decay power. Besides that, Van Dam [89] showed that the maximum power of the first power surge is only very weakly dependent on the neutron source strength. The (time-dependent) source strength expressed in power units was

$$Q(t) = 3.75 \cdot 10^{-2} \exp(-\lambda_{dq7} t) \text{ [W]} , \quad (5.22)$$

where  $t$  is the transient time in seconds. The stationary fission power in the subcritical state is equal to (eq. 17 of [89])

$$P_{fis} = \frac{Q}{-\rho} . \quad (5.23)$$

The relation between fission power, source strength and reactivity can be illustrated by the following example. Inserting the minimum reactivity  $\rho_{min} = -0.016$  of the (1 g/EOL/LOCI)-case of table 5.9 in eq. 5.23 and inserting the corresponding  $t_{\rho_{min}} = 6.1 \text{ hr}$  in eq. 5.22 yields, according to eq. 5.23, a fission power of 1.9 W. This corresponds to the minimum fission power of the EOL/LOCI-curve in fig. 5.28.

Ref. [89] gave an equation (see eq. 5.16) for the direct fission power at first criticality as a function of the reactivity ramp rate, the inherent source strength and  $\frac{\beta}{\lambda}$ , which was based on a one-group delayed neutron approach and the prompt-jump approximation. Inserting  $Q(t_{crit})$  according to eq. 5.22,  $\beta/\lambda$  and  $\frac{d\rho}{dt}(t_{crit})$  from table 5.9 in eq. 5.16 yields the 'analytical'  $P_{f,crit}$  listed in table 5.9. Table 5.9 shows that the analytical  $P_{f,crit}$  values are underestimated compared to those obtained from the full-core calculations (also listed in table 5.9) by maximally 30%.

### Point-reactor heat capacity. I

Using a modification of the classical Fuchs ramp input model, ref. [89] gave an analytical expression in which the maximum power of the first power surge  $P_{f,max}$  is expressed in terms of  $C$ ,  $\alpha$  and  $P_{f,crit}$  and the reactivity ramp rate at first criticality  $\frac{d\rho}{dt}(t_{crit})$ . Rewriting this equation (eq. 25 of [89]) gives eq. 5.17. Inserting  $\frac{d\rho}{dt}(t_{crit})$ ,  $P_{f,crit}$  and  $P_{f,max}$  (obtained from the PANTHERMIX-calculations) yields the point-reactor parameter  $C/\alpha$ , which is listed at the bottom of table 5.9.

Multiplying  $C/\alpha$  [MJ/pcm] by the previously determined  $\alpha$  [pcm/K] of table 5.9, gives an estimation of the point-reactor's heat capacity, which reads  $C \approx 14 - 21 \text{ MJ/K}$ . On the basis of the graphite mass of both the reflectors and the pebble bed, and the specific heat capacity of the graphite, a heat capacity for the reactor of 100-200 MJ/K is found, which

is an order of magnitude larger. The discrepancy is probably due to the fact that on the time scale of a single power surge most of the energy is deposited in only a part of the pebble bed, which means that the heat capacity is effectively much smaller. Assuming that the 'active' part of the pebble bed has a height of 1 m, we have a graphite volume of  $4.4 \cdot 10^6 \text{ cm}^3$ ; in combination with a volumetric heat capacity of  $3.5 \text{ J cm}^{-3} \text{ K}^{-1}$  at  $1100 \text{ }^\circ\text{C}$  (according to [44]) this gives an effective heat capacity of  $C = 15 \text{ MJ/K}$ , which is in a better agreement with previously mentioned ones.

## Point-reactor heat capacity. II

One of the results of ref. [89]'s linear stability analysis for the point-reactor under passive cooling conditions is eq. 5.18, where  $T_{osc}$  is the oscillation period of the reactivity and  $P_o$  is the equilibrium fission power. Table 5.9 shows that the  $C/\alpha$ -values according to eq. 5.18 are, in general, in good agreement with those of eq. 5.17. The largest discrepancy is found in case of 1 g/pebble at EOL.

## 5.7 Conclusions

In this chapter, the behaviour of the HTR-Pu with loadings of 1 and 2 g Pu/pebble was investigated. Special attention was paid to the passive safety features of the system. Two loss-of-forced-cooling incidents without scram were simulated. In all cases, the temperature remained well below the presumed temperature limit of  $1444 \text{ }^\circ\text{C}$ . Table 5.10 shows the asymptotic temperatures that were obtained in the various loss-of-cooling incidents. The asymptotic temperatures are calculated as

$$T_{max}(100 \text{ h}) = T_{max}(0 \text{ h}) + \Delta T_{max}(0 \rightarrow 100 \text{ h}) \quad , \quad (5.24)$$

where the quantities at the RHS are listed in table 5.9. The following can be inferred from

**Table 5.10:** *Asymptotic maximum temperatures (i.e. at 100 hours after the beginning of the transient) for the Pu-loadings of 1 and 2 g/pebble, the BOL and EOL cores and two loss-of-cooling scenarios (LOCI and LOFI).*

Pu-loadings core	1 gram/pebble				2 gram/pebble			
	BOL		EOL		BOL		EOL	
scenario	LOCI	LOFI	LOCI	LOFI	LOCI	LOFI	LOCI	LOFI
$T_{max}(100 \text{ h}) [^\circ\text{C}]$	1256	1251	1265	1267	1096	1094	1204	1211

table 5.10:

- The differences between the LOCI and LOFI scenarios are small, which is due to the following.

At 100 hr after the beginning of the transient the power in both the LOCI and the LOFI-case are so small that the xenon concentration is more than 10 times smaller than under nominal conditions. This means that the positive reactivity introduction due to

the decrease of xenon is nearly equal to the xenon defect. At the equilibrium under passive cooling conditions, this positive reactivity is fully compensated by a negative one, realised by an increase of the temperature. As the xenon defect is independent of the loss-of-cooling scenario, the temperature increase is about the same for the LOCI and the LOFI scenario.

- Despite the BOL-cores have higher maximum temperatures at  $t = 0$  than their EOL-counterparts, their asymptotic maximum temperature are lower than those of the EOL cores. This is because of a much smaller  $\Delta T_{max}(0 \rightarrow 100 \text{ h})$ , which is due to both a lower xenon defect and a stronger negative temperature coefficient for the BOL-core.
- The Pu-loadings of 2 g/pebble show lower asymptotic temperatures than those of 1 g/pebble. This is due to a lower xenon defect and a stronger negative temperature coefficient for the Pu-loading of 2 g/pebble.

As far as the start-up is concerned, the Pu-loading of 2 g/pebble has preference, because in that case the power coefficient is negative for the entire power range from 0 to 40 MW<sub>th</sub>. The reactivity of the Pu-loading of 1 g/pebble exhibits a maximum at 15 MW<sub>th</sub>; below this maximum, the power coefficient is positive. The consequences of these findings for the safety during start-up and shut-down as well as for the safety of reactor operation below 15 MW<sub>th</sub> have to be investigated in future studies.

## 5.8 Recommendations for follow-up research

The presented conceptual design of the pebble-bed HTR fuelled with pure reactor-grade plutonium and the accompanying full-core calculations are the first of their kind. Until so far, no optimisation of the design and no verification of the calculational method (as far as a *Pu-fuelled* pebble-bed reactor is concerned), have been performed yet. Therefore, future research should embrace both optimisation of the reactor design, and refinement and verification of the calculational method. Below, some recommendations for further investigations are presented:

### 5.8.1 Recommendations with regard to the calculations

In order to improve, extend and verify the existing calculations the following recommendations are given:

- The current calculational model has hexagonal meshes with sides of 10.4 cm and a height of 12 cm. Since the diffusion length ( $L$ ) is minimally 12 cm (for fresh fuel), refinement of the mesh may be considered for future calculations.
- The current calculations are based on two energy groups. The number of groups may be extended with a high-energy group. An important parameter with regard to performance of the graphite matrix and the coatings is the fast fluence ( $> 0.1 \text{ MeV}$ ) [28]. To be able to calculate the fast fluence in the core, a third group with a lower boundary of 0.1 MeV should be included. The time-integrated flux of this group yields the fast fluence.
- The data generation was performed for one historical power density. As the power density determines the nuclide composition as a function of burnup, it is recommended



to generate a database with more than one historical power density, so that PANTHER can interpolate between data belonging to different power density histories.

- In THERMIX a 'homogeneous' model for the pebble bed was adopted, which means that each mesh possesses a single temperature. This temperature is associated with the surface temperature of a pebble and does not give any information of the pebble's temperature profile. For a given surface temperature, the temperature profile and hence the maximum temperature in the pebble can be determined by the power density distribution inside the pebble. The maximum temperature (at the center) should of course not exceed the maximally permissible temperature for the coated particles. The higher the power generated by a pebble, the larger the difference between the maximum temperature and the surface temperature. In a loss-of-cooling event the maximum power density is of the order of only 1% of the nominal power density, which means that the temperature gradient inside a pebble is very weak. This implies that the maximum temperature hardly deviates from the surface temperature, which is illuminated by the following. Taking into account a power density of  $0.11 \text{ W cm}^{-3}$  (i.e. 1% of the maximum power density under nominal conditions) and a conservative (i.e. low) graphite heat conductivity coefficient of  $\lambda = 10 \text{ W m}^{-1} \text{ K}^{-1}$ , eq. B.7 shows that the maximum temperature difference inside a pebble becomes approximately  $4.3 \text{ }^\circ\text{C}$ .

However, under nominal conditions the maximum temperature may be significantly higher than the surface temperature, and hence a heterogeneous treatment of a pebble that accounts for a temperature gradient inside it is necessary. Since THERMIX' possibility to model the pebble bed in a heterogeneous sense has not been exploited yet, this remains an issue for follow-up calculations.

- The loss-of-cooling events that were investigated refer to pre-defined scenarios. However, in a realistic loss-of-cooling scenario there exists an interaction between the core and the energy conversion system. At NRG, a coupling between PANTHERMIX (neutronic/thermal-hydraulic core calculations) and RELAP (used for the thermal-hydraulics of the energy conversion system) which accounts for that interaction is being developed [113, 114]. In future studies, more realistic loss-of-cooling scenarios for the HTR-Pu can be simulated using the PANTHERMIX-RELAP system.

## 5.8.2 Recommendations with regard to the design

As mentioned before, the conceptual design of the HTR-Pu presented in this thesis is only a first try. This means that modifications are necessary to optimise the concept. Below, some ideas with regard to the modification of the design are given.

- Fig. 5.11 shows that the power density is relatively high at BOL. Furthermore, fig. 5.13 indicates that the maximum power density occurs in the pebbles just above the bottom reflector. This is due to the thermalising influence of the bottom reflector. Since the pebbles constitute a relatively fast system (i.e. the pebble bed itself is quite strongly under-moderated) the surrounding graphite reflectors contribute significantly to the slowing-down process. The neutrons undergo, so to speak, a 'thermalisation shock' in the reflectors. The relatively high thermal flux in the vicinity of the reflector causes a high local power density at BOL.

This high local power density could be reduced by flattening the power profile, which

will most probably be accompanied by a flattening of the temperature profile. This allows one to increase the reactor power without exceeding the temperature limits, which is of course advantageous from the economical point of view.

Flattening of the power-density profile can probably be established by adding burnable poisons in the reflectors. A suitable candidate would be  $\text{Er}_2\text{O}_3$  (erbium oxide) because of its expected negative contribution to the reflector temperature coefficient. However, it is probable that the gain in reactor power, made possible by the flattening of the power-density profile, will be at the cost of the burnup at EOL, since more neutrons are parasitically absorbed by the poison and are, therefore, not available for the conversion from even to odd Pu-isotopes. It is clear that this trade-off is amenable to optimisation procedures, e.g. the maximisation of an objective function  $G$  with respect to the Er-concentration. This objective function could be constructed as  $G(Er) = w_1 P(Er) + w_2 BU_{ave,EOL}(Er)$  where  $P$  is the reactor power and  $BU_{ave,EOL}$  is the average burnup at EOL, which are functions of the Er-concentration  $Er$ . The weights  $(w_1, w_2)$  depend on the choice of the user.

- A more exotic option in this respect could be to start with a pebble-bed layer of which its constituent pebbles do not contain fuel but a burnable poison. A suggestion is to use  $^{99}\text{Tc}$ -bearing coated particles in these pebbles, for why should one not use a neutron absorber that has positive side-effects in terms of radiotoxicity reduction? As the thermal cross section of  $^{99}\text{Tc}$  is not so high (19 barn) ([115] and p. 37 of [1]), one should take advantage of the large 5.6-eV resonance (total cross section at the resonance energy of the lowest-lying resonance:  $\sigma_0 = 4.6 \cdot 10^3$  barn, according to JEF2.2 [58]). A high effective one-group cross section could be established by dilution (i.e. by sufficiently small coated  $^{99}\text{Tc}$  particles), since this results in a high resonance integral. It is clear that such a burnable- $^{99}\text{Tc}$  concept should be subject to a parameter study, in which the  $^{99}\text{Tc}$ -mass per pebble, the number of  $^{99}\text{Tc}$ -pebbles and the size of the  $^{99}\text{Tc}$ -kernels are to be varied.
- In this thesis, only one type of pebble per batch has been considered. However, the pebble-bed HTR offers great flexibility concerning fuelling scenarios. One might consider, for instance, to start the reactor with an initial core with pebbles of a particular type and proceed thereafter by adding pebbles of another type. Moreover, a mixture of fuel pebbles and moderator pebbles belongs to the possibilities. Whether such concepts enable a flattening of the power profile or an enhancement of the burnup has to be investigated in future studies.
- Only some aspects of the start-up procedure of the HTR-Pu are illuminated until so far. A more extensive study needs to be performed in the future. In particular, loss-of-cooling incidents for the (1 g Pu/pebble, EOL)-core operated at a power  $< 15 \text{ MW}_{th}$  might be interesting, because of the positive power coefficient of reactivity in that range.

# Chapter 6

---

## Conclusions & Discussion

---

This thesis presents a conceptual design of the pebble-bed High Temperature Reactor dedicated to the burning of reactor-grade plutonium. To obtain the maximum TRU-consumption rate in combination with a low TRU-discharge rate in terms of mass per unit of thermal energy produced, the fuel considered in the calculational models consists of pure reactor-grade plutonium and hence contains neither uranium or thorium, nor any burnable poisons. Point of departure as regards the design of the HTR-Pu is the preservation of the passive safety features, like present in HTRs that are operated with conventional  $\text{UO}_2$ -fuel.

### 6.1 Conclusions

#### Temperature coefficients of reactivity.

As far as the safety of the system is concerned, the temperature coefficients of reactivity play an essential role. The coefficients of both the fuel and the moderator have been investigated thoroughly in this thesis. The primary conclusions following from this study read:

- Despite the absence of  $^{238}\text{U}$ , the fuel temperature coefficient of the Pu-fuel is negative. The fuel temperature coefficient increases, in absolute sense, with increasing Pu-loading.
- The moderator temperature coefficient is much stronger than the fuel temperature coefficient and, moreover, shows some unconventional behaviour. For a low plutonium mass per pebble as well as for a high plutonium mass per pebble in combination with a high burnup, it decreases from a positive value at a low moderator temperature to a negative value at a higher temperature. However, for a high plutonium mass per pebble in combination with a low burnup it is negative in the full moderator-temperature range of interest.

Because of the latter properties, the quite strongly under-moderated configurations of 1 and 2 g Pu/pebble were considered as suitable candidates to operate the HTR-Pu with. Loadings of 3 g Pu/pebble and higher were discarded because the fast fluence at 700 MWd/kgHM exceeds the presumed maximally permissible value. Full-core thermal-hydraulics/neutronics-coupled calculations referring to a  $\text{Pu}$ -à- $\text{Pu}$  type pebble-bed HTR, were carried out for both Pu-loadings. The main conclusions that can be drawn from these calculations read:

**Burnup.**

The loading of 2 g Pu/pebble yields a slightly higher burnup than its 1 g counter part. The burnup of the '2 g' reactor reads 643 MWd/kgHM (average) and 740 MWd/kgHM (maximum). This corresponds to:

$$\begin{aligned}\text{Transuranic Mass Consumption} &= 375 \text{ kg/GW}_{\text{th,a}} \\ \text{Transuranic Mass Discharge} &= 195 \text{ kg/GW}_{\text{th,a}}\end{aligned}$$

See fig. 1.5 on page 10 for a comparison with other Pu-burners. The maximum burnup of 740 MWd/kgHM equals the maximum burnup for which the integrity of Pu-bearing coated particles was demonstrated in irradiation experiments in the 1970s.

**Start-up & Shut-down.**

The reactor design with 1 g Pu/pebble shows a positive power coefficient at low powers (End Of Life, Zero Xenon), which might pose stability problems. Since the power coefficient of the 2 g reactor is negative in all cases, this design has preference.

On the basis of the preceding two categories one can conclude that the loading of 2 g Pu/pebble has preference.

**Passive Safety.**

In the case of two postulated loss-of-cooling incidents without scram, the maximum temperature during the transients remains well below the maximally permissible one, implying that no (significant) release of radioactivity occurs. As far as these loss-of-cooling incidents are concerned the HTR-Pu turns out to be passively safe.

**Radiotoxicity.**

As mentioned above the HTR-Pu is able to realise a high transuranic-mass destruction rate. Whether this also results in a reduction of the radiotoxicity depends on the composition of the spent Pu-fuel in comparison with that of the fresh Pu-fuel. Fig. 6.1 shows the radiotoxicity production in Sv per generated  $\text{GW}_{\text{th,a}}$ . This reveals that the HTR-Pu is responsible for a radiotoxicity increase in the first  $\sim 30$  years, while in the period thereafter up to 10,000 years it provides for a reduction of the radiotoxicity. The radiotoxicity production in the first period stems from  $^{244}\text{Cm}$  and  $^{238}\text{Pu}$  in the spent Pu-fuel.

**Introducing the HTR-Pu in the fuel cycle.**

The previously mentioned transuranic mass consumption and discharge rates imply a plutonium supply to the HTR-Pu of 570 kg/ $\text{GW}_{\text{th,a}}$ . Since the Pu-discharge of a PWR (burnup = 47.5 MWd/kgHM,  $\epsilon = 33\%$ ) amounts to  $\sim 90$  kg/ $\text{GW}_{\text{th,a}}$ , this would allow a symbiosis of a PWR and a HTR-Pu with thermal power contributions of 86% and 14%, respectively. In terms of power stations, this means one PWR (1  $\text{GW}_e$ ,  $\epsilon = 33\%$ ) in combination with 12 HTR-Pu modules (40  $\text{MW}_{\text{th}}$ ,  $\epsilon = 40\%$ ), generating 1.2  $\text{GW}_e$  together. Fig. 6.2 shows the radiotoxicity generated by such a park ("PARK B") in comparison with a conventional park consisting solely of PWRs ("PARK A").

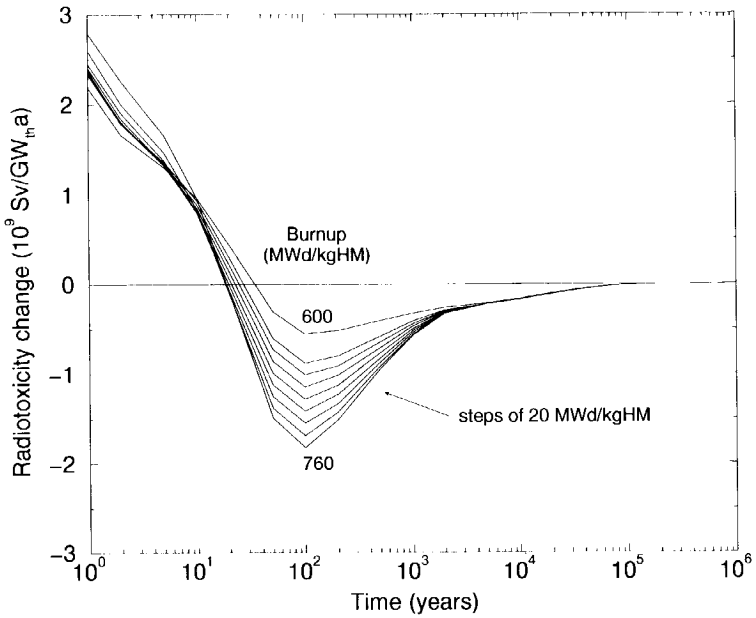


**Figure 6.1:** Radiotoxicity (ingestion) change due to plutonium burning in the HTR-Pu, expressed in  $10^9$  Sv/GW<sub>th,a</sub>. The radiotoxicity change refers to the difference between spent Pu-fuel and fresh Pu-fuel normalised to the thermal energy produced.

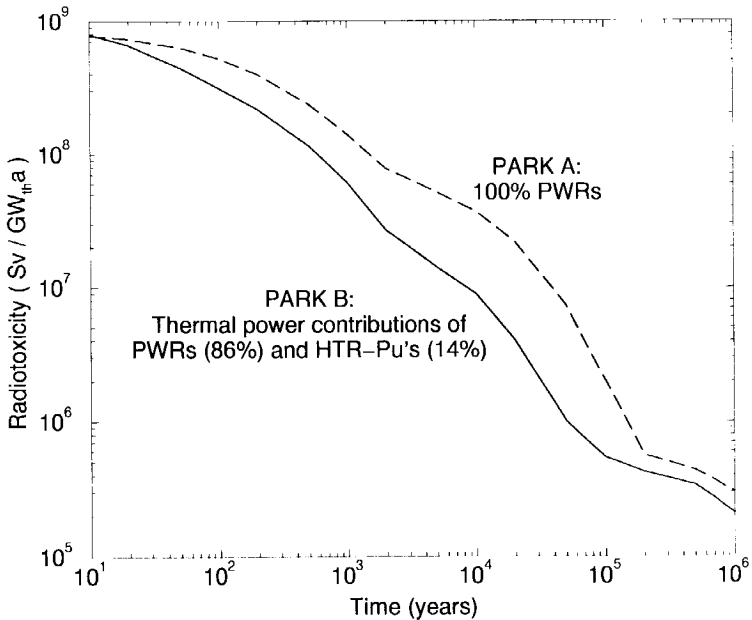


**Figure 6.2:** Generated radiotoxicity (ingestion) due to a conventional park of PWRs, on the one hand, and due to a park consisting of PWRs and Pu-burning HTRs, on the other.

## 6.2 Discussion

### Comparison with other U-free fuels.

Presently, much efforts are made to develop inert matrices as support materials for plutonium [116] with the aim to achieve the maximum Pu-incineration rate. These matrices ( $\text{MgO}$ ,  $\text{Al}_2\text{O}_3$ ,  $\text{MgAl}_2\text{O}_4$ , etc.) have to meet a variety of selection criteria, which have to be examined in experiments. In this respect, it is good to realise that the Pu-bearing HTR pebbles in fact constitute an inert-matrix fuel. Moreover, the pebble-bed HTR is a system whose neutronic, chemical and physical properties are well known for more than two decades. Therefore, one might say that the pebble-bed HTR has a considerable lead in comparison with all inert matrix fuels that are presently under investigation. However, as far as reprocessing is concerned, HTR fuel has some unfavourable properties compared to other fuel types. The reprocessing is complicated because of the excellent encapsulation of the fuel by the coated particles. Some techniques were proposed to separate the fuel kernels from the pebbles. As these techniques seem to be rather complex, the generally adhered strategy to date is to refrain from reprocessing and to dispose of the pebbles directly.

### Comparison with other Pu-burners.

Obviously, the HTR-Pu realises a much higher TRU-consumption rate than MOX-fuelled reactors. Compared to U-free reactor concepts, as discussed in chapter 1 (see fig. 1.5 on p. 10), the HTR-Pu shows a lower TRU-discharge rate than the fast reactor concept (CAPRA-Inert Matrix) which is due to a lower burnup of the latter. This may be attributed to material restrictions as well as to reactivity restrictions due to the fixed core without breeding blankets. The Molten Salt Reactor with on-line plutonium fuelling and on-line fission product removal has, regardless of small losses, no TRU-discharge whatsoever. As far as this feature is concerned the Molten Salt Reactor is to be preferred. However, the Molten Salt Reactor is quite an exotic concept which requires still a lot of research, while the HTR-Pu seems to be a far more realistic concept, based on proven technology, and moreover having favourable safety features.

### Water ingress.

The HTR-Pu presented in this study is a strongly under-moderated system, which implies that water/steam ingress is under no circumstances acceptable since this will lead to a positive reactivity introduction. Therefore, the steam cycle for the HTR-Pu was discarded and instead a direct gas turbine cycle was envisaged. The HTR-Pu is based on the ACACIA design, which involves a Closed Cycle Gas Turbine system with a secondary helium loop under high pressure.

### Optimisation of the HTR-Pu.

From the economical point of view it is desirable to increase the reactor power per module. Flattening of the power density profile allows an increase of the total power without the power density exceeding the maximally permissible value. As the maximum power density occurs in the pebbles of the fresh core that are adjacent to the bottom reflector, it is useful to consider a fresh core of which the bottom layer of pebbles contains a burnable poison. In this way, the profile will be flattened, which enables an increase of the reactor power. Furthermore, cores that contain pebbles with different Pu-loadings might be considered.

## References

- [1] H. Gruppelaar, J.L. Kloosterman, and R.J.M. Konings. *Advanced Technologies for the Reduction of Nuclear Waste*. Technical Report ECN-R-98-008, Netherlands Energy Research Foundation (ECN), Petten, The Netherlands, 1998.
- [2] *NEW. Nuclear Europe Worldscan (from report on Waste and Decommissioning 1993-94, Scottish Nuclear Ltd. Redwood Crescent, East Kilbride G74 5PR, UK)*, 11-12:30, 1994.
- [3] J.A.B. Gresley. *Urenco Experience in Enriching Reprocessed U*. *NEW. Nuclear Europe Worldscan*, 11-12:42-43, 1994.
- [4] D. Albright, F. Berkhout, and W. Walker. *Plutonium and Highly Enriched Uranium 1996. World Inventories, Capabilities and Policies*. Oxford University Press, 1997.
- [5] OECD/NEA. *The Economics of the Nuclear Fuel Cycle*. Technical Report ISBN 92-64-14154-5, Organisation for Economic Co-operation and Development, Paris, France, 1994.
- [6] ICRP. *Dose coefficients for Intakes of Radionuclides by Workers. Replacement of ICRP publication 61*. Technical Report Publication 68, ICRP, 1994.
- [7] N. Cadelli, P. Escalier des Orres, J. Marivoet, K.H. Martens, and J. Prij. *Evaluation of Elements Responsible for the Effective Engaged Dose Rates Associated with the Final Storage of Radioactive Waste: EVEREST project*. Technical Report EUR 17122 EN, European Commission, Brussels, Luxembourg, 1996.
- [8] E.E. Bende and J.L. Kloosterman. *A comparison of Pu-burning in advanced reactors*. *NEW. Nuclear Europe Worldscan*, 5-6:42, 1998.
- [9] J.L. Kloosterman. *Ecn's contribution to oecd wppr plutonium recycling benchmark, defined in document nea/sen/nsc/wppr(95)1*. Technical report, Netherlands Energy Research Foundation (ECN), Petten, The Netherlands, 1995.
- [10] J.C. Garnier, R. Sunderland, T. Newton, E. Kiefhaber, and D. Verrier. *CAPRA PRELIMINARY FEASIBILITY STUDIES. Oxide Reference Option: Neutronics and Design Studies*. Technical Report RT-SIS/CAPRA-94-003, CEA, Cadarache, France, 1994.
- [11] A. Conti, J.C. Garnier, P. Lo Pinto, and W. Mascheck. *CAPRA PRELIMINARY FEASIBILITY STUDIES. Synthesis of Exploratory Studies on Pu without U cores*. Technical Report NT-SIS/CAPRA-94-1009A, CEA, Cadarache, France, 1994.

- [12] J.H. Bultman. *Actinide Transmutation in Nuclear Reactors. (PhD-Thesis)*. Technical Report ECN-R-95-004, Netherlands Energy Research Foundation (ECN), Petten, The Netherlands, January 1995.
- [13] J.H. Bultman. *Molten salt reactor: optimal transuranics burner. (appeared also as a chapter in Technical Report ECN-RX-95-035, ECN, the Netherlands)*. In *GLOBAL'95, Versailles, France*, page 1616, September 1995.
- [14] M. Khorochev and E. Teuchert. *Use of Plutonium in Pebble Bed HTRs in a Two Ball Type Concept*. In *IAEA Technical Committee Meeting on Advanced Fuels with Reduced Actinide Generation*, pages 1–5, November 1990.
- [15] M. Khorochev and E. Teuchert. *Use of Plutonium in Pebble Bed HTRs in a Two Ball Type Concept*. In *Jahrestagung Kerntechnik'96*, pages 43–46, May 1996.
- [16] M. Khorochev. *Nutzung von Plutonium im Kugelhaufen-Hochtemperaturreaktor. (Dissertation)*. Technical report, Fakultät für Maschinenwesen, Technischen Hochschule Aachen, 1996.
- [17] J.L. Kloosterman. *ECN Results of the PSI Benchmarks on Non-fertile Fuels*. Technical Report ECN-R-97-014, Netherlands Energy Research Foundation (ECN), Petten, The Netherlands, October 1997.
- [18] H. Bairiot, L. Aerts, E. Trauwaert, and J. Vangeel. *Plutonium Coated Particle Development*. *Nuclear Technology*, 23:240–255, September 1974.
- [19] D. Alberstein *et al.* *MHTGR Plutonium Consumption Study Phase II Final Report*. Technical Report GA/DOE-051-94, General Atomics, PO BOX 85608, San Diego, CA 92186-9784, April 1994.
- [20] P. Barr, N. Pollitt, G.B. Redding, A. Sorensen, and P. Svensson. *High-Temperature Irradiation Experiments on Plutonium-Bearing Coated Particle Fuel*. In *Proc. of Symp. on Plutonium as a Reactor Fuel, IAEA, Brussels, SM-88/38*, pages 391–417, 1967.
- [21] N.G. Hoogen and E.R. Merz. *Evaluation of potential head-end procedures for graphite-containing fuel elements*. *Nuclear Technology*, 61:380–387, 1983.
- [22] R.P.C. Schram and J.Prij. *Back-End of the HTR Fuel Cycle*. Technical Report ECN-I-97-015, Netherlands Energy Research Foundation (ECN), Petten, The Netherlands, September 1997.
- [23] B.R.W. Haverkate, A.I. van Heek, and J.F. Kikstra. *An HTR Cogeneration System for Industrial Applications*. Technical Report ECN-RX-99-001, Netherlands Energy Research Foundation (ECN), Petten, The Netherlands, January 1999.
- [24] P.M. Williams, T.L. King, and J.N. Wilson. *Draft preapplication safety evaluation report for the modular high-temperature gas-cooled reactor*. Technical Report NUREG-1338, U.S. Nuclear Regulatory Commission, March 1989.
- [25] *Conceptual Design Summary Report Modular MHTGR Plant*. Technical Report DOE-HTGR-87-092, Bechtel National Inc, September 1987.



- [26] *Conceptual Design Summary Report Modular MHTGR Plant*. Technical Report DOE-GT-MHR-100002, Gas-Cooled Reactor Associates, San Diego, California, USA, February 1994.
- [27] W.A. Simon, A.J. Neylan, and F.A. Silady. *Design Features of the Gas Turbine Modular Helium Reactor (GT-MHR)*. Technical Report GA-A21351, General Atomics, PO BOX 85608, San Diego, CA 92186-9784, June 1993.
- [28] K. Kugeler and R. Schulten. *Hochtemperaturreaktortechnik*. Springer-Verlag, 1989.
- [29] R. Schulten *et al.* *Der Hochtemperaturreaktor*. *Die Atomwirtschaft*, 9, 1959.
- [30] R. Schulten, W. Bellermann, H. Braun, H.W. Schmidt, A. Setzwein and W. Stürmer. *Der Hochtemperaturreaktor von BBC/Krupp*. *Die Atomwirtschaft*, 1959.
- [31] M. Cautius, J. Engelhard, and G. Ivens. *Der Betrieb des Versuchskraftwerks AVR und die HTR-Entwicklung*. *Atomwirtschaft/Atomtechnik*, 8/9, 1959.
- [32] H. Knüfer. *Preliminary operating experiences with the AVR reactor at an average hot gas temperature of 950 degC*. *Nuclear Engineering and Design*, 34, 1975.
- [33] R. Schulten and F. Schniedel. *Kurzbeschreibung des THTR-300 MWel. Ergebnisbericht des THTR-Projektes Jülich*, July 1968.
- [34] E. Baust. *Inbetriebnahme des THTR-300*. *Atomwirtschaft/Atomtechnik*, 1985.
- [35] H. van Dam. *Physics of Nuclear Reactor Safety*. *Rep. Prog. Phys.*, 11:2025–2077, 1992.
- [36] D. Mathews and R. Chawla. *LEU-HTR PROTEUS Computational Benchmark Specifications*. Technical Report TM-41-90-32, Paul Scherrer Institut, Labor für Reaktorphysik and Systemtechnik, Villigen, Switzerland, October 1998.
- [37] H. Sommer and B. Ribbat. *GHR 10 MW: The technical concept of a gas cooled heating reactor*. *Nuclear Engineering and Design*, 109:123–128, 1988.
- [38] H. Schmitt. *The 20 MW gas cooled heating reactor*. *Nuclear Engineering and Design*, 121:287–291, 1990.
- [39] E. Teuchert, H. Gerwin, and K.A. Haas. *Simplification of the pebble bed high-temperature reactor*. In *International Specialists' Meeting on Potential of Small Nuclear Reactors for Future Clean and Safe Energy Sources*. Tokyo, October 23-25, 1991., 1991.
- [40] E. Teuchert, H. Gerwin, K.A. Haas, R. Schulten, and Y. Sun. *Features of passive control of a small pebble bed HTR for gas turbine cycle*. In *Eighth Proceedings of Thermal Hydraulics Division of the ANS*, November 1992.
- [41] E. Teuchert, K.A. de Haas, Y. Sun, and A. Dudkin. *Strikte Ausnutzung der Eigenschaften des Kugelhaufen-Hochtemperaturreaktors*. *Monographien des Forschungszentrum Juelich*. *Fortschritte in der Energietechnik*. Herausgegeben von K. Kugeler, H. Neis. G. Ballensiefen. Technical Report Band 8, Forschungszentrum Juelich GmbH, Juelich, Germany, 1993.

- [42] E. Teuchert and K.A. Haas. *Features of safety and simplicity of advanced pebble bed HTR's, IAEA TCM on Development Status of Modular High Temperature Reactors and their Future Role*. Technical Report ECN-R-95-026, Netherlands Energy Research Foundation (ECN), Petten, The Netherlands, September 1995.
- [43] K.G. Hackstein, W. Heit, W. Theymann, and G.Kaiser. *Stand der Brennelementtechnologie für Hochtemperatur-Kugelhaufenreaktoren*. *Atomenergie-Kerntechnik*, 47/3, 1985.
- [44] S. Struth. THERMIX-DIREKT: Ein Rechenprogramm zur instationären, zweidimensionalen Simulation thermohydraulischer Transienten. Forschungszentrum Juelich GmbH, September 1995.
- [45] E. Teuchert, H.J. Ruetten, and K.A. de Haas. *Rechnerische Darstellung des HTR-Modul Reaktors*. Technical Report Juel-2618, Forschungszentrum Juelich GmbH, Juelich, Germany, May 1992.
- [46] T.D. Gulden and H. Nickel. *Coated particle fuel*. *Nuclear Technology*, 35:206–213, 1977.
- [47] K. Verfondere, W. Schenk, and H. Nabelek. *Passive Safety Characteristics of Fuel for a Modular High-Temperature Reactor and Fuel Performance Modeling under Accident Conditions*. *Nuclear Technology*, 91:235–246, 1990.
- [48] K. Verfondere and H. Nabelek. *PANAMA ein Rechenprogramm zur Vorhersage des Partikelbruchanteils von TRISO-Partikeln unter Störfallbedingungen*. Technical Report Juel-Spez.-298, Forschungszentrum Juelich GmbH, Juelich, Germany, February 1985.
- [49] H. Nabelek, W. Schenk, W. Heit, A.W. Mehner, and D.T. Goodin. *The Performance of High-Temperature Reactor Fuel Particles at Extreme Temperatures*. *Nuclear Technology*, 84:62–81, 1989.
- [50] IAEA. *Fuel performance and fission product behaviour in gas cooled reactors*. Technical Report IAEA-TECDOC-978, IAEA, 1997.
- [51] P. Groot, E.H.P. Cordfunke, and R.J.M. Konings. *The Chemical Stability of TRISO-coated HTGR Fuel. Part I. Status report*. Technical report, Netherlands Energy Research Foundation (ECN), Petten, The Netherlands, ECN-I-94-055.
- [52] K. Minato *et al.* *Fission Product Palladium-Silicon Carbide Interaction in HTGR Fuel Particles*. *Journal of Nuclear Materials*, 172:184–196, 1990.
- [53] R.W. Mills. *Fission Product Yield Evaluation (PhD-Thesis)*. Technical report, School of Physics and Space Research, University of Birmingham, March 1995.
- [54] K. Minato, T. Ogawa, and K. Fukuda. *Review of experimental studies of zirconium carbide coated fuel particles for high temperature gas-cooled reactors*. Technical Report JAERI-REVIEW-95-004, Tokai-mura (JA) : Japan Atomic Energy Research Institute, 1995.

- [55] E.E. Bende. *Unit-cell Calculations for Plutonium Fuelled HTR pebbles*. Technical Report ECN-R-98-023, Netherlands Energy Research Foundation (ECN), Petten, The Netherlands, December 1998.
- [56] N.M. Greene. *BONAMI-S, Resonance Self-Shielding by the Bondarenko Method*. Oak Ridge National Laboratory, Oak Ridge, Tennessee, USA, August 1981.
- [57] N.M. Greene *et al.* *NITAWL-II, SCALE Module for Performing Resonance Shielding and Working Library Production*. Oak Ridge National Laboratory, Oak Ridge, Tennessee, USA, June 1989.
- [58] R.C.L. van der Stad *et al.* *EIJ2-XMAS Contents of the JEF2.2 based Neutron Cross Section Library in the XMAS Group Structure*. Technical Report ECN-CX-95-087, Netherlands Energy Research Foundation (ECN), Petten, The Netherlands, February 1996.
- [59] J. Oppe and J.C. Kuijper. *WILITO VERSION 9502 (WIMS Library Tool)*. Technical Report ECN-CX-95-010, Netherlands Energy Research Foundation (ECN), Petten, The Netherlands, March 1995.
- [60] A. Hogenbirk *et al.* *HTR-Proteus Benchmark Calculations*. Technical Report ECN-C-95-087, Netherlands Energy Research Foundation (ECN), Petten, The Netherlands, September 1995.
- [61] K.M. Case, F. de Hoffmann, and G. Placzek. *Introduction to the Theory of Neutron Diffusion*. Los Alamos Scientific Laboratory, 1953.
- [62] E.C. Verkerk. *Resonance treatment with the Subgroup Method in WIMS*. Technical Report ECN-I-98-061, Netherlands Energy Research Foundation (ECN), Petten, The Netherlands, (To be published) 1998.
- [63] AEA Technology. *The ANSWERS Software Package WIMS. (A WIMS Modular Scheme for Neutronics Calculations)*. User Guide. ANSWERS/WIMS(95)4, Issue 3. Atomic Energy Agency Technology (AEA), Winfrith, United Kingdom, 1997. AEEW-R-2442.
- [64] E.E. Bende, A.H. Hogenbirk, J.L. Kloosterman, and H. van Dam. *Analytical Calculation of the Average Dancoff-factor for a fuel kernel in a Pebble-Bed High Temperature Reactor*. *Nuclear Science and Engineering*, 133:147–162, October 1999.
- [65] N.M. Greene and L.M. Petrie. *XSDRNPM-S, A One-Dimensional Discrete-Ordinates Code for Transport Analysis*. Oak Ridge National Laboratory, Oak Ridge, Tennessee, USA, January 1983.
- [66] J.F. Briesmeister. *MCNP-4A: A General Monte Carlo Code for Neutron and Photon Transport*. Technical Report LA-7396-M, Rev 2, Los Alamos National Laboratory, Los Alamos, New Mexico, USA, 1986.
- [67] A. Hogenbirk. *EJ2-MCNP. Contents of the JEF-2.2 based neutron cross section library for MCNP4A*. Technical Report ECN-I-95-017, Netherlands Energy Research Foundation (ECN), Petten, The Netherlands, May 1995.

- [68] E.E. Bende. *Transmutation of Plutonium in Pebble Bed Type High Temperature Reactors*. In *GLOBAL'97, Yokohama, Japan*, pages 378–383. Japan Atomic Energy Research Institute (JAERI) and the Power Reactor and Nuclear Fuel Development Corporation (PNC), October 1997.
- [69] J.J. Duderstadt and L.J. Hamilton. *Nuclear Reactor Analysis*. John Wiley and Sons, 1986.
- [70] W.J.M. de Kruijf and A.J. Janssen. *On the definition of the fuel temperature coefficient of reactivity for pin-cell calculations on an infinite lattice*. Technical Report ECN-R-93-012, Netherlands Energy Research Foundation (ECN), Petten, The Netherlands, March 1993.
- [71] O.W. Hermann and R.M. Westfall. *ORIGEN-S, SCALE Module to Calculate Fuel Depletion, Actinide Transmutation, Fission Product Buildup and Decay, and Associated Radiation Source Terms*. Oak Ridge National Laboratory, Oak Ridge, Tennessee, USA, February 1989.
- [72] J.L. Kloosterman, J.C. Kuijper, and P.F.A. de Leege. *The OCTOPUS Burnup and Criticality Code System*. Technical Report ECN-RX-96-032, Netherlands Energy Research Foundation (ECN), Petten, The Netherlands, June 1996.
- [73] J. Kopecky *et al.* *The European Activation File EAF3 with Neutron Activation and Transmutation Cross Sections*. Technical Report ECN-C-92-058, Netherlands Energy Research Foundation (ECN), Petten, The Netherlands, September 1992.
- [74] E.E. Bende. *Temperature reactivity effects in pebbles of a High Temperature Reactor fuelled with reactor-grade plutonium without any additional resonance absorbers. (Accepted for publication)*. *Nuclear Technology*, pages –, 1999.
- [75] W.J.M. de Kruijf and A.J. Janssen. *On the definition of the fuel temperature coefficient of reactivity for pin-cell calculations on an infinite lattice*. *Annals of Nuclear Energy*, 20:639–648, 1993.
- [76] J.L. Kloosterman. *PROGRAM VAREX. A tool for Variational Analysis of Reactivity Effects with XSDRNPM*. Technical Report ECN-I-95-037, Netherlands Energy Research Foundation (ECN), Petten, The Netherlands, October 1995.
- [77] J.H. Bultman. *VAREX2. A tool for Variational Analysis of Reactivity Effects with XSDRNPM*. Technical Report NUC-RFA-96-01, Netherlands Energy Research Foundation (ECN), Petten, The Netherlands, February 1996.
- [78] E.E. Bende. *VAREX3. Modification of VAREX2, A tool for Variational Analysis of Reactivity Effects with XSDRNPM. J.H. Bultman, NUC-RFA-96-01*. Technical Report memo 71273/NUC/EB/MH/9500, Netherlands Energy Research Foundation (ECN), Petten, The Netherlands, October 1997.
- [79] E.E. Bende. *Maximisation of the Doppler effect in Thermal Reactors*. Technical Report ECN-R-97-007, Netherlands Energy Research Foundation (ECN), Petten, The Netherlands, March 1998.

- [80] E.E. Bende. *Maximisation of the Doppler effect in Thermal Reactors*. In *International Conference on Emerging Nuclear Energy Systems, ICENES'98, Herzliya, Israel*, pages 92–99. the Israel Nuclear Society, June 1998.
- [81] E.E. Bende. *Maximisation of the Doppler effect in Thermal Reactors*. In *International Conference on the Physics of Nuclear Science and Technology, Long-Island, New-York*, pages 240–247. the American Nuclear Society Inc., La Grange Park, Illinois 60526, USA., October 1998.
- [82] K. Schwarzer. *Abschätzung der  $^{14}\text{C}$ -Produktion in einem Hochtemperaturreaktor*. Technical Report KFA-ISF-IB-10/75, Forschungszentrum Juelich GmbH, Juelich, Germany, 1975.
- [83] H. Bonka. *Strahlenschutzprobleme im Zusammenhang mit der Verwendung von Tritium und Kohlenstoff-14 und ihren Verbindungen of STF Berichte, chapter 2.3, pages 17-26*, volume 12. Dietrich Reimer Verlag, 1980.
- [84] J.L. Kloosterman and E.E. Bende. *Plutonium Recycling in PWRs: Influence of the moderator-to-fuel ratio*. *Nuclear Technology*, 1999, accepted for publication.
- [85] S.F. Mughabghab. *Neutron Cross Sections, Part B*. Academic Press, 1984.
- [86] G.I. Bell and S. Glasstone. *Nuclear Reactor Theory*. Van Nostrand Reinhold Company, 1970.
- [87] N. Fujimoto, K. Yamashita, and H.J. Ruetten. *Study on Temperature Coefficients of Actinide Burning HTGRs*. Technical Report Juel-3449, Forschungszentrum Juelich GmbH, Juelich, Germany, 1997.
- [88] H. van Dam. *Dynamics of Passive Reactor Shutdown*. *Progress in Nuclear Energy*, 30:255, 1996.
- [89] H. van Dam. *Role of Neutron Sources, Xenon and Decay Heat Dynamics in Autonomous Reactor Shutdown and Recriticality*. *Nuclear Science and Engineering*, 129:273, 1998.
- [90] X.L. Yan and L.M. Lidsky. *HTR-GT Nuclear Cogeneration. Conceptual Design of the HTR Gas Turbine Cogeneration Plant*. Technical Report LPI-HTR-11019501(96), Longmark Power International, Inc., Cambridge, Massachusetts 02139, USA, April 1996.
- [91] A.I. van Heek. *De vereenvoudigde Kogelbedreactor: Het Peu-à-Peu Concept*. Technical Report ECN-I-95-035, Netherlands Energy Research Foundation (ECN), Petten, The Netherlands, October 1995.
- [92] J.C. Kuijper, J.B.M. de Haas, H.Th. Klippel, A. Hogenbirk, J. Oppe, C.M. Sciolla, R.C.L. van der Stad, and B.C. Zhang. *Reactor Physics Calculations on the Dutch Small HTR Concept*. Technical Report ECN-RX-97-020, Netherlands Energy Research Foundation (ECN), Petten, The Netherlands, June 1997.
- [93] J. Oppe, J.B.M. de Haas, and J.C. Kuijper. *PANTHERMIX - a PANTHER-THERMIX interaction*. Technical Report ECN-I-96-022, Netherlands Energy Research Foundation (ECN), Petten, The Netherlands, May 1996.

- [94] A.I. van Heek, J.C. Kuijper, J.B.M de Haas, and J. Oppe. *INCOGEN. Pre-feasibility Study*. Technical Report ECN-CX-97-015, Netherlands Energy Research Foundation (ECN), Petten, The Netherlands, August 1997.
- [95] S. Pelloni, W. Seifritz, J. Stepanek, P. Stiller, W. Giesser, and D. Leithner. *Parameter study on water ingress in a high temperature reactor*. *Kerntechnik*, 53:233-238, 1989.
- [96] E. Teuchert, K.A. Haas, H.J. Ruetten, and Yuliang Sun. *Reduction of the Reactivity of Water Ingress in Modular Pebble-Bed High-Temperature Reactors*. *Nuclear Technology*, 102:68-72, 1993.
- [97] J.F. Kikstra and A.H.M. Verkooijen. *Dynamic Modeling of a Closed Cycle Gas Turbine CHP Plant with a Nuclear Heat Source*. In ASME, pages 99-GT-002, 1998.
- [98] AEA Technology. WIMS-6/WIMSE User Manual. Atomic Energy Agency Technology (AEA), Winfrith, United Kingdom, 1995. AEEW-R-2442.
- [99] P.K. Hutt. *Overview Functional Specification of PANTHER: A Comprehensive Thermal Reactor Code for Use in Design, Assessment and Operation*. Technical Report PANTHER/FSPEC/OVERVIEW 2.0, Nuclear Electric Plc., UK, December 1992.
- [100] J.L. Rowlands. *Delayed Neutron Yield Data Recommended for Fast and Thermal Reactor Calculations*. Technical Report FRDC/PPWP/P(74)29,RPNK/P(74)51, AEA Technology, October 1975.
- [101] H.Th. Klippel *et al.* *Reactor physics calculations of HTR type configurations*. In *ECN workshop on the role of modular HTRs in the Netherlands, Petten, The Netherlands (Proceedings published by ECN as report ECN-R-95-027, June 1995)*, pages 43-46, June 1994.
- [102] H. Gerwin and W. Scherer. *Treatment of the Upper Cavity in a Pebble-Bed High-Temperature Gas-Cooled Reactor by Diffusion Theory*. *Nuclear Science and Engineering*, 97:9-19, 1987.
- [103] K. Tasaka, J. Katakura, T. Yoshida, T. Kato, and R. Nakasima. *Recommended values of decay heat power and method to utilize the data*. Technical Report JAERI-M 91-034, Japan Atomic Energy Research Institute (JAERI), March 1991.
- [104] J. Banaschek. *Berechnungsmethoden und Analysen zum dynamischen Verhalten von Kraftwerksanlagen mit Hochtemperaturreaktor*. Technical Report Juel-1841 (Dissertation), Forschungszentrum Juelich GmbH, Juelich, Germany, 1983.
- [105] K. Petersen. *Zur Sicherheitskonzeption des Hochtemperaturreaktors mit natürlicher Wärmeableitung aus dem Kern des Hochtemperaturreaktors im Störfall*. Technical Report Juel-1872 (Dissertation), Forschungszentrum Juelich GmbH, Juelich, Germany, 1983.
- [106] K. Vefonderen. *Experimentelle Überprüfung des Thermohydraulikprogramms THERMIX und rechnerische Analyse der transienten Temperatur- und Strömungsfelder im Core-Bereich des THTR-Reaktors nach Ausfall der Nachwärme abfuhr*. Technical Report KFA-IRE-IB-13/78, Forschungszentrum Juelich GmbH, Juelich, Germany, 1978.

- [107] P. Zehner and E. U. Schluender. *Einfluss der Wärmestrahlung und des Druckes auf den Wärmetransport in nicht durchströmten Schüttungen*. *Chemie-Ing.-Technik*, 44:1303, 1972.
- [108] B. Pershagen. *Light Water Reactor Safety*. Pergamon Press, 1989.
- [109] S. Nakagawa, A. Saikusa, and K. Kunitomi. Safety evaluation during a depressurization accident of the sfhtr. In *IAEA Technical Committee Meeting on Safety Related Design and Economic Aspects of High Temperature Gas Cooled Reactors.*, Institute of Nuclear Technology, Tsinghua University, Beijing, China, November 1998.
- [110] H. Gottaut and K. Krüger. *Results of experiments at the AVR reactor*. *Nuclear Engineering and Design*, 121:143–153, 1990.
- [111] K. Krueger *et al.* *Simulation of the Loss-of-Coolant accident with the AVR Reactor. AVR - Experimental High-Temperature Reactor*. Technical Report VDI-Verlag, ASSOCIATION OF GERMAN ENGINEERS (VDI) (Ed.), Duesseldorf, 1990.
- [112] E.C. Verkerk. (*private communications*). Technical report, Netherlands Energy Research Foundation (ECN), Petten, The Netherlands, 1998.
- [113] E.C. Verkerk. *Coupling Thermal Hydraulics with Neutronics for Pebble-Bed High Temperature Reactor Calculations (also appeared as Technical Report ECN-RX-98-047, ECN, the Netherlands)*. In *International Conference on the Physics of Nuclear Science and Technology, Long-Island, New-York*. the American Nuclear Society Inc., La Grange Park, Illinois 60526, USA., October 1998.
- [114] E.C. Verkerk. *Transient Analysis for the High Temperature Pebble-Bed Reactor coupled to the Energy Conversion System (also appeared as Technical Report ECN-RX-98-064, ECN, the Netherlands)*. In *IAEA TCM on Safety Related Design and Economic Aspects of High Temperature Gas-cooled Reactors.*, November 1998.
- [115] R.J.M. Konings, J.L. Kloosterman, J.A. Hendriks, and H. Gruppelaar. *Transmutation of Technetium in the Petten High Flux Reactor: A comparison of Measurement and Calculations*. *Nuclear Science and Engineering*, 128:70–75, 1998.
- [116] N. Cocuauud, E. Picard, R.J.M. Konings, A. Conti, and Hj. Matzke. *Inert Matrices, Uranium-free Plutonium Fuels and Americium Targets. Synthesis of CAPRA, SPIN and EFFTRA studies*. In *GLOBAL'97, Yokohama, Japan*, page 1044. Japan Atomic Energy Research Institute (JAERI) and the Power Reactor and Nuclear Fuel Development Corporation (PNC), October 1997.
- [117] J. Chernick. *The theory of uranium water lattices*. In *Proceedings Conference on Peaceful Uses of Atomic Energy, Geneva*, page 603, 1955.
- [118] L.W. Nordheim. The theory of resonance absorption. In *Symposia on Applied Mathematics. Vol.XI, Am. Math. Soc., Providence*, page 58, 1961.
- [119] E. Teuchert. *Resonanzabsorption in einer zweifach heterogenen Anordnung kugelförmiger Brennelemente*. *Nukleonik*, 11:68–72, 1968.

- [120] E. Teuchert and R. Breitbarth. *Resonanzintegralberechnung für mehrfach heterogene Anordnungen*. Technical Report Juel-551-RG, Forschungszentrum Juelich GmbH, Juelich, Germany, September 1968.
- [121] G.F. Kuncir. A program for the calculations of resonance absorption. Technical report, General Atomics, PO BOX 85608, San Diego, CA 92186-9784, September 1961.
- [122] L.W. Nordheim and G.F. Kuncir. *A program of research and calculations of resonance absorption*. GA-2527, TID-4500, August 1961.
- [123] R.K. Lane, L.W. Nordheim, and J.B. Sampson. *Resonance Absorption in Materials with Grain Structure*. *Nuclear Science and Engineering*, 14:390–396, 1962.
- [124] E.P. Wigner *et al.* *Review of the measurements of the resonance absorption of neutrons by uranium in bulk*. *Journal of Applied Physics*, 2:257,260,271, 1955.
- [125] S.M. Dancoff and M. Ginsburg. *Surface resonance absorption in a close-packed lattice*. CP-2157, October 1944.
- [126] S. Fehér, J.E. Hoogenboom, P.F.A. de Leege, and J. Valkó. *Monte Carlo Calculation of Dancoff Factors in Irregular Geometries*. *Nuclear Science and Engineering*, 117:227–238, 1994.
- [127] S. Fehér and P.F.A. de Leege. *DANCOFF-MC A Computer Program for Monte Carlo Calculation of Dancoff Factors in Irregular Geometries*. Technical Report IRI-131-95-003, Interfaculty Reactor Institute, Delft University of Technology, Delft, The Netherlands, June 1995.
- [128] J. Valkó, J.E. Hoogenboom, and H. van Dam. *IRI Results for the LEU-HTR Proteus Computational Benchmarks, Part 1, Lattice Calculations for LEUPRO-1 & LEUPRO-2*. Technical Report IRI-131-94-010, Interfaculty Reactor Institute, Delft University of Technology, Delft, The Netherlands, April 1994.
- [129] R.M. Westfall. *Cosine Current Transmission Probabilities for Spherical Shells*. *Transactions of the American Nuclear Society*, 18:147–148, 1974.
- [130] A.J. Janssen. *Enkele Opmerkingen over de Dancoff-factor*. Technical Report FYS-LWR-89-11, Netherlands Energy Research Foundation (ECN), Petten, The Netherlands, January 1990.
- [131] I.S. Gradshteyn and I.M. Ryzhik. *Table of Integrals, Series, and Products*. Academic Press, 1980.
- [132] Oak Ridge National Laboratory, Oak Ridge, Tennessee, USA. *SCALE-Material Information Processor, NUREG/CR-0200, ORNL/NUREG/CSD-2/R4, RSIC/ccc-545*.
- [133] J.R. Knight. *SUPERDAN Computer Programs for Calculating the Dancoff Factor of Spheres, Cylinders and Slabs*. Technical Report ORNL/NUREG/CSD-TM-2, Oak Ridge National Laboratory, Oak Ridge, Tennessee, USA, March 1978.



- [134] E. Hellstrand, P. Blomberg, and S. Horner. *The Temperature Coefficient of the Resonance Integral for Uranium Metal and Oxide*. *Nuclear Science and Engineering*, 8:497–506, 1960.
- [135] K. Bakker and R.J.M. Konings. *On the thermal conductivity of inert-matrix fuels containing americium oxide*. *Journal of Nuclear Materials*, 254:129–134, 1998.
- [136] L.E. Strawbridge and R.F. Barry. *Criticality Calculations for Uniform Water-Moderated Lattices*. *Nuclear Science and Engineering*, 23:58–73, 1965.
- [137] E. Hellstrand. *Measurements of the Effective Resonance Integral in Uranium Metal and Oxide in Different Geometries*. *Journal of Applied Physics*, 28:1493–1502, 1957.
- [138] R.M. Pearce. *Radial Dependence of the Doppler effect in bars of uranium and thorium*. *Journal of Nuclear Energy, Pt.A, Reactor Science*, 11:136, 1960.
- [139] W. Rothenstein. *Collision Probabilities and Resonance Integrals for Lattices*. *Nuclear Science and Engineering*, 7:162–171, 1960.
- [140] E.P. Wigner *et al.* *Resonance Absorption of Neutrons by Spheres*. *Journal of Applied Physics*, 26:260–270, 1955.
- [141] J.H. Ferziger and P.F. Zweifel. *The theory of Neutron Slowing Down in Nuclear Reactors*. The M.I.T. Press, 1966.
- [142] L. Dresner. *Resonance Absorption in Nuclear Reactors*. Pergamon Press, 1960.
- [143] N.F. Landers, L.M. Petrie, and J.A. Bucholz. *The material information processor for SCALE*. Oak Ridge National Laboratory, Oak Ridge, Tennessee, USA, June 1989.



# Appendix A

---

## Analytical Derivation of the Average Dancoff-factor for a Fuel Kernel

---

*An<sup>1</sup> analytical expression for the average Dancoff factor of a fuel kernel ( $C^{fk}$ ) in a pebble of a High Temperature gas-cooled Reactor was derived. This Dancoff factor accounts for the probability that a neutron escaping from a fuel kernel enters another fuel kernel, in the same pebble or in other pebbles, without making a collision with a moderator nucleus in between. If the fuel zone (FZ) of the pebble is thought to be of infinite dimensions, the Dancoff factor becomes equal to the so-called infinite-medium Dancoff factor ( $C_{\infty}^{fk}$ ). The  $C_{\infty}^{fk}$  has been determined by the evaluation of three existing analytical expressions and by two Monte Carlo calculations performed with the code MCNP-4A, for various coated particle (CP) densities. The Dancoff factor  $C^{fk}$  can be written as  $C_{\infty}^{fk}$  times a correction factor. The latter has been calculated for different FZ-radii and pebble shell thicknesses. For the standard pebble,  $C^{fk}$  as a function of the number of CPs has been calculated both analytically and with MCNP. The results of both methods are in good agreement. The analytical calculation method has preference, since it consumes practically no CPU time and obviates the building of MCNP models.*

### A.1 Introduction

A pebble bed type High Temperature Reactor (HTR) is fueled with graphite spherical fuel elements of 6 cm diameter. Within these pebbles one can distinguish an outer fuel-free spherical shell ( $2.5 < R < 3$  cm) and a fuel zone ( $R < 2.5$  cm), in which tens of thousands of tiny coated fuel particles (CPs) are embedded. A pile of pebbles can be considered as a double-heterogeneous system. The first heterogeneity, on the smallest geometrical scale, is the fuel kernel that is surrounded by coating layers and graphite matrix, successively. The second one, is the heterogeneity of the fuel zone and the pebble shell. A standard calculational scheme starts with the preparation of group cross sections on the finest geometrical scale, which would be in case of an HTR the fuel kernel surrounded by coating layers and graphite. The structure on this elementary level is then translated into a unit cell, which could for instance be a spherical multi-region unit cell with white boundary conditions, in which the thermalisation and neutron slowing-down problems are treated. The resonance

---

<sup>1</sup>This appendix is identical to ref. [64]

absorption is usually calculated by the collision probability method applied for a unit cell with a fuel and moderator region. For such a two-region unit cell the neutron slowing-down process can be described by two coupled integral equations as originally proposed by Chernick [117]. By assuming flat sources in both the fuel region and the moderator region, applying the reciprocity theorem and assuming a  $1/E$ -flux in the moderator, these two coupled equations reduce to a single slowing-down equation for the energy-dependent flux in the fuel region (see many text books, for example [69], p. 430). The numerical integration of this equation [118], with respect to the energy-dependent flux, is referred to as the Nordheim integral method [57]. With the energy-dependent flux, the shielded group cross sections can be generated (i.e.  $\bar{\sigma} = \int \sigma(E)\phi(E)dE / \int \phi(E)dE$ ). The integral equation depends among others on the escape probability  $P_F$ , which is the probability that a neutron originating in the fuel region (homogeneously and isotropically) will reach the surface of the lump without any collisions in the fuel region. For simple geometries, including a sphere, analytical expressions for  $P_F$  given by Case *et al.* [61] have been built in in many codes. For a single lump in an infinite moderator the neutron that escapes from the lump will obviously have its next collision in the moderator. However, if the distance between lumps is not large compared to the mean free path of the moderator, the possibility exists that a neutron escaping from a fuel lump hits another fuel lump without making a moderator collision in between. The distance between fuel kernels in an HTR pebble is typically of the order of millimeters, while the mean free path of graphite at resonance energies is about 2.5 cm, which implies that the kernels influence each other. In order to account for this effect, the escape probability  $P_F$  needs to be replaced or modified.

Teuchert *et al.* [119, 120] developed an escape probability  $P_F(\sigma)$  for double-heterogeneous systems (CPs in rods and spheres). The double-heterogeneous  $P_F(\sigma)$  is calculated by a collection of analytical and numerical integrations, which were implemented in the resonance-treatment code ZUT [121, 122]. Since the double-heterogeneous escape probability  $P_F(\sigma)$  depends on the total cross section of the absorber, which varies of course strongly with energy, it has to be recalculated continuously with varying energy.

A different approach that obviates the modification of codes is to adopt Nordheim's ([118] or p. 434 of [69]) well-known *effective* or *Dancoff-corrected* escape probability, which is already incorporated in many codes and which accounts for the double-heterogeneity via the so-called Dancoff(-Ginsburg) factor. The effective escape probability reads

$$P_F^* = P_F \cdot \frac{1 - C}{1 - C(1 - \Sigma_t^F \bar{l}_F P_F)} \quad (\text{A.1})$$

where  $\Sigma_t^F$  is the energy-dependent total macroscopic cross section of the fuel,  $\bar{l}_F$  is the mean chord length ( $4 \times \text{volume/surface}$  for convex bodies [61]) of the fuel kernel and  $C$  is the Dancoff factor. In case of an HTR,  $P_F$  is the (single-heterogeneous) probability to escape from a single fuel kernel. The Dancoff factor in eq. A.1 should account for fuel kernel 'shadowing' in a double-heterogeneous sense. It depends only on the geometry of the system and on the total macroscopic cross section of the moderator. Since the latter hardly varies in the resonance range, the Dancoff factor is usually calculated only once.

## A.2 Calculation of Dancoff-factors

The Dancoff factor can be calculated through the averaging of the Dancoff factors of individual fuel kernels. The Dancoff factor for an individual kernel is the probability that a neutron escaping in a random direction from the kernel enters another kernel, either in the same or in another pebble, without having a moderator collision in between. Eq. A.1 takes care of the possibility that neutrons may traverse more than one fuel kernel before making a moderator collision. It is strictly correct if the absorber lumps are randomly distributed [118, 123], which is the case for the CPs in the graphite matrix. It is useful to note that if Wigner's rational approximation [124] (i.e.  $P_F = (1 + \Sigma_f^f \bar{l}_F)^{-1}$ ) is inserted into eq. A.1, one obtains for the *Dancoff-corrected* escape probability also the Wigner form, viz.  $P_F^* = (1 + \Sigma_f^f \bar{l}_F^*)^{-1}$ , but with a *corrected* mean chord length  $\bar{l}_F^* = \bar{l}_F / (1 - C)$ . This correction can be seen as a reduction of the surface of the lump by a factor  $(1 - C)$ , if the volume of the lump is thought to be constant. This was originally introduced by Dancoff and Ginsburg [125], although they formulated the lump-lump interaction in another way [126]. For simple lattice cells, the Dancoff factor is usually internally calculated by the resonance shielding code. However, if the geometry is more complicated it has to be given as an input parameter. To calculate Dancoff factors in irregular geometries some codes have been developed. The code DANCOFF-MC [126, 127], based on the Monte Carlo method, is able to calculate Dancoff factors in an arbitrary arrangement of cylindrical pins or spherical fuel elements. However, in case of the HTR pebble it only accounts for fuel kernel interactions within a single pebble [128]. The Monte Carlo code MCNP-4A [66] offers the possibility to model all kinds of complex geometries in which Dancoff factors can be calculated by using a special option [60]. However, as will be seen later, there are some modelling restrictions, and moreover, in the case of the HTR, the MCNP calculation requires quite a lot of computing time.

In this paper, an analytical expression for the average fuel kernel Dancoff factor, that accounts for the double heterogeneity, is presented. For various fuel pebble specifications, the analytical Dancoff factors are computed by a FORTRAN code and compared to those obtained by MCNP calculations.

## A.3 Translation from pebble geometry to equivalent unit cells

For calculational purposes, the heterogeneity of the fuel kernel surrounded by coatings and graphite matrix is translated into a 'grain cell'. On this geometric level, the resonance shielding calculations take place and hence a Dancoff factor for the fuel kernel has to be provided. For the analytical calculation of this Dancoff factor we will consider an equivalent spherical unit cell with white boundary conditions, which seems expedient for a random distribution of CPs. This 'grain cell' consists of an inner sphere with radius  $r_1$ , corresponding to the fuel kernel, and a spherical shell with outer radius  $r_2$ , which contains the coating layers and the graphite matrix, homogeneously mixed. The stochastically stacked pile of fuel pebbles is also modelled as a spherical two-region unit cell with white boundary conditions. This equivalent 'pebble cell' consists of an inner sphere, representing

the fuel zone of the pebble, with radius  $R_1$  of 2.5 cm, and an outer spherical shell with outer radius  $R_2$ . The outer shell contains a homogeneous mixture of the 0.5 cm pebble shell, the moderator balls if present, and possibly the void between the pebbles. The radius  $R_2$  is determined by the volume occupied by the aforementioned materials. In the absence of moderator balls, one obtains  $R_2 = 3$  cm if the void between the pebbles is neglected, or  $R_2 = 3.52$  cm if void and pebble shell are merged. In the latter case, the shell of the unit cell contains graphite with a lower density than that of the actual 0.5 cm pebble shell.

The preceding consideration shows that the heterogeneity of the fuel kernel in the graphite matrix, as well as the heterogeneity of the spherical fuel zone of the pebble with the surrounding amount of graphite (shell and moderator pebbles) are translated into equivalent spherical two-region white boundary unit cells. Of course these two unit cells differ with respect to radii and macroscopic cross section of the outer spherical shell. Hereafter, the parameters corresponding to the 'grain cell' will be written in lower-case, while those of the 'pebble cell' will be written in upper-case.

## A.4 Transmission probabilities in a two-region white boundary unit cell

The first-flight escape and transmission probabilities for a spherical white-boundary unit cell have been derived by Westfall [129]. Fig. A.2 shows that the equivalent spherical two-region grain cell is characterised by the radius of the inner sphere ( $r_1$ ) and by the outer radius of the spherical shell ( $r_2$ ). The surfaces of the inner and outer zone are denoted by  $i$  and  $o$ , respectively. The total macroscopic cross section of the outer spherical shell reads  $\Sigma_o^m$ . For the pebble cell these parameters are replaced according to  $(r_1, r_2, \Sigma_i^m, i, o) \rightarrow (R_1, R_2, \Sigma_i^m, I, O)$ . The surfaces are treated as white-boundaries, which means that uniformly distributed isotropic sources with corresponding cosine currents are assumed at the interfaces. The transmission probabilities that can be distinguished for the mentioned geometry read:

$t_{io}$  is the probability that a neutron which leaves the inner boundary isotropically reaches the outer boundary without collisions;

$t_{oi}$  is the probability that a neutron which leaves the outer boundary isotropically reaches the inner boundary without collisions;

$t_{oo}$  is the probability that a neutron which leaves the outer boundary isotropically reaches again the outer boundary without collisions and without passing through the inner region.

$t_{ii}$  is the probability that a neutron which leaves the inner boundary isotropically reaches again the inner boundary without collisions and without passing through the outer region.

For the white-boundary condition mentioned above,  $t_{io}$  is given by

$$t_{io} = \frac{\int ds \int_{\hat{n} \cdot \hat{\Omega} > 0} d\Omega \hat{n} \cdot \hat{\Omega} \exp[-\Sigma_i^m l(\vec{r}, \hat{\Omega})]}{\int ds \int_{\hat{n} \cdot \hat{\Omega} > 0} d\Omega \hat{n} \cdot \hat{\Omega}} \quad (\text{A.2})$$

where  $l$  is the length of a vector with direction  $\hat{\Omega}$  leading from the surface point  $\vec{r}$  on surface  $i$  through the outer spherical shell to surface  $o$ ,  $\Sigma_i^m$  is the total macroscopic cross section of

the outer spherical shell,  $\hat{n}$  is the normal vector on surface  $i$  in the point  $\vec{r}$ . The integrals extend in  $\hat{\Omega}$  over all angles  $\hat{n} \cdot \hat{\Omega} > 0$  and in  $\vec{r}$  over surface  $i$ . Because of the spherical symmetry, the double-integral of eq. A.2 can be reduced [130] to

$$t_{io} = \frac{\int_0^{r_1} dy \, 2\pi y \exp[-\Sigma_i^m u]}{\int_0^{r_1} dy \, 2\pi y} = \frac{1}{\pi r_1^2} \int_0^{r_1} dy \, 2\pi y \exp[-\Sigma_i^m u], \quad (\text{A.3})$$

where only the integration over variable  $y$  has to be carried out. The variables  $y$  and  $u = \sqrt{r_2^2 - y^2} - \sqrt{r_1^2 - y^2}$  are shown in fig. A.2. In this new representation, the problem is reduced to one in which only neutron paths parallel to  $x$ -axis have to be considered. In order to avoid cumbersome integrals in the remainder of this article, we introduce

$$\mathcal{T}_{r_a, r_b}^{r_c, r_d} \equiv \frac{\int_{r_c}^{r_d} dy \, 2\pi y \circ}{\int_{r_a}^{r_b} dy \, 2\pi y \cdot 1} = \frac{1}{r_b^2 - r_a^2} \int_{r_c}^{r_d} dy \, 2y \circ, \quad (\text{A.4})$$

which is an integral operator that has to act on a particular operand. The latter is usually the probability that a neutron moves a distance without any interaction, and is usually of the form  $\exp[-\Sigma l(y)]$ , where  $\Sigma$  is a macroscopic cross section and  $l$  a certain distance, that is a function of parameter  $y$ . With this tool the transmission probabilities through the spherical shell, including their final form given by Westfall, read

$$\begin{aligned} t_{io} &= \mathcal{T}_{0, r_1}^{0, r_1} \circ \exp[-\Sigma_i^m u] \\ &= \frac{1}{2(r_1 \Sigma_i^m)^2} [(a+1)e^{-a} - (b+1)e^{-b} + \frac{a^4}{b^2} E_3(b) - a^2 E_3(a)], \end{aligned} \quad (\text{A.5})$$

$$t_{oi} = \mathcal{T}_{0, r_2}^{0, r_1} \circ \exp[-\Sigma_i^m u] = \left(\frac{r_1}{r_2}\right)^2 t_{io}, \quad (\text{A.6})$$

$$\begin{aligned} t_{oo} &= \mathcal{T}_{0, r_2}^{r_1, r_2} \circ \exp[-\Sigma_i^m \sqrt{r_2^2 - y^2}] \\ &= \frac{1}{2(r_2 \Sigma_i^m)^2} [1 - (1+2a)\exp(-2a)], \end{aligned} \quad (\text{A.7})$$

in which  $E_3$  is the exponential-integral function of the third order [131], and

$$a = \Sigma_i^m \sqrt{r_2^2 - r_1^2} \quad \text{and} \quad b = \Sigma_i^m (r_2 - r_1). \quad (\text{A.8})$$

The first-flight escape probability for a sphere with radius  $r_1$  has been given by Case *et al.* [61] and reads

$$P_F = \mathcal{P}_{r_1} \circ \exp[-s \Sigma_i^F] = \frac{3}{4\lambda} \left[ 1 - \frac{1}{2\lambda^2} [1 - (1+2\lambda)e^{-2\lambda}] \right], \quad (\text{A.9})$$

where  $\Sigma_i^F$  is the total macroscopic cross section of the inner region,  $\lambda = \Sigma_i^F r_1$  and  $\mathcal{P}_{r_1}$  is an integral operator, defined as

$$\mathcal{P}_{r_1} \equiv \frac{\int_0^{r_1} dy \, 2\pi y \int_0^{\sqrt{r_1^2 - y^2}} ds \circ}{\int_0^{r_1} dy \, 2\pi y \int_0^{\sqrt{r_1^2 - y^2}} ds \cdot 1}. \quad (\text{A.10})$$

Here, the integration over the entire volume of the inner sphere in fig. A.2 is accounted for by the double integral over the variables  $y$  and  $s$ . For any convex lump the transmission probability through the lump [118] can be expressed as

$$t_{ii} = 1 - \bar{l}_F \Sigma_i^F P_F, \quad (\text{A.11})$$

where  $\bar{l}_F$  is the mean chord length of the lump, which equals  $\frac{4}{3}r_1$  for a sphere.

## A.5 Dancoff-factor for a random distribution of fuel kernels in an infinite medium

The Dancoff factor accounts for the probability that a neutron which leaves an absorber lump passes through the moderator without collisions and enters another absorber lump. In an infinite medium in which fuel kernels are randomly distributed in the moderator, the Dancoff factor is given by the summation of the probabilities for neutrons to enter a particular fuel kernel positioned at a particular distance, before making a collision. In the invariant embedding theory [130], the distance covered by a neutron from absorber lump to absorber lump, corresponds with that in a unit cell allowing for a number of reflections at its white boundary. The probability that a neutron which leaves the surface of the fuel kernel isotropically, passes through the moderator without collisions and reaches the white boundary ( $o$ ) of the unit cell is equal to  $t_{io}$ . The probability that it moves  $n$  times from the outer white boundary to the same boundary without collisions and without passing through a kernel is  $(t_{oo})^n$ . The probability that, after the last isotropic reflection at the white boundary  $o$ , the neutron re-enters a fuel kernel without collisions in the moderator reads  $t_{oi}$ . The Dancoff-factor of the infinite medium is equal to the probability that a neutron leaving the fuel kernel reaches another fuel kernel without collisions with moderator nuclei after an arbitrary number of reflections at the white boundary  $o$  and hence reads [130]

$$C_{\infty}^{fk} = \sum_{n=0}^{\infty} t_{io} t_{oo}^n t_{oi} = \frac{t_{io} t_{oi}}{1 - t_{oo}}. \quad (\text{A.12})$$

Eqs. A.5-A.7 show that  $C_{\infty}^{fk}$  can be expressed as a function of two parameters, e.g.  $\Sigma_r^m r_1$  and  $r_2/r_1$ . The transmission probabilities of eqs. A.5-A.7 are also programmed in SCALE (section F.2.3.7 of [132]). However, these are used for the calculation of the first-flight escape probability of *annular* spherical pellets and are unfortunately not used for the calculation of the Dancoff factor. Instead, SCALE uses routines taken from SUPERDAN [133], a program which uses a double numerical integration to analytically determine Dancoff factors. It accounts for the over-shadowing of lumps up to and including the third nearest neighbours in a lattice. Since the algorithms were observed to be inadequate in some applications, in SCALE a correction factor has been added to the Dancoff factor to treat the interaction of all subsequent neighbours (section M.7.2.5.3 of [132]). However, for the purpose of tiny fuel kernels dispersed in graphite with a large number of equivalent unit cells per mean free path, this approximation gives questionable values [60, 128].

Janssen [130] derived from the exact expression of eq. A.12 a rational approximation for  $C_{\infty}^{fk}$ , which reads

$$C_{\infty}^{fk} = \frac{1}{1 + \Sigma_r^m \bar{l}_M}, \quad (\text{A.13})$$

where  $\bar{l}_M$  is a sort of a mean chord length of the moderator region, defined as

$$\bar{l}_M = \frac{4V_M}{S_F} = \frac{4 \cdot \frac{4}{3}\pi(r_2^3 - r_1^3)}{4\pi r_1^2}. \quad (\text{A.14})$$

In the limits of  $r_2/r_1 \rightarrow 1$  and  $r_2/r_1 \rightarrow \infty$  the rational approximation equals the exact expression of eq. A.12. A rather simple analytic method described by Lane *et al.* [123]



yields for the Dancoff factor of the infinite medium with a random kernel distribution the same expression as that of eq. A.13, except that  $\bar{l}_M$  is now given by

$$\bar{l}_M = \frac{4(V_M + V_F)}{S_F} = \frac{4 \cdot \frac{4}{3}\pi r_2^3}{4\pi r_1^2} \quad (\text{A.15})$$

Their method is justified in case of a high dilution of the fuel kernels, that is, the volume fraction of the fuel should be small. This means that  $V_F \ll V_M$  and hence the  $\bar{l}_M$  of eq. A.15 tends to that of eq. A.14. Fig. A.3 shows the Dancoff factor as a function  $r_2/r_1$ , with  $\sum_i^m r_1$  as a parameter, calculated, on the one hand, by the exact expression of Janssen (eq. A.12), and on the other by eq. A.13 with for  $\bar{l}_M$  the expressions of Janssen (eq. A.14) and Lane *et al.* (eq. A.15).

## A.6 Transmission probabilities in a double heterogeneous system

The resonance self-shielding calculations will be performed at the level of the grain cell. In this calculation a Dancoff factor is needed that accounts for the effect of neighbouring fuel kernels as well as for fuel kernels in other pebbles. This Dancoff factor can therefore be calculated as the sum of two probabilities. The first is the probability that a neutron leaving a fuel kernel will enter another kernel without any collision in the moderator within the *same* pebble, which will be designated as the intra-pebble Dancoff factor ( $C_{\text{intra}}$ ). The other is the probability that a neutron leaving a particular kernel will enter a fuel kernel in *another* pebble without collisions in the moderator, which will be designated as the inter-pebble Dancoff factor ( $C_{\text{inter}}$ ). The latter is usually much smaller than the first one, which is basically due to the neutron's increased probability to collide with a nucleus of the graphite in the pebble shell (and in some cases the moderator pebbles) which it has to pass through.

Fig. A.1 shows a schematic overview of the double-heterogeneous medium with three trajectories, in which a neutron which leaves a fuel kernel finally ends up in another kernel, that are typical for all possible histories. The arrow  $T_{ii'}$  in fig. A.1 corresponds to the transmission probability of a neutron leaving a fuel kernel (with white boundary  $i$ ) and entering the white boundary ( $i'$ ) of another fuel kernel in the same pebble, and hence contributes to the intra-pebble Dancoff factor. The intra-pebble Dancoff factor accounts for the set of paths between all possible pairs of kernels within the same pebble, which can be calculated by a double-summation of  $T_{ii'}$  over  $i$  and  $i'$ .

The other two histories contribute to the inter-pebble Dancoff-factor. The four arrows denoted by  $T_{iI}T_{IO}T_{OI}T_{iI}$  in fig. A.1 correspond to the history in which a neutron leaves the white boundary  $i$  of a fuel kernel, reaches the white boundary  $I$  at which it is isotropically transmitted, reaches the white boundary  $O$  at which it is isotropically reflected, reaches again the white boundary  $I$  of another pebble at which it is isotropically transmitted in the direction of the pebble's fuel zone and hits a fuel kernel with white boundary  $i$ , successively. This means that the neutron finally enters a fuel kernel of a neighbouring pebble without any collision with a graphite nucleus. The concatenation of arrows denoted by

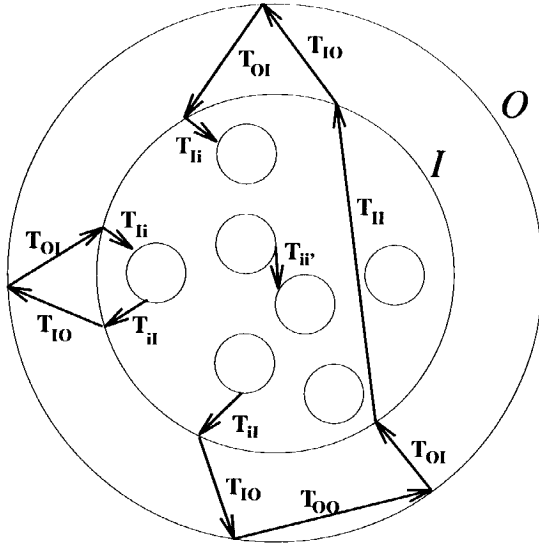


**Figure A.1:** Schematic over-view of the double-heterogeneous spherical system. The first heterogeneity is that of the fuel kernels which are surrounded by the graphite matrix. The second one is the fuel zone of the pebble that is surrounded by a graphite shell. Three exemplifying neutron trajectories are shown. The one denoted by  $T_{ii}$  contributes to the intra-pebble Dancoff factor, while the other two contribute to the inter-pebble Dancoff factor.

$T_{ii}T_{iO}T_{OO}T_{OI}T_{iI}T_{iO}T_{OI}T_{ii}$  corresponds to a history in which a neutron escapes from the first pebble ( $T_{ii}T_{iO}$ ), passes through the shell ( $T_{OO}$ ) of a second one, passes successively through shell, fuel zone and again shell ( $T_{OI}T_{iI}T_{iO}$ ) of a third pebble without collisions and without crossing any kernel, and finally enters the fourth pebble at which it eventually hits a fuel kernel ( $T_{OI}T_{ii}$ ). These two histories form only a subset of the infinite number of histories that contribute to the inter-pebble Dancoff factor. An arbitrary history contributing to  $C_{inter}$  is minimally built up by the product of four factors: The probability to escape from the fuel zone of the 'initial' pebble ( $T_{ii}$ ), the probability to escape from the pebble shell ( $T_{iO}$ ), the probability to reach the surface of the fuel zone of the 'final' pebble ( $T_{OI}$ ) and the probability to enter a fuel kernel in this fuel region ( $T_{ii}$ ). This 'basic' history is extended if between the departure from the 'initial' pebble and the arrival at the 'final' pebble, the neutron crosses  $i$  times the shells of intermediate pebbles  $(T_{OO})^i$  and, moreover, passes  $j$  times through complete pebbles  $(T_{OI}T_{iI}T_{iO})^j$ . The inter-pebble Dancoff-factor accounts for all possible combinations and hence reads

$$C_{inter} = T_{ii}T_{iO} [1 + T_{OO} + T_{OO}^2 + \dots] \{1 + (T_{OI}T_{iI}T_{iO}) + (T_{OI}T_{iI}T_{iO})^2 + \dots\} T_{OI}T_{ii} \quad , \quad (A.16)$$

in which the series between the square and the curly brackets correspond to transmissions through shells of pebbles and through complete pebbles, respectively. By progression of the series and rearrangement of the terms, eq. A.16 can be written as

$$C_{inter} = \frac{T_{iO}T_{OI}}{1 - T_{OO}} \frac{T_{ii}T_{ii}}{1 - T_{OI}T_{iI}T_{iO}} \quad , \quad (A.17)$$

where the first fraction can be identified through eq. A.12 as the infinite medium Dancoff factor of the pebble's fuel zone, which leads to the introduction

$$C_{\infty}^{fz} = \frac{T_{io}T_{oi}}{1 - T_{oo}} \quad (\text{A.18})$$

The (upper-case) transmission probabilities are equal to those of eqs. A.5-A.7, except that the parameters  $(\Sigma_i^m, r_1, r_2)$  have to be replaced by  $(\Sigma_i^M, R_1, R_2)$  which are the total macroscopic cross section of the outer spherical shell, the inner radius and the outer radius of the equivalent pebble cell, respectively.

The total Dancoff factor for the fuel kernel in the double heterogeneous system now becomes

$$C^{fk} = C_{\text{mra}} + C_{\infty}^{fz} \frac{T_{ii}T_{ii}}{1 - T_{ii}T_{io}T_{oi}} \quad (\text{A.19})$$

It should be noted that eq. A.19 is not only valid for an HTR pebble, but is also applicable to other double heterogeneous systems, such as the so-called sphere-pac LWR fuel rod. The transmission probabilities in eq. A.19 depend of course on the geometry under consideration.

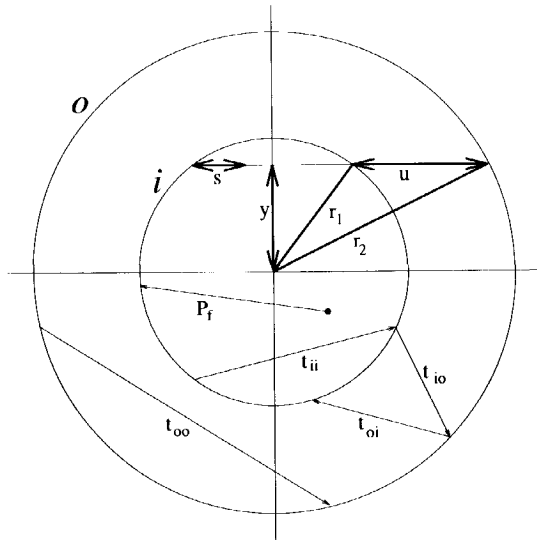


**Figure A.2:** A spherical two-region unit cell ('grain cell') with white boundary conditions. The inner and outer boundary are denoted by  $i$  and  $o$ , respectively. The upper half-plane shows the parameters which are used in the various integrals. In the lower half-plane, the first-flight escape probability ( $P_f$ ) and various transmission probabilities are depicted. By replacing the lower-case parameters by their upper-case counterparts, the figure becomes applicable to the 'pebble cell'.

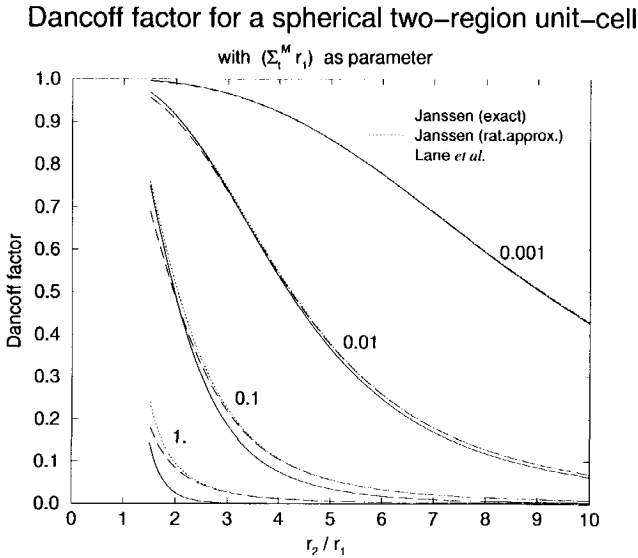


**Figure A.3:** Dancoff factor for a spherical two-region unit cell as a function of  $r_2/r_1$ , calculated by three methods. The solid ("Janssen exact"), dotted ("Janssen rational approximation") and dashed ("Lane et al.") lines are calculated with eq. A.12, eqs. A.13+A.14 and eqs. A.13+A.15, respectively.

## A.7 Calculation of the Dancoff factor

As mentioned previously, the Dancoff factor is equal to the sum of the inter- and intra-pebble Dancoff factor. These will be evaluated successively.

### A.7.1 The intra-pebble Dancoff factor

For the calculation of the intra-pebble Dancoff factor it will be assumed that each kernel 'emits' as many neutrons as the others and since the kernels are distributed randomly, the fuel region of the pebble can be considered as containing a uniform source distribution. In order to account for this uniform source distribution an integration over the volume of the pebble's fuel region has to be carried out. The integrand is then equal to the probability that a neutron, departing from coordinates  $(s, y)$  and subsequently moving parallel to the horizontal axis in fig. A.2, will enter a fuel kernel before it reaches the surface  $l$  of the fuel region. The distance  $s$ , which the neutron can travel before it reaches the surface of the fuel region, assuming that the neutron moves in the negative  $x$ -direction in fig. A.2, corresponds to a certain number of unit cells that will be passed through. The average number of grain cells that is traversed in between the 'departure' and 'arrival' cell is given by the distance  $s'$  divided by the mean chord length of a single grain cell. Here  $s' = s - \bar{l}_{gc}$ , which is the actual distance  $s$  corrected for the average distance that the neutron travels in the 'departure' and 'arrival' cell together ( $\bar{l}_{gc}$ ). If the number of unit cells that is crossed, without colliding with

a moderator nucleus and without crossing a fuel kernel, is equal to  $n - 1$  given by  $s'/\bar{l}_{gc}$ , it can be seen that  $n = s/\bar{l}_{gc}$ . Considering a neutron trace in which maximally  $n - 1$  grain cells are traversed, the corresponding probability of leaving a kernel and entering another kernel within distance of  $s$  reads  $t_{io}(1 + t_{oo} + \dots + t_{oo}^{n-1})t_{oi}$ . This series can be written as  $\frac{t_{io}t_{oi}}{1 - t_{oo}}(1 - t_{oo}^n)$ . Analogously to the calculation of the first-flight escape probability according to eq. A.9, the intra-pebble Dancoff factor now becomes

$$C_{\text{intra}} = \mathcal{P}_{R_1} \circ \left[ \frac{t_{io}t_{oi}}{1 - t_{oo}}(1 - t_{oo}^n) \right] = \frac{t_{io}t_{oi}}{1 - t_{oo}} [1 - \mathcal{P}_{R_1} \circ t_{oo}^n] , \quad (\text{A.20})$$

where  $\mathcal{P}_{R_1}$  has been defined in eq. A.10. The fraction in front of the term between the square brackets at the RHS of eq. A.20 is equal to the infinite-medium Dancoff-factor for a fuel kernel (i.e.  $C_{\infty}^k$ ). If we replace the integer  $n$  by the equivalent real number  $s/\bar{l}_{gc}$ , the integral-part of eq. A.20 can be written as

$$\mathcal{P}_{R_1} \circ t_{oo}^n = \mathcal{P}_{R_1} \circ \exp\left[-\left(\frac{-\ln t_{oo}}{\bar{l}_{gc}}\right)s\right] . \quad (\text{A.21})$$

Comparing this to eq. A.9, leads to the introduction of the pseudo cross section

$$\Sigma^* \equiv \left( \frac{-\ln t_{oo}}{\bar{l}_{gc}} \right) . \quad (\text{A.22})$$

This pseudo cross section can physically be interpreted as the probability per unit path length traveled that a neutron will either collide with a moderator nucleus or will enter a fuel kernel. It should be noted that in the absence of moderator material in between the kernels the pseudo cross section is not zero, but reads

$$\Sigma^* \rightarrow -\frac{1}{\frac{4}{3}r_2} \ln\left[1 - \left(\frac{r_1}{r_2}\right)^2\right] , \quad (\text{A.23})$$

where the ( $\Sigma_i^m \rightarrow 0$ )-limit of eq. A.7 has been used. If the kernels occupy only a small volume of the fuel zone, which implies that  $\frac{r_1}{r_2} \ll 1$ , one obtains  $\Sigma^* = \pi r_1^2 / (\frac{4}{3}\pi r_2^3)$ . This pseudo macroscopic cross section is now equal to the kernel density  $1/(\frac{4}{3}\pi r_2^3)$  times the 'microscopic' cross section  $\pi r_1^2$  of a kernel. The reciprocal of this  $\Sigma^*$  is in agreement with Lane's expression [123] for the mean free path between kernels, if the moderator were not present. Another interesting case is the limit of very small kernels, but now with the moderator material in between them. In the limit of  $r_1/r_2 \rightarrow 0$  the expected result of  $\Sigma^* \rightarrow \Sigma_i^m$  is found. Combining eq. A.20 through A.22 gives, analogously to eq. A.9,

$$C_{\text{intra}} = C_{\infty}^k [1 - P_F(\Sigma^* R_1)] . \quad (\text{A.24})$$

Eq. A.24 shows that the intra-pebble Dancoff factor is equal to Dancoff factor for the (single heterogeneous) infinite medium ( $C_{\infty}^k$ ) corrected for the probability that the neutron leaves the fuel zone of the pebble. This probability is similar to the first-flight escape probability  $P_F$  of a sphere. However, its argument is now the pseudo cross section  $\Sigma^*$  times the radius of the fuel zone  $R_1$ , which can be written as

$$\Sigma^* R_1 = (-\ln t_{oo}) \frac{R_1}{\bar{l}_{gc}} = \frac{3}{4} (-\ln t_{oo}) N_{gr}^{\frac{1}{3}} , \quad (\text{A.25})$$

where we have used the fact that the mean chord length of the grain cell is equal to  $\frac{4}{3}r_2$  and that the volume of the fuel zone ( $\frac{4}{3}\pi R_1^3$ ) divided by the volume of a grain cell ( $\frac{4}{3}\pi r_2^3$ ) is equal to the number of grains in the fuel zone ( $N_{gr}$ ). It should be noted that in the limit of  $R_1 \rightarrow \infty$ , while  $\Sigma^*$  remains constant, the intra-pebble Dancoff factor becomes equal to the infinite-medium Dancoff factor ( $C_{\infty}^k$ ).

### A.7.2 The inter-pebble Dancoff factor

According to eq. A.19 the inter-pebble Dancoff factor is equal to the product of two terms. The first term is the infinite-medium Dancoff factor for the fuel zone of a pebble. The second term depends on the transmission probabilities  $T_{I0}$ ,  $T_{0I}$ ,  $T_{II}$ ,  $T_{II}$  and  $T_{II}$ , where the first two can be calculated by eqs. A.5-A.8. The last one is the transmission probability that a neutron leaving isotropically the surface  $I$  of the fuel region will reach this surface again without having a collision with a moderator nucleus and without passing through a kernel. It can be calculated by integrating the probability  $t_{oo}^n$  along chords from one point on surface  $I$  to another point on surface  $I$ , where the directions of the chords are again isotropically distributed. Here,  $t_{oo}$  is the probability that a neutron traverses a grain cell without collisions with a moderator nucleus and without crossing a fuel kernel, and  $n$  is the number of grain cells the neutron has to traverse from one point on surface  $I$  to the other point on surface  $I$ . The latter is again given by the distance the neutron has to move divided by the mean chord length of a grain cell. Fig. A.2 shows that the length of the straight line along which the neutron moves from inner surface to inner surface, parallel to the horizontal axis, is equal to  $2\sqrt{R_1^2 - y^2}$ . Therefore, the probability  $t_{oo}^n$  can be written as  $\exp(-\Sigma^* 2\sqrt{R_1^2 - y^2})$ , where  $\Sigma^*$  is again given by eq. A.22. Integration of this probability over  $y$ , implicitly corresponding to a cosine current distribution at the interface  $I$ , gives according to eq. A.4,

$$T_{II} = T_{0,R_1}^{0,R_1} \circ \exp(-\Sigma^* 2\sqrt{R_1^2 - y^2}) = 1 - \left(\frac{4}{3}\Sigma^* R_1\right) P_F(\Sigma^* R_1), \quad (\text{A.26})$$

which is analogous to eq. A.11.

The term that remains to be calculated for the inter-pebble Dancoff factor is the product  $T_{II}T_{II}$ . This is the probability that a neutron leaving a fuel kernel isotropically reaches the surface  $I$  of the pebble's fuel zone, times the probability that a neutron isotropically leaving the surface  $I$  (of another pebble) enters a fuel kernel somewhere in the fuel zone. Both probabilities of course without moderator collisions and without passing through intermediate kernels. The product  $T_{II}T_{II}$  can now, analogously to the expression of the intra-pebble Dancoff factor of eq. A.24, be determined as the infinite-medium Dancoff factor for the fuel kernel multiplied by the probability to escape from the fuel zone ( $P_F$ ) times the non-transmission probability of the fuel zone ( $1 - T_{II}$ ) of the next pebble. This means that we have

$$T_{II}T_{II} = C_{\infty}^{fk} P_F(\Sigma^* R_1) [1 - T_{II}]. \quad (\text{A.27})$$

If this term is inserted into the expression for the inter-pebble Dancoff factor, given by eq. A.19, one obtains

$$C_{\text{mer}} = C_{\infty}^{fk} C_{\infty}^{\text{FZ}} \frac{P_F(\Sigma^* R_1) [1 - T_{II}]}{1 - T_{II}T_{I0}T_{0I}}. \quad (\text{A.28})$$

### A.7.3 Final expression for the Dancoff factor

The sum of the intra-pebble (eq. A.24) and the inter-pebble (eq. A.28) Dancoff factor yields the total Dancoff factor, which becomes

$$C^{fk} = C_{\infty}^{fk} \left[ 1 - P_F(\Sigma^* R_1) + C_{\infty}^{\text{FZ}} \frac{P_F(\Sigma^* R_1) [1 - T_{II}]}{1 - T_{II}T_{I0}T_{0I}} \right], \quad (\text{A.29})$$

where we recall (see eq. A.26) that,

$$T_{II} = 1 - \left(\frac{4}{3}\Sigma^*R_1\right) P_F(\Sigma^*R_1), \quad (\text{A.30})$$

in which  $P_F$  is the first-flight escape probability from a sphere, given by eq. A.9, and its argument,  $\Sigma^*R_1$  is given by eq. A.25. Eq. A.29 shows that the Dancoff factor is equal to that of an infinite medium times the correction factor between the square brackets. The infinite medium Dancoff factor for the fuel kernel  $C_\infty^{fk}$  is given by eq. A.12, where the transmission probabilities  $t_{io}$ ,  $t_{oi}$  and  $t_{oo}$  (eqs. A.5-A.7) are functions of  $(\Sigma^m, r_1, r_2)$ , which are the total macroscopic cross section of the spherical shell of the grain cell, the inner radius and the outer radius of the grain cell. The infinite-medium Dancoff factor for the fuel zone is obtained in a similar way, but now the upper-case transmission probabilities  $T_{IO}$ ,  $T_{OI}$ ,  $T_{OO}$  are functions of  $(\Sigma_t^M, R_1, R_2)$ , where  $\Sigma_t^M$  is the total macroscopic cross section of the spherical shell of the pebble cell,  $R_1$  is the 2.5 cm radius of the fuel zone and  $R_2$  is the outer radius of the pebble cell. Eq. A.29 shows that if  $T_{IO} = T_{OI} = 1$ ,  $T_{OO} = 0$ , and hence  $C_\infty^{FZ} = 1$ , implying that a neutron which leaves the fuel zone always reaches a neighbouring fuel zone, the Dancoff factor is equal to that of the infinite medium, i.e.  $C^{fk} = C_\infty^{fk}$ . Furthermore, if the Dancoff factor for the fuel zone  $C_\infty^{FZ}$  is zero, which means that a neutron can not reach another fuel zone without collisions, the total Dancoff factor is equal to the intra-pebble Dancoff factor (see eq. A.24).

## A.8 Comparison with Monte Carlo Results

The results obtained from the analytical formulae have been verified by Monte Carlo calculations performed with the code MCNP-4A [66]. The Dancoff factor has been calculated as the number of neutrons entering a fuel kernel divided by the number of neutrons started from a fuel kernel boundary (uniformly and isotropically in the outward direction). The neutrons are followed until they enter a fuel kernel or they collide with a moderator nucleus [60]. The Dancoff factor depends, besides the geometry and the density of the moderator, on the total microscopic cross section of the moderator, which varies only with less than 1% from 0.2 eV to 10 keV. In the MCNP-calculations the source neutrons have an energy of 100 eV, which corresponds to a total microscopic cross section of 4.7388 barn. This yields for the graphite matrix material a macroscopic cross section of  $0.4097 \text{ cm}^{-1}$ , which implies that the radius of the pebble's fuel zone is about equal to the mean free path in the moderator.

Below, the results of the analytical model are compared to those of the MCNP calculations, and the assumptions made in both methods are discussed. This is done for the infinite-medium Dancoff factor of the pebble's fuel zone ( $C_\infty^{FZ}$ ) and that of the fuel kernel ( $C_\infty^{fk}$ ). Thereafter, the intra-pebble Dancoff factor ( $C_{\text{intra}}$ ) as a function of the fuel zone radius is studied and the Dancoff factor  $C^{fk}$  as a function of the outer radius of the pebble cell ( $R_2$ ) is investigated. Finally, the results of the total fuel kernel Dancoff factor ( $C^{fk}$ ) as a function of the number of grains in the fuel zone are given for fuel kernels with radii of 100, 110 and 250  $\mu\text{m}$ .

### A.8.1 The infinite-medium Dancoff factor for the fuel zone

In the analytical model the inter-pebble Dancoff factor is proportional to the infinite-medium Dancoff factor of the pebble's fuel zone ( $C_{\infty}^{FZ}$ ). The latter accounts for the probability that a neutron, leaving the fuel zone surface isotropically in the outward direction reaches the fuel zone of another pebble without collisions. Let a spherical *three*-region white-boundary pebble cell be the reference model for the stochastically stacked infinite pile of fuel pebbles. This pebble cell comprises the fuel zone ( $R < 2.5$  cm), the pebble shell ( $2.5 < R < 3$  cm) and the void belonging to the pebble ( $3 < R < 3.52$  cm) and gives after 16 million neutron histories a Dancoff factor of  $0.4435 \pm 0.0002$ . A *two*-region cell, of which the spherical shell ( $2.5 < R < 3.52$  cm) contains a homogenised mixture of the void and the graphite of the pebble shell, yields (0.45337 analytically,  $0.4532 \pm 0.0002$  MCNP), which is a deviation from the reference case of +2%. A two-region cell, of which the spherical shell is equal to the actual pebble shell ( $2.5 < R < 3$  cm) and where the void region is simply ignored, yields (0.44352 analytically,  $0.4435 \pm 0.0002$  MCNP), which is within the error margin (i.e. 0.05%) of the reference case. This means that, in case of the absence of moderator pebbles, the two-region Dancoff factor with neglect of the void region gives the best result compared to that of the reference case. This is of course only justified if the total macroscopic cross section of the void region is negligibly small, which is true if there is helium gas, even under high pressure, in between the pebbles.

### A.8.2 Homogenisation of coatings and graphite matrix

The number of CPs per pebble ( $N_{gr}$ ) has been varied from 5,000 to 60,000 (step 5,000) per pebble in the MCNP calculations. The outer radius of an equivalent spherical white boundary grain cell ( $r_2$ ) is given by  $r_2 = R_1 / N_{gr}^{\frac{1}{3}}$ , where we recall that  $R_1$  is the 2.5 cm radius of the fuel zone. In the analytic model the coating layers surrounding each fuel kernel have been homogenised with the graphite matrix in between the kernels. In order to estimate the error made by homogenising the coating materials with the graphite, the Dancoff factor has been calculated for a two-region spherical grain cell and for a multi-region grain cell in which the coating layers are modelled explicitly. This has been done for grain cells (kernel radius of 250  $\mu\text{m}$ ) for which  $N_{gr} = 5,000$  and 60,000, and shows an under-estimation for the two-region case of 0.3% and 0.01%, respectively.

### A.8.3 The infinite-medium Dancoff factor for a fuel kernel

The infinite-medium Dancoff factor for a fuel kernel has been calculated both analytically and with MCNP for grain densities corresponding to  $N_{gr}$  grains per fuel zone with the nominal volume of  $\frac{4}{3}\pi(2.5)^3 \text{ cm}^3$ . The analytical calculation embraces the evaluation of the expressions of Janssen and its rational approximation, as well as that of Lane. The MCNP calculations are performed for two geometries.

The first is a cubic unit cell containing one fuel kernel only, with specular reflecting boundary conditions. This geometry is equivalent with an infinite rectangular lattice of cubic unit cells.

The second one is the infinite medium in which CPs are randomly dispersed. The infinite



medium was artificially created by a graphite sphere with isotropic reflecting boundary conditions in which 980 CPs were randomly positioned. (This was due to limitations, viz. no more than 1000 cells, of the used algorithm in MCNP.) The radius of the sphere was chosen in such a way that the CP-density was equal to a density of  $N_{gr}$  grains per fuel zone volume. In order to compare the MCNP results to those of the analytic models (no coating layers), the coating layers in the MCNP models were simply replaced by the graphite matrix. An MCNP calculation on a spherical two-region unit cell with isotropic reflecting boundary conditions has been discarded, because this yields exactly the same results as the analytical expression of Janssen (eq. A.12). This has been verified for a number of  $N_{gr}$  values.

The results of the calculations mentioned above are presented in fig. A.4. It can be

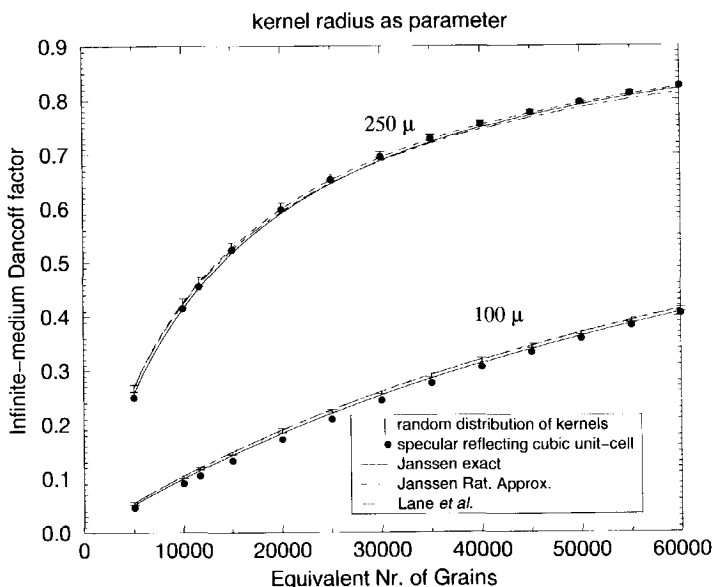


**Figure A.4:** The infinite-medium Dancoff factor  $C_{\infty}^{fk}$  for the fuel kernel as a function of the equivalent number of grains, based on five methods. The equivalent number of grains (i.e.  $N_{gr}$ ) on the horizontal axis corresponds to a grain density in the infinite medium that is equivalent with a density of  $N_{gr}/(\frac{4}{3}\pi(2.5)^3) \text{ cm}^{-3}$ , i.e.  $N_{gr}$  grains per nominal fuel zone of a pebble. The symbols (two types) correspond to MCNP calculations, whereas the curves (three types) correspond to analytical calculations. The solid ("Janssen exact"), dashed ("Janssen rational approximation") and long-dashed ("Lane et al.") lines are calculated with eq. A.12, eqs. A.13+A.14 and eqs. A.13+A.15, respectively.

seen that the Dancoff factors of the specular reflecting unit cell are in all cases lower than those of the random distribution of CPs. The relative difference is the largest for a small equivalent number of grains ( $N_{gr}$ ), i.e. low grain density, and for a small fuel kernel. The cubic unit cell with specular reflecting boundaries is equivalent to an infinite rectangular

lattice of cubic unit cells, which means that channel effects will occur. In such a system the neutrons can 'stream' in CP-free volumes, which results in an under-estimation of the Dancoff factor. In case of  $N_{gr} = 5,000$ , the maximal relative differences of 7% and 18% for the 250 and 100  $\mu\text{m}$  kernel, respectively, were found. It should however be noted that in these cases the Dancoff factor itself is relatively low, which means that the error in the effective first-flight escape probability ( $P_f^*$ ) due to the error in the Dancoff factor is relatively low. The relative differences between results of the random distribution MCNP-calculations and Janssen's exact expression of the Dancoff factor are maximal for  $N_{gr} = 5,000$  and amount 4% and 5% for the 250  $\mu\text{m}$  and 100  $\mu\text{m}$  kernels, respectively. The Dancoff factor values of Lane *et al.* lie within the error margins of the random distribution MCNP-values, except for  $N_{gr} > 20,000$  in case of the 250  $\mu\text{m}$  kernel. This can be understood since the theory on which Lane's formula is based assumes a high dilution of the fuel kernels, i.e. the kernels occupy only a small part of the volume. Surprisingly, the rational approximation of Janssen's Dancoff factor fits better than Janssen's analytical expression and lies always within the error margins of the random distribution MCNP-results. This can not be explained by physics considerations but rests mainly on lucky coincidence.

#### A.8.4 The intra-pebble Dancoff factor as a function of the fuel zone radius

In order to verify the analytic expression of the intra-pebble Dancoff factor (eq. A.24) MCNP-calculations on a single pebble with a varying fuel zone radius ( $R_1$ ) have been performed. The single pebble was modelled by placing an infinite rectangular lattice of cubic unit cells in a sphere with radius  $R_1$  as is shown in fig. 3.4 of chapter 3. A random distribution of CPs was unfortunately not possible for this geometry due to limitations of the MCNP-code. For the calculation of the intra-pebble Dancoff factor, the spherical boundaries of the pebble cell in fig. 3.4 were transparent instead of reflecting. The Dancoff factor has been calculated through volume-averaging the Dancoff factors of individual CPs at different radial positions, which is described in paragraph A.8.6.

Fig. A.5 shows the averaged *intra-pebble* Dancoff factors, normalised to the infinite medium fuel kernel Dancoff factor, ( $C_{\text{intra}}/C_{\infty}^{fk}$ ) as a function of the fuel zone radius, normalised to the nominal 2.5 cm-radius ( $R_1/(R_1)_{\text{nom}}$ ). This has been done for kernels with radii of 100 and 250  $\mu\text{m}$ , at a constant CP-density. This CP-density corresponds to a loading of 30,000 CPs in the standard ( $R_1 = 2.5$  cm) fuel zone volume. The dots are the volume-averaged intra-pebble Dancoff factors calculated by MCNP. The curves represent the analytical expression of the intra-pebble Dancoff factor given by eq. A.24, which can be rewritten as  $C_{\text{intra}}/C_{\infty}^{fk} = 1 - P_F(\Sigma^* R_1)$ . This shows that for large  $R_1$ -values the curves tend to unity, implying that the intra-pebble Dancoff factor becomes equal to the infinite-medium Dancoff factor. For the 100  $\mu\text{m}$ -kernel, the MCNP-dots are lower than the analytical curve. This is due to the previously mentioned channel-effects in the rectangular lattice.

#### A.8.5 The Dancoff factor as a function of the pebble shell thickness

In order to study the interaction between the fuel zones of different pebbles, the outer radius of the pebble-shell ( $R_2$ ) has been varied, while the fuel zone radius has been kept constant ( $R_1 = 2.5$  cm). The fuel zone of a pebble contains 30,000 CPs. Fig. A.6 shows the volume-

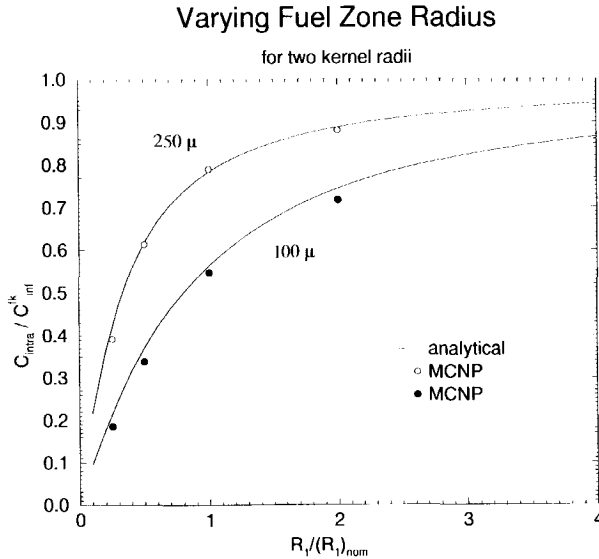


**Figure A.5:** The intra-pebble Dancoff factor normalised to the infinite-medium Dancoff factor ( $C_{intra} / C_{\infty}^{fk}$ ) as a function of the fuel zone radius, normalised to the nominal one of 2.5 cm, for two fuel kernel radii. The CP-density is kept constant (viz. 30,000 CPs per nominal fuel zone volume). For large fuel zone radii the intra-pebble Dancoff factor tends to the infinite medium Dancoff factor.

averaged Dancoff factor, normalised to the infinite-medium Dancoff factor, ( $C^{fk} / C_{\infty}^{fk}$ ) as a function of  $R_2 / R_1$ . The latter is the outer radius of the pebble shell ( $R_2$ ) divided by the fuel zone radius ( $R_1$ ). For the standard pebble  $R_2 = 3$  cm and, hence,  $R_2 / R_1 = 1.2$ . At this value the  $C^{fk} / C_{\infty}^{fk}$  reads about 0.87 and 0.77 for the 250 and 100  $\mu$ m kernels, respectively. For high  $R_2 / R_1$ -values, the probability that a neutron which leaves the fuel zone of a pebble reaches the fuel zone of another pebble without collisions becomes negligible. This implies that the fuel zone Dancoff factor ( $C_{\infty}^{FZ}$  in eq. A.29) becomes zero. In that case, the inter-pebble Dancoff factor becomes zero and hence the total Dancoff factor becomes equal to the intra-pebble Dancoff factor. Note that the Dancoff factors for  $R_2 / R_1 \rightarrow \infty$  in fig. A.6, correspond to those at  $R_1 / (R_1)_{nom} = 1$  in fig. A.5. The ( $C_{intra} / C_{\infty}^{fk}$ )-values for the standard pebble read 0.78 and 0.56 for fuel kernels with radii of 250 and 100  $\mu$ m, respectively. From this it can be inferred that, for the standard pebbles, the contributions of the intra-pebble Dancoff factor to the total fuel kernel Dancoff factor read  $\frac{0.78}{0.87} \cdot 100\% = 90\%$  and  $\frac{0.56}{0.77} \cdot 100\% = 73\%$  for 250 and 100  $\mu$ m-kernels, respectively. Hence, the contributions of the inter-pebble Dancoff factor are 10% and 26%, respectively.

### A.8.6 The fuel kernel Dancoff factor for a standard pebble

Figs. A.7-A.8 show the total (intra + inter-pebble) Dancoff factor of individual kernels as a function of their radial position.

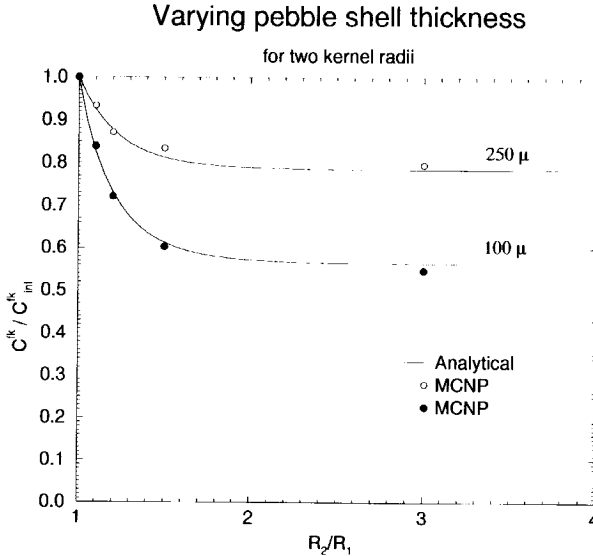


**Figure A.6:** The Dancoff factor, normalised to the infinite-medium Dancoff factor, ( $C^{jk}/C_{\infty}^{jk}$ ) as a function of  $R_2/R_1$ , for two fuel kernel radii. Here,  $R_2/R_1$  is the outer radius of the pebble-shell, normalised to the nominal 2.5 cm fuel zone radius ( $R_1$ ). The FZ-radius  $R_1$  has been kept constant. The  $R_2/R_1 = 1.2$  case correspond to a standard pebble, without moderator pebbles. If  $R_2/R_1 = 1$ , i.e. zero pebble shell thickness, the Dancoff factor becomes equal to the infinite-medium Dancoff factor. In this case, the fuel zones of the pebbles are not separated by graphite from each other and notionally form an infinite medium. For very thick pebble shells ( $R_2/R_1 \rightarrow \infty$ ) the Dancoff factor tends to the intra-pebble Dancoff factor. In this case, a fuel zone is isolated from the other ones, and the inter-pebble Dancoff factor is therefore zero.

Each 'open' symbol in these figures corresponds to the Dancoff factor of a single fuel kernel and is obtained after one million neutron histories in MCNP. The fuel zone is divided by the vertical dashed lines in ten regions with equal volumes. It should be noted that about half of the number of the CPs is positioned in the outer spherical ( $2 < R < 2.5$  cm)-shell of the fuel zone. Fig. 3.4 shows that some of the fuel kernels are cut by the spherical ( $R_1 = 2.5$  cm)-surface. For these kernels no Dancoff factor could be calculated. To obtain, nevertheless, data in the vicinity of the boundary, for each set a point was added through extrapolation of the outer five MCNP-points. The extrapolated data are represented by the filled symbols in figs. A.7-A.8. The Dancoff factor is calculated by volume-averaging the Dancoff factors of the individual kernels. The volume-averaged Dancoff factor as a function of the number of grains in the fuel zone, with the kernel radius as a parameter, is shown in fig. A.9. The curves are obtained analytically through the evaluation of eq. A.29, while the symbols correspond to the volume-averaged Dancoff factors calculated with MCNP. Each symbol in fig. A.9 is obtained through volume-averaging of 20 to 35 Dancoff factors of individual kernels with different radial positions. The Dancoff factor of an individual kernel has been determined after one million neutron histories, which results, without variance reduction techniques in

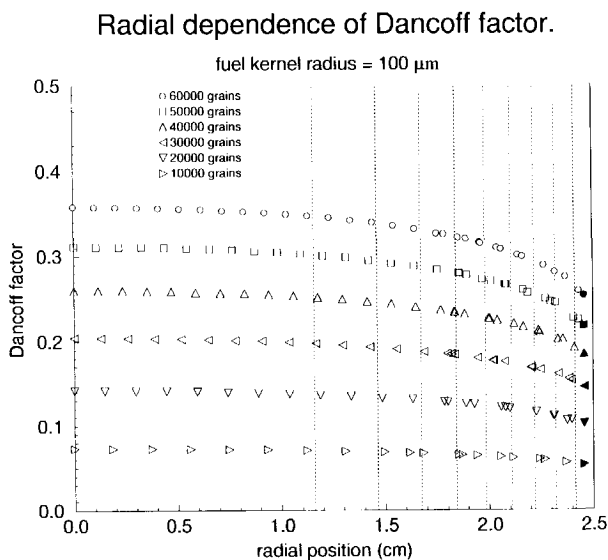


**Figure A.7:** Fuel kernel Dancoff factor as a function of the radial position in the pebble's fuel zone for a fuel kernel with a radius of 100  $\mu\text{m}$ . Each point corresponds to one million MCNP neutron histories. The fuel zone is divided by the dashed vertical lines into 10 equi-volumes. The filled symbols are extrapolated (2<sup>nd</sup> order function) from the five outer MCNP-points.

MCNP, in a statistical uncertainty of about 0.5%. One Dancoff factor calculation involves a CPU time of about 15 min. on a 300 MHz Dec Alpha. For example, if 28 individual kernel Dancoff factors are included for a particular volume-averaged Dancoff factor calculation, the total CPU time equals 7 hrs. This means that every symbol in fig. A.9 needed a CPU time of this order of magnitude. The evaluation of the analytical formula (eq. A.29) by a FORTRAN code requires, on the other hand, less than one second. The MCNP results are in good agreement with the analytical results for the 250  $\mu\text{m}$  kernel. However, for the 100 and 110  $\mu\text{m}$  kernels the MCNP results are everywhere lower than the analytical results. The maximal differences amount to 0.01 in absolute sense and 8% in a relative sense. The differences are probably caused by 'streaming' of the neutrons in fuel kernel-free planes. These channel effects become relatively important if the spacing between kernels becomes larger, which is the case for small kernels and for low kernel densities.

## A.9 Dancoff-factor sensitivity of resonance integrals and other parameters

In this appendix, we will investigate whether an accurate calculation of the Dancoff factor is important for obtaining core performance parameters of an HTR. First, the sensitivity of resonance integrals (RI's) to the Dancoff factor is studied in a theoretical way. This is

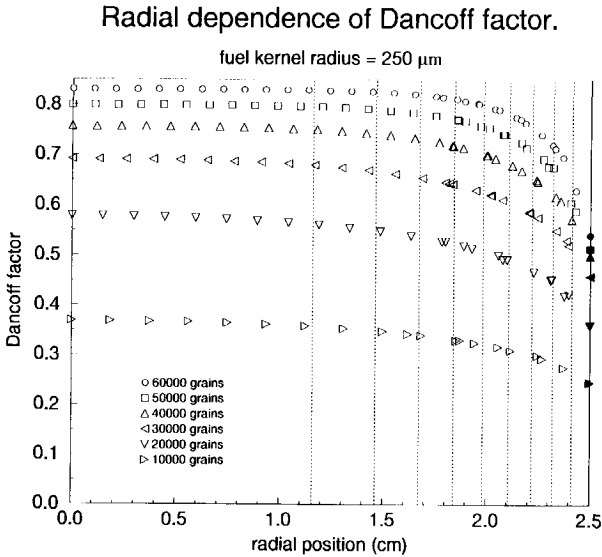


**Figure A.8:** Fuel kernel Dancoff factor as a function of the radial position in the pebble's fuel zone for a fuel kernel with a radius of 250  $\mu\text{m}$ . Each point corresponds to one million MCNP neutron histories. The fuel zone is divided by the dashed vertical lines into 10 equi-volumes. The filled symbols are extrapolated ( $2^{\text{nd}}$  order function) from the five outer MCNP-points.

done for unbroadened ( $T = 0$  K) resonances, since this allows a rather simple analytical approach. It will turn out that the resonance parameters of each resonance determine a certain lump size for which the corresponding RI is most sensitive to the Dancoff-factor. As an example, we will determine the radius of a spherical lump for which the Dancoff-factor sensitivity of the important 6.7 eV RI of  $^{238}\text{U}$  is maximal. If the Dancoff factor equals 0.667, this radius appears to be identical to that of a  $\text{UO}_2$  fuel kernel. The combination of the mentioned radius and Dancoff factor corresponds to an HTR pebble that contains about 38,000 CPs. For this pebble, a double-heterogeneous unit-cell calculation was carried out, for which the Dancoff-factor sensitivity of several reactor physics parameters was examined.

### A.9.1 Analytical approach

The Narrow Resonance Infinite Mass (NRIM) theory, in conjunction with Wigner's rational approximation for the first-flight escape probability, yields for the RI of an unbroadened ( $T = 0$  K) resonance [69]

$$I = I_{\infty} \sqrt{\frac{\beta}{1 + \beta}}, \quad (\text{A.31})$$

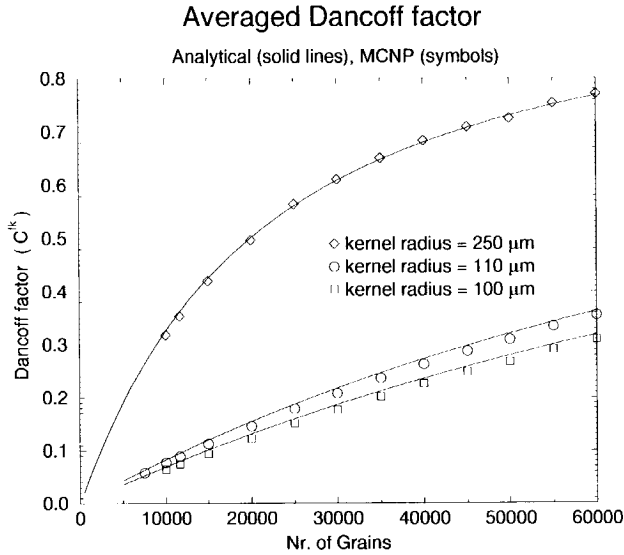


**Figure A.9:** The average fuel kernel Dancoff factor as a function of the number of coated particles (grains) in the fuel zone, with the fuel kernel radius as a parameter.

where  $I_\infty$  is the infinite dilution RI, and

$$\beta = \frac{\sigma_p + (N_a \bar{l}_F)^{-1}}{\sigma_0} \frac{\Gamma}{\Gamma_\gamma}, \quad (\text{A.32})$$

in which  $\sigma_p$  is the potential scattering cross section of the resonance absorber,  $\sigma_0$  is the total microscopic cross section at the resonance energy,  $\Gamma_\gamma$  the natural line width for capture and  $\Gamma$  the total natural line width. The term  $(N_a \bar{l}_F)^{-1}$  is commonly known as the microscopic escape cross section, in which  $N_a$  is the nuclide density of the resonance absorber and  $\bar{l}_F$  is the Dancoff-corrected (or effective) mean chord length of the fuel lump, that reads

$$\bar{l}_F = \frac{\bar{l}_F}{1 - C}. \quad (\text{A.33})$$

Here,  $\bar{l}_F$  is the mean chord length of the fuel lump ( $4 \times \text{volume}/\text{surface}$  [61]) and  $C$  is the Dancoff factor. The Dancoff-factor sensitivity coefficient of the RI reads

$$\frac{C}{I} \frac{\partial I}{\partial C} = \frac{C}{2(1 - C)} \frac{\frac{\sigma_p}{\sigma_0} - \beta}{\beta(1 + \beta)}. \quad (\text{A.34})$$

A maximum of the sensitivity coefficient occurs if

$$\beta = \frac{\sigma_p}{\sigma_0} + \sqrt{\frac{\sigma_p}{\sigma_0} \left(1 + \frac{\sigma_p}{\sigma_0}\right)} \approx \sqrt{\frac{\sigma_p}{\sigma_0}}, \quad (\text{A.35})$$

where the approximation is valid for dominating resonances with  $\sigma_p \ll \sigma_0$ . Fig. A.10 shows the Dancoff-factor sensitivity coefficient  $\frac{C}{I} \frac{\partial I}{\partial C}$ , multiplied by  $2(1 - C)/C$ , as a function of  $\beta(\sigma_p/\sigma_0)^{-1/2}$ , with  $\sigma_p/\sigma_0$  as parameter. Eqs. A.32-A.33 show that  $\beta = \sqrt{\frac{\sigma_p}{\sigma_0}}$  corresponds with

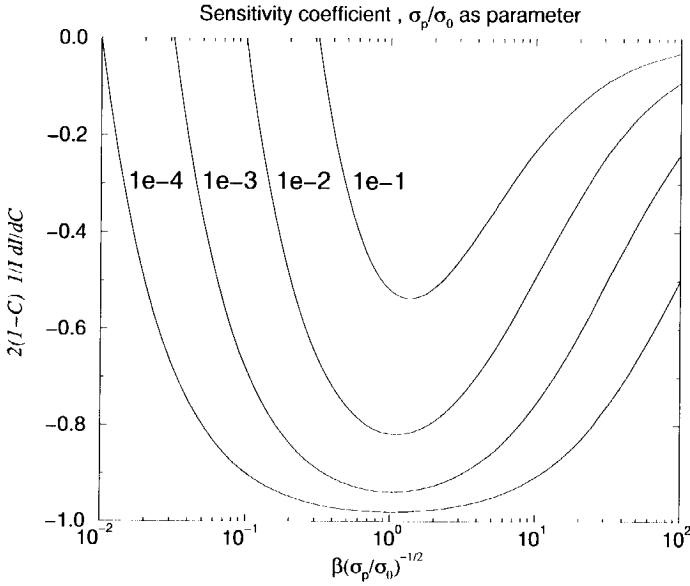


**Figure A.10:** The Dancoff-factor sensitivity coefficient of the resonance integral,  $\frac{C}{\Gamma} \frac{\partial I}{\partial C}$ , multiplied by  $2(1 - C)/C$ , as a function of  $\beta(\sigma_p/\sigma_0)^{-1/2}$  with  $\sigma_p/\sigma_0$  as parameter.

$$\bar{V}_F = \frac{\bar{I}_F}{1 - C} \approx \frac{1}{N_A \sqrt{\sigma_p \sigma_0}} \frac{\Gamma}{\Gamma_\gamma} \quad (A.36)$$

This expression gives the effective mean chord length of a fuel lump for which the RI of a particular resonance is most sensitive to the Dancoff factor.

For  $\beta = \sqrt{\frac{\sigma_p}{\sigma_0}}$  the Dancoff-factor sensitivity coefficient for the RI is maximal (in absolute sense) and becomes

$$\left( \frac{C}{\Gamma} \frac{\partial I}{\partial C} \right)_{\max} \approx -\frac{C}{2(1 - C)} \quad (A.37)$$

This reveals that if the Dancoff factor is tending to unity the RI becomes more sensitive to the Dancoff factor. When  $C = 0.667$  the Dancoff-factor sensitivity coefficient of the RI reads  $\frac{C}{\Gamma} \frac{\partial I}{\partial C} = -1$ . This means that if the Dancoff factor is over-estimated by 1%, the RI (and thus the group cross section that embraces the resonance) is under-estimated by 1%. The 6.7-eV resonance of  $^{238}\text{U}$  is characterised by  $\Gamma_\gamma = 23.0 \cdot 10^{-3}$  eV,  $\Gamma = 24.5 \cdot 10^{-3}$  eV,  $\sigma_0 = 2.4 \cdot 10^4$  eV and  $\sigma_p = 11$  barn. For a nuclide density of  $0.021 \text{ barn}^{-1}\text{cm}^{-1}$ , eq. A.36 shows that the RI of the mentioned resonance is most sensitive to the Dancoff factor if  $\bar{I}_F/(1 - C) = 0.099$  cm. The radius of a spherical lump that corresponds to this chord length is equal to  $r_F = \frac{3}{4}\bar{I}_F = 0.074 * (1 - C)$ . For  $C = 0.667$ ,  $r_F = 0.025$ , which is identical to that of a  $\text{UO}_2$  fuel kernel in a high temperature reactor. The mentioned Dancoff factor refers to a pebble that contains about 38,000 CPs (with  $\text{UO}_2$  kernels), which corresponds to 22.8 gr HM per pebble.



## A.9.2 Dancoff-factor sensitivity of several parameters obtained from calculations

For the mentioned HTR pebble ( 38,000  $\text{UO}_2$  CPs, 22.8 gr HM/pebble, 5.8% enrich.) a double-heterogeneous cell calculation with the SCALE code package has been performed. This involves, subsequently, a 'grain cell' calculation, in which the resonance shielding is carried out, and a 'pebble cell' calculation. The weighted fine-group cross sections of the grain cell are passed on to eigenvalue calculation of the pebble cell. The validity of this two-step approach has been demonstrated in [60] by comparing several reactor physics parameters to those obtained by MCNP calculations. Moreover, the same document shows that single-heterogeneous calculations yield unsatisfying results. As the preceding theoretical analysis was based on unbroadened resonances, the calculation has been done at a temperature that was as low as possible, viz. 10 K. However, to obtain results for a realistic pebble as well, the same calculation was repeated with  $T = 1200$  K. Table A.1 shows the change of some reactor physics parameters due to a reduction of the Dancoff factor by 10%. The Dancoff factor is denoted by  $C$ ,  $\sigma_g^y$  [barn] is the shielded group cross section between 5.04 eV and 9.2 eV (containing the 6.7-eV resonance of  $^{238}\text{U}$ ),  $I_{res}$  [barn] is the effective RI (Nordheim Method) of all resolved resonances lying between 1 eV and 677 eV,  $k_\infty$  is the infinite multiplication factor,  $p$  is the resonance escape probability, and  $C^*$  is defined as the  $^{238}\text{U}$  capture rate divided by the  $^{235}\text{U}$  fission rate. Table A.1 shows that the reduction of the Dancoff factor by 10% causes an increase of  $\sigma_g^y$ , also by almost 10%. This is in agreement with the Dancoff-factor sensitivity coefficient of  $\frac{C}{T} \frac{\partial I}{\partial C} = -1$  mentioned previously. For  $T = 1200$  K, the changes of the parameters due to a reduction of  $C$  are slightly larger than those of  $T = 10$  K. The changes in  $k_\infty$  and  $C^*$  amount to -3.7% and +9%, respectively.

In conclusion, the Dancoff-factor sensitivity coefficient of the RI of a single resonance is determined by the size of the lump, the absorber density, the Dancoff factor and the resonance parameters. The closer the Dancoff factor to unity the larger this coefficient. The degree to which the RI of a single resonance contributes to the total RI determines the Dancoff-factor sensitivity of the latter. Because both the moderator-to-fuel ratio and the total RI determine the resonance absorption rate and thus  $p$  and  $k_\infty$ , each system requires its own Dancoff-factor sensitivity study.

**Table A.1:** Changes of several reactor physics parameters due to a reduction of the Dancoff factor by 10%.

C	uniform-T = 10 K					uniform-T = 1200 K				
	$\sigma_g^y$	$I_{res}$	$k_\infty$	$p$	$C^*$	$\sigma_g^y$	$I_{res}$	$k_\infty$	$p$	$C^*$
0.6667	33.48	281.0	1.339	0.569	0.585	52.34	290.1	1.085	0.457	0.988
0.6	35.87	282.6	1.299	0.556	0.625	56.73	290.9	1.044	0.438	1.074
-10%	+7%	+0.6%	-3%	-2.4%	+7%	+8%	+0.3%	-3.7%	-4.2%	+9%

## A.10 Conclusion

The Dancoff factor for fuel kernels embedded in a graphite matrix of infinite dimensions ( $C_{\infty}^{fk}$ ) has been calculated by three existing analytical methods and two MCNP calculations. The MCNP model, in which fuel kernels are randomly positioned in a graphite matrix, is the reference case. The  $C_{\infty}^{fk}$ -values obtained with the MCNP model, in which the fuel kernels are positioned in a rectangular cubic lattice, differ from those of the reference case by maximally 18%, which is caused by channel effects in the lattice. Janssen's analytical formula for  $C_{\infty}^{fk}$  shows an underestimation of maximally 5% with the reference case. The maximal relative errors appear at low CP densities and for small kernel radii. In these cases the Dancoff factor is low, which implies that the effective escape probability is fortunately relatively insensitive to an error in the Dancoff factor. Janssen's rational expression, which is a simplification of the analytical one, gives results that are within the error margins of those of the reference case. The results of Lane's formula lie for low CP densities and low kernel diameters within the error margins of those of the reference case.

An analytical formula for the average Dancoff factor of fuel kernels embedded in the fuel zone of a pebble ( $C^{fk}$ ) has been derived. It turns out that  $C^{fk}$  can be written as  $C_{\infty}^{fk}$  times a 'correction' factor, which accounts for the double heterogeneity of the system. This correction factor depends on the radius of the fuel zone (FZ) of the pebble, the Dancoff factor of the pebble's fuel zone ( $C_{\infty}^{fz}$ ), the CP-density in the FZ and so on. The dependence of the correction factor with respect to the FZ-radius and pebble shell thickness has been studied. The results of the analytical formula were in close agreement with the MCNP results.

The average Dancoff factor for the fuel kernel ( $C^{fk}$ ) as a function of the number of grains in the FZ has been calculated analytically and with MCNP. This has been done for the standard pebble, with a diameter of 6 cm and an FZ diameter of 5 cm. In case of a fuel kernel radius of 250  $\mu\text{m}$ , the methods are in good agreement. However, for the kernel radii of 100 and 110  $\mu\text{m}$  the MCNP calculation shows smaller  $C^{fk}$ -values than those of the analytical method. This is due to channel effects in the rectangular lattice used in the MCNP model.

The calculation of an averaged fuel kernel Dancoff factor by MCNP requires typically a CPU time of 7 hours. Since it is, until so far, impossible to model ten thousands of randomly positioned CPs in the pebble's fuel zone, one has to rely on CPs arranged on a rectangular lattice, which introduces for small kernels and low CP-densities errors due to channel effects. It is recommended to calculate Dancoff factors with the analytical formula presented in this paper, since this method does practically consume no CPU time, does not require building of MCNP models and, moreover, gives very good results.

## Appendix B

---

### Average and effective temperatures in a power generating pebble.

---

In the calculations presented in chapters 3 and 4 a uniform temperature has been assumed over the entire pebble. This means that the fuel kernels and the moderator (i.e. the inter-granular graphite and graphite of the pebble shell) have the same temperature. In this appendix, we investigate to which degree this uniform temperature profile deviates from the actual temperature profile in a power generating pebble. Moreover, average and effective temperatures will be calculated. To this end, we will set up a model for the heat transport in such a pebble. The following parameters are introduced:

$r$	: radial coordinate in the pebble geometry	[cm]
$R_i$	: radius of the fuel zone of the pebble	2.5 cm
$R_o$	: radius of the pebble	3.0 cm
$T_{FZ}(r)$	: Temperature in the fuel zone ( $0 < r < R_i$ )	[K]
$T_{Sh}(r)$	: Temperature in the pebble shell ( $R_i < r < R_o$ )	[K]
$T_o$	: Temperature at the surface of the pebble	[K]
$T_c$	: Temperature at the centre of the pebble	[K]
$P$	: Power generated by the pebble	[W/pebble]
$\lambda$	: Heat conductivity coefficient for graphite	[W cm <sup>-1</sup> K <sup>-1</sup> ]

We adopt the stationary heat equations (in radial coordinates) and boundary conditions, for fuel zone and pebble shell, of [28] (page 104 ff). These read

$$\frac{1}{r^2} \frac{d}{dr} \left( r^2 \lambda \frac{dT_{FZ}}{dr} \right) = - \frac{P}{\frac{4}{3} \pi R_i^3} \quad (\text{B.1})$$

$$\frac{1}{r^2} \frac{d}{dr} \left( r^2 \lambda \frac{dT_{Sh}}{dr} \right) = 0 \quad (\text{B.2})$$

with the boundary conditions

$$\begin{aligned} r = 0 & : \frac{dT_{FZ}}{dr} = 0 \\ r = R_i & : \frac{dT_{FZ}}{dr} = \frac{dT_{Sh}}{dr} \quad \text{and} \quad T_{FZ} = T_{Sh} \\ r = R_o & : T_{Sh} = T_o \end{aligned}$$

The temperature  $T_o$  at the boundary of the pebble is determined by the temperature of the coolant and the heat transfer coefficient. (Ref. [28] shows that  $T_o = T_g + P/(\alpha 4\pi R_o^2)$ , where  $T_g$  is the coolant temperature and  $\alpha$  [ $\text{W cm}^{-2} \text{K}^{-1}$ ] is the heat transfer coefficient.) In eqs. B.1-B.2 it is assumed that the power density (i.e.  $P/(\frac{4}{3}\pi R_i^3)$ ) is homogeneous over the fuel zone of the pebble. Furthermore, the heat conductivity coefficient ( $\lambda$ ) is assumed to be constant and equal for fuel zone and pebble shell. Solving the differential equations in combination with the boundary conditions results in:

$$T_{FZ}(r) = T_o + \frac{P}{4\pi\lambda} \left\{ -\frac{1}{R_o} + \frac{3}{2R_i} - \frac{r^2}{2R_i^3} \right\} \quad (\text{B.3})$$

$$T_{Sh}(r) = T_o + \frac{P}{4\pi\lambda} \left\{ -\frac{1}{R_o} + \frac{1}{r} \right\} \quad (\text{B.4})$$

This shows that the temperature is decreasing from the centre to the surface of the pebble. The maximal temperature, at  $r = 0$ , reads  $T_o + \frac{P}{4\pi\lambda} \left( -\frac{1}{R_o} + \frac{3}{2R_i} \right)$ . The maximal temperature differences of the fuel zone, pebble shell and entire pebble read

$$\Delta T_{FZ} = \frac{P}{4\pi\lambda} \left( \frac{1}{2R_i} \right) \quad , \quad (\text{B.5})$$

$$\Delta T_{Sh} = \frac{P}{4\pi\lambda} \left( -\frac{1}{R_o} + \frac{1}{R_i} \right) \quad , \quad (\text{B.6})$$

$$\Delta T = \Delta T_{FZ} + \Delta T_{Sh} = \frac{P}{4\pi\lambda} \left( -\frac{1}{R_o} + \frac{3}{2R_i} \right) \quad , \quad (\text{B.7})$$

respectively. For a pebble bed with an overall power density of  $3 \text{ W cm}^{-3}$  and a packing fraction of 62%, the power per pebble is equal to  $P = 547 \text{ W}$ . If we assume a heat conductivity coefficient for the graphite of  $\lambda = 0.06 \text{ W cm}^{-1} \text{K}^{-1}$  (see fig.4.7 of [28]), the maximal temperature difference over the pebble becomes  $\Delta T = 193 \text{ K}$ .

## B.1 Average temperatures

With eq. B.3 the average temperature in the fuel zone becomes

$$T_{FZ}^{ave} = \frac{\int_0^{R_i} T_{FZ}(r) 4\pi r^2 dr}{\int_0^{R_i} 4\pi r^2 dr} = T_o + \frac{P}{4\pi\lambda} \left\{ -\frac{1}{R_o} + \frac{6}{5R_i} \right\} \quad , \quad (\text{B.8})$$

whereas that of the pebble shell becomes with eq. B.4

$$T_{Sh}^{ave} = \frac{\int_{R_i}^{R_o} T_{Sh}(r) 4\pi r^2 dr}{\int_{R_i}^{R_o} 4\pi r^2 dr} = T_o + \frac{P}{4\pi\lambda} \left\{ -\frac{1}{R_o} + \frac{3}{2} \frac{R_o^2 - R_i^2}{R_o^3 - R_i^3} \right\} \quad . \quad (\text{B.9})$$

The graphite temperature, averaged over the entire pebble, is equal to the volume weighted average of the average temperatures of the fuel zone and pebble shell, and hence reads

$$T_{Peb}^{ave} = \frac{R_i^3 T_{FZ}^{ave} + (R_o^3 - R_i^3) T_{Sh}^{ave}}{R_o^3} \quad . \quad (\text{B.10})$$

For the time being, we assume that there is no temperature difference between a fuel kernel and the ambient graphite (neglecting the coatings), which means that the average fuel

temperature will be identical to the average graphite temperature in the fuel zone. This is valid assumption if the thermal conductivity of the fuel kernels is very large and the surface-to-volume ratio of the kernel is very small. In section B.3, it will be shown that the average temperature of the fuel kernel is about one degree K higher than the temperature of the ambient graphite. The difference between the average fuel temperature and the average graphite temperature becomes

$$\begin{aligned}
 T_{fuel}^{ave} - T_{peb}^{ave} &\approx T_{FZ}^{ave} - T_{peb}^{ave} \\
 &= \frac{R_o^3 - R_i^3}{R_o^3} \{ T_{FZ}^{ave} - T_{Sh}^{ave} \} \\
 &= \frac{R_o^3 - R_i^3}{R_o^3} \left\{ \frac{6}{5R_i} - \frac{3}{2} \frac{R_o^2 - R_i^2}{R_o^3 - R_i^3} \right\} \frac{P}{4\pi\lambda} \\
 &= 3.935 \cdot 10^{-3} \left( \frac{P}{\lambda} \right) .
 \end{aligned} \tag{B.11}$$

This reveals that the difference between the average temperature of the fuel and that of the graphite is proportional with the power and inversely proportional with the heat conductivity of the graphite. Inserting  $P = 547 \text{ W}$ ,  $\lambda = 0.06 \text{ W cm}^{-1} \text{ K}^{-1}$ , yields  $T_{fuel}^{ave} - T_{peb}^{ave} = 36 \text{ K}$ . One should note that this difference is independent of  $T_0$ , and thus independent of the temperature of the gas and the heat transfer coefficient of the gas. The temperature difference of 36 K shows that the uniform temperature assumption (i.e.  $T_{fuel}^{ave} = T_{peb}^{ave}$ ) used in this document does not represent reality. On the other hand, the temperature difference of 36 K is small, which will be illustrated by the following: A real, power generating pebble has a 36 K higher average fuel temperature than its 'uniform-temperature' counterpart with the same average graphite temperature. Since the Doppler coefficient is of the order of  $-5 \text{ pcm/K}$ , the uniform temperature assumption will lead to a  $k_\infty$  that is about 0.2% higher compared to that of a real pebble.

## B.2 Effective temperatures

Since the temperature varies in the radial direction of the pebble, temperature-dependent cross sections  $\sigma(T)$  vary in this direction, too. The volume weighted average of a temperature-dependent cross section yields an *effective* cross section. This effective cross section equals  $\sigma(T_{eff})$ , where  $T_{eff}$  is the corresponding effective temperature. If a particular cross section is linear with  $T$ , the effective temperature equals the average temperature. However, for cross sections with e.g.  $\sqrt{T}$  or  $1/\sqrt{T}$ -dependencies the effective temperature differs from the average temperature. Below, the effective temperatures for fuel and graphite are calculated.

The resonance integrals, and thus the group cross sections in the resonance range, are dependent on the fuel temperature. A widely used correlation for the temperature-dependence of the effective resonance integral [134] reads:

$$I = A + B\sqrt{T}.$$

The effective fuel temperature should therefore be calculated as

$$\left(T_{fuel}^{eff}\right)^{\frac{1}{2}} = \frac{\int_0^{R_i} T_{fuel}^{\frac{1}{2}}(r) 4\pi r^2 dr}{\int_0^{R_i} 4\pi r^2 dr} \quad (B.12)$$

The temperature of the moderator determines the thermal part of the spectrum. If the moderator temperature increases, the thermal spectrum shifts to higher energies. Since the cross sections exhibit, to first approach, a  $1/v$ -behaviour in the thermal energy range, a shift of the thermal part of the spectrum causes a decrease of the thermal group constants. If we assume that the thermal part of the spectrum is perfectly Maxwellian (i.e. the neutrons are exactly in thermal equilibrium with the medium) and that the absorption cross section is of the  $1/v$ -form, the thermal-group cross section obeys

$$\Sigma_{a,th} \sim \frac{1}{\sqrt{T}},$$

which can be inferred from p. 383 of [69]. This implies that the effective moderator temperature can be calculated as

$$\left(T^{eff}\right)^{-\frac{1}{2}} = \frac{\int_V T^{-\frac{1}{2}}(r) 4\pi r^2 dr}{\int_V 4\pi r^2 dr}, \quad (B.13)$$

where  $V$  refers to either the fuel zone or the pebble shell. We will now use eqs. B.12 and B.13 to calculate the effective fuel and graphite temperature, successively.

### B.2.1 Effective fuel temperature

Assuming again that  $T_{fuel}(r) \approx T_{FZ}(r)$ , and inserting eq. B.3 into eq. B.12 gives

$$\left(T_{fuel}^{eff}\right)^{\frac{1}{2}} = \frac{\int_0^{R_i} T_{fuel}^{\frac{1}{2}}(r) 4\pi r^2 dr}{\int_0^{R_i} 4\pi r^2 dr} = \frac{3}{\sqrt{2}} R_i^{-\frac{9}{2}} \left(\frac{P}{4\pi\lambda}\right)^{\frac{1}{2}} \int_0^{R_i} r^2 (a - r^2)^{\frac{1}{2}} dr,$$

in which

$$a \equiv 2R_i^3 \left(\frac{1}{\xi} - \frac{1}{R_o} + \frac{3}{2R_i}\right), \quad (B.14)$$

and

$$\xi \equiv \frac{P}{4\pi\lambda T_o}. \quad (B.15)$$

With formula 2.272.2 of [131], the effective fuel temperature becomes

$$\left(T_{fuel}^{eff}\right)^{\frac{1}{2}} = \frac{3}{\sqrt{2}} R_i^{-\frac{9}{2}} \left(\frac{P}{4\pi\lambda}\right)^{\frac{1}{2}} \left\{ -\frac{R_i}{4} (a - R_i^2)^{\frac{3}{2}} + \frac{a R_i}{8} \sqrt{a - R_i^2} + \frac{a^2}{8} \arcsin\left(\frac{R_i}{\sqrt{a}}\right) \right\}. \quad (B.16)$$

Dividing both sides of eq. B.16 by  $T_o^{\frac{1}{2}}$  shows that  $T_{fuel}^{eff}/T_o$  is a function of  $\xi$ .

### B.2.2 Effective graphite temperature in fuel zone

Inserting eq. B.3 into eq. B.13 yields for the effective graphite temperature in the fuel zone

$$\left(T_{FZ}^{eff}\right)^{-\frac{1}{2}} = \frac{\int_0^{R_i} T_{FZ}^{-\frac{1}{2}}(r) 4\pi r^2 dr}{\int_0^{R_i} 4\pi r^2 dr} = 3\sqrt{2} R_i^{-\frac{3}{2}} \left(\frac{P}{4\pi\lambda}\right)^{-\frac{1}{2}} \int_0^{R_i} r^2 (a - r^2)^{-\frac{1}{2}} dr,$$

where  $\xi$  is given by eq. B.15. Evaluation of the integral (formula 2.272.3 of [131]) gives

$$\left(T_{FZ}^{eff}\right)^{-\frac{1}{2}} = \frac{3}{\sqrt{2}} R_i^{-\frac{3}{2}} \left(\frac{P}{4\pi\lambda}\right)^{-\frac{1}{2}} \left\{ -R_i \sqrt{a - R_i^2} + a \arcsin\left(\frac{R_i}{\sqrt{a}}\right) \right\}. \quad (\text{B.17})$$

### B.2.3 Effective graphite temperature in pebble shell

Inserting eq. B.4 into eq. B.13 yields for the effective graphite temperature in the pebble shell

$$\left(T_{Sh}^{eff}\right)^{-\frac{1}{2}} = \frac{\int_{R_i}^{R_o} T_{Sh}^{\frac{1}{2}}(r) 4\pi r^2 dr}{\int_{R_i}^{R_o} 4\pi r^2 dr} = \frac{3}{R_o^3 - R_i^3} \left(\frac{P}{4\pi\lambda}\right)^{-\frac{1}{2}} \int_{R_i}^{R_o} r^2 \left(c + \frac{1}{r}\right)^{-\frac{1}{2}} dr,$$

in which

$$c \equiv \frac{1}{\xi} - \frac{1}{R_o}, \quad (\text{B.18})$$

where  $\xi$  is given by eq. B.15. Through substituting  $r$  by  $y^2$ , the integral can be evaluated with formula 2.274.3 of [131], which eventually gives

$$\begin{aligned} \left(T_{Sh}^{eff}\right)^{-\frac{1}{2}} &= \frac{6}{R_o^3 - R_i^3} \left(\frac{P}{4\pi\lambda}\right)^{-\frac{1}{2}} \left( \sqrt{R_o} \sqrt{cR_o + 1} \left(\frac{R_o^2}{6c} - \frac{5R_o}{24c^2} + \frac{5}{16c^3}\right) \right. \\ &\quad - \sqrt{R_i} \sqrt{cR_i + 1} \left(\frac{R_i^2}{6c} - \frac{5R_i}{24c^2} + \frac{5}{16c^3}\right) \\ &\quad \left. - \frac{5}{16c^3} I_1 \right), \end{aligned} \quad (\text{B.19})$$

where

$$I_1 = \begin{cases} \frac{1}{\sqrt{c}} \ln \left( \frac{\sqrt{cR_o} + \sqrt{cR_o + 1}}{\sqrt{cR_i} + \sqrt{cR_i + 1}} \right) & \text{for } c > 0 \\ \frac{1}{\sqrt{-c}} \left( \arcsin(\sqrt{-cR_o}) - \arcsin(\sqrt{-cR_i}) \right) & \text{for } c < 0 \end{cases}. \quad (\text{B.20})$$

### B.2.4 Effective graphite temperature for the entire pebble

The effective graphite temperature for the entire pebble is given by

$$\left(T_{peb}^{eff}\right)^{-\frac{1}{2}} = \frac{R_i^3 \left(T_{FZ}^{eff}\right)^{-\frac{1}{2}} + (R_o^3 - R_i^3) \left(T_{Sh}^{eff}\right)^{-\frac{1}{2}}}{R_o^3}. \quad (\text{B.21})$$

Inserting eq. B.19 and B.17 into eq. B.21, gives

$$\begin{aligned} \left(T_{peb}^{eff}\right)^{-\frac{1}{2}} &= R_o^{-3} \left(\frac{P}{4\pi\lambda}\right)^{-\frac{1}{2}} \left\{ \frac{3}{\sqrt{2}} R_i^{\frac{3}{2}} [-R_i \sqrt{a - R_i^2} + a \arcsin\left(\frac{R_i}{\sqrt{a}}\right)] \right. \\ &\quad + 6 \left( \sqrt{R_o} \sqrt{cR_o + 1} \left(\frac{R_o^2}{6c} - \frac{5R_o}{24c^2} + \frac{5}{16c^3}\right) \right. \\ &\quad - \sqrt{R_i} \sqrt{cR_i + 1} \left(\frac{R_i^2}{6c} - \frac{5R_i}{24c^2} + \frac{5}{16c^3}\right) \\ &\quad \left. \left. - \frac{5}{16c^3} I_1 \right) \right\}, \end{aligned} \quad (\text{B.22})$$

where  $I_1$  is given by eq. B.20. If we multiply both sides of eq. B.22 with  $T_o^{\frac{1}{2}}$ , we see that  $T_{peb}^{eff}/T_o$  can be expressed in one variable only, viz.  $\xi$  given by eq. B.15.

### B.3 Average temperature of the fuel kernel

The fuel kernels in the fuel zone have a high surface-to-volume ratio, which means that their generated heat is transported efficiently to the ambient graphite. This implies that the temperature gradient within a fuel kernel is expected to be small. Analogously to the solution of the temperature in the fuel zone of the pebble, we can derive for the temperature in the fuel kernel

$$T_{fk}(r) = T_{Amb} + \frac{P}{4\pi\lambda_{fk}N_{gr}} \left( \frac{1}{2r_{fk}} - \frac{r^2}{2r_{fk}^3} \right), \quad (\text{B.23})$$

in which  $N_{gr}$  is the number of grains per pebble and  $r_{fk}$  is the radius of the fuel kernel. It has been assumed that the temperature on the surface of the kernel is equal to that of the ambient graphite (neglecting coating layers), which gives the boundary condition  $T_{fk}(r_{fk}) = T_{Amb}$ . Eq. B.23 shows that the temperature difference between centre and surface of the fuel kernel is equal to

$$\Delta T_{fk} = \frac{P}{4\pi\lambda_{fk}N_{gr}} \cdot \frac{1}{2r_{fk}}. \quad (\text{B.24})$$

Let's assume that we have  $N_{gr} = 19406$  and  $r_{fk} = 0.011$  cm, which corresponds to case 5 of table 3.2. (This case has the smallest  $N_{gr}r_{fk}$ -product of all cases in the table.) The heat conductivity coefficient for  $\text{PuO}_2$  [135] reads

$$\lambda_{\text{PuO}_2}(T) = \frac{1}{0.5 \cdot 10^{-2} + 2.81 \cdot 10^{-4} T} \quad [\text{W m}^{-1}\text{K}^{-1}]. \quad (\text{B.25})$$

For a temperature of  $T = 900$  K, this yields  $\lambda_{\text{PuO}_2} = 0.039$  W cm<sup>-1</sup> K<sup>-1</sup>. According to eq. B.24, the maximal temperature difference in the fuel kernel then becomes  $\Delta T_{fk} = 2.6$  K. This implies that the *average* kernel temperature minus the temperature of the ambient graphite is even *less* than 2.6 K. The average fuel kernel temperature can be calculated as

$$T_{fk}^{ave} = \frac{\int_0^{r_{fk}} T_{fk}(r) 4\pi r^2 dr}{\int_0^{r_{fk}} 4\pi r^2 dr} = T_{Amb} + \frac{P}{4\pi\lambda_{fk}N_{gr}} \cdot \frac{1}{5r_{fk}}. \quad (\text{B.26})$$

The difference between the average temperature of the fuel kernel and the temperature of the ambient graphite is now equal to

$$\Delta T_{fk}^{ave} \equiv T_{fk}^{ave} - T_{Amb} = \frac{2}{5} \Delta T_{fk}, \quad (\text{B.27})$$

where  $\Delta T_{fk}$  is given by eq. B.24. For  $\Delta T_{fk} = 2.6$  K, this gives  $\Delta T_{fk}^{ave} = 1$  K, only. This shows that the average fuel kernel temperature is of the order of one degree K higher than that of the ambient graphite.

### B.4 Comparison of Average and Effective Temperatures

Fig. B.1 shows both the average and the effective graphite temperatures for the fuel zone, the pebble shell and the entire pebble. The temperatures are normalised to the surface temperature  $T_o$  of the pebble. The temperatures are plotted as function of  $\frac{P}{4\pi\lambda T_o}$ . The average temperatures for fuel zone, pebble shell and entire pebble are calculated with eqs. B.8, B.9



and B.10, respectively. The effective temperatures for fuel zone, pebble shell and entire pebble are calculated with eqs. B.17, B.19 and B.22, respectively.

Fig. B.2 shows the average and effective temperatures for the fuel, normalised to the surface temperature  $T_o$ , as function of  $\frac{P}{4\pi\lambda T_o}$ .

Figs. B.1-B.2 reveal that for  $\frac{P}{4\pi\lambda T_o} = 0$ , which corresponds to a pebble with zero power or infinite thermal conductivity, the effective and average temperatures are equal to the surface temperature  $T_o$ . This means that there is a uniform temperature profile in the pebble. For a typical pebble with  $P = 547$  W,  $\lambda = 0.06$  W K<sup>-1</sup> cm<sup>-1</sup> and  $T_o = 600$  K, we obtain  $\frac{P}{4\pi\lambda T_o} = 1.2$  cm. Figs. B.1-B.2 show that for this value the effective and average temperature are about equal. From fig. B.3 it can be seen that for  $\frac{P}{4\pi\lambda T_o} = 1.2$  cm the effective temperatures are less than 0.2% smaller than the average temperatures. Even for the high value of  $\frac{P}{4\pi\lambda T_o} = 20$  cm the differences are less than 5%. Supposing that the average temperature, in this extreme case, is 600 K, the effective temperature amounts to 570 K. Furthermore, if we assume that the moderator temperature coefficient of reactivity is of the order -10 pcm/K, the use of an average temperature for the graphite instead of an effective one will result in a  $k_\infty$  that is about 0.3% too low.

From this, one can conclude that for calculational purposes it seems accurate enough to use average temperatures instead of effective temperatures. We recall that the average fuel and graphite temperatures obey a simple relation, that reads

$$T_{fuel}^{ave} - T_{Peb}^{ave} = 3.935 \cdot 10^{-3} [\text{cm}^{-1}] \frac{P [\text{W}]}{\lambda [\text{W cm}^{-1}\text{K}^{-1}]}, \quad (\text{B.28})$$

in which  $P$  is the power per pebble and  $\lambda$  the heat conductivity coefficient for the graphite. Eq. B.28 is independent of the surface temperature  $T_o$ . Once the average graphite temperature is calculated from  $P$ ,  $\lambda$  and  $T_o$  by eqs. B.8-B.10, the average fuel temperature can be calculated by eq. B.28. However, this  $T_{fuel}^{ave}$  needs to be corrected for the difference between average kernel temperature and the ambient graphite, given by eq. B.27. This correction is usually small, i.e. typically of the order of one degree K.

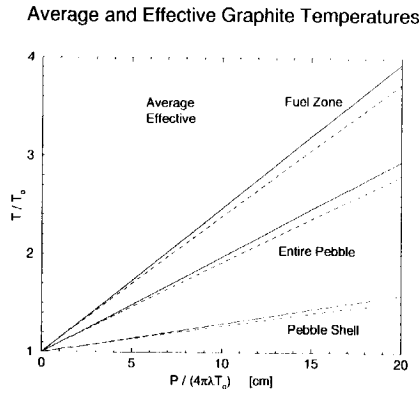


Figure B.1: Average and effective graphite temperatures, normalised to the surface temperature  $T_0$ , as function of  $\frac{P}{4\pi\lambda T_0}$ .

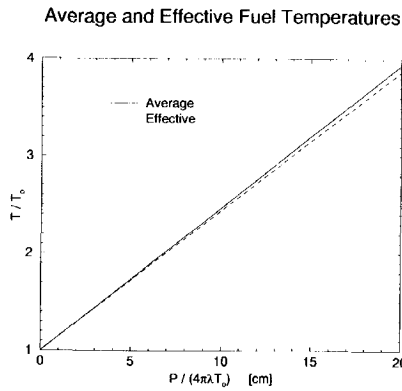


Figure B.2: Average and effective fuel temperatures, normalised to the surface temperature  $T_0$ , as function of  $\frac{P}{4\pi\lambda T_0}$ .

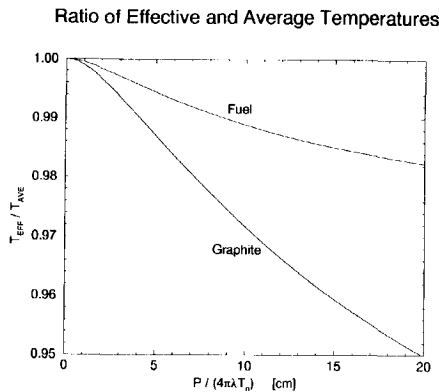


Figure B.3: Ratios of effective and average temperature as function of  $\frac{P}{4\pi\lambda T_0}$ . The "graphite"-curve corresponds to the "Entire Pebble"-curves in fig.B.1.

# Appendix C

---

## Maximisation of the Doppler effect

---

Increase of the fuel temperature in a nuclear reactor leads, or can lead, to

1. A Doppler broadening of the resonances of the nuclides in the fuel.
2. An expansion of the fuel.
3. A shift of the Maxwellian part of the spectrum to higher energies.

These processes together introduce a certain amount of reactivity, which can be expressed in the so-called fuel temperature reactivity coefficient. The reactivity effect of the third process is very small, because the Maxwell spectrum is to a major extent determined by the moderator temperature. Moreover, the reactivity effect due to an expansion of the fuel is small too, for most thermal systems. When the second and third processes can be neglected, the fuel temperature reactivity effect is fully determined by the Doppler effect. The fuel temperature reactivity coefficient is then called the Doppler coefficient of reactivity.

The Doppler broadening of the resonances causes an increase of resonance absorption, due to a decrease of self-shielding. The competition between resonance fission at the one hand and resonance capture at the other hand determines the sign and magnitude of the reactivity induced by an increase of the fuel temperature. In well-designed nuclear reactors the Doppler effect due to resonance capture by fertile nuclides exceeds the Doppler effect due to resonance fission, which implies that an increase of the fuel temperature causes a negative reactivity effect and a correspondingly negative Doppler coefficient. Since the Doppler effect is a prompt effect, occurring simultaneously with the dissipation of kinetic energy of the fission products into temperature, it is very important in the study of rapid power transients.

In this appendix<sup>1</sup>, the Doppler coefficient of reactivity is defined in section C.1. Section C.2 discusses the geometry of the unit cell for which the calculations are performed and describes the fuel types that have been investigated. In section C.3 the "Doppler efficiency" is introduced and three methods by which it can be calculated are presented. Section C.4 discusses the results of the calculations of the Doppler efficiency, based on both the NR(IM)-theory and the Nordheim Integral Method. Section C.5 presents the results of the calculations of the Doppler coefficient of reactivity under the constraint of constant  $k_{\infty}$ . In this calculation, the Doppler coefficient of reactivity is calculated for different configu-

---

<sup>1</sup>This appendix appeared also as [79].

rations of the unit cell, but all yielding the same  $k_{\infty}$ . This is done for both realistic fuels and artificial fuels. For the latter the fissile resonance absorbers are replaced by artificial  $1/v$  fissile nuclides in order to isolate the resonance absorption effects caused by the dominant resonance absorbers. The conclusions with respect to the maximisation of the absolute value of the Doppler coefficient are presented in section C.6. Appendices D and E are auxiliary to section C.3.

## C.1 Definition of the Doppler coefficient of reactivity

The Doppler coefficient of reactivity, in formula form, reads

$$\alpha_D = \frac{d\rho}{dT} = \frac{1}{k^2} \frac{dk}{dT}. \quad (\text{C.1})$$

Here,  $k$  is the multiplication factor,  $\rho$  ( $\equiv \frac{k-1}{k}$ ) is the reactivity and  $T$  is the fuel temperature. Equation C.1 holds for a system that is about critical ( $k \approx 1$ ). This is for instance the case when a whole core calculation is performed. However, many computational studies involve infinite lattice calculations. In these cases, infinite multiplication factors ( $k_{\infty}$ ) are being calculated, that are not necessarily equal to unity. De Kruijf and Janssen [75] have shown that in these situations the appropriate definition of the Doppler coefficient reads

$$\alpha_D = \frac{1}{k_{\infty}} \frac{dk_{\infty}}{dT}. \quad (\text{C.2})$$

A good way to analyse the infinite multiplication factor of a thermal reactor is to make use of the four factor formula, which reads

$$k_{\infty} = \eta \cdot f \cdot \epsilon \cdot p. \quad (\text{C.3})$$

Here,  $\eta$  is defined as the neutron production rate by thermal neutrons divided by the thermal neutron absorption in the fuel zone. The thermal utilisation factor  $f$  is defined as the thermal neutron absorption rate in the fuel zone divided by the total thermal neutron absorption rate. The non-thermal fission factor  $\epsilon$  is defined as the total neutron production rate divided by the thermal neutron production rate. The resonance escape probability  $p$  is the probability that a neutron, that is born in the non-thermal energy range as a fission neutron, slows down to the thermal energy range without being absorbed by resonance absorbers in the non-thermal energy range. A precise definition of  $p$  from the four-factor formula will be given in section C.3. If the expression for the infinite multiplication factor (eq. C.3) is inserted in eq. C.2 we obtain

$$\alpha_D = \frac{1}{(\eta f \epsilon)} \frac{d(\eta f \epsilon)}{dT} + \frac{1}{p} \frac{dp}{dT}. \quad (\text{C.4})$$

The Doppler broadening of the resonances, due to an increase of the fuel temperature, causes a decrease of self-shielding and consequently an increase of the resonance absorption. Since  $p$  incorporates the resonance absorption, a change of the fuel temperature will basically lead to a change of  $p$ , whereas the other factors of the four-factor formula are hardly dependent on the fuel temperature. Hence, a good approximation for the Doppler coefficient reads

$$\alpha_D \approx \frac{1}{p} \frac{dp}{dT}. \quad (\text{C.5})$$

In the following sections, it will be indicated whether the Doppler coefficient of reactivity will be calculated by eq. C.2 or eq. C.5.

## C.2 Geometry and fuel properties

In this study the Doppler coefficient ( $\alpha_D$ ) has been calculated for different fuel types. The dominating resonance absorbers in these fuels are  $^{232}\text{Th}$ ,  $^{238}\text{U}$  and  $^{240}\text{Pu}$ , respectively. For each fuel type, calculations on a spherical two-region white-boundary unit cell have been performed. The inner sphere contains the oxide fuel, while the outer spherical shell contains the moderator, which is graphite. This unit cell is chosen since it resembles very much the unit cell belonging to the High Temperature Reactor, for which a coated fuel particle is embedded in a graphite matrix.

The radius of the fuel sphere ( $r_F$ ) and the outer radius of the moderator ( $r_M$ ) characterise the unit cell in the following way: The atomic moderator-to-fuel ratio of the unit cell is proportional to the ratio of the volume of the moderator shell and the volume of the fuel sphere, and hence is proportional to  $((\frac{r_M}{r_F})^3 - 1)$ . The Dancoff-factor ( $C$ ) of the fuel zone can be expressed as a function of  $r_F$  and  $\frac{r_M}{r_F}$  (see appendix D). The Dancoff-corrected mean chord length ( $\bar{l}_F$ ), which is a function of the mean chord length  $\bar{l}_F = \frac{4}{3}r_F$ , (see appendix D) and the Dancoff factor, determines the effective resonance integral. In fact, there is an infinite number of combinations of  $l_F$  and  $C$  that lead to the same  $\bar{l}_F$  and thus to the same effective resonance integral. Moreover, there is an infinite number ( $r_F, r_M$ )-combinations that give either the same resonance escape probability  $p$  or the same  $k_\infty$ . In this study, the Doppler coefficient and other quantities have been calculated for various ( $r_F, r_M$ )-combinations.

The fuels used in this study can be divided in two groups: The first group comprises the realistic fuels, i.e. an oxide of a fertile resonance absorber in combination with a fissile resonance absorber, like  $^{235}\text{U}$ . In the second group, the fissile resonances absorbers are replaced by an artificial  $1/v$  fissile nuclide. This has as a consequence that only the main resonance absorbers ( $^{232}\text{Th}$ ,  $^{238}\text{U}$  and  $^{240}\text{Pu}$ , respectively) determine the resonance absorption and hence the Doppler coefficient. In this way, a better interpretation of effects related with resonance absorption due to a single resonance absorber is possible.

For all fuel types, the total absorber atomic density equals  $2.322 \cdot 10^{-2} \text{ barn}^{-1}\text{cm}^{-1}$  and the oxygen atomic density in the fuel equals two times this value. The carbon density of the graphite moderator is  $8.646 \cdot 10^{-2} \text{ barn}^{-1}\text{cm}^{-1}$ . The fuel temperature is 600 K. The compositions of the different fuel types are listed in table C.1. The second column of table C.1 shows the resolved energy range of the dominant resonance absorber, in which  $E_l$  and  $E_h$  are the lower and upper boundary, respectively. The  $E_l$  is also the cut-off energy that separates the thermal and the non-thermal energy range, used for calculating the factors of the four-factor formula, later on. The third column shows the infinite diluted resonance integral of the resolved resonance energy range for  $^{232}\text{Th}$ ,  $^{238}\text{U}$  and  $^{240}\text{Pu}$ . The artificial  $1/v$  fissile absorber "ArtNuc1" has 2200 m/s cross sections of 100 and 1 barn for fission and capture, respectively. For "ArtNuc2" these cross sections are 310 and 220 barn for fission and capture, respectively. The number of neutrons per fission ( $\bar{\nu}$ ) is for both artificial absorbers equal to 3.27. The plutonium mixture is from spent fuel of an LWR with a burnup of 47.5 MWd/kgHM.

Table C.1: The different fuels investigated in this study.

dominant resonance absorber	resolved resonance energy range ( $E_l - E_h$ )	$I_{\text{resolv}}^{\infty}$ (barn)	realistic fuel	artificial fuel
$^{232}\text{Th}$	6.16 eV - 3.53 keV	65	98.0% $^{232}\text{Th}$ 2.0% $^{233}\text{U}$	94.0% $^{232}\text{Th}$ 6.0% ArtNuc1
$^{238}\text{U}$	3.38 eV - 5.00 keV	274	95.0% $^{238}\text{U}$ 5.0% $^{235}\text{U}$	95.0% $^{238}\text{U}$ 5.0% ArtNuc1
$^{240}\text{Pu}$	0.50 eV - 3.53 keV	8425	23.1% $^{240}\text{Pu}$ 2.7% $^{238}\text{Pu}$ 55.5% $^{239}\text{Pu}$ 12.0% $^{241}\text{Pu}$ 6.7% $^{242}\text{Pu}$	23.1% $^{240}\text{Pu}$ 76.9% ArtNuc2

## C.3 Theory

### C.3.1 Introduction

A widely used formula for the resonance escape probability is the Wigner expression [136] which reads

$$p = \exp\left(-\frac{I_{\text{eff}}}{\xi\sigma_{sM}MF}\right), \quad (\text{C.6})$$

where  $\xi\sigma_{sM}$  is the moderating power of a nuclide belonging to the moderator,  $MF$  is the cell-averaged atomic moderator-to-fuel ratio and  $I_{\text{eff}}$  is the effective resonance integral. In the past, several measurements have been performed giving the effective resonance integral as functions of the dimensions of  $\text{UO}_2$  rods. The dependence of the effective resonance integral on the geometry of the fuel element is often expressed in the form

$$I_{\text{eff}} = a + b\frac{S}{M}, \quad (\text{C.7})$$

in which  $a$  and  $b$  are constants dependent on the absorption and scattering cross sections and the temperature,  $S$  is the surface exposed to the neutrons and  $M$  the mass [134, 136]. At most times, the effective resonance was measured using activation techniques. With the knowledge of the effective resonance integral, the resonance escape probability  $p$  could be calculated according to eq. C.6. However, sometimes the effective resonance integral was deduced from  $p$  measurements [137].

According to eq. C.5 the Doppler coefficient of reactivity is given by

$$\alpha_D \approx \frac{1}{p} \frac{dp}{dT}. \quad (\text{C.8})$$

If the expression for  $p$  of eq. C.6 is inserted into eq. C.8, this gives

$$\alpha_D \approx \ln(p) \alpha_0, \quad (\text{C.9})$$

with

$$\alpha_0 \equiv \frac{1}{I_{eff}} \frac{dI_{eff}}{dT}, \quad (C.10)$$

which is sometimes called the Doppler coefficient. It is the fractional change of the effective resonance integral per degree K and depends only on the dimensions and the temperature of the lump. (As will be seen later, a correction for fuel-shadowing effects have to be made, which leads to the use of an effective dimension of the lump.) Equation C.9 shows that, for a fuel lump with constant dimensions, and thus for a constant  $\alpha_0$ , a decrease of  $p$  causes an increase (of the absolute value) of the Doppler coefficient of reactivity. Equation C.6 shows that a decrease of  $p$  can be established by a decrease of the moderator-to-fuel ratio  $MF$ . On the other hand, eq. C.9 shows that for unit cells with different configurations, but all having the same  $I_{eff}/MF$  and thus giving the same  $p$ , the Doppler coefficient  $\alpha_0$  determines the magnitude of the Doppler coefficient of reactivity  $\alpha_D$ . In this way, the maximisation of the Doppler coefficient of reactivity  $\alpha_D$  under the constraint of a constant  $p$  is equivalent with the maximisation of the Doppler coefficient  $\alpha_0$ . In other words,  $\alpha_0$  determines the magnitude of the Doppler coefficient of reactivity at a given resonance absorption rate (corresponding to a certain  $p$ ). For this reason and in order to avoid confusion between the Doppler coefficient and the Doppler coefficient of reactivity,  $\alpha_0$  will be designated as the *Doppler efficiency*.

In literature, either an increasing or a decreasing  $\frac{1}{I_{eff}} \frac{dI_{eff}}{dT}$ , with increasing size of the fuel lump, is reported.

The decreasing Doppler efficiency is subject of an article of Pearce [138]. This article embraces an extensive study of both measurements and calculations of the Doppler efficiency for rather large sizes of the fuel lump. The Doppler efficiency is measured and sometimes calculated for cylindrical rods with radii varying from 0.2 to 5 cm which contain either thorium metal,  $\text{ThO}_2$ , uranium metal or  $\text{UO}_2$ . According to this article, the  $\alpha_0$  increases with increasing surface-to-mass ratio of the cylindrical rod.

The opposite is found by Lane *et al.* [123]. They studied thorium oxide grains, with radii smaller than 0.03 cm, and observed an increase of  $\frac{1}{I_{eff}} \frac{dI_{eff}}{dT}$  with increasing grain radii. The authors inferred from this that for increasing grain radii "*one can either maintain the same Doppler coefficient of reactivity with a reduced resonance absorption or increase the Doppler coefficient for the same resonance absorption.*" A close look to eq. C.9 gives a confirmation of this statement. The first part of this statement can be understood as follows: The Doppler coefficient of reactivity  $\alpha_D$  remains equal when an increase of  $\frac{1}{I_{eff}} \frac{dI_{eff}}{dT}$  is compensated by a decrease of  $|\ln p|$ . The latter implies a reduced resonance absorption. The second part of the statement says: If  $(\ln p)$  remains constant, i.e. the same resonance absorption, the Doppler coefficient increases because  $\frac{1}{I_{eff}} \frac{dI_{eff}}{dT}$  increases with increasing grain radii.

In this paper, the Doppler efficiency  $\frac{1}{I_{eff}} \frac{dI_{eff}}{dT}$  is studied in a broad range of the fuel lump size. In this way, at the one hand, the range of the small lump sizes, for which the Doppler efficiency increases with increasing lump size, and at the other hand the range of the large lump sizes, exhibiting the opposite behaviour, are connected. As will turn out, the intermediate range possesses a maximum value of  $\frac{1}{I_{eff}} \frac{dI_{eff}}{dT}$ .

In this study, the mentioned quantities, like the resonance escape probability and the

resonance integral are calculated by virtue of three different methods. The first method uses the Narrow Resonance (Infinite Mass) approximation. The second is based on the Nordheim Integral Method and the last method is based on the four factor formula. The first two methods have the same slowing down equation for the flux in the fuel zone as a starting point. Subsection C.3.2 describes how this equation is obtained. Thereafter, the mentioned methods will be discussed successively.

### C.3.2 The slowing down equation for the fuel zone

The set of equations describing neutron slowing-down in a two-region (fuel and moderator) unit cell, in which the spatial dependence of the flux both in the moderator region and in the fuel region is neglected, was originally introduced by Chernick [117, 139]. In a two region system the mentioned set of equations consists of two coupled integral equations, describing the slowing down in each region. Isotropic scattering in the centre-of-mass system is assumed for these equations, so that the maximum fractional energy loss of a neutron in an elastic scattering with a nuclide  $i$ , of scattering cross section  $\Sigma_{si}$ , is  $(1 - \alpha_i)$  where  $\alpha = [(A_i - 1)/(A_i + 1)]^2$  and  $A_i$  is the atomic mass number. Progress in solving the mentioned set of (two) equations is made by applying the narrow resonance approximation for the moderator, illustrated by

$$\Delta E |_M = \left(\frac{1 - \alpha_M}{2}\right) E_0 \gg \Gamma_p, \quad (\text{C.11})$$

which says that average energy loss of a neutron in collision with a moderator nucleus is large compared to the practical width of a resonance. The practical width [140] is defined as the full width of the energy interval in which the resonance cross section is greater than the off-resonance cross section of the fuel region. It represents qualitatively the interval in which the flux in an absorbing region is reduced by the large cross section of the resonance. The practical width is given by

$$\Gamma_p \equiv \Gamma \left[ \frac{\Sigma_0}{(\Sigma_p + \Sigma_{iM}^f)} \right]^{\frac{1}{2}}, \quad (\text{C.12})$$

where  $\Sigma_p$  is the macroscopic potential scattering cross section of the absorber,  $\Sigma_{iM}^f$  the macroscopic scattering cross section of the moderator admixed in the fuel region,  $\Gamma$  the full line width of the resonance at half-height and  $\Sigma_0$  is the total macroscopic cross section of the natural line shape (i.e. Breit-Wigner single-level cross section) at the resonance energy  $E_0$ . Usually, the practical width is much larger than the full width (e.g. a factor 50 for the first resonance of  $^{238}\text{U}$  in U-metal). By applying the Narrow Resonance approximation for the moderator the average flux in the moderator can be replaced by its asymptotic value  $\Phi_M \sim 1/E$ . The assumption of isotropic and uniform sources in both fuel and moderator region makes application of the two-region reciprocity theorem of Rothenstein [139, 141] possible. This reads

$$P_{iF} V_F \Sigma_{iF} = P_{iM} V_M \Sigma_{iM}, \quad (\text{C.13})$$

where the subscripts F and M denote the fuel and moderator region, respectively, and  $P_{ii}$  is the first-flight escape probability from region  $i$ ,  $V_i$  is the volume and  $\Sigma_{ii}$  is the macroscopic



cross section of region  $i$ . Application of the Narrow Resonance approximation for the moderator and the two-region reciprocity theorem leads to a decoupling of the mentioned equations and results in a single slowing-down equation for the flux in the fuel zone, which reads

$$\Sigma_t(E)\Phi(E) = [1 - P_o^*(E)] \int_E^{E/\alpha_A} \frac{\Sigma_s(E')\Phi(E')}{(1 - \alpha_A)E'} dE' + \frac{P_o^*(E)\Sigma_t(E)}{E} . \quad (C.14)$$

Here,  $\Phi(E)$  is the neutron flux in the fuel zone,  $\Sigma_t(E)$  and  $\Sigma_s(E)$  are the total and scattering macroscopic cross section of the fuel zone, respectively,  $\alpha_A$  the maximal fractional energy loss of a neutron in an elastic collision with an absorber nuclide and  $P_o^*(E)$  is the Dancoff-corrected first-flight escape probability from the fuel region. The latter reads [69]

$$\frac{1}{P_o^*(E)} = \frac{1}{P_o(E)} + \left(\frac{C}{1 - C}\right)\Sigma_t\bar{l}_F , \quad (C.15)$$

where  $P_o$  is the first-flight escape probability from the fuel sphere situated in an infinite sea of moderator, which is given by Case *et al.* [61] and presented in appendix D,  $\bar{l}_F$  is the mean chord-length ( $4 \times \text{volume/surface}$ ) of the fuel region,  $\Sigma_t$  is the total macroscopic cross section of the fuel region and  $C$  is the Dancoff-Ginsberg factor which accounts for the fuel-shadowing effect caused by neutrons that escape from the fuel lump, pass through the moderator without a collision and enter a next fuel lump. The Dancoff-Ginsberg factor only depends on the unit cell's geometry and on the total macroscopic cross section of the moderator. An analytical expression for the Dancoff-Ginsberg factor in a two-region spherical white boundary unit cell is presented in appendix D.

Inclusion of a moderator admixed in the fuel, such as oxygen in case of an oxide fuel, would lead to an extra integral term [57] in eq. C.14, but is omitted for the sake of simplicity here. The treatment of such internal moderators is given in many standard references [141, 142]. Equation C.14 is the starting point for both the NR(IM)-approximation and the Nordheim Integral methods. The next sections will discuss both methods, successively.

### C.3.3 The NR(IM) approximation method

Equation C.14 has two approximate solutions for the energy dependent flux in the fuel zone. The first is based on the narrow resonance (NR) and the second on the narrow resonance infinite mass (NRIM) approximation. The NR approximation is valid for the case that the practical width of the resonance is very narrow compared to the energy loss suffered in a collision with an absorber nucleus [69]. The NRIM approximation holds for the opposite situation. It should be noted that in both the NR and NRIM cases the practical width is assumed to be small compared to the energy loss suffered in a collision with a moderator nucleus present in the fuel zone.

For both solutions of the energy-dependent flux, the resonance integral of a single resonance can be calculated. The resonance integral for capture of a single resonance reads

$$I_i^{\text{NR(IM)}} = \int_{E_0} \sigma_\gamma^F(E) \Phi_F^{\text{NR(IM)}} dE . \quad (C.16)$$

Here,  $E_0$  is the energy at which the resonance is positioned,  $\sigma_\gamma^F$  is the Doppler broadened microscopic capture cross section of the absorber and  $\Phi_F^{\text{NR(IM)}}$  is the energy-dependent flux

in the fuel calculated by either the NRIM or the NR approximation. The energy-dependent flux in the NR and NRIM approximation are given explicitly in [69, 142]. Inserting the expressions of the flux for both approximations yields

$$I^{\text{NR(IM)}} = \frac{\sigma_0 \Gamma_\gamma}{E_0} \left( \int_0^\infty \frac{\psi(\zeta, x)}{\psi(\zeta, x) + \beta_{\text{NR(IM)}}} dx + \int_0^\infty \frac{P_o^*(\zeta, \beta, x) \psi^2(\zeta, x)}{\psi(\zeta, x) + \beta_{\text{NR(IM)}}} dx \right), \quad (\text{C.17})$$

where  $\psi(\zeta, x)$  is the Bethe-Placzek Doppler function, given by eq. E.4. The explanation of the remaining parameters in eq. C.17 will be deferred until later. The first integral is often called the volume term of the resonance integral, whereas the second is called the surface term. The latter accounts via the Dancoff-corrected first-flight escape probability ( $P_o^*$ ) for the heterogeneity of the cell. Wigner introduced a rational approximation for the first-flight escape probability (eq. D.3), which tremendously simplifies the expression of the individual resonance integral. Wigner's rational approximation for the first-flight escape probability reads

$$P_o = \frac{1}{1 + \frac{\Sigma_i^f \bar{l}_F}{\mathcal{A}}}, \quad (\text{C.18})$$

where  $\mathcal{A}$  is the so-called Bell factor. For  $\mathcal{A} = 1$  the original Wigner approximation is obtained. Strictly speaking, the Bell factor is not constant [130] but varies with  $\Sigma_i^f \bar{l}_F$  between 1 and 1.8 in such a way that Wigner's rational approximation coincides with the exact expression for the  $P_o(\Sigma_i^f \bar{l}_F)$ . However, in practice one chooses a constant  $\mathcal{A}$ . In analogy to the module WHEAD of the WIMS-code system [98]  $\mathcal{A} = 1.16$  is chosen in this study. A similar expression is obtained for the *Dancoff-corrected* first-flight escape probability, by inserting  $P_o$  in eq. C.15

$$P_o^* = \frac{1}{1 + \Sigma_i^f \bar{l}_F}, \quad (\text{C.19})$$

where

$$\bar{l}_F = \bar{l}_F \left( \frac{1}{\mathcal{A}} + \frac{C}{1 - C} \right) \quad (\text{C.20})$$

can be designated as the Dancoff-corrected mean chord length. The  $P_o^*$ , expressed in terms of the  $\psi$ -function, is presented in appendix D. When Wigner's rational approximation is applied and the  $P_o^*$  is inserted in eq. C.17, the surface term of eq. C.17 is absorbed by its volume term through a conversion from  $\beta_{\text{NR(IM)}}$  to  $\beta'_{\text{NR(IM)}}$ . This gives

$$I^{\text{NR(IM)}} = \frac{\sigma_0 \Gamma_\gamma}{E_0} \beta'_{\text{NR(IM)}} J(\zeta, \beta'_{\text{NR(IM)}}), \quad (\text{C.21})$$

with

$$\zeta \equiv \frac{\Gamma}{\Gamma_D} = \sqrt{\frac{A \Gamma^2}{4 E_0 k_B T}}, \quad (\text{C.22})$$

and

$$\beta'_{\text{NR}} = \frac{\sigma_p^{\text{NR}} + \sigma_e}{\sigma_0}, \quad (\text{C.23})$$

$$\beta'_{\text{NR(IM)}} = \frac{\sigma_p^{\text{NR(IM)}} + \sigma_e}{\sigma_0} \cdot \frac{\Gamma}{\Gamma_\gamma}, \quad (\text{C.24})$$

in which

- $J(\zeta, \beta')$  : The Doppler broadening function, given by  

$$J(\zeta, \beta') = \int_0^\infty \frac{\psi(\zeta, x)}{\psi(\zeta, x) + \beta'} dx .$$
- $A$  : The mass number of the absorber nuclide.
- $E_0$  : The energy at which the resonance is positioned.
- $\Gamma_\gamma$  : The natural line width for capture.
- $\Gamma_n$  : The natural line width for scattering.
- $\Gamma$  : The total natural line width, given by  $\Gamma = \Gamma_\gamma + \Gamma_n$ .
- $\Gamma_D$  : The Doppler width, given by  $\Gamma_D = \sqrt{\frac{4E_0 k_B T}{A}}$ .
- $k_B T$  : The temperature in eV.
- $\sigma_0$  : The total cross section of the Breit-Wigner single level cross section at the resonance energy  $E_0$ , which is given by  

$$\sigma_0 = 2.608 \cdot 10^6 \left(\frac{A+1}{A}\right)^2 \frac{1}{E_0} \frac{\Gamma_n}{\Gamma} g .$$
- $g$  : The statistical spin factor, which is equal to unity for  $l=0$ -resonances.
- $\sigma_e$  : The so-called escape cross section, given by  $\sigma_e = \frac{1}{N_A \bar{l}_F}$ .
- $N_A$  : The absorber nuclide density in the fuel.
- $\bar{l}_F$  : The effective or Dancoff-corrected mean chord length of the fuel zone, given by  $\bar{l}_F = \bar{l}_F \left(\frac{1}{A} + \frac{C}{1-C}\right)$ .
- $\mathcal{A}$  : The Bell-factor, used to adjust Wigner's rational approximation.
- $\sigma_p^{\text{NR}}$  :  $\sigma_p^{\text{NR}} \equiv \sigma_{,M}^F N_M^F / N_A + \sigma_p$ .
- $\sigma_p^{\text{NRIM}}$  :  $\sigma_p^{\text{NRIM}} \equiv \sigma_{,M}^F N_M^F / N_A$ .
- $\sigma_p$  : The potential scattering cross section of the absorber nuclide.
- $N_M^F$  : The nuclide density of the moderator admixed in the fuel.
- $\sigma_{,M}^F$  : The microscopic scattering cross section of the moderator admixed in the fuel.

The resonance parameters of the five lowest lying resonances of the resonance absorbers, investigated in this study, are listed in table E.5. Equation C.21 shows that the individual resonance integral is proportional to  $\beta J(\zeta, \beta)$ . The function  $\frac{2}{\pi} \beta J(\zeta, \beta)$  is plotted as a function of  $\beta$  with  $\zeta$  as a parameter in fig. C.1. Since  $\beta'$  is linear with  $1/(N_A \bar{l}_F)$ , a high  $\beta'_{\text{NRIM}}$  corresponds with a low degree of self shielding and vice versa. In the infinite dilution limit, in which  $N_A \rightarrow 0$ , and hence  $\beta' \rightarrow \infty$ , self shielding is absent and the function  $\beta J(\zeta, \beta) = \frac{\pi}{2}$ . Inserting this in C.21, gives the infinite dilution limit of the resonance integral, which reads

$$I^\infty = \frac{\pi \sigma_0 \Gamma_\gamma}{2 E_0} . \quad (\text{C.25})$$

The opposite limit, of maximal self shielding where  $\beta' \rightarrow 0$ , can be obtained by concentrating the fuel (high  $N_A$ ) and by lumping the fuel (high  $\bar{l}_F$ ). When  $\beta'$  is lowered, the resonance integral is tending to zero.

Fig. C.1 shows that in both limits the temperature derivative of the resonance integral is tending to zero. This implies that in the case of both minimal and maximal self shielding the Doppler effect is zero. In the intermediate range a maximum of the temperature derivative of the resonance integral is to be expected.

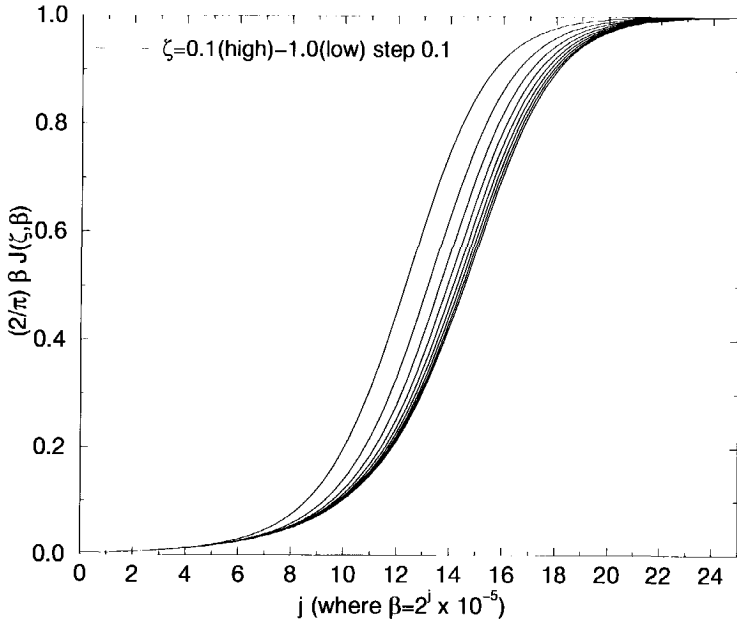


Figure C.1:  $(2/\pi)\beta J(\zeta, \beta)$  as a function of  $\beta$  with  $\zeta$  as a parameter.

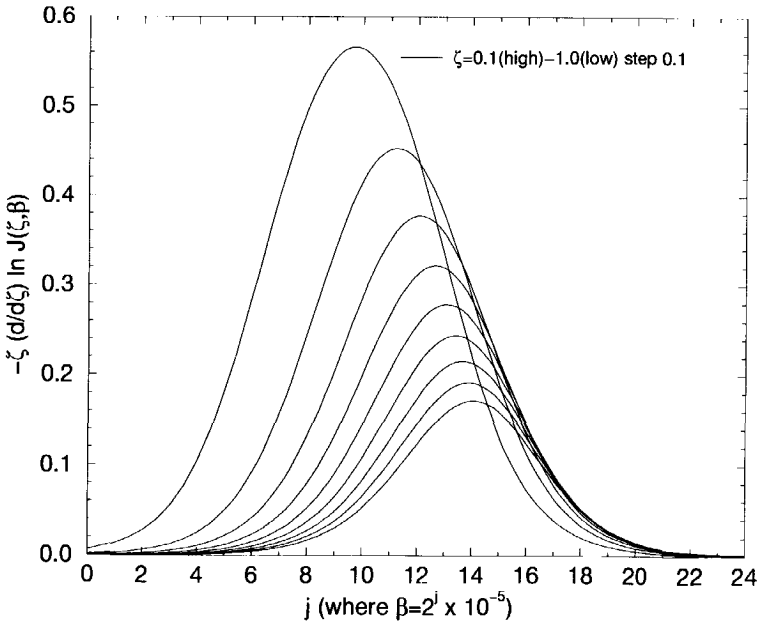


Figure C.2:  $-\zeta \frac{\partial}{\partial \zeta} \ln J(\zeta, \beta)$  as a function of  $\beta$  with  $\zeta$  as a parameter.

From the expression of the individual resonance integral the resonance escape probability can be derived. The probability that a neutron slows down without being absorbed by resonance  $i$  reads [69]

$$p_i = 1 - \frac{I_i}{\xi \sigma_s MF} \quad (C.26)$$

Here, the atomic moderator-to-fuel ratio is defined as

$$MF = \frac{N_C V_M + N_{O16} V_F}{N_A V_F} \quad (C.27)$$

and the cell-averaged moderating power is given by

$$\overline{\xi \sigma_s} = \frac{\xi_C \sigma_{sC} N_C V_M + \xi_{O16} \sigma_{s,O16} N_{O16} V_F}{N_C V_M + N_{O16} V_F} \quad (C.28)$$

where the subscripts O16 and C denote the oxygen of the oxide fuel (i.e. the internal moderator) and the graphite in the moderator region, respectively. Furthermore,  $\xi$  is the average logarithmic energy loss of a neutron in collision with a moderator nuclide and  $\sigma_s$  is the microscopic scattering cross section of the moderator. In eq. C.28, it is assumed that the flux in the fuel and moderator have the same value. Furthermore, the second term of the numerator of eq. C.28 is usually much smaller than the first one.

The probability that a neutron can escape from a series of resonances is given by the product of all individual escape probabilities. This gives

$$p = \prod_i p_i = \prod_i \left( 1 - \frac{I_i}{\xi \sigma_{sM} MF} \right) \quad (C.29)$$

This is correct under the assumption that the resonances are well-separated and hence do not interfere with each other [69]. In general  $\frac{I_i}{\xi \sigma_{sM} MF} \ll 1$  which implies that the resonance escape probability can be approximated by

$$p \approx \prod_i \exp \left( -\frac{I_i}{\xi \sigma_{sM} MF} \right) = \exp \left( -\frac{\sum_i I_i}{\xi \sigma_{sM} MF} \right) \quad (C.30)$$

Equations C.21-C.24 and C.10, show that the Doppler efficiency depends on the properties of the fuel lump. Only via the Dancoff factor ( $C$ ), that is incorporated in the Dancoff-corrected mean chord length ( $\bar{l}_F$ ), the  $I_{eff}$  and thus  $\alpha_0$  depend on the properties of the moderator that surrounds the fuel lump. The temperature derivative of the individual resonance integral from eq. C.21 yields

$$\frac{dI_i}{dT} = \left( \frac{\sigma_0 \Gamma_\gamma}{E_0} \right)_i \beta_i \frac{\partial J}{\partial \xi} \frac{\partial \xi}{\partial T} = -\frac{1}{2T} \left( \frac{\sigma_0 \Gamma_\gamma}{E_0} \right)_i \beta_i \xi_i \frac{\partial J}{\partial \xi} (\xi_i, \beta'_i) \quad (C.31)$$

From eq. C.10, C.21 and C.31 one obtains

$$\alpha_0 = \frac{\frac{d}{dT} \sum_{i=1}^N I_i}{\sum_{i=1}^N I_i} = - \left( \frac{1}{2T} \right) \frac{\sum_{i=1}^N \left( \frac{\sigma_0 \Gamma_\gamma}{E_0} \right)_i \beta_i \xi_i \frac{\partial J}{\partial \xi} (\xi_i, \beta'_i)}{\sum_{i=1}^N \left( \frac{\sigma_0 \Gamma_\gamma}{E_0} \right)_i \beta'_i J(\xi_i, \beta'_i)} \quad (C.32)$$

It can be proven analytically [142] that  $\frac{\partial J}{\partial \xi} < 0$ . This implies that the resonance absorption increases with increasing temperature and hence is a mathematical representation of the Doppler effect.

When only the lowest lying resonance is taken into account (i.e.  $N = 1$  in equation C.32) the Doppler efficiency becomes

$$\frac{1}{I_1} \frac{dI_1}{dT} = \frac{1}{2T} \left[ -\zeta_1 \frac{\partial \ln J}{\partial \zeta} (\zeta_1, \beta'_1) \right]. \quad (\text{C.33})$$

The function between the brackets, with  $\zeta$  as parameter, is shown in fig. C.2. Some typical values of  $\zeta$  are presented in table E.5. Fig. C.2 shows that each  $-\zeta \frac{\partial \ln J}{\partial \zeta} (\zeta, \beta)$ -curve possesses a maximum. Both the height of the maximum and its position are dependent on the value of  $\zeta$ . The height of the maximum decreases with increasing  $\zeta$ . Its position, denoted by  $\beta_{\max}$ , increases with increasing  $\zeta$ . For a range of  $\zeta$ 's with realistic values, a numerical fit procedure shows that  $\beta_{\max}$  obeys the following relation

$$\beta_{\max} = a_0 + a_1 \zeta \quad \text{for } 0.2 < \zeta < 0.8, \quad (\text{C.34})$$

with  $a_0 = -0.0189 \pm 0.0007$  and  $a_1 = 0.209 \pm 0.001$ . For  $\zeta$ -values less than 0.2 the actual  $\beta_{\max}$  is slightly higher than as it would be calculated by eq. C.34. For  $\zeta$ -values higher than 0.8,  $\beta_{\max}$  approximately obeys eq. C.34, but the uncertainties in the calculations increase.

Since  $\zeta$  is inversely proportional to  $\sqrt{T}$ , we can infer that a four times higher temperature (in K) corresponds with a two times smaller  $\zeta$ . According to eq. C.34 this means that  $\beta_{\max}$  will approximately be smaller by factor two. By eqs. C.23-C.24 the  $\beta_{\max}$  can be translated into the Dancoff-corrected mean chord length. Since  $\sigma_p$  is of the order of 10 barn, whereas  $\sigma_e$  is of the order of  $10^2$ - $10^4$  barn,  $\beta'$  is approximately proportional to  $\sigma_e$  and thus inversely proportional to  $\bar{l}_F$ . So, eventually a four times higher temperature corresponds with a two times bigger Dancoff-corrected mean chord length ( $\bar{l}_F$ ), for which the maximal individual Doppler efficiency is obtained.

If we now consider the Doppler efficiency for the entire series of resonances, eq. C.32 shows us that both  $\beta'_i \zeta_i \frac{\partial J}{\partial \zeta} (\zeta_i, \beta'_i)$  and  $\beta'_i J (\zeta_i, \beta'_i)$  are weighted by the term  $(\frac{\sigma_0 \Gamma_\gamma}{E_0})_i$  in numerator and denominator, respectively. This weight is proportional to  $E_0^{-2} (\frac{1}{\Gamma_\gamma} + \frac{1}{\Gamma_n})^{-1}$ , which implies that the resonances positioned at the lowest energies dominate the Doppler efficiency  $\frac{1}{I_{eff}} \frac{dI_{eff}}{dT}$ .

Summarising, the calculation of the NR(IM) approximated resonance integrals involves the following assumptions:

- The integrals are calculated by either the NRIM or the NR approximation.
- The NR approximation is applied for both the internal and external moderator, i.e. oxygen and graphite, respectively.
- The flux in the moderator is of the form  $\phi \sim 1/E$ , which is generally met if the moderating medium is large and low-absorbing.
- The neutron flux is spatially uniform in the fuel and moderator region.
- Neutron transport into and out of the fuel region is treated with the Wigner approximation for the first-flight escape probability.
- The moderating region is not absorbing.
- Interference between successive resonances is neglected. This means that a flux depression at a particular resonance caused by a resonance above it, is not taken into account. Hence, a  $1/E$ -flux above each resonance is assumed.

Besides that, the expression for the resonance escape probability  $p$  of eq. C.29 is based on the assumption that the resonances do not interfere with each other, which allows to

multiply the individual resonance escape probabilities ( $p_i$ ) to obtain the probability to escape from all resonances ( $p$ ). Furthermore, the assumption that  $\frac{I_i}{\xi\sigma_{s,M}MF} \ll 1$  leads to the expression of  $p$  according to eq. C.30.

### C.3.4 The Nordheim Integral Method

The numerical solution of eq. C.14 for the energy-dependent flux constitutes what is commonly referred to as the Nordheim Integral Method [57]. This calculation is performed by the code NITAWL-II of the SCALE [56] code package. The calculated flux is used for the calculation of the resonance integral, according to

$$I_{\text{NIT}} = \int_{E_l}^{E_h} \sigma_\gamma(E) \Phi_{\text{NIT}}(E) dE . \quad (\text{C.35})$$

Here, the subscript NIT is the abbreviation of Nordheim Integral Method, and  $E_l$  and  $E_h$  are the lower and upper energy boundaries of the resolved resonances energy range, respectively. The Doppler efficiency, calculated with the Nordheim resonance integrals, reads

$$\alpha_0^{\text{NIT}} = \frac{1}{I_{\text{NIT}}} \frac{dI_{\text{NIT}}}{dT} . \quad (\text{C.36})$$

The Nordheim Integral Methods involves the same assumptions as for the NR(IM) approximation, except that:

- Equation C.14 is integrated numerically.
- Interference between successive resonances is taken into account.
- For energies lower than  $5k_B T_M$  the  $1/E$ -flux in the moderator is replaced by a Maxwellian distribution.
- An analytical expression for the first-flight escape probability is used, instead of the Wigner-approximation.
- The integration range for the resonance integral is bounded between  $E_l$  and  $E_h$ .

### C.3.5 Method based on the four factor formula

An alternative way to determine the resonance integral is to calculate the resonance escape probability  $p$  using the four factor formula and then applying eq. C.6 to obtain the resonance integral. In this way, the resonance integral is defined by  $p$ , instead of the other way around, like for the NR/NRIM method as described previously. Inversion of eq. C.6 leads to the definition

$$I_p \equiv -\overline{\xi\sigma_{s,M}MF} \ln(p) , \quad (\text{C.37})$$

where  $\overline{\xi\sigma_{s,M}MF}$  is the moderating power times the moderator-to-fuel ratio as described in sec. C.3.3 and  $p$  is the factor of the four factor formula. The latter reads

$$p \equiv \frac{k_\infty}{\eta f \epsilon} . \quad (\text{C.38})$$

The definitions of the neutron production per thermally absorbed neutron in the fuel zone  $\eta$ , the thermal utilisation factor  $f$  and the non-thermal fission factor  $\epsilon$  have been given in section C.1. The infinite multiplication factor  $k_\infty$  is of course defined as the total

neutron production rate divided by the total absorption rate. These definitions, together with eq. C.38, leads to the following expression for the resonance escape probability

$$p \equiv \frac{\text{total thermal absorption rate}}{\text{total thermal absorption rate} + \text{total non-thermal absorption rate}} \quad (\text{C.39})$$

It is evident that  $p$  depends on the cut-off energy that separates the thermal from the non-thermal energy range. The cut-off energies used in this study coincide with the lower energy boundaries of the resolved resonances energy range ( $E_i$ ) presented in table C.1.

Equation C.39 shows that  $p$  depends on the entire non-thermal energy range and not solely on the resolved resonances range, which is a subset of the non-thermal energy range. This means that  $p$  also involves unresolved resonance absorption,  $(n,xn)$  reactions and so on. The resonance integrals calculated with either the NR(IM) approximation or Nordheim method are only dependent on the dimensions of the lump (and of the Dancoff factor). If this is true for  $I_p$  of eq. C.37 too, remains to be seen.

The Doppler efficiency corresponding with  $I_p$  reads

$$\alpha_0^p \equiv \frac{1}{I_p} \frac{dI_p}{dT} = \frac{d}{dT} \ln(-\ln p) \quad (\text{C.40})$$

in which the term  $\overline{\xi\sigma_s MF}$  of eq. C.37 is cancelled out. It should be noted that the resonance escape probability and its derived quantities ( $I_p$  and  $\alpha_0^p$ ) have the following properties:

- The  $p$  of eq. C.39 is dependent on the cut-off energy that separates the thermal from the non-thermal energy range.
- The resonance escape probability contains information on the unresolved resonance absorption and fast processes like  $(n,xn)$  reactions.
- The definition of  $I_p$  does not require a  $1/E$ -behaviour of the flux in the moderator.
- It is expected that  $I_p$  tends to  $I_{\text{NR}}$  under the following conditions:
  - The unresolved resonance absorption,  $(n,xn)$  reaction rates etc. are small compared to the resolved resonance absorption.
  - The moderator region is non-absorbing and so large that the flux in the moderator shows an  $1/E$  behaviour.

It is evident that  $\alpha_0^p \rightarrow \alpha^{\text{NR}}$  holds as well under these assumptions.

## C.4 Calculation of the Doppler efficiency

### C.4.1 The NR(IM) approximation method and the Nordheim Integral Method

The Doppler efficiency has been calculated by means of two methods. The first method is based on the NR(IM) approximation and the second is based on the Nordheim Integral Method.

**The NR(IM) approximation method.** The Doppler efficiency  $\frac{d}{dT} \frac{\sum_{i=1}^N I_i}{\sum_{i=1}^N I_i}$  of eq. C.32 has been calculated for different values of  $N$ , where the  $N = 1$ -case corresponds to the calcu-



lation of the Doppler efficiency based on the lowest lying resonance only. Each resonance is characterised by the temperature and a set of basic resonance parameters. These read  $(E_0, \Gamma_\gamma, \Gamma_n, g)$  and are listed for the five lowest lying resonances of each resonance absorber in table E.5. In order to decide whether the NR or the NRIM approximation will be applied, the quantity  $(\frac{1-\beta A}{2})\frac{E_0}{\Gamma_p}$  has been calculated for each resonance. It is equal to the average energy loss of a neutron suffered in a collision with an absorber nucleus divided by the practical width of the resonance. If it is larger than unity the NR approximation is applied and  $\beta$  is correspondingly calculated by eq. C.23. For the opposite situation the NRIM approximation is applied and  $\beta$  is calculated by eq. C.24. All resonances listed in table E.5, except the fifth resonance of  $^{238}\text{U}$ , are calculated by the NRIM approximation. The Doppler efficiency  $\alpha_0(N)$  for different values of  $N$  has been plotted as a function of the Dancoff-corrected mean chord length  $(\bar{l}_F)$  in figs. C.4-C.5.

**The Nordheim Integral Method.** The Doppler efficiency calculated with the Nordheim Integral Method reads  $(\frac{1}{I_{\text{NIT}}} \frac{dI_{\text{NIT}}}{dT})$ . The code NITAWL-II calculates the resonance integral  $I_{\text{NIT}}$  given by eq. C.35.

#### C.4.2 Estimation of the optimal Dancoff-corrected mean chord length

Both methods show the same general behaviour for  $\frac{1}{I} \frac{dI}{dT}$ . For small Dancoff-corrected chord lengths the  $\frac{1}{I} \frac{dI}{dT}$  increases with increasing  $\bar{l}_F$  until a maximum is reached, after which the  $\frac{1}{I} \frac{dI}{dT}$  starts to decrease again.

Figs. C.4-C.5 show that the positions of the maxima are, to first approach, determined by the Doppler efficiency of the first resonance of each resonance absorber. The individual Doppler efficiency  $\frac{1}{I} \frac{dI}{dT}$  of eq. C.33 has, according to fig. C.2, for each  $\zeta_1$  a certain  $\beta_1$  for which its maximum is reached. Equation C.24 shows that this  $\beta_1$  corresponds to  $N_A \bar{l}_F$ , in the following way

$$(N_A \bar{l}_F)^{-1} = \beta_1 \sigma_0 \frac{\Gamma_\gamma}{\Gamma} - \sigma_p^{\text{NRIM}}. \quad (\text{C.41})$$

Under the assumption that  $0.2\Gamma_D < \Gamma < 0.8\Gamma_D$ , eq. C.34 can be inserted in eq. C.41. This yields:

$$(N_A \bar{l}_F)^{-1} \approx a_1 \sigma_0 \frac{\Gamma_\gamma}{\Gamma} \zeta + a_0 \sigma_0 \frac{\Gamma_\gamma}{\Gamma} - \sigma_p^{\text{NRIM}}, \quad (\text{C.42})$$

where  $a_0 = -0.019$ ,  $a_1 = 0.21$ . Substituting  $\zeta$  by eq. C.22 yields

$$(N_A \bar{l}_F)^{-1} \approx \sigma_0 \frac{\Gamma_\gamma}{\Gamma} (a_1 \sqrt{\frac{A}{4E_0 k_B T}} \Gamma + a_0) - \sigma_p^{\text{NRIM}}. \quad (\text{C.43})$$

Equation C.43 shows that a high  $\sigma_0$  yields a small lump (i.e. a small  $N_A \bar{l}_F$ ) for which the Doppler efficiency is maximal. Furthermore,  $(N_A \bar{l}_F)^{-1}$  is linear with  $T^{-\frac{1}{2}}$ . This implies that a higher fuel temperature results in a larger optimal lump size. If the second and third term of the RHS of eq. C.43 can be neglected, a four times higher fuel temperature leads to a two times higher optimal  $N_A \bar{l}_F$  at which the individual Doppler efficiency is maximal.

**Interpretation of the expression for the optimal  $N_A \bar{l}_F$ .** The first term of the RHS of eq. C.42 is proportional to the height of the Doppler broadened capture cross section at the resonance energy. The exact value of the Bethe-Placzek function at the resonance energy  $\psi(\zeta, 0)$  is given in E.7. For  $0 < \zeta < 0.8$ , this can, within an accuracy of 10%, be approximated by  $\psi(\zeta, 0) \approx \frac{\sqrt{\pi}}{2} \zeta$ . This means that the first term of the RHS of eq. C.42 can be approximated by  $a_1 \zeta_1 \sigma_0 \frac{\Gamma}{2} \approx a_1 \frac{2}{\sqrt{\pi}} \sigma_\gamma(E_0, T)$ . This term is inversely proportional to  $\sqrt{T}$ . Analogously, the second term of the RHS of eq. C.42 is equal to  $a_0 \sigma_\gamma(E_0, T=0)$ , which is equal to  $a_0$  times the capture cross section at the resonance energy of the natural (Breit-Wigner) line shape.

If we insert the aforementioned quantities into eq. C.42 and divide both sides by  $N_A$  this yields the following expression for the optimal Dancoff-corrected mean chord length:

$$\bar{l}_F \approx \frac{1}{\left(\frac{2a_1}{\sqrt{\pi}}\right) \Sigma_\gamma(E_0, T) + a_0 \Sigma_\gamma(E_0, T=0) - \Sigma_{sM}^F} \quad (\text{C.44})$$

Here, the  $\Sigma_\gamma$ 's are the macroscopic capture cross sections and  $\Sigma_{sM}^F$  is the macroscopic scattering cross section of the moderator admixed in the fuel zone. Equation C.44 illustrates that the optimal Dancoff-corrected mean chord length can be expressed in the mean free path for capture for neutrons having energies equal to the resonance energy, i.e.  $1/\Sigma_\gamma(E_0, T)$ . The quantity  $\bar{l}_F \Sigma_\gamma(E_0, T)$  determines the 'blackness' of the lump. If it is much bigger than unity the lump is 'black' for these neutrons. In this case, the flux depression at energy  $E_0$  is very strong, which results in absorption of all neutrons with energy  $E_0$  in a very thin rim of the lump. If the opposite is true, the lump is 'white' for these neutrons and the flux depression is very weak. In the intermediate case, the lump is 'grey' and the characteristic length of the flux depression is of the order of the size of the lump. An increase of the temperature causes a decrease of  $\Sigma_\gamma(E_0, T)$ , a weaker flux depression, less self-shielding and hence an increase of the resonance absorption. At the optimal chord length, the fractional change of the resonance integral per degree K is maximal. The resonance having the highest  $\frac{\sigma_0 \Gamma}{E_0}$  has the highest contribution to the (infinite diluted) resonance integral (see eq. C.32). Roughly speaking, the fractional change of the resonance integral is maximal if the fractional change of the *individual* resonance integral of this dominant resonance is maximal. This implies that if one has determined the optimal mean chord length for which the individual Doppler efficiency of the dominant resonance is maximal, one also has an idea of the order of magnitude of the optimal mean chord length for which the total Doppler efficiency is maximal.

### C.4.3 Comparison of the Nordheim Integral Method and the NR(IM) approximation

As mentioned before, the resonance parameters of the lowest lying resonance give an estimation of the order of magnitude of  $N_A \bar{l}_F$  at which the Doppler efficiency is maximal. However, all resonances together determine this value more accurately. The Nordheim Integral Method takes all (resolved) resonances into account and the optimal  $N_A \bar{l}_F$ 's according to this method, are listed in table C.2 This table shows that each resonance absorber has its own  $N_A \bar{l}_F$  for which the Doppler efficiency is maximal. As mentioned previously,  $N_A \bar{l}_F$  increases if the  $\sigma_0$  of the lowest lying resonance decreases. The latter varies quite a lot for the different resonance absorbers, viz.  $8.7 \cdot 10^3$ ,  $2.4 \cdot 10^4$  and  $1.9 \cdot 10^5$  barn for  $^{232}\text{Th}$ ,

**Table C.2:** Different parameters, for which the Doppler efficiency, based on the Nordheim Integral Method (i.e.  $\frac{1}{I_{\text{NIM}}} \frac{dI_{\text{NIM}}}{dT}$ ), is maximal.

	$\bar{l}_F$ (cm)	$N_A$ (barn $^{-1}$ cm $^{-1}$ )	$N_A \bar{l}_F$ (barn $^{-1}$ )	$\sigma_c$ (barn)
$^{232}\text{Th}$	$4 \cdot 10^{-1}$	0.0218	$9 \cdot 10^{-3}$	$1.1 \cdot 10^2$
$^{238}\text{U}$	$4 \cdot 10^{-2}$	0.02206	$1 \cdot 10^{-3}$	$1.1 \cdot 10^3$
$^{240}\text{Pu}$	$6 \cdot 10^{-3}$	0.00536	$3 \cdot 10^{-5}$	$3.1 \cdot 10^4$

$^{238}\text{U}$  and  $^{240}\text{Pu}$ , respectively. Below, the Doppler efficiency curves, based at the one hand on the Nordheim Integral Method and at the other on the NR/NRIM-approximation, are discussed for each resonance absorber.

$^{238}\text{U}$ . Fig. C.3 shows the curves of the Doppler efficiency based on the NRIM-approximation

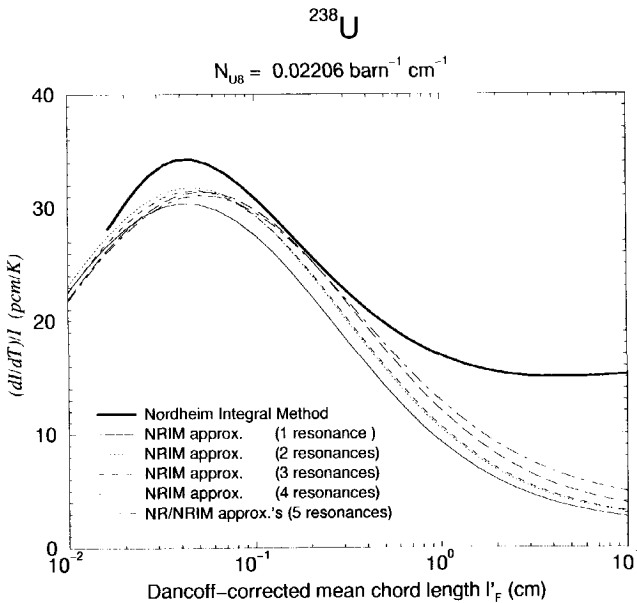


**Figure C.3:** The Doppler efficiency of  $^{238}\text{U}$  calculated with the Nordheim Integral Method and the NR(IM) approximation.

with the inclusion of 1 to 5 resonances ( $\alpha_0(N)$  with  $N = 1, 2, 3, 4, 5$ ) and the Doppler efficiency based on the Nordheim Integral Method ( $\alpha_0^{\text{NIM}}$ ). Again, the first resonance determines, to first approach, the position and the height of the maximum, whereas for large lumps ( $\bar{l}_F > 0.4$  cm) the  $\alpha_0(N)$ -curves deviate strongly from the  $\alpha_0^{\text{NIM}}$ -curve. The maximum of the  $\alpha_0^{\text{NIM}}$ -curve amounts to 34 pcm/K, which is comparable to the maximum of the Doppler efficiency of the thorium fuel, and is positioned at a Dancoff-corrected mean chord length  $\bar{l}_F$  of  $0.040 \pm 0.001$  cm, which is about an order of magnitude smaller than in the thorium case.

<sup>232</sup>Th. Fig. C.4 shows that the curve of  $\alpha_0(N = 1)$  from eq. C.32 (i.e. the Doppler

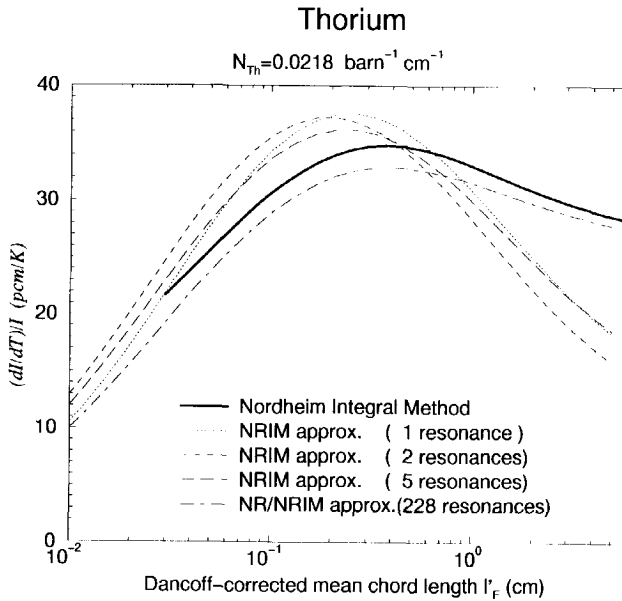


**Figure C.4:** The Doppler efficiency of <sup>232</sup>Th calculated with the Nordheim Integral Method and the NR(IM) approximation.

efficiency only including the lowest lying resonance) determines to first approach the shape of the curve. The second resonance has a  $\zeta$  that hardly differs from that of the first resonance (see table E.5). This implies that both resonances correspond roughly to the same curve in fig. C.2, which means that both individual Doppler efficiencies are maximal for the same  $\beta$ . Since, the second resonance has a  $\sigma_0$  that is higher than that of the first, eq. C.24 shows that the maximum of its individual Doppler efficiency is positioned at a lower  $\bar{l}_F$ . This has as a consequence that the  $\alpha_0(N = 2)$ -curve is pulled slightly to lower  $\bar{l}_F$ 's with respect to the  $\alpha_0(N = 1)$ -curve. Moreover, the second resonance is characterised by a higher  $\frac{\sigma_0 \Gamma_\gamma}{E_0}$ , which implies that this resonance gives a higher contribution to the resonance integral than the lowest lying resonance. Inclusion of more resonances ( $\alpha_0(N = 3)$ ,  $\alpha_0(N = 5)$ ) does not change the shape and maximum of the curve much. However, if 228 resonances are taken into account the maximum of the  $\alpha_0(N = 228)$ -curve shifts slightly to the right and, furthermore, the right wing is lifted. This curve is within an error of 10% in agreement with the Doppler efficiency following from the Nordheim Integral Method ( $\alpha_0^{NIT}$ ) given by eq. C.36. The maximum of the  $\alpha_0^{NIT}$ -curve is about 35 pcm/K and is positioned at a Dancoff-corrected mean chord length  $\bar{l}_F$  of 0.4 cm. The lift of the right wing of the  $\alpha_0(N)$  curves with increasing  $N$  is due to the fact that the resonances lying at higher resonances have in general lower  $\zeta$ -values, and this means that the individual Doppler efficiencies of these resonances have maxima at lower  $\beta$ 's according to fig. C.2, which corresponds with higher  $\bar{l}_F$ 's.

$^{240}\text{Pu}$ . The weight  $(\frac{\sigma_0 \Gamma_\nu}{E_0})_1$  in eq. C.32, belonging to the first resonance of  $^{240}\text{Pu}$ , is about 400 times bigger than that of its successor. This implies that the Doppler efficiency of the first resonance determines the shape of  $\frac{d}{dT} \sum_{i=1}^N \frac{I_i}{I_i}$  even when  $N \gg 1$ . Fig. C.5 shows that the

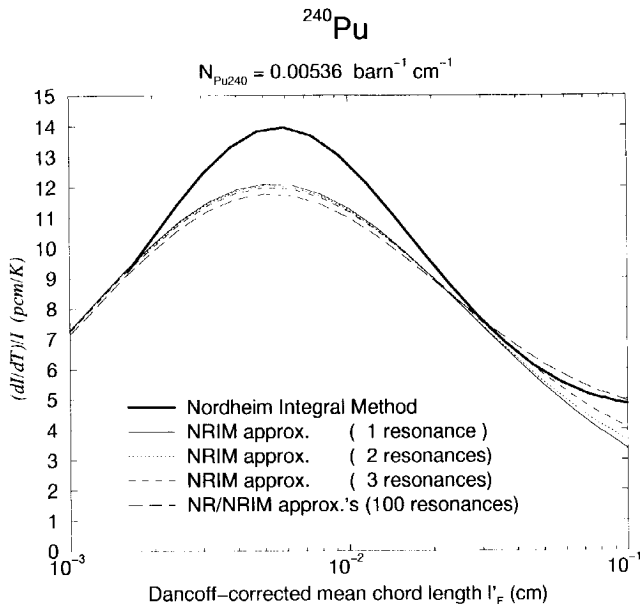


**Figure C.5:** The Doppler efficiency of  $^{240}\text{Pu}$  calculated with the Nordheim Integral Method and the NR(IM) approximation.

Doppler efficiency  $\alpha_0(N = 100)$  hardly differs from  $\alpha_0(N = 1)$  indeed. The discrepancy between the Doppler efficiency based on the Nordheim Integral Method, at the one hand, and those based on the NR/NRIM-approximations, at the other hand, is due to the fact that the lower boundary ( $E_l$ ) of the Nordheim resonance integral of eq. C.35 is positioned at 0.5 eV. Since the first resonance is positioned at  $E_0 = 1.056$  eV, whereas its practical width amounts about 2 eV, the cut-off energy  $E_l$  lies still in the range where the flux is depressed. In formula form, this can be written as  $E_0 - \Gamma_{\nu}/2 < E_l < E_0$ . This also indicates that the Doppler-broadening and the corresponding flux depression belonging to the lowest lying  $^{240}\text{Pu}$  resonance at 1.056 eV is still noticeable for energies tending to 0 eV, although the total line width  $\Gamma$  is only 32 meV ! Furthermore, below an energy of 0.5 eV the flux is determined by the Maxwell-spectrum, which means that the  $1/E$ -assumption for the flux in the moderator is violated. Summarising, this means that both methods, i.e. Nordheim Integral Method and the NR/NRIM-approximation method, show their own inaccuracies. Nevertheless, the Doppler efficiencies corresponding to the mentioned methods both show a Dancoff-corrected chord length of  $0.006 \pm 0.001$  cm. The height of the maximum amounts 14 pcm/K (Nordheim Integral Method) and  $11.5 \pm 0.5$  pcm/K (NR/NRIM-approximation), which is much smaller than that of  $^{232}\text{Th}$  or  $^{238}\text{U}$ . This reveals that, despite of having the highest and lowest lying resonance ( $\sigma_0 \approx 1.9 \cdot 10^5$  barn,  $E_0 = 1$  eV),  $^{240}\text{Pu}$  possesses the less

efficient Doppler effect of all. This is caused by the high  $\zeta$  of 1.06 (see table E.5), which corresponds to the lower curves of fig. C.2.

**Summary of the results.** The Doppler coefficient of reactivity can be written as  $\alpha_D = \ln(p) \frac{1}{l} \frac{dl}{dT}$ . For unit cells with different configurations but all yielding the same  $p$ , the magnitude of the Doppler coefficient of reactivity is imposed by the Doppler efficiency  $\frac{1}{l} \frac{dl}{dT}$ . It can be shown that all physics parameters of the unit cell are functions of the variables  $\bar{V}_F$  and  $MF$ . In the  $(\bar{V}_F, MF)$ -coordinate system, the Doppler efficiency  $\frac{1}{l} \frac{dl}{dT}$  is solely dependent on  $\bar{V}_F$  (and thus independent on  $MF$ ). This means that the maximisation of the Doppler coefficient of reactivity under the constraint of a constant  $p$ , is equivalent with the maximisation of the Doppler efficiency with respect to the effective mean chord length  $\bar{V}_F$ .

In this section, the Doppler efficiency has been calculated by the NR(IM)-approximation method and the Nordheim Integral Method. For the former method, the resonance integral is calculated by the sum of the resonance integrals of the individual resonances. The *individual* Doppler efficiency of a *single* resonance of a particular resonance absorber reads  $\frac{1}{l_i} \frac{dl_i}{dT}$ . If the index  $i$  corresponds to the resonance with the highest  $\frac{\sigma_0 \Gamma_\gamma}{E_0}$ -value, the individual Doppler efficiency  $\frac{1}{l_i} \frac{dl_i}{dT}$  determines, to first approach, the  $\frac{1}{l_{\text{NIT}}} \frac{dl_{\text{NIT}}}{dT}$ , which is the Doppler efficiency calculated by the Nordheim Integral Method and which involves all resolved resonances. The  $N_A \bar{V}_F$ -value for which the *individual* Doppler efficiency  $\frac{1}{l_i} \frac{dl_i}{dT}$  is maximal is of the same order of magnitude as the  $N_A \bar{V}_F$ -value for which  $\frac{1}{l_{\text{NIT}}} \frac{dl_{\text{NIT}}}{dT}$  is maximal. Hence, the resonance parameters of the resonance with the highest  $\frac{\sigma_0 \Gamma_\gamma}{E_0}$ -value determine the order of magnitude of the  $N_A \bar{V}_F$ -value for which  $\frac{1}{l_{\text{NIT}}} \frac{dl_{\text{NIT}}}{dT}$  is maximal.

The  $N_A \bar{V}_F$ -value at which the *individual* Doppler efficiency is maximal, is given by

$$(N_A \bar{V}_F)^{-1} \approx \sigma_0 \frac{\Gamma_\gamma}{\Gamma} \left[ 0.21 \Gamma \sqrt{\frac{A}{4E_0 k_B T}} - 0.019 \right] - \sigma_p^{\text{NRIM}}, \quad (\text{C.45})$$

under the condition that  $0.2 < \Gamma \left( \frac{4E_0 k_B T}{A} \right)^{-\frac{1}{2}} < 0.8$ . Here,  $E_0$  is the resonance energy,  $A$  is the atomic mass number,  $k_B T$  is the fuel temperature in eV,  $\sigma_0$  is the total cross section of the Breit-Wigner cross section at the resonance energy,  $\Gamma$  is the total natural line width of the resonance,  $\Gamma_\gamma$  in the natural line width for capture and  $\sigma_p^{\text{NRIM}}$  is the scattering cross section per absorber atom of the moderator admixed in the fuel.

## C.5 Maximisation of the Doppler coefficient of reactivity with a constant $k_\infty$ as constraint

### C.5.1 Introduction

We recall the expression for the Doppler coefficient of reactivity

$$\alpha_D = \ln(p) \left[ \frac{1}{l_{eff}} \frac{dl_{eff}}{dT} \right]. \quad (\text{C.46})$$

Equation C.46 shows that, for a constant  $p$ , the Doppler efficiency  $\frac{1}{I_{eff}} \frac{dI_{eff}}{dT}$  determines the magnitude of the Doppler coefficient of reactivity ( $\alpha_D$ ). There is an infinite number of combinations of the unit cell's  $r_F$  and  $r_M$  that lead to the same  $p$ . If we move notionally in the  $(r_F, r_M)$ -plane along an iso- $p$  curve, the Doppler efficiency ( $\frac{1}{I_{eff}} \frac{dI_{eff}}{dT}$ ) changes. The maximal Doppler efficiency found on the iso- $p$  curve corresponds with the maximal Doppler coefficient of reactivity. In this way, the maximal Doppler coefficient under the constraint of a constant resonance absorption (i.e. constant  $p$ ) can be found.

However, in practice one is more interested in the maximisation of the Doppler coefficient of reactivity under the constraint of a constant  $k_\infty$ . This means that the Doppler coefficient of reactivity will be maximised without loss of reactivity. To this end, we should notionally move along an iso- $k_\infty$  curve in the  $(r_F, r_M)$ -plane and calculate  $\alpha_D$ . Besides that, a constant  $k_\infty$  is uniquely defined, while a constant  $p$ -calculation depends on the definition of  $p$  (see eq. C.39).

Instead of moving along an iso- $k_\infty$  curve in the  $(r_F, r_M)$ -plane, it is also possible to move in the  $(\bar{V}_F, MF)$ -plane. Here,  $\bar{V}_F$  is the Dancoff-corrected chord length, which is a function of  $r_F$  and the Dancoff-factor. The latter is a function of both  $r_F$  and  $r_M$ . The Dancoff-corrected mean chord length is given by eqs. D.6. The atomic moderator-to-fuel ratio  $MF$  of the spherical unit cell can be expressed as

$$MF = \frac{N_C}{N_A} \left[ \left( \frac{r_M}{r_F} \right)^3 - 1 \right] + \frac{N_{O16}}{N_A}. \quad (C.47)$$

It can be shown that the Jacobian  $|\frac{\partial(\bar{V}_F, MF)}{\partial(r_F, r_M)}| \neq 0$ . The inverse function theorem tells us that the mapping  $(r_F, r_M) \rightarrow (\bar{V}_F, MF)$  then is unique and unambiguous.

This mapping has two advantages:

Firstly, the Doppler efficiency depends on one variable only, viz.  $\bar{V}_F$ . This holds, at least, for the Doppler efficiency calculated with the NR(IM)-approximation theory. This originates from the fact that the first-flight escape probabilities for different geometries are covered by the Wigner's rational approximation (see appendix D).

Secondly, the variables  $\bar{V}_F$  and  $MF$  are general quantities that exist for unit cells, having geometries other than the spherical geometry, as well.

Figure C.6 shows the mapping of iso- $r_F$  lines  $1.1r_F < r_M < 10r_F$  from the  $(r_F, r_M)$ -plane to the  $(\bar{V}_F, MF)$ -plane. The iso- $r_F$  curves in the  $(\bar{V}_F, MF)$ -plane are tending to vertical lines for high  $MF$ -values. For high  $MF$ -values, the fuel shadowing is low and  $\bar{V}_F \rightarrow \frac{4}{3} \frac{1}{A} r_F$  (see eq. D.6). For decreasing  $MF$ -values the fuel shadowing increases, hence the Dancoff-factor increases and  $\bar{V}_F > \frac{4}{3} \frac{1}{A} r_F$ .

Figure C.7 shows the  $k_\infty$  as a function of the atomic moderator-to-fuel ratio, with  $r_F$  as a parameter, for the artificial  $UO_2$  fuel of table C.1. The curves in fig. C.7 correspond with the iso- $r_F$  curves of fig. C.6. Each curve in fig. C.7 has a maximum. Both the left wings and the right wings of the curves intersect the straight constant- $k_\infty$  line (here  $k_\infty = 1.25$  is shown). Fig. C.7 shows that left-wings intersect the constant  $k_\infty$ -line at  $(r_F, MF)$ -coordinates that read (10, 20), (1, 50), (0.1, 150), (0.01, 300) etc.. The intersections of the right-wings of the curves with the constant- $k_\infty$  line give another set of  $(r_F, MF)$ -combinations. The  $k_\infty = 1.25$ -curves are presented as dashed curves in fig. C.6, as well. The vertical  $k_\infty$ -line

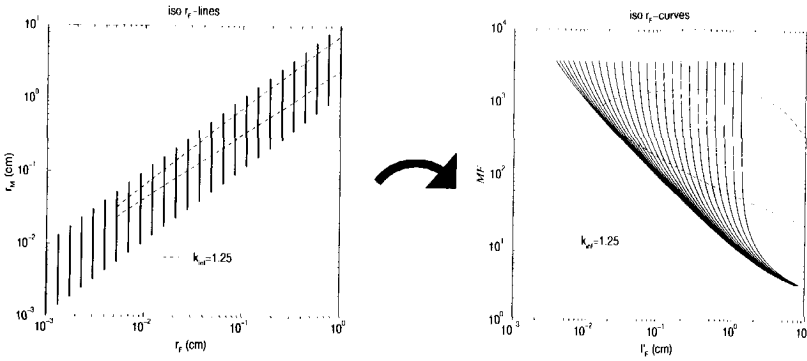


Figure C.6: Mapping from  $(r_F, r_M)$ -plane to  $(\bar{l}_F, MF)$ -plane. The solid curves are the  $iso-r_F$  curves and the dashed ones are the  $iso-k_\infty$  curves.

95%  $^{238}\text{U}$ , 5%  $1/v$ -fissile nuclide

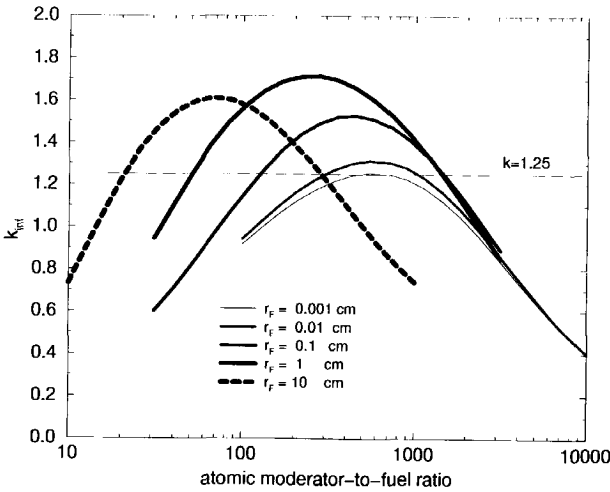


Figure C.7:  $k_\infty$  as a function of the atomic moderator-to-fuel ratio with  $r_F$  as a parameter. The fuel is  $^{238}\text{U}$  oxide in combination with an artificial  $1/v$  fissile nuclide.

of fig. C.7 that intersects with the right-wings of the curves corresponds with the higher dashed curve in fig. C.6. At the other hand, the vertical  $k_\infty$ -line of fig. C.7 that intersects with the left-wings of the curves corresponds with the lower dashed curve in fig. C.6. The left-wing of each curve in fig. C.7 corresponds with the *under*-moderated case, whereas the right-wing corresponds with the *over*-moderated case. In the under-moderated situation  $p < f \leq 1$ , while in the over-moderated situation  $f < p \leq 1$ , in which  $f$  is the thermal utilisation factor and  $p$  the resonance escape probability defined by eq. C.39. For a constant  $r_F$ , the resonance escape probability increases, whereas the thermal utilisation factor decreases, with increasing  $MF$ . The four-factors as functions of  $\bar{l}_F$ , corresponding



to the ( $k_\infty = 1.25$ ) *under*-moderated case, are presented in fig. C.8. This figure shows that

95%  $^{238}\text{U}$ , 5%  $1/v$ -fissile nuclide

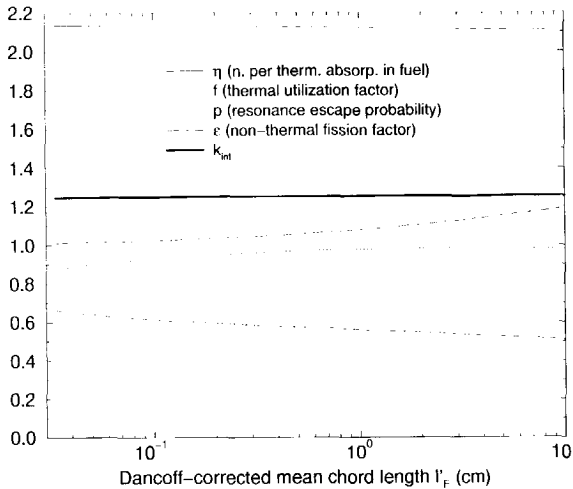


**Figure C.8:** The factors of the four factor formula as a function of the Dancoff-corrected mean chord length of the fuel zone  $\bar{V}_F$ . The fuel is  $^{238}\text{U}$  oxide in combination with an artificial  $1/v$  fissile nuclide. During the calculation, the  $k_\infty$  is kept constant by adjusting the atomic moderator-to-fuel ratio  $MF$  of the unit cell.

$\eta$  hardly varies over the entire  $\bar{V}_F$ -range,  $f$  varies between 0.87 and 0.97, the non-thermal fission factor  $\epsilon$  varies between 1 and 1.2 and the resonance escape probability  $p$  (defined by C.38) varies from 0.66 at  $\bar{V}_F = 0.034$  cm to 0.51 at  $\bar{V}_F = 11.4$  cm. The latter means that  $\ln(p)$  varies between -0.42 and -0.67, respectively. Equation C.46 shows that for a constant  $\ln(p)$ , the Doppler efficiency  $\frac{1}{I_{eff}} \frac{dI_{eff}}{dT}$ , determines the magnitude of the Doppler coefficient of reactivity. In the next section, it will be shown that  $\frac{1}{I_{eff}} \frac{dI_{eff}}{dT}$  still dominates the Doppler coefficient of reactivity, although  $\ln(p)$  is not constant during the constant  $k_\infty$ -calculation. Due to this domination of the Doppler efficiency, the Doppler coefficient is maximal at a certain Dancoff-corrected chord length of the fuel zone, independent of the value of  $k_\infty$  of the constant  $k_\infty$ -calculation.

## C.5.2 Calculation Method

For a constant  $k_\infty$ -calculation the following calculation sequence is performed: The resonance shielding calculations are performed by the BONAMI-S code (Bondarenko method) for the unresolved energy range and by the NITAWL-II (Nordheim Integral Method) code for the resolved resonance range. Both codes use the Dancoff factor as an input parameter. With the discrete ordinate code XSDRNPM-S a  $r_M$ -search is performed in such a way that the desired  $k_\infty$  is obtained. With the new  $r_M$ , the Dancoff factor is calculated by eq. A.12. The calculated Dancoff-factor is used for a new BONAMI-S, NITAWL-II, XSDRNPM-S-calculation, etc.. This iteration process is terminated if

the Dancoff-corrected mean chord length of the fuel zone approaches a constant value. With the iterated Dancoff factor, a BONAMI-S,NITAWL-II-calculation, followed by a  $k_{\infty}$ -calculation with XSDRNPM-S, is performed. This is done for fuel temperatures of 550 and 650 K, successively. The code VAREX3 calculates the factors of the four factor formula and the reactivity effects due to the fuel temperature increase from 550 to 650 K.

The calculation sequence, described above, is repeated for different values of the fuel radius ( $r_F$ ). The first guess for the outer radius of the moderator region ( $r_M$ ) determines, whether an *under*-moderated or an *over*-moderated constant  $k_{\infty}$ -calculation is performed. For example, in case of an  $r_F$  of 10 cm corresponding to fig. C.7, an initial guess of  $r_M$  so that  $MF = 20$  yields the under-moderated case, while an  $MF = 200$  yields the over-moderated case. It should be noted that for two unit cells with the same  $\bar{V}_F$  and the same  $k_{\infty}$ , but of which one is under-moderated and the other is over-moderated, the former exhibits always a stronger Doppler effect. This is due to the fact that in the under-moderated case the resonance escape probability  $p$  is smaller. This means that  $\ln(p)$  is more negative, whereas  $\frac{1}{I_{eff}} \frac{dI_{eff}}{dT}$  is equal for the two the unit cell's. Equation C.46 shows that, for the same  $\frac{1}{I_{eff}} \frac{dI_{eff}}{dT}$  the  $\ln(p)$  determines the magnitude of the Doppler coefficient of reactivity.

In the next two sections the constant- $k_{\infty}$  calculations are performed for three fuel types. These fuels are based on the resonance absorbers  $^{232}\text{Th}$ ,  $^{238}\text{U}$  and  $^{240}\text{Pu}$ , successively. The usual fissile nuclides ( $^{233}\text{U}$ ,  $^{235}\text{U}$  etc.) are replaced by artificial  $1/\nu$  fissile nuclides, which are described in section C.2. In this way, the resonance absorption and hence the Doppler effect is purely determined by the resonance absorbers  $^{232}\text{Th}$ ,  $^{238}\text{U}$  and  $^{240}\text{Pu}$ , successively. This provides for a better analysis of the relation between the Doppler effect and the dominant resonance absorbers,  $^{232}\text{Th}$ ,  $^{238}\text{U}$  and  $^{240}\text{Pu}$ . The 'artificial' fuels are listed in the right column of table C.1.

Subsection C.5.3 discusses the Doppler efficiency  $\frac{1}{I_p} \frac{dI_p}{dT}$ , based on the four factor formula. This Doppler efficiency will be compared with the one calculated by the Nordheim Integral Method  $\frac{1}{I_{NIT}} \frac{dI_{NIT}}{dT}$ . Subsection C.5.4 presents the Doppler coefficient of reactivity  $\frac{1}{k_{\infty}} \frac{dk_{\infty}}{dT}$  as a function of the Dancoff-corrected chord length for the different fuel types.

Below, the relationship between the Doppler efficiency and the Doppler coefficient of reactivity is given. Equation C.38 shows that the Doppler coefficient of reactivity reads

$$\frac{1}{k_{\infty}} \frac{dk_{\infty}}{dT} = \frac{1}{p} \frac{dp}{dT} + \frac{1}{(\eta\epsilon f)} \frac{d(\eta\epsilon f)}{dT}. \quad (\text{C.48})$$

Usually the last term is small compared to first term of the RHS of eq. C.48. Equation C.37 shows that the Doppler coefficient can be written as

$$\frac{1}{k_{\infty}} \frac{dk_{\infty}}{dT} = \ln(p) \frac{1}{I_p} \frac{dI_p}{dT} + \frac{1}{(\eta\epsilon f)} \frac{d(\eta\epsilon f)}{dT}. \quad (\text{C.49})$$

In this way, the Doppler coefficient of reactivity is expressed in terms of the Doppler efficiency  $\frac{1}{I_p} \frac{dI_p}{dT}$ . If  $\ln(p)$  is constant during the constant  $k_{\infty}$ -calculation and if the last term of eq. C.49 can be neglected, the Doppler coefficient is proportional to the Doppler efficiency  $\frac{1}{I_p} \frac{dI_p}{dT}$  (i.e.  $\frac{1}{k_{\infty}} \frac{dk_{\infty}}{dT} \sim \frac{1}{I_p} \frac{dI_p}{dT}$ ). The latter tends to the  $\frac{1}{I_{NIT}} \frac{dI_{NIT}}{dT}$ , obtained from the Nordheim

Integral Method, under the conditions described at the end of section C.3.5. The Doppler efficiency  $\frac{1}{I_p} \frac{dI_p}{dT}$  is discussed in section C.5.3.

In a constant  $k_\infty$ -calculation,  $\ln(p)$  changes steadily with changing  $\bar{V}_F$ . Besides that,  $\frac{1}{(\eta\epsilon f)} \frac{d(\eta\epsilon f)}{dT}$  is not always negligible. This means that  $\frac{1}{k_\infty} \frac{dk_\infty}{dT} \sim \frac{1}{I_p} \frac{dI_p}{dT}$  is not valid anymore. A deformed version of the  $(\text{const} \times \frac{1}{I_p} \frac{dI_p}{dT})$ -curve, where the constant is of course negative, now gives the  $\frac{1}{k_\infty} \frac{dk_\infty}{dT}$ -curve. The  $\frac{1}{k_\infty} \frac{dk_\infty}{dT}$  as a function of  $\bar{V}_F$  is presented for the different fuel types in section C.5.4.

### C.5.3 Artificial fuels: The Doppler efficiency $\frac{1}{I_p} \frac{dI_p}{dT}$

In this section, the Doppler efficiency, as defined by eq. C.40, is calculated as a function of  $\bar{V}_F$ . The calculations are performed at notional constant  $k_\infty$ -curves in the  $(\bar{V}_F, MF)$ -plane. The Doppler efficiency  $\frac{1}{I_p} \frac{dI_p}{dT}$  is compared with the Doppler efficiency  $\frac{1}{I_{\text{NIT}}} \frac{dI_{\text{NIT}}}{dT}$ , based on the Nordheim Integral Method.

<sup>238</sup>U. Figure C.9 shows the Doppler efficiencies  $\frac{1}{I_{\text{NIT}}} \frac{dI_{\text{NIT}}}{dT}$  and  $\frac{1}{I_p} \frac{dI_p}{dT}$ , based on the Nordheim

95% <sup>238</sup>U, 5% 1/v-fissile nuclide

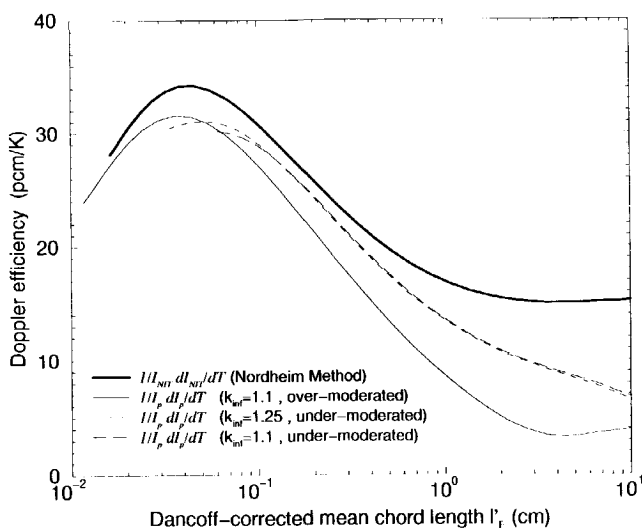
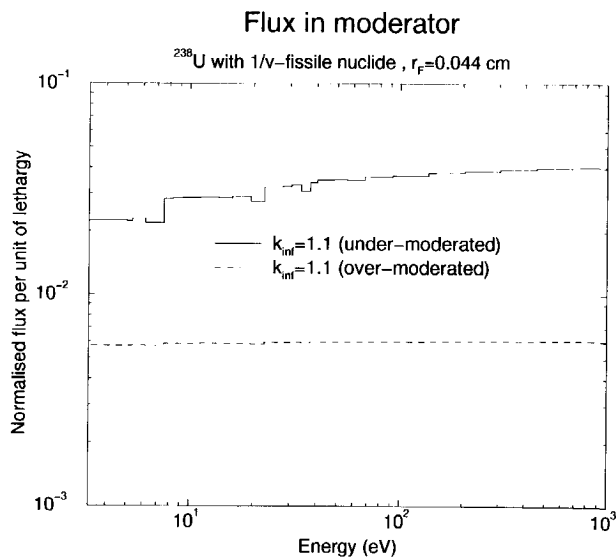


Figure C.9: The Doppler efficiencies  $(\frac{1}{I_{\text{NIT}}} \frac{dI_{\text{NIT}}}{dT}$  and  $\frac{1}{I_p} \frac{dI_p}{dT})$  as a function of the Dancoff-corrected mean chord length. The fuel is <sup>238</sup>U oxide in combination with an artificial 1/v fissile nuclide.

Integral Method (eq. C.35) and the "four factor formula"-method (eq. C.40), respectively. The  $\frac{1}{I_p} \frac{dI_p}{dT}$ -curves deviate from the  $\frac{1}{I_{\text{NIT}}} \frac{dI_{\text{NIT}}}{dT}$ -curve for large values of the  $\bar{V}_F$ . This is due to the unresolved resonance absorption which is not taken into account by  $\frac{1}{I_{\text{NIT}}} \frac{dI_{\text{NIT}}}{dT}$ . For large

lump sizes the *resolved* resonances are strongly shielded, which has as a consequence that the *unresolved* resonance absorption becomes relatively important. Since the temperature dependence of the *unresolved* resonance absorption is weak, the ratio  $\frac{1}{I_p} \frac{dI_p}{dT}$  becomes much smaller than  $\frac{1}{I_{NR}} \frac{dI_{NR}}{dT}$ .

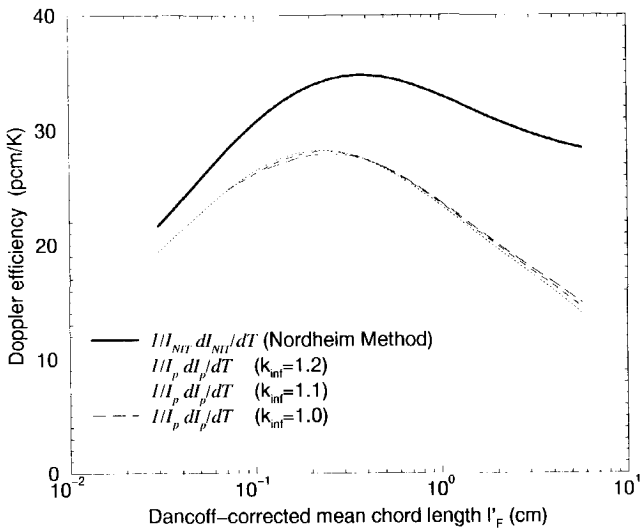
The discrepancy between the under-moderated and over-moderated  $\frac{1}{I_p} \frac{dI_p}{dT}$ -curves are probably due to a deviation of the flux in the moderator from the  $1/E$ -form, in the under-moderated case. As argued at the end of section C.3.3 the flux in the moderator is of the form  $\Phi \sim 1/E$  if the moderating region is large and non-absorbing. In the over-moderated case the moderator region is large enough to provide for a  $1/E$ -flux, but this is not true for the under-moderated case. Figure C.10 shows, for a fuel sphere radius of 0.044 cm, the group fluxes in the moderator region for both the under-moderated and over-moderated ( $k_\infty = 1.1$ )-case. The group fluxes have been calculated by the code XSDRNPM-S. It



**Figure C.10:** The group flux in the moderator as a function of the energy for both the under-moderated and the over-moderated ( $k_\infty = 1.1$ )-case. The radius of the fuel region is 0.044 cm. The fuel is  $^{238}\text{U}$  oxide in combination with an artificial  $1/v$  fissile nuclide.

is obvious that the flux corresponding to the under-moderated case deviates from the  $\Phi(u) \sim \text{constant}$  (i.e.  $\Phi(E) \sim 1/E$ ) behaviour, while  $\Phi(u) \sim \text{constant}$  holds quite well for the over-moderated case.

**<sup>232</sup>Th.** Figure C.11 shows that there is quite a large difference between  $\frac{1}{I_p} \frac{dI_p}{dT}$ -curves, for different under-moderated  $k_\infty$ -values, and the  $\frac{1}{I_{NR}} \frac{dI_{NR}}{dT}$ -curve. Figure C.11 shows that  $\frac{1}{I_p} \frac{dI_p}{dT}$  is almost independent of  $k_\infty$ , and hence independent of the moderator-to-fuel ratio. The maxima of the  $\frac{1}{I_p} \frac{dI_p}{dT}$ -curves are positioned at an  $\bar{r}_F$  of 0.25 cm, while the maximum of the

94%  $^{232}\text{Th}$ , 6%  $1/\nu$ -fissile nuclide

**Figure C.11:** The Doppler efficiencies ( $\frac{1}{I_{\text{NIT}}}\frac{dI_{\text{NIT}}}{dT}$  and  $\frac{1}{I_p}\frac{dI_p}{dT}$ ) as a function of the Dancoff-corrected mean chord length. The fuel is  $^{232}\text{Th}$  oxide in combination with an artificial  $1/\nu$  fissile nuclide.

$\frac{1}{I_{\text{NIT}}}\frac{dI_{\text{NIT}}}{dT}$ -curve is positioned at 0.4 cm. Moreover, the height of the maxima corresponding with the  $\frac{1}{I_p}\frac{dI_p}{dT}$ -curves is 28 pcm/K, while that of  $\frac{1}{I_{\text{NIT}}}\frac{dI_{\text{NIT}}}{dT}$  amounts 35 pcm/K.

The mentioned difference between the  $\frac{1}{I_p}\frac{dI_p}{dT}$ -curves, at the one hand, and the  $\frac{1}{I_{\text{NIT}}}\frac{dI_{\text{NIT}}}{dT}$ -curve, at the other hand, can be ascribed to the *unresolved* resonance absorption. In the infinite diluted case the resolved resonance integral is equal to 64.7 barn (see table C.1), whereas the unresolved resonance integral amounts about 10% of that value. If the fuel is lumped, the resolved resonance integral is reduced, while the unresolved resonance integral hardly decreases. This implies that the unresolved resonance absorption becomes relatively important. Since  $\frac{1}{I_{\text{NIT}}}\frac{dI_{\text{NIT}}}{dT}$  does not account for the unresolved resonance absorption, while  $\frac{1}{I_p}\frac{dI_p}{dT}$  does, there is a discrepancy between them. Because the unresolved resonance absorption contributes more to the resonance integral  $I_p$  itself than to its temperature derivative  $\frac{dI_p}{dT}$ , the  $\frac{1}{I_p}\frac{dI_p}{dT}$ -curves are lower than the  $\frac{1}{I_{\text{NIT}}}\frac{dI_{\text{NIT}}}{dT}$ -curve. Since the maximum height of the  $\frac{1}{I_p}\frac{dI_p}{dT}$ -curves is only about 28 pcm/K, whereas that of  $^{238}\text{U}$  amounts  $31 \pm 1$  pcm/K, it can be concluded that  $^{238}\text{U}$  has a more 'efficient' Doppler effect than  $^{232}\text{Th}$ . This means that for the same  $p$ ,  $^{238}\text{U}$  exhibits the strongest Doppler effect.

**$^{240}\text{Pu}$ .** Figure C.12 shows the Doppler efficiencies  $\frac{1}{I_p}\frac{dI_p}{dT}$ , at the one hand, and  $\frac{1}{I_{\text{NIT}}}\frac{dI_{\text{NIT}}}{dT}$ , at the other hand. It should be noted that  $\frac{1}{I_p}\frac{dI_p}{dT}$  is hardly dependent on the  $k_{\infty}$ . The discrepancy between the two methods is caused by absorption in the unresolved/fast energy range. The major part of this is due to fast fission. This is illustrated by the non-thermal fission factor  $\epsilon$ .

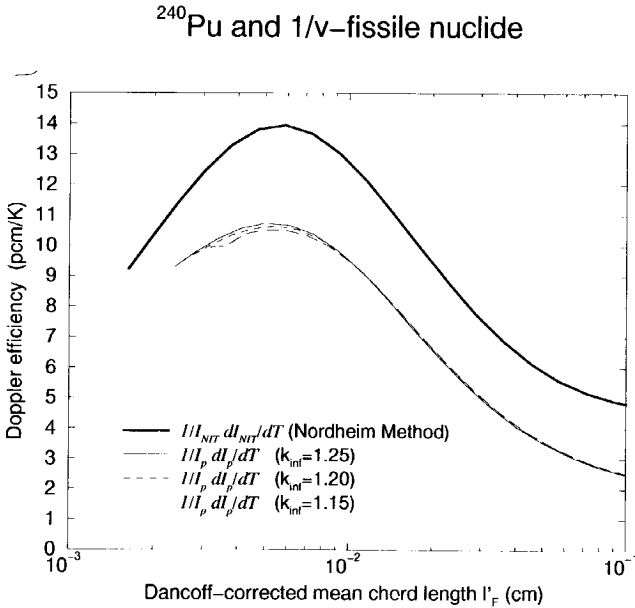


**Figure C.12:** The Doppler efficiencies ( $\frac{1}{I_{NT}} \frac{dI_{NT}}{dT}$  and  $\frac{1}{I_p} \frac{dI_p}{dT}$ ) as a function of the Dancoff-corrected mean chord length. The fuel is <sup>240</sup>Pu oxide in combination with an artificial 1/v fissile nuclide.

The  $\epsilon$  varies between 1.04 and 1.50, and between 1.08 and 2.37 for the ( $k_\infty = 1.25$ ) and the ( $k_\infty = 1.15$ )-case, respectively. The non-thermal fission factor increases with increasing  $\bar{l}_F$ . This means that for fuel spheres with increasing radii, the fast absorption rate (mainly due to fast fission) increases relatively compared to the resolved resonance absorption. The  $\frac{1}{I_{NT}} \frac{dI_{NT}}{dT}$  involves only the resolved resonance absorption, while  $\frac{1}{I_p} \frac{dI_p}{dT}$  involves both resolved and unresolved resonance/fast absorption. The relative contribution of the unresolved resonance and fast absorption to  $I_p$  is much higher than to  $\frac{dI_p}{dT}$ . This implies that the relative difference between  $\frac{1}{I_{NT}} \frac{dI_{NT}}{dT}$  and  $\frac{1}{I_p} \frac{dI_p}{dT}$  increases with increasing radii, illustrated by fig. C.12.

#### C.5.4 Artificial fuels: The Doppler coefficient $\frac{1}{k_\infty} \frac{dk_\infty}{dT}$

In this section, the Doppler coefficient, defined as  $\frac{1}{k_\infty} \frac{dk_\infty}{dT}$ , is calculated as a function of  $\bar{l}_F$ . The calculations are performed at notional constant  $k_\infty$ -curves in the ( $\bar{l}_F$ ,  $MF$ )-plane. We recall the expression for the Doppler coefficient of eq. C.49

$$\frac{1}{k_\infty} \frac{dk_\infty}{dT} = \ln(p) \frac{1}{I_p} \frac{dI_p}{dT} + \frac{1}{(\eta\epsilon f)} \frac{d(\eta\epsilon f)}{dT}. \quad (\text{C.50})$$

Equation C.50 shows that the Doppler coefficient depends on the Doppler efficiency  $\frac{1}{I_p} \frac{dI_p}{dT}$ . If  $\ln(p)$  is constant during the constant  $k_\infty$ -calculation and if the last term of eq. C.50 can be neglected, the Doppler coefficient is proportional to the Doppler efficiency  $\frac{1}{I_p} \frac{dI_p}{dT}$  (i.e.

$\frac{1}{k_\infty} \frac{dk_\infty}{dT} \sim \frac{1}{I_p} \frac{dI_p}{dT}$ ). The Doppler efficiency  $\frac{1}{I_p} \frac{dI_p}{dT}$  has been discussed in the previous section (sec. C.5.3).

<sup>238</sup>U. Figure C.13 shows the Doppler coefficient of reactivity as a function of the Dancoff-corrected mean chord length, with  $k_\infty$  as a parameter. The Doppler coefficients of reactivity,

95% <sup>238</sup>U, 5% 1/v-fissile nuclide

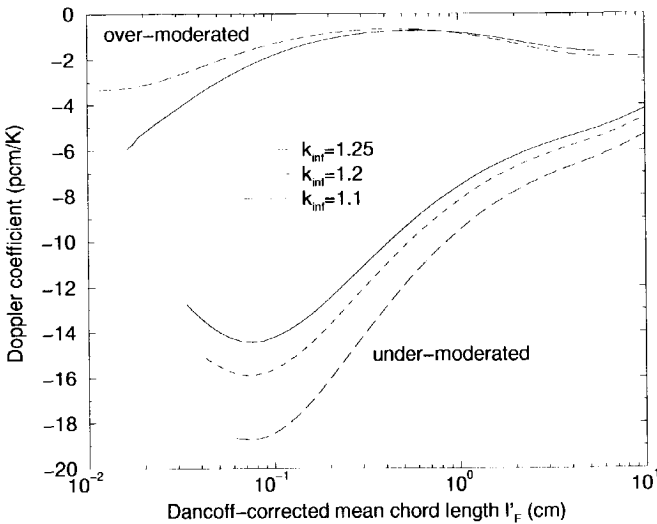


**Figure C.13:** The Doppler coefficient as a function of the Dancoff-corrected mean chord length with  $k_\infty$  as a parameter. The fuel is <sup>238</sup>U oxide in combination with an artificial 1/v fissile nuclide.

with  $k_\infty$ -values of 1.1 and 1.25 for the over-moderated case, and, with  $k_\infty$ -values of 1.1, 1.2 and 1.25 for the under-moderated case, are shown. All curves correspond to notional horizontal lines in fig. C.7, similar to that of  $k_\infty = 1.25$ . As mentioned previously, the Doppler coefficients in the over-moderated cases are smaller (in absolute sense) than in the under-moderated cases. This is due to a higher  $p$  and hence a less negative  $\ln(p)$  (see eq. C.46). The under-moderated curves in fig. C.13 show minima that lie between an  $\bar{l}'_F$  of 0.7 and 0.8 cm. These values are about two times higher than those based on the maximal Doppler efficiencies based on the Nordheim Integral Method, presented in table C.2. This is due to the fact that in fig. C.13  $\ln(p)$  is not constant, but varies slightly with  $r_F$ , which means that the Doppler coefficient of reactivity is not solely determined by the Doppler efficiency ( $\frac{1}{I} \frac{dI}{dT}$ ) but rather by the product of the latter and  $\ln(p)$  (see eq. C.46). (For the under-moderated  $k_\infty = 1.25$  case, the variation of  $p$  is demonstrated in fig. C.8.) For the over-moderated case  $\ln(p)$  varies much more with varying  $r_F$  (e.g. between -0.14 and -0.02 for  $k_\infty = 1.1$ ), which has as a consequence that the shape of the  $\frac{1}{I} \frac{dI}{dT}$  'disappears' if it is multiplied by the varying  $\ln(p)$ .

<sup>232</sup>Th. Figure C.14 shows the Doppler coefficient as a function of the Dancoff-corrected

94% <sup>232</sup>Th, 6% 1/v-fissile nuclide

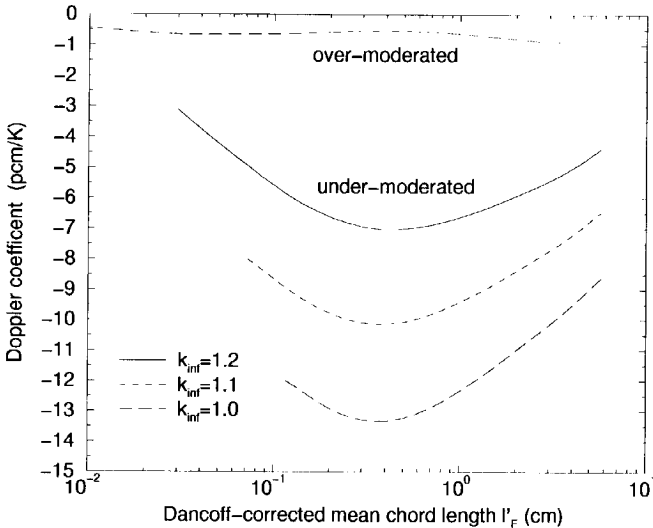


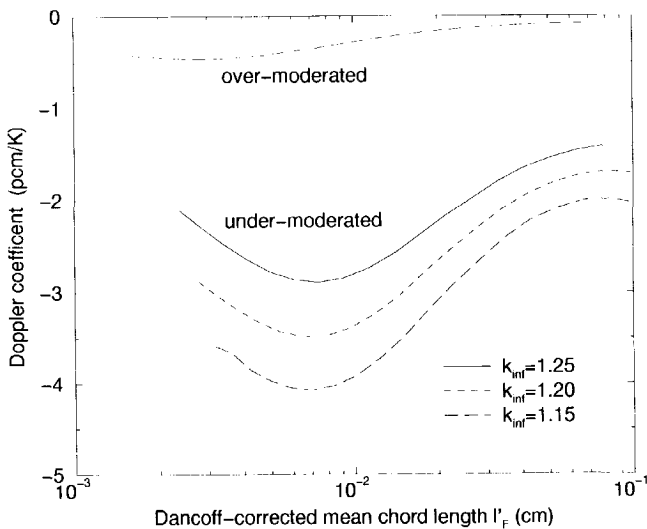
**Figure C.14:** The Doppler coefficient as a function of the Dancoff-corrected mean chord length with  $k_{\infty}$  as a parameter. The fuel is <sup>238</sup>U oxide in combination with an artificial 1/v fissile nuclide.

mean chord length with the (under-moderated)  $k_{\infty}$  as a parameter. The minima of the curves are positioned at  $\bar{l}_F = (4.5 \pm 0.5) \cdot 10^{-1}$  cm, while the maxima of the  $\frac{1}{l_F} \frac{dl_F}{dT}$ -curves are positioned at 0.2 cm. This is due to the fact that  $\ln(p)$  varies during the constant  $k_{\infty}$ -calculation. The expression for the Doppler coefficient of reactivity ( $\alpha_D = \ln(p) \frac{1}{l_F} \frac{dl_F}{dT}$ ) shows that for a constant  $p$ , the minima of  $\alpha_D$  were on the same position of the  $\frac{1}{l_F} \frac{dl_F}{dT}$  maxima. For the ( $k_{\infty} = 1.2$ )-case the Doppler coefficient varies between -3 and -6.5 pcm/K, which is an increase of more than 100%! Since the lowest  $k_{\infty}$  corresponds with the most negative  $\ln(p)$ , this case shows the strongest Doppler effect.

<sup>240</sup>Pu. Figure C.15 shows the Doppler coefficient of reactivity as a function of the Dancoff-corrected mean chord length. The curves corresponding to the under-moderated case all show minima positioned at  $\bar{l}_F = 7 \cdot 10^{-3}$  cm. This position is comparable to that of the  $\frac{1}{l_{NIT}} \frac{dl_{NIT}}{dT}$ -curve of  $\bar{l}_F = 6 \cdot 10^{-3}$  cm. Due to the varying  $\ln(p)$  the minima are shifted slightly to higher values of  $\bar{l}_F$ .

**Summary of the artificial fuel results.** The (under-moderated) constant- $k_{\infty}$  calculations in case of fuels, consisting of a single resonance absorber, an artificial 1/v-fissile nuclide and oxygen, show the following  $N_A \bar{l}_F$ -values at which the absolute value of the Doppler coefficient is maximal.



<sup>240</sup>Pu and 1/v-fissile nuclide

**Figure C.15:** The Doppler coefficient as a function of the Dancoff-corrected mean chord length with  $k_{\infty}$  as a parameter. The fuel is <sup>240</sup>Pu oxide in combination with an artificial 1/v fissile nuclide.

resonance absorber	$\bar{l}'_F$ (cm <sup>-1</sup> )	$N_A \bar{l}'_F$ (barn <sup>-1</sup> )
<sup>232</sup> Th	$(4 \pm 1) \cdot 10^{-1}$	$(9 \pm 2) \cdot 10^{-3}$
<sup>238</sup> U	$(7 \pm 1) \cdot 10^{-2}$	$(1.5 \pm 0.2) \cdot 10^{-3}$
<sup>240</sup> Pu	$(7 \pm 1) \cdot 10^{-3}$	$(3.8 \pm 0.5) \cdot 10^{-5}$

### C.5.5 Realistic Fuels

In this section the constant- $k_{\infty}$  calculations are performed for realistic fuels, listed in table C.1. This means that the fuels contain real fissile resonance absorbers, like <sup>233</sup>U, <sup>235</sup>U and <sup>239</sup>Pu, instead of the artificial 1/v fissile nuclide in the previous section. The Plutonium fuel consists even of five Pu-isotopes.

**Uranium.** The minima of all curves in fig. C.16 lie at a Dancoff-corrected mean chord length of  $(6.0 \pm 0.5) \cdot 10^{-2}$  cm. The Doppler efficiency  $\frac{1}{l'_{NR}} \frac{dI'_{NR}}{dT}$  for this lump size is close to the maximum value of 34 pcm/K, which can be seen from fig. C.3. In comparison with the artificial <sup>238</sup>U fuel (see fig. C.13), the minima of the curves have shifted to the left. This is due to the <sup>235</sup>U present in the UO<sub>2</sub>. Below, we compare the mentioned optimal dimension of the lump to those of existing thermal reactors.

**Comparison with a typical HTR unit cell.** The fuel kernels of coated particles in an HTR-M have radii of 0.025 cm. The average Dancoff factor between the fuel kernels

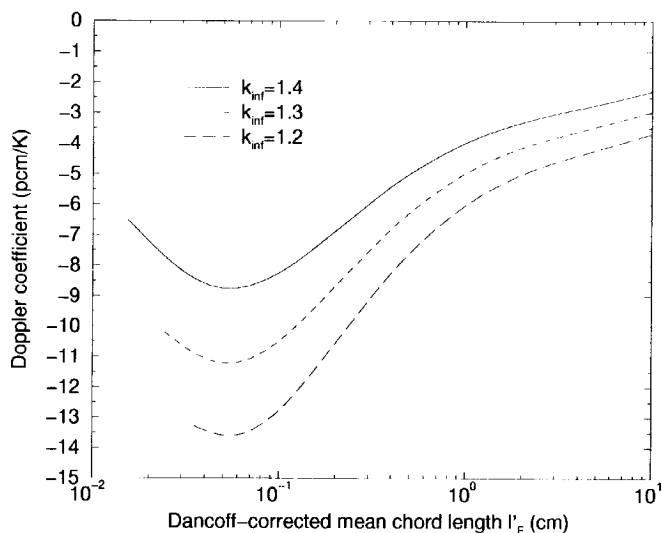


Figure C.16: The Doppler coefficient as a function of the Dancoff-corrected mean chord length with  $k_{\infty}$  as a parameter. The fuel is  $UO_2$  (5 at% enriched).

dispersed in the graphite matrix amounts to approximately 0.36. Equation C.20 shows that these figures correspond with a Dancoff-corrected mean chord length of 0.047 cm, which is close to the optimal value of  $(6.0 \pm 0.5) \cdot 10^{-2}$  cm.

**Comparison with a typical PWR pin-cell.** Now, we compare the dimension of the fuel lump in a PWR to the optimal one. The fuel is equal to the 'realistic'  $UO_2$  fuel of table C.1. The pin-cell has the following properties: The diameter of the fuel rod is 0.8 cm, the outer diameter of the zirconium cladding is 0.9 cm, the pitch is 1.215 cm, the moderator temperature is 550 K, the fuel temperature is 600 K and the  $H_2O$  density is  $2.2074 \cdot 10^{-2}$  barn $^{-1}$ cm $^{-1}$ . The Dancoff factor for this unit cell is 0.372. Since the mean chord length of an infinite cylinder is equal to its diameter, eq. D.6 shows that the Dancoff-corrected mean chord length of the fuel rod amounts to 1.16 cm. The code XSDRNPM-S calculates a  $k_{\infty} = 1.4$  for the described unit cell. The Doppler efficiency  $\frac{1}{I_{NIT}} \frac{dI_{NIT}}{dT}$  calculated from NITAWL-II is only 16 pcm/K, which is less than half of the maximum value, corresponding to fig. C.3. The Doppler efficiency of the fuel rod (i.e. an infinite cylinder) can be compared to that of a sphere, presented in fig. C.3, because both configurations possess first-flight escape probabilities  $P_0^*(\Sigma_i \bar{l}_F)$ 's of which the difference between them does not exceed 2% over the entire  $\Sigma_i \bar{l}_F$ -range [142]. These  $P_0^*(\Sigma_i \bar{l}_F)$ 's are used in eq. C.14, which is the starting point for the  $I_{NIT}$ -calculation. Figure C.3, corresponding to the spherical unit cell, shows that an  $\bar{l}_F$  of 1.16 cm yields a  $\frac{1}{I_{NIT}} \frac{dI_{NIT}}{dT}$  of 16 pcm/K, indeed. The Doppler coefficient of reactivity ( $\frac{1}{k_{\infty}} \frac{dk_{\infty}}{dT}$ ) is equal to -3.5 pcm/K for the PWR pin-cell. Fig. C.16 shows, that for the graphite moderated, spherical unit cell having  $k_{\infty} = 1.4$  and  $\bar{l}_F = 1.16$  cm, the Doppler coefficient amounts to about -3.7 pcm/K,

which is only slightly higher than that of the PWR pin-cell. It should be noted that for the graphite moderated, spherical unit cell with  $k_{\infty} = 1.4$  the maximal Doppler coefficient amounts about  $-8.5$  pcm/K for  $\bar{l}_F = 0.06$  cm, which is more than two times stronger than that at  $\bar{l}_F = 1.16$  cm. The preceding consideration shows that, from the view-point of Doppler efficiency, the PWR-pin radius is too large.

**Thorium.** Figure C.17 shows the Doppler coefficient as a function of the Dancoff-corrected mean chord length, for thorium oxide fuel that contains 2 wt%  $^{233}\text{U}$ . The minima lie at  $\bar{l}_F$ -values between 0.5 and 0.8 cm. Since the minima of the artificial fuel were all

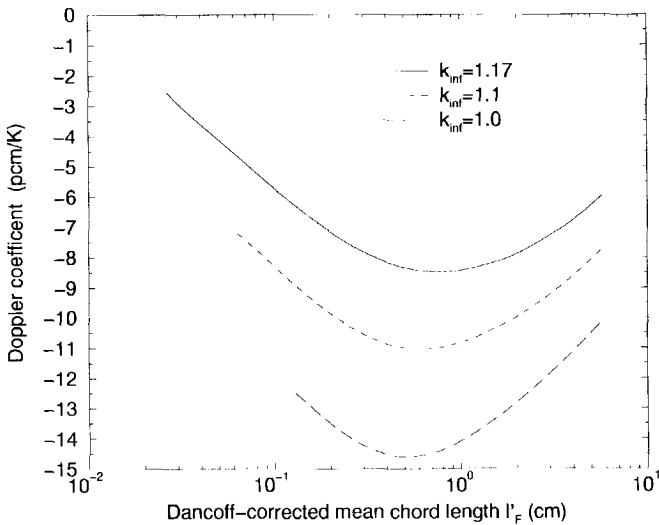


**Figure C.17:** The Doppler coefficient as a function of the Dancoff-corrected mean chord length with  $k_{\infty}$  as a parameter. The fuel is thorium oxide including 2 wt%  $^{233}\text{U}$ .

positioned at  $\bar{l}_F$  of 0.4 cm, the  $^{233}\text{U}$  can be held responsible for the increase of the optimal  $\bar{l}_F$  with increasing  $k_{\infty}$ .

It should be noted that optimal Dancoff-corrected mean chord length of the thorium fuel is an order of magnitude larger than that of the  $\text{UO}_2$  fuel. For the ( $k_{\infty} = 1.17$ )-curve, the Doppler coefficient varies from  $-2.5$  pcm/K at an  $\bar{l}_F = 0.013$  cm to  $-8.5$  pcm/K at an  $\bar{l}_F$  of 0.8 cm, which is an increase by more than a factor three.

**Plutonium.** Figure C.18 shows the Doppler coefficient as a function of the Dancoff-corrected mean chord length, for the  $\text{PuO}_2$  fuel. The plutonium mixture is from spent fuel of an LWR with a burnup of 47.5 MWd/kgHM. Table C.1 shows its isotopic vector. The isotope  $^{240}\text{Pu}$  is the dominant resonance absorber in the mixture. Its contribution to the reactivity effect amounts from about 99% for fuel radii of 0.001 cm to about 60% for fuel radii of 0.1 cm. For radii of 0.1 cm, the self shielding of the 1-eV resonance is high

and its Doppler efficiency is low. The nuclide that is the second best contributor to the Doppler effect is  $^{242}\text{Pu}$ . Its contribution to the reactivity effect varies from about 1% to 30%, respectively. The minima of the curves in fig. C.18 are positioned at  $(7 \pm 1) \cdot 10^{-3}$  cm. Although the  $\text{PuO}_2$  fuel consists of a mixture of different Pu-isotopes, the minima of the Doppler coefficient curves are still determined by the position of the maximum of the Doppler efficiency curve of  $^{240}\text{Pu}$  which is equal to  $6 \cdot 10^{-3}$  cm.

**Comparison with the fuel design of the HTR Pu-burner.** Reference [68] deals with the fuel design of a pebble bed type High Temperature gas cooled Reactor as a plutonium burner without uranium. The 'realistic'  $\text{PuO}_2$ -fuel considered before, has been taken from ref.[68]. The fuel design of the Pu-burner has the following properties: The  $\text{PuO}_2$  fuel is contained by thousands of coated particles that are dispersed in graphite balls. The fuel kernels of the coated particles have radii of either 0.01 or 0.011 cm. The Dancoff-factors, accounting for the fuel shadowing between the kernels, lie between 0.1 and 0.3, dependent on the number of particles that are embedded in the ball. This implies that the Dancoff-corrected mean chord length of a  $\text{PuO}_2$  kernel lie between 0.013 and 0.019 cm. This means that the Dancoff-corrected chord lengths of the mentioned design are more than two times bigger than the optimal one of  $6 \cdot 10^{-3}$  cm. However, this holds for the fresh  $\text{PuO}_2$  fuel. During burnup the  $^{240}\text{Pu}$  will be depleted and the optimal Dancoff-corrected chord length will shift to values higher than  $6 \cdot 10^{-3}$  cm.

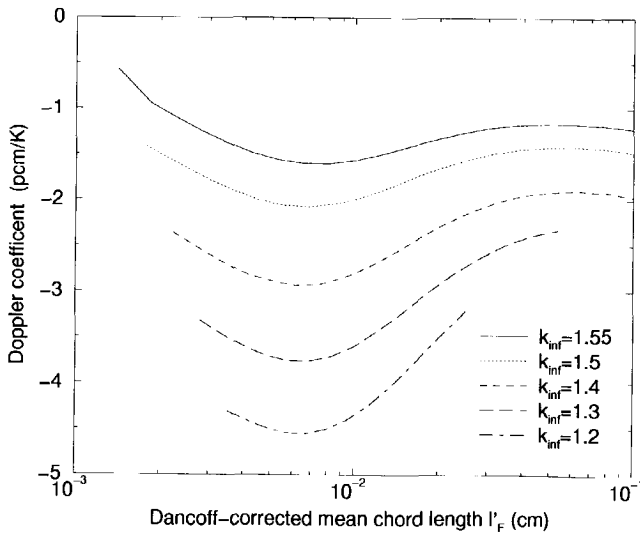


**Figure C.18:** The Doppler coefficient as a function of the Dancoff-corrected mean chord length with  $k_{\infty}$  as a parameter. The fuel is  $\text{PuO}_2$ . The plutonium vector is from spent fuel of an LWR with a burnup of 47.5 MWd/kgHM.

**Summary of the realistic fuel results.** The (under-moderated) constant- $k_\infty$  calculations in case of the 'realistic' oxide fuels, show the following  $N_A \bar{l}_F$ -values at which the absolute value of the Doppler coefficient is maximal.

fuel	$\bar{l}_F(\text{cm}^{-1})$	$N_A \bar{l}_F$ (barn $^{-1}$ )
( 98% $^{232}\text{Th}$ , 2% $^{233}\text{U}$ )O <sub>2</sub>	$(4 \pm 1) \cdot 10^{-1}$	$(9 \pm 2) \cdot 10^{-3}$
UO <sub>2</sub> (5% enriched)	$(6 \pm 2) \cdot 10^{-2}$	$(1.3 \pm 0.3) \cdot 10^{-3}$
PuO <sub>2</sub> (Pu from spent LWR-fuel)	$(7 \pm 1) \cdot 10^{-3}$	$(3.8 \pm 0.5) \cdot 10^{-5}$

The atomic density  $N_A$  corresponds to that of the dominant resonance absorbers  $^{232}\text{Th}$ ,  $^{238}\text{U}$  and  $^{240}\text{Pu}$ . The  $N_A \bar{l}_F$ -values are in agreement with those of the 'artificial' fuels. This implies that the optimal  $N_A \bar{l}_F$ -values for the realistic fuels are determined by the dominant resonance absorbers.

## C.6 Conclusions

- For unit cells with different dimensions, but all having the same resonance escape probability  $p$ , the Doppler coefficient ( $\frac{1}{p} \frac{d\rho}{dT}$ ) is proportional to the Doppler efficiency ( $\frac{1}{I} \frac{dI}{dT}$ ). Here,  $I$  is the effective resonance integral. This implies that maximisation of the absolute value of the Doppler coefficient of reactivity, under the constraint of a constant  $p$ , is equivalent with the maximisation of the Doppler efficiency.
- All physics parameters of the two-region unit cell used in this study are functions of the radius of the fuel sphere ( $r_F$ ) and of the outer radius of the moderator region ( $r_M$ ). It is possible to map the ( $r_F, r_M$ )-coordinates to ( $\bar{l}_F, MF$ )-coordinates. Then all physics parameters are functions of ( $\bar{l}_F, MF$ ). Here,  $\bar{l}_F$  is the Dancoff-corrected mean chord length of the fuel lump and  $MF$  is the cell-averaged atomic moderator-to-fuel ratio.
- Application of the Wigner approximation for the first-flight escape probability results in a resonance integral and a Doppler efficiency that depends solely on  $\bar{l}_F$ , which now includes the Dancoff correction, and is thus independent of  $MF$ . The Dancoff-corrected mean chord length of the fuel zone is a general parameter that is defined for any convex lump. This implies that, once the  $\bar{l}_F$  is determined at which the Doppler efficiency is maximal, the  $\bar{l}_F$  can be translated into the dimensions of the geometry under consideration.
- The Doppler efficiencies  $\frac{1}{I} \frac{dI}{dT}$ , calculated by three different methods, all show the same behaviour as a function of  $\bar{l}_F$ . For small sizes of the lump  $\frac{1}{I} \frac{dI}{dT}$  increases with increasing size of the lump until a maximum is reached, beyond which  $\frac{1}{I} \frac{dI}{dT}$  decreases with further increasing size of the lump.
- The Doppler efficiency  $\frac{1}{I_{\text{NIT}}} \frac{dI_{\text{NIT}}}{dT}$ , calculated by the Nordheim Integral Method, is maximal at a particular value of  $N_A \bar{l}_F$ , where  $N_A$  is the density in barn $^{-1}\text{cm}^{-1}$  of the resonance absorber in the fuel region. These values read, for the three resonance absorbers of this study:

resonance absorber	$N_A \bar{V}_F$ (barn <sup>-1</sup> )
<sup>232</sup> Th	$9 \cdot 10^{-3}$
<sup>238</sup> U	$1 \cdot 10^{-3}$
<sup>240</sup> Pu	$3 \cdot 10^{-5}$

- The *individual* Doppler efficiency  $\frac{1}{i} \frac{dI_i}{dT}$  of a single resonance of a particular resonance absorber can be calculated by the NR(IM)-approximation method. If the index  $i$  corresponds with the resonance with the highest  $\frac{\sigma_0 \Gamma_\gamma}{E_0}$ -value, the individual Doppler efficiency  $\frac{1}{i} \frac{dI_i}{dT}$  determines, to first approach, the  $\frac{1}{I_{\text{NIT}}} \frac{dI_{\text{NIT}}}{dT}$ , which involves all (resolved) resonances. The  $N_A \bar{V}_F$ -value for which the *individual* Doppler efficiency  $\frac{1}{i} \frac{dI_i}{dT}$  is maximal is of the same order of magnitude as the  $N_A \bar{V}_F$ -value for which  $\frac{1}{I_{\text{NIT}}} \frac{dI_{\text{NIT}}}{dT}$  is maximal. Hence, the resonance parameters of the resonance with the highest  $\frac{\sigma_0 \Gamma_\gamma}{E_0}$ -value determine the order of magnitude of the  $N_A \bar{V}_F$ -value for which  $\frac{1}{I_{\text{NIT}}} \frac{dI_{\text{NIT}}}{dT}$  is maximal.
- The  $N_A \bar{V}_F$ -value at which the *individual* Doppler efficiency is maximal, is given by

$$(N_A \bar{V}_F)^{-1} \approx \sigma_0 \frac{\Gamma_\gamma}{\Gamma} \left[ 0.21 \Gamma \sqrt{\frac{A}{4E_0 k_B T}} - 0.019 \right] - \sigma_p^{\text{NRIM}}, \quad (\text{C.51})$$

under the condition that  $0.2 < \Gamma \left( \frac{4E_0 k_B T}{A} \right)^{-\frac{1}{2}} < 0.8$ . Here,  $E_0$  is the resonance energy,  $A$  is the atomic mass number,  $k_B T$  is the fuel temperature in eV,  $\sigma_0$  is the total cross section of the Breit-Wigner cross section at the resonance energy,  $\Gamma$  is the total natural line width of the resonance,  $\Gamma_\gamma$  in the natural line width for capture and  $\sigma_p^{\text{NRIM}}$  is the scattering cross section per absorber atom of the moderator admixed in the fuel.

- The expression for the Doppler coefficient, using the four-factor formula reads

$$\frac{1}{k_\infty} \frac{dk_\infty}{dT} = \ln(p) \frac{1}{I_p} \frac{dI_p}{dT} + \frac{1}{(\eta \epsilon f)} \frac{d(\eta \epsilon f)}{dT}. \quad (\text{C.52})$$

When the dimensions of the spherical two-region unit cell are changed in such a way that  $k_\infty$  remains constant, the resonance escape probability  $p$  is not constant, but varies steadily with varying  $\bar{V}_F$ . Since the change of  $\ln(p)$  with varying  $\bar{V}_F$  is relatively small compared to that of  $\frac{1}{I_p} \frac{dI_p}{dT}$ , the Doppler efficiency  $\frac{1}{I_p} \frac{dI_p}{dT}$  still dominates the Doppler coefficient of reactivity  $\frac{1}{k_\infty} \frac{dk_\infty}{dT}$ . The Doppler efficiency  $\frac{1}{I_p} \frac{dI_p}{dT}$  is defined as  $\frac{d}{dT} \ln(-\ln(p))$ , where  $p$  is calculated by means of the four-factor formula.

- The  $N_A \bar{V}_F$ -values for which  $\frac{1}{I_p} \frac{dI_p}{dT}$  is maximal are of the same order of those for which  $\frac{1}{I_{\text{NIT}}} \frac{dI_{\text{NIT}}}{dT}$  is maximal. The Doppler efficiency  $\frac{1}{I_p} \frac{dI_p}{dT}$  is hardly dependent on  $MF$ , similar to the  $\frac{1}{I_{\text{NIT}}} \frac{dI_{\text{NIT}}}{dT}$  which is completely independent of  $MF$ .
- An under-moderated unit cell shows always a stronger Doppler-effect than its over-moderated counterpart with the same  $k_\infty$  and  $\bar{V}_F$ .
- The (under-moderated) constant- $k_\infty$  calculations in case of fuels, consisting of a single resonance absorber, an artificial  $1/v$ -fissile nuclide and oxygen, show the following  $N_A \bar{V}_F$ -values at which the absolute value of the Doppler coefficient is maximal.

resonance absorber	$\bar{V}_F$ (cm <sup>-1</sup> )	$N_A \bar{V}_F$ (barn <sup>-1</sup> )
<sup>232</sup> Th	$(4 \pm 1) \cdot 10^{-1}$	$(9 \pm 2) \cdot 10^{-3}$
<sup>238</sup> U	$(7 \pm 1) \cdot 10^{-2}$	$(1.5 \pm 0.2) \cdot 10^{-3}$
<sup>240</sup> Pu	$(7 \pm 1) \cdot 10^{-3}$	$(3.8 \pm 0.5) \cdot 10^{-5}$

- The (under-moderated) constant- $k_\infty$  calculations in case of the 'realistic' oxide fuels, show the following  $N_A \bar{V}_F$ -values at which the absolute value of the Doppler coefficient is maximal.

fuel	$\bar{V}_F$ (cm <sup>-1</sup> )	$N_A \bar{V}_F$ (barn <sup>-1</sup> )
(98% <sup>232</sup> Th, 2% <sup>233</sup> U)O <sub>2</sub>	$(4 \pm 1) \cdot 10^{-1}$	$(9 \pm 2) \cdot 10^{-3}$
UO <sub>2</sub> (5% enriched)	$(6 \pm 2) \cdot 10^{-2}$	$(1.3 \pm 0.3) \cdot 10^{-3}$
PuO <sub>2</sub> (Pu from spent LWR-fuel)	$(7 \pm 1) \cdot 10^{-3}$	$(3.8 \pm 0.5) \cdot 10^{-5}$

The atomic density  $N_A$  corresponds to that of the dominant resonance absorbers <sup>232</sup>Th, <sup>238</sup>U and <sup>240</sup>Pu. The  $N_A \bar{V}_F$ -values are in agreement with those of the 'artificial' fuels. This implies that the optimal  $N_A \bar{V}_F$ -values for the realistic fuels are determined by the dominant resonance absorbers.

- From the view-point of Doppler efficiency, the radius of an LWR rod, fuelled with UO<sub>2</sub>, is too large. At the other hand, the UO<sub>2</sub> kernels of the coated particles, that are embedded in graphite pebbles of an HTR-M, have dimensions ( $\bar{V}_F = 0.047$  cm) that are close to the optimal one of  $6 \cdot 10^{-2}$  cm. The  $\bar{V}_F$ 's of the design of the fresh PuO<sub>2</sub>-kernel of ref. [68] are more than two times higher than the optimal one of  $7 \cdot 10^{-3}$  cm, found in this study.





# Appendix D

## First-Flight Escape Probability for a Sphere

The first-flight escape probability  $P_{FO}$  is defined as the probability that a neutron, appearing uniformly and isotropically in the fuel, makes its next collision in the moderator. The first-flight escape probability for a *single* sphere reads [61, 143]

$$P_{FO}(E) = \left( \frac{3}{8\lambda^3} \right) [2\lambda^2 - 1 + (1 + 2\lambda)e^{-2\lambda}], \quad \text{with } \lambda = \frac{3}{4} \bar{l}_F \Sigma_f^f(E). \quad (\text{D.1})$$

Here,  $\Sigma_f^f(E)$  is the total macroscopic cross section of the fuel, which of course varies strongly in the resonance domain. The mean chord length  $\bar{l}_F$  reads

$$\bar{l}_F = \frac{4V_F}{S_F}, \quad (\text{D.2})$$

in which  $V_F$  is the volume and  $S_F$  the surface area of an arbitrary convex body. In case of a sphere  $\bar{l}_F = \frac{4}{3} r_F$ , where  $r_F$  is its radius. Ref. [61] also presents analytical expressions for  $P_{FO}(E)$  in case of an infinite cylinder and an infinite slab. Wigner introduced a simple approximation for the first-flight escape probability that is applicable to all geometries mentioned, which reads

$$P_{FO}(E) = \frac{1}{1 + \frac{\Sigma_f^f(E)\bar{l}_F}{\mathcal{A}}}, \quad (\text{D.3})$$

where  $\mathcal{A}$  is the so-called Bell factor. For  $\mathcal{A} = 1$  Wigner's original rational approximation is obtained. Strictly speaking, the Bell factor is not constant [130] but varies with  $\Sigma_f^f \bar{l}_F$  between 1 and 1.8 in such a way that Wigner's rational approximation coincides with the exact expression for the  $P_{FO}(\Sigma_f^f \bar{l}_F)$ . However, in practice one chooses a constant  $\mathcal{A}$ . In analogy to the module WHEAD of the WIMS-code system [98]  $\mathcal{A} = 1.16$  is chosen in this study. This approximation is valid to within 10% of the analytical expressions of  $P_{FO}(E)$  [142]. The use of eq. D.3 enables a simple analytical expression for the resonance integral (see appendix E).  $P_{FO}(E)$  represents the probability that a neutron appearing in the fuel lump will have its next collision in the moderator. However, if one has a lattice of unit cells, instead of a single lump in a sea of moderator, the possibility exists that a neutron escaping from the fuel lump may pass through the moderator without a collision and entering the next fuel lump. Nordheim [118] derived a first-flight escape probability that corrects for this 'shadowing' effect, which reads (e.g. see [143])

$$\frac{1}{P_{FO}^*(E)} = \frac{1}{P_{FO}(E)} + \left( \frac{C}{1-C} \right) \Sigma_f^f(E) \bar{l}_F. \quad (\text{D.4})$$

Here,  $C$  is the so-called Dancoff-Ginsberg factor that depends on the unit-cell's geometry and on the total macroscopic cross section of the moderator only. If  $C \rightarrow 0$  (no shadowing) it can readily be seen that  $P_{FO}^* \rightarrow P_{FO}$ . If Wigner's rational approximation (eq. D.3) for  $P_{FO}(E)$  is inserted into eq. D.4 one obtains

$$P_{FO}^*(E) = \frac{1}{1 + \Sigma_f'(E) \bar{l}_F}, \quad (\text{D.5})$$

where the Dancoff-corrected mean chord length is defined as

$$\bar{l}_F = \bar{l}_F \left( \frac{1}{\mathcal{A}} + \frac{C}{1-C} \right). \quad (\text{D.6})$$

Appendix A presents an analytical expression for the Dancoff-Ginsberg factor for a two-region spherical white boundary unit cell (exact: eq. A.12, rational approximation: eqs. A.13 and A.14)

# Appendix E

---

## Narrow Resonance Approximations

---

The effective resonance integral for capture of a single resonance reads

$$I_i = \int_{E_0} \sigma_\gamma^f(E) \Phi_F(E) dE. \quad (\text{E.1})$$

Here,  $E_0$  is the energy at which the resonance is positioned,  $\sigma_\gamma^f$  is the Doppler broadened microscopic capture cross section of the absorber and  $\Phi_F(E)$  is the energy-dependent flux in the fuel. In order to calculate effective resonance integral, first  $\sigma_\gamma^f$  and after that the flux  $\Phi_F(E)$  will be evaluated.

### E.1 The Doppler broadened resonance.

A widely used formula for the Doppler broadened resonance cross section is the Bethe-Placzek formula. Briefly speaking, it is a convolution of the Maxwellian energy distribution of the resonance absorbers and the resonance cross section, that is a function of the neutron energy in the centre-of-mass system of the neutron and target nucleus, described by the Breit-Wigner formula. The Bethe-Placzek resonance cross section for capture reads

$$\sigma_\gamma = \sigma_0 \frac{\Gamma_\gamma}{\Gamma} \psi(\zeta, x), \quad (\text{E.2})$$

where  $\Gamma_\gamma$  is the natural line width for capture,  $\Gamma$  is the total natural line width,  $\sigma_0$  is the total cross section at the resonance energy for the *unbroadened* cross section. The latter reads

$$\sigma_0 = 2.608 \cdot 10^6 \left( \frac{A+1}{A} \right)^2 \frac{1}{E_0} \frac{\Gamma_n}{\Gamma} g, \quad (\text{E.3})$$

where  $A$  is the mass number of the absorber nuclide,  $\Gamma_n$  is the natural line width for resonance scattering and  $g$  is the statistical spin factor. The statistical spin factor  $g$  equals unity for the  $l=0$ -resonances, which are of primary interest in nuclear reactor calculations. The Bethe-Placzek function  $\psi(\zeta, x)$  reads

$$\psi(\zeta, x) = \frac{\zeta}{2\sqrt{\pi}} \int_{-\infty}^{+\infty} \frac{\exp[-\frac{1}{4}\zeta^2(x-y)^2]}{1+y^2} dy, \quad (\text{E.4})$$

where

$$x = \frac{2(E - E_0)}{\Gamma}, \quad (\text{E.5})$$

and

$$\zeta \equiv \Gamma / \Gamma_D = \Gamma / \sqrt{\frac{4E_0 k_B T}{A}} = \sqrt{\frac{A\Gamma^2}{4E_0 k_B T}}, \quad (\text{E.6})$$

in which  $\Gamma_D$  is the Doppler width of the resonance and  $k_B T$  the temperature in eV. Furthermore, the exact value [142] of function  $\psi$  at the resonance energy reads

$$\psi(\zeta, 0) = \frac{\sqrt{\pi}}{2} \zeta \exp\left(\frac{1}{4}\zeta^2\right) \operatorname{erfc}(\zeta/2). \quad (\text{E.7})$$

## E.2 The energy-dependent flux

The energy-dependent flux  $\Phi_F(E)$  in eq. E.1 can be obtained by solving the slowing down equations for a two-region unit cell [69]. Two approximate solutions exist: The narrow resonance (NR) and the narrow resonance infinite mass (NRIM) approximation. In the narrow resonance approximation the practical width of the resonance is small compared to the average energy loss of a neutron suffered in a collision with an absorber nucleus. The narrow resonance infinite mass approximation is valid for the opposite situation. This means for the NRIM-case that

$$\Delta E |_{A} = \left(\frac{1 - \alpha_A}{2}\right) E_0 \ll \Gamma_{pr}, \quad (\text{E.8})$$

where the practical width reads

$$\Gamma_{pr} \equiv \sqrt{\frac{\sigma_0}{\sigma_{pF}}} \Gamma, \quad (\text{E.9})$$

in which  $\sigma_{pF}$  is the potential scattering cross section of the absorber nucleus and  $\alpha_A = \left(\frac{A-1}{A+1}\right)^2$  where  $A$  is the mass number of the absorber nucleus. In the NRIM approximation the absorber nucleus mass is taken infinite, which implies that the absorber does not contribute to the slowing down process of the neutron. It should be noted that in both cases the practical width of the resonance is still wide compared to the average energy loss of a neutron suffered in a collision with a moderator nucleus both in the fuel region and in the moderator region. The energy-dependent flux in the NR and NRIM approximation are given explicitly in [69, 142].

## E.3 The effective resonance integral

Inserting both the flux and the Doppler-broadened cross section in eq.E.1 results in

$$I_i = \frac{\sigma_0 \Gamma_\gamma}{E_0} [ \beta J(\zeta, \beta) + L(\zeta, \beta) ], \quad (\text{E.10})$$

where the Doppler broadening function  $J(\zeta, \beta)$  reads

$$J(\zeta, \beta) \equiv \int_0^\infty \frac{\psi(\zeta, x)}{\psi(\zeta, x) + \beta} dx, \quad (\text{E.11})$$

and

$$L(\zeta, \beta) \equiv \int_0^\infty \frac{P_{FO}(\zeta, \beta, x) \psi^2(\zeta, x)}{\psi(\zeta, x) + \beta} dx, \quad (\text{E.12})$$

with

$$\beta_{\text{NR}} = \frac{\sigma_p^{\text{NR}}}{\sigma_0} \quad \text{and} \quad \beta_{\text{NRIM}} = \frac{\sigma_p^{\text{NRIM}}}{\sigma_0} \frac{\Gamma}{\Gamma_Y}. \quad (\text{E.13})$$

Here,  $\sigma_p^{\text{NRIM}}$  is the potential scattering cross section per absorber nuclide in the fuel, defined as

$$\sigma_p^{\text{NR}} = \sigma_{SM}^F N_M^F / N_A + \sigma_p \quad \text{and} \quad \sigma_p^{\text{NRIM}} = \sigma_{SM}^F N_M^F / N_A, \quad (\text{E.14})$$

where  $\sigma_p$  is the potential scattering cross section of the absorber nuclide,  $N_M^F$  is the nuclide density of the moderator admixed in the fuel,  $\sigma_{SM}^F$  the microscopic scattering cross section of the moderator admixed in the fuel.

## E.4 Application of Wigner's rational approximation

A considerable simplification is achieved when Wigner's rational approximation for  $P_{FO}$  is inserted into eq. E.10. For the NR-case we recall eq. D.5 and rewrite it as

$$\begin{aligned} P_{FO}^{\text{NR}}[\zeta, \beta, x] &= [1 + \Sigma_i^f \bar{L}_F]^{-1} \\ &= [1 + (\sigma_p^{\text{NR}} + \sigma_0 \psi(\zeta, x)) N_A \bar{L}_F]^{-1} \\ &= [1 + (\beta_{\text{NR}} + \psi(\zeta, x)) \sigma_0 N_A \bar{L}_F]^{-1}. \end{aligned} \quad (\text{E.15})$$

The rational approximation for  $P_{FO}$  in the NRIM-case [142] differs slightly from that of the NR-case:

$$\begin{aligned} P_{FO}^{\text{NRIM}}[\zeta, \beta, x] &= [1 + (\Sigma_i^f - N_A \sigma_{SA}^F) \bar{L}_F]^{-1} \\ &= \left[ 1 + (\sigma_p + \sigma_Y^F + \frac{N_M^F}{N_A} \sigma_{SM}^F) N_A \bar{L}_F \right]^{-1} \\ &= [1 + (\beta_{\text{NRIM}} + \psi(\zeta, x)) \frac{\sigma_0 \Gamma_Y}{\Gamma} N_A \bar{L}_F]^{-1}. \end{aligned} \quad (\text{E.16})$$

If these expressions for the first-flight escape probabilities are inserted in eq. E.10, one obtains the remarkably simple expression for the individual effective resonance integral:

$$I^{\text{NRIM}} = \frac{\sigma_0 \Gamma_Y}{E_0} \beta'_{\text{NRIM}} J(\zeta, \beta'_{\text{NRIM}}), \quad (\text{E.17})$$

where

$$\beta'_{\text{NR}} = \frac{\sigma_p^{\text{NR}} + \sigma_e}{\sigma_0} \quad \text{and} \quad \beta'_{\text{NRIM}} = \frac{\sigma_p^{\text{NRIM}} + \sigma_e}{\sigma_0} \cdot \frac{\Gamma}{\Gamma_Y}, \quad (\text{E.18})$$

with the escape cross section  $\sigma_e = \frac{1}{N_A \bar{L}_F}$ .

## E.5 Resonance Parameters and Derived Parameters

Table E.5 shows the resonance parameters and quantities derived from them. Only the five lowest lying  $l=0$ -resonances of the nuclides of interest are listed. The basic resonance parameters  $E_0$ ,  $\Gamma_n$  and  $\Gamma_\gamma$  are taken from the EIJ2-XMAS library [58]. The meaning of the quantities are listed below

- $E_0$  : The energy at which the resonance is positioned (in eV).  
 $\Gamma_n$  : The natural line width for scattering (in meV).  
 $\Gamma_\gamma$  : The natural line width for capture (in meV).  
 $\sigma_0$  :  $\sigma_0 = 2.608 \cdot 10^6 \left(\frac{A+1}{A}\right)^2 \frac{1}{E_0} \frac{\Gamma_n}{\Gamma} g$  (in barn)  
 in which spin factor  $g=1$  and  $A$  is the mass number.  
 $\left(\frac{1-\alpha A}{2}\right) \frac{E_0}{\Gamma_{pr}}$  : Parameter that indicates the applicability of the NR/NRIM-approximation.  
 If  $\left(\frac{1-\alpha A}{2}\right) \frac{E_0}{\Gamma_{pr}} \ll 1$  : NRIM-approximation.  
 If  $\left(\frac{1-\alpha A}{2}\right) \frac{E_0}{\Gamma_{pr}} \gg 1$  : NR-approximation.  
 $\zeta$  : Fraction of total natural line width and the Doppler width, defined by E.6. (Fuel temperature = 600 K.)  
 $\frac{\sigma_0 \Gamma_\gamma}{E_0}$  : The infinite diluted resonance integral ( $I^\infty$ ) times  $2/\pi$  (see eq. C.25). It is the 'weight' in eq. E.17.

**Table E.1:** Resonance parameters and derived parameters of the first five ( $l = 0$ )-resonances for three nuclides.

<sup>238</sup> U resonances					
res.par.	1	2	3	4	5
$E_0$	6.674	20.87	36.68	66.03	80.75
$\Gamma_n$	1.493	10.26	34.13	24.6	1.865
$\Gamma_\gamma$	23.0	22.91	22.89	23.36	23.0
$\sigma_0$	24020	38980	42920	20430	2442
$(\frac{1-\alpha_A}{2})\frac{E_0}{\Gamma_{pr}}$	0.04	0.07	0.07	0.22	1.5
$\zeta$	0.32	0.25	0.32	0.20	0.09
$\frac{\sigma_0 \Gamma_\gamma}{E_0}$	82.8	42.8	26.8	7.2	0.7
<sup>232</sup> Th resonances					
res.par.	1	2	3	4	5
$E_0$	21.78	23.45	59.46	69.13	112.9
$\Gamma_n$	2.00	3.74	4.00	42.0	12.4
$\Gamma_\gamma$	25.9	25.9	25.9	25.9	25.9
$\sigma_0$	8658	14155	5918	23537	7543
$(\frac{1-\alpha_A}{2})\frac{E_0}{\Gamma_{pr}}$	0.19	0.15	0.60	0.15	0.79
$\zeta$	0.20	0.21	0.13	0.27	0.12
$\frac{\sigma_0 \Gamma_\gamma}{E_0}$	10.3	15.6	2.6	8.8	1.7
<sup>240</sup> Pu resonances					
res.par.	1	2	3	4	5
$E_0$	1.056	20.46	38.34	41.64	66.66
$\Gamma_n$	2.44	2.20	17.0	15.5	50.0
$\Gamma_\gamma$	29.6	30.0	30.0	33.0	31.0
$\sigma_0$	189650	8782	24810	20184	24352
$(\frac{1-\alpha_A}{2})\frac{E_0}{\Gamma_{pr}}$	0.002	0.15	0.12	0.14	0.12
$\zeta$	1.06	0.24	0.26	0.26	0.34
$\frac{\sigma_0 \Gamma_\gamma}{E_0}$	5316	12.9	19.4	16.0	11.3





# Nomenclature

a	year
AVR	Arbeitsgemeinschaft Versuchsreaktor
BBC	Brown Boveri and Cie
BISO	Two-layer coating (PorC-PyC)
BOL	Begin Of Life
BONAMI-S	SCALE module for resonance self-shielding by the Bondarenko method
BWR	Boiling Water Reactor
Bq	Bequerel (1 Bq = 1 disintegration per second)
CAPRA	Consommation Acrué de Plutonium dans réacteurs RAPide
CCGT	Closed Cycle Gas Turbine
CP	Coated Particle
CZP	Cold Zero Power
Ci	Curie (1 Ci $\equiv$ $3.7 \cdot 10^{10}$ Bq)
diam	diameter
EOL	End Of Life
eV	electronVolt (1 eV = $1.6022 \cdot 10^{-19}$ J)
FIMA	Fissions per Initial Metal Atoms
FPY	Full-Power Year
FP	Fission Product
FTCs	Fuel Temperature Coefficient of Reactivity
FZ	5-cm-diam Fuel Zone of an HTR pebble
FI	Fuel
GHR	Gasgekühlter HeizReaktor
g	gram
GT	Gas Turbine
GW	GigaWatt ( $10^9$ W)
GW <sub>th</sub> <sup>a</sup>	GigaWatt thermal year
GW <sub>e</sub> <sup>a</sup>	GigaWatt electric year
HFP	Hot Full Power
HM	Heavy Metal
HTR	High Temperature (gas cooled) Reactor
HZP	Hot Zero Power
hr	hour
ISR	Institut für Sicherheitsforschung und Reaktortechnik, Forschungszentrum Jülich
JEF	Joint Evaluated File

kgHM	kilogram Heavy Metal
kgPu	kilogram plutonium
KWU	Kraftwerkunion
kW	kiloWatt
LEUPRO	Low-Enriched Uranium PROTEUS Experiment
LHS	Left Hand Side
LOCI	Loss Of Coolant Incident
LOCWS	Loss Of Cooling Without Scram
LOFI	Loss Of Flow Incident
LWR	Light Water Reactor
MCNP	A general Monte Carlo code for Neutron and Photon transport
MEDUL	MEhrfachDUrchLauf
MF	moderator-to-fuel ratio
MHTGR	Modular High Temperature Gas-Cooled Reactor
MJ	MegaJoule ( $10^6$ J)
MOX	Mixed OXide
MTC	Moderator Temperature Coefficient of reactivity
MW	MegaWatt ( $10^6$ W)
MWd	MegaWatt day
NITAWL	SCALE system module for performing resonance shielding and working library production
NRG	the Nuclear Research and Consultancy group, the Netherlands
NRIM	Narrow Resonance Infinite Mass
ORIGEN	SCALE system module to calculate fuel depletion, actinide transmutation, fission product buildup and decay, and associated radiation source terms
PAP	Peu-à-Peu
PUREX	Plutonium Uranium Recovery by Extraction
PWR	Pressurised Water Reactor
PorC	Porous Carbon
PyC	Pyrolytic Carbon
RHS	Right Hand Side
RI	Resonance Integral
RB	Release/Birth ratio
SCALE	A modular code system for performing standardized computer analyses for licensing evaluation
START	Strategic Arms Reduction Treaty
SiC	Silicon Carbide
Sv	Sievert, unit of Dose Equivalent ( $1 \text{ Sv} = 1 \text{ J/kg}$ )
TRISO	Four-layer coating (PorC-PyC-SiC-PyC)
TRU	TRansUranium elements
UTC	Uniform Temperature Coefficient of reactivity
WIMS	ANSWERS Software Package for Neutronics Calculations
XSDRNPM-S	A 1-D discrete-ordinates module of the SCALE system for transport analysis
ZrC	Zirconium Carbide

spectral parameters are in good agreement. Burnup calculations performed with SCALE and WIMS7b reveal that the evolution of the infinite multiplication factor is quite sensitive to the effective energy yields per fission. Extension of the WIMS '1997' library with resonance data for  $^{241}\text{Pu}$ ,  $^{242}\text{Pu}$  and the minor actinides shows an improvement.

A parameter study, in which the plutonium mass per pebble, the coated particle type, the moderator temperature and the fuel temperature are varied, is performed with the code system WIMS7b. For different combinations of these parameters, several reactor physics parameters are calculated. The fuel and moderator temperature coefficients of reactivity are studied comprehensively. All pebble configurations show a negative fuel temperature coefficient. A generic study on the maximisation of the Doppler effect is presented in appendix C. The moderator temperature coefficient shows quite an unconventional behaviour. It decreases from a positive value at low moderator temperatures to a negative value at high temperature, in case of relatively low plutonium masses per pebble. However, plutonium loadings of 1 g per pebble and more show a negative moderator temperature coefficient for the full temperature range of interest in combination with a broad burnup range. The Pu-loading is constrained by the maximally allowed fast fluence. The presumed boundary value is exceeded in case of 3 g plutonium per pebble and higher.

On the basis of these findings a reactor design with both 1 and 2 g plutonium per pebble is presented. Coupled thermal-hydraulic/neutronical calculations are performed with the PANTHER/THERMIX-DIREKT code system. The nuclear data for the purpose of PANTHER is supplied by WIMS7b. The reactor design (40 MW<sub>th</sub>, Peu-à-Peu fuelling) constitutes a first try that has not been subject to any optimisation yet. Burnup calculations are performed for both Pu-loadings. To this end, the pebble bed of the calculational model is continuously increased until the top of the core is reached. At 'End of Life', the 2-g configuration realises a fissioned fraction per initial heavy metal atom of 65%, on average, and 75%, maximally. The startup and shutdown behaviour is studied for both Pu-loadings, for both the initial and the final core. A startup procedure analogous to that of a Pressurised Water Reactor is presumed. The core with 1 g Pu/pebble shows a positive power coefficient of reactivity for powers lower than 15 MW<sub>th</sub> (no Xenon, End Of Life). Since the 1-g configuration achieves, moreover, a lower burnup than its 2-g counterpart, the 2-g configuration has preference. Two loss-of-cooling incidents without scram are simulated for both Pu-loadings, for both the initial and the final core. The results of the PANTHER/THERMIX-DIREKT calculations are interpreted by means of some analytical expressions that appeared in a publication in which the fundamental physical aspects of a loss-of-cooling incident were studied on the basis of a space-independent reactor model. In all loss-of-cooling scenarios, the temperature remains well below the presumed limit of 1444 °C, which demonstrates the passive safety of the system.

---

## Summary

---

Since the beginning of the nuclear era plutonium has been separated in reprocessing plants in many countries. As any serious reuse of the plutonium never got off the ground, the world inventories of plutonium have been increasing ever since. The stocks have been increasing even more due to the dismantlement of nuclear arms as a result of the implementation the START-treaties. In 1994, the world-wide stocks amounted to 1160 tons. The recycling of plutonium failed to come due to low natural uranium prices caused by the declined growth rate of world-wide nuclear energy production and the discovery of new uranium-ore sites as well as the unforeseen stay-away of fast reactors in the fuel cycle. Although there are no economical motives to use the plutonium as reactor fuel, many countries presently make efforts to recycle the plutonium in existing reactors or to develop advanced reactors dedicated to this task. These efforts seem to be based on incentives like fear for proliferation, a sparingly use of the natural resources and reduction of the radiotoxicity of the nuclear waste.

Various reactor concepts are assessed on the basis of their plutonium burning characteristics. In view of radiotoxicity reduction the transuranic (TRU) consumption is regarded rather than solely the plutonium consumption. The maximum TRU-consumption of 375 MWd/kgHM is obtained in the absence of uranium. Achieving this maximum TRU-consumption is the first objective of this thesis. The second one embraces the minimisation of the TRU-discharge. In the absence of uranium, this simply corresponds to a maximisation of the burnup. Properties like the possibility of continuous fuelling and de-fuelling, a solid moderator and the feasibility of high burnups make the pebble-bed HTR a viable candidate as a plutonium burner.

The aforementioned objectives can only be achieved within the safety constraints of the system. The basic principle as regards the design of plutonium burning HTR embraces the preservation of the passive safety features similar to most UO<sub>2</sub>-fuelled HTRs. This essentially means that the reactor should be able to endure a loss-of-cooling incident without scram without the temperature exceeding the maximally permissible value. Irradiation experiments in the 1970s pointed out that coated particles remain intact up to a burnup of 740 MWd/kgHM in conjunction with a temperature of 1444 °C. Therefore, these figures are adopted as boundary values of the design.

Unit-cell calculations for 1 and 2 g Pu per pebble as well as for different types of coated particles are performed with the code packages MCNP4A, WIMS7b and SCALE-4. The calculational models do not contain any uranium, thorium, nor any burnable poisons. For the purpose of the resonance shielding calculations, carried out by the latter two codes, an analytically derived expression for the Dancoff factor of the fuel kernel of a coated particle is used. Appendix A presents its derivation. The infinite multiplication factors and

---

## Samenvatting

---

Door de ontdekking van nieuwe uraniumertslocaties, het afvlakken van de groei van kernenergie in de wereld, de daaraan gekoppelde lage uraniumprijs en het uitblijven van snelle reactoren in de splijstofcyclus, wordt het plutonium dat tot op heden in opwerkingsfabrieken is afgescheiden slechts op bescheiden schaal gerecycleerd in kernreactoren. Hierdoor stapelt de hoeveelheid plutonium in de wereld zich op. Door de ontmanteling van kernwapens op basis van de START-akkoorden is zij nog verder toegenomen. In 1994 bedroeg de wereldvoorraad plutonium 1160 ton. Hoewel voor het hergebruik van plutonium vooralsnog geen economische motieven bestaan, spannen veel landen zich in om het plutonium in bestaande of nog te ontwikkelen reactoren te versplijten. Deze inspanningen lijken te zijn ingegeven door een mengeling van politieke en maatschappelijke prikkels zoals angst voor proliferatie, het spaarzaam gebruik van natuurlijke hulpbronnen en de reductie van de radiotoxiciteit van het kernafval.

Verscheidene reactorconcepten zijn vergeleken op grond van hun plutoniumverbrandingskarakteristieken. Uit het oogpunt van radiotoxiciteit-reductie is gekeken naar de transuranium (TRU)-consumptie in plaats van louter de plutoniumconsumptie. De TRU-consumptie is maximaal als het gebruik van uranium vermeden wordt; in dat geval bedraagt zij, voor een willekeurige reactor, ongeveer 375 kg/GW<sub>th</sub>a. Het behalen van deze TRU-consumptie is een van de doelstellingen bij het ontwerp van een kogelbedtype Hoge Temperatuur Reactor. De tweede doelstelling behelst het streven naar een minimale ontlasting van de TRU-massa, hetgeen overeenkomt met het maximaliseren van de opbrand. Eigenschappen als een continue ballentoevoer en -afvoer, een vaste moderator en een hoge opbrand maken de kogelbedtype HTR een geschikte kandidaat voor het 'verbranden' van plutonium.

De genoemde doelstellingen kunnen uiteraard alleen worden gerealiseerd binnen dusdanige randvoorwaarden dat de veiligheid van het systeem te allen tijde gewaarborgd is. Uitgangspunt bij het ontwerp van de HTR-Pu is de handhaving van de passieve veiligheidskenmerken zoals die voor de meeste, met UO<sub>2</sub> bedreven, HTR's gelden. Dit betekent bijvoorbeeld dat de reactor een incident, waarbij het actieve koelvermogen van de reactor wegvalt en waarbij bovendien de reactor niet met regelstaven afgeschakeld wordt, kan doorstaan zonder dat daarbij de temperatuur boven de toegestane waarde uitkomt. Bestralingsexperimenten bij een temperatuur van 1444 °C hebben aangetoond dat speciale TRISO 'coated particles' intact blijven tot een opbrand van 740 MWd/kgHM. Genoemde getallen zijn dan ook als randvoorwaarden verondersteld.

Eenheidcelberekeningen met betrekking tot HTR-ballen met 1 en 2 gram plutonium per bal en verschillende 'coated particle' typen zijn uitgevoerd met de codepakketten MCNP4A,

WIMS7b en SCALE-4. De modellen bevatten geen uranium, geen thorium, noch enig slijtend gif. Ten behoeve van de resonantiezelfafschermingsberekeningen met WIMS7b en SCALE-4 is gebruikt gemaakt van een formule voor de Dancoff-factor van een splijstofkorreltje. Appendix A presenteert de afleiding hiervan. Voor de drie codes komen de oneindige multiplicatiefactoren en spectrale parameters goed overeen. Opbrandberekeningen met SCALE-4 en WIMS7b tonen aan dat het verloop van de oneindige multiplicatiefactor gevoelig is voor de energieproductie-getallen per splijting. Uitbreiding van de WIMS-bibliotheek met resonantie-data voor  $^{241}\text{Pu}$  en  $^{242}\text{Pu}$  en de 'minor actinides' laat een verbetering zien.

Een parameterstudie is uitgevoerd met WIMS7b, waarbij de plutoniummassa per bal, het type 'coated particle', de temperatuur van de splijstof en de temperatuur van de moderator zijn gevarieerd. Voor verschillende parametercombinaties zijn diverse reactorfysische parameters berekend. De splijstof- en moderator temperatuurcoëfficiënt zijn uitgebreid bestudeerd. Alle configuraties laten een negatieve splijstoftemperatuurcoëfficiënt zien. Een generieke studie naar de maximalisatie van de splijstoftemperatuurcoëfficiënt is gepresenteerd in appendix C. In het geval van relatief lage plutoniummassa's per bal neemt de moderator temperatuurcoëfficiënt met het toenemen van de moderator temperatuur af, van een positieve waarde tot een negatieve. Echter, plutoniumbeladingen van 1 gram per bal en hoger laten, tot aan een hoge opbrand, een negatieve moderator temperatuurcoëfficiënt zien. De plutoniummassa per bal is aan de bovenzijde begrensd door de fluentie van snelle neutronen. Voor 3 gram Pu per bal wordt bij 700 MWd/kgHM de maximaal toelaatbaar geachte snelle fluentie overschreden.

Op grond van het voorafgaande is gekozen voor een reactorontwerp met 1 en 2 gram Pu per bal. Met het PANTHER/THERMIX-DIREKT codesysteem zijn neutronisch-thermohydraulisch gekoppelde berekeningen uitgevoerd. De nucleaire data ten behoeve van PANTHER zijn gegenereerd met WIMS7b. Het reactorontwerp (40 MWth, Peu-à-Peu ballentoevoer) betreft een 'first try' waarvoor nog geen optimalisatie heeft plaatsgevonden. Voor beide configuraties zijn opbrandberekeningen uitgevoerd. Hiertoe wordt in het reactormodel het kogelbed opgehoogd totdat de bovenkant van de kern bereikt wordt. Met de 2-gram configuratie wordt een versplijtingsgraad verkregen van gemiddeld 65% en maximaal 75%. Het opstart- en afschakelgedrag van de reactor is bestudeerd voor beide beladingen, voor zowel de begin- als de eindkern. Hierbij is een procedure verondersteld die analoog is aan die van een drukwaterreactor. De kern met 1 gram Pu per bal laat een positieve vermogenscoëfficiënt beneden 15 MW<sub>th</sub> zien. Dit gegeven, evenals een lagere opbrand in het geval van 1 gram Pu per bal, betekent dat de Pu-belading van 2 gram per bal de voorkeur heeft. Voor beide Pu-ladingen evenals voor de begin- en eindkern zijn twee gepostuleerde incidenten gesimuleerd, waarbij het koelvermogen wegvalt en waarbij bovendien verzuimd wordt de reactor af te schakelen. In alle scenario's blijkt de splijstoftemperatuur onder de maximaal toelaatbare waarde van 1444 °C te blijven, hetgeen de passieve veiligheid van het systeem in het geval van deze incidenten aantoont. De resultaten van de PANTHER/THERMIX-DIREKT transiëntberekeningen zijn verklaard aan de hand van een in de literatuur verschenen analyse van het hiervoor beschreven incident op basis van een puntreactormodel.

---

# Acknowledgement

---

First of all, I would like to thank Prof. Dr Ir H. van Dam for his encouragement, his fruitful advice and the pleasant co-operation he established.

I wish to express my gratitude to my daily supervisor Dr Ir J.L. Kloosterman for coaching me, for the valuable discussions we had and for the useful comments he gave on my draft texts.

I acknowledge the financial support of my research by PINK (the Programme to maintain nuclear competence) of the Dutch Ministry of Economic Affairs.

Furthermore, I would like to thank Dr Ir E. Hoogenboom and Prof. Dr Ir T.H.J.J. van der Hagen of the Interfaculty Reactor Institute in Delft for teaching me the basic principles of reactor physics.

Afraid of unintentionally omitting somebody I do not mention any of my colleagues at NRG explicitly, but instead I would like to thank all of them who in some way made a contribution to the realisation of this thesis. Without their help this work would never have been accomplished.

Finally, I owe a great debt of gratitude to the late Dr H. Gruppelaar, who passed away last November after a long struggle with the disease ALS, for the opportunity of performing this Ph.D. study at ECN/NRG.





---

## Curriculum Vitae

---

Evert Bende was born on March 13, 1969 in the Zuidelijke IJsselmeerpolders, the Netherlands. After completing his secondary school education ("VWO") at the Geert Groote College in Deventer, he started to study physics at the University of Utrecht. In his fourth year at university he did research in the field of two-dimensional electron transport in sub-micron semiconductors at Philips Research Laboratories ("Natuurkundig Laboratorium") in Eindhoven. He performed his graduate work at the FOM Institute of Plasma Physics, Rijnhuizen under the supervision of Prof. Dr Ir T.J. Schep. He wrote a Master's dissertation entitled "Current-sheet dynamics with resistivity and inertia effects in a two-fluid plasma". He obtained his Master's degree in Theoretical Physics in October 1993. From November 1993 to September 1994 he fulfilled his military service as "Wachtmeester Anti-Tank" at B-104 Reconnaissance Battalion of the "Huzaren van Boreel" in Nunspeet. From October 1994 to May 1995 he was employed by Cap Gemini as a software engineer. The next four years the author was affiliated with the Nuclear Energy Department of the Energy Research Foundation ECN in Petten, which in 1998 became, through a merger with the Nuclear Energy unit of the KEMA in Arnhem, the Nuclear Research and Consultancy Group, NRG. With the financial support of the "Programme to maintain nuclear competence" (PINK) of the Dutch Ministry of Economic Affairs he performed a study on plutonium burning in a pebble-bed type High Temperature Nuclear Reactor which resulted in this doctoral thesis. This study was supervised by Dr Ir J.L. Kloosterman and by promotor Prof. Dr Ir H. van Dam of the Interfaculty Reactor Institute (IRI) of Delft University of Technology.

